The Dissertation Committee for Andrew Jeffrey Gross Certifies that this is the approved version of the following dissertation:

Towards the predictive modeling of ductile failure

Committee:

Krishnaswamy Ravi-Chandar, Supervisor

Chad Landis

Desiderio Kovar

Kenneth Liechti

Stelios Kyriakides

Towards the predictive modeling of ductile failure

by

Andrew Jeffrey Gross, B.S.

Dissertation

Presented to the Faculty of the Graduate School of

The University of Texas at Austin

in Partial Fulfillment

of the Requirements

for the Degree of

Doctor of Philosophy

The University of Texas at Austin

December 2015

Dedication

To my wife, Allie, for encouraging me to pursue this degree in the first place, and for the sacrifices that you have made along the way.

Acknowledgements

I am appreciative for the support of my family during the last several years. For Allie's encouragement and genuine understanding throughout each stage of earning this degree, for the always enjoyable discussions with Ben as we both continue on in academia, and for all the ways my parents have equipped me to take on such an endeavor. I am also fortunate to have worked with Dr. Ravi-Chandar as my Ph.D. adviser and am very appreciative of the experiences he has provided me while under his mentorship. Finally, this time would not have been the same if not for the fellow students and postdocs that I have met over the past years: Adam Sierakowski, Seung Na, Sundeep Palvadi, Hamed Khatam, Shixuan Yang, Nikolas Bouklas, Ian Jesse, Khai Pham, Nate Bechle, Martin Scales, Isaac Lee, Xavier Poulain, and Gary Simpson.

Towards predictive modeling of ductile failure

Andrew Jeffrey Gross, Ph.D.

The University of Texas at Austin, 2015

Supervisor: Krishnaswamy Ravi-Chandar

The ability to predict ductile failure is considered by an experimental examination of the failure process, validation exercises to assess predictive ability, and development of a coupled experimental-numerical strategy to enhance model development.

In situ loading of a polycrystalline metal inside a scanning electron microscope is performed on Al 6061-T6 that reveals matrix-dominated response for both deformation and failure. Highly localized deformation fields are found to exist within each grain as slip accumulates preferentially on a small fraction of crystallographic planes. No evidence of damage or material softening is found, implying that a strain-to-failure model is adequate for modeling fracture in this and similar material.

This modeling insight is validated through blind predictive simulations performed in response to the 2012 and 2014 Sandia Fracture Challenges. Constitutive and failure models are calibrated and then embedded in highly refined finite element simulations to perform blind predictions of the failure behavior of the challenge geometries. Comparison of prediction to experiment shows that a well-calibrated model that captures the essential elastic-plastic constitutive behavior is necessary to capture confidently the response for structures with complex stress states, and is a prerequisite for a precise prediction of material failure.

The validation exercises exposed the need to calibrate sophisticated plasticity models without a large experimental effort. To answer this need, a coupled experimental and numerical method is developed for characterizing the elastic-plastic constitutive properties of ductile materials using local deformation field information to enrich calibration data. The method is applied to a tensile test specimen and the material's constitutive model, whose parameters are unknown *a priori*, is determined through an optimization process that compares these experimental measurements with iterative finite element simulations. The final parameters produce a simulation that tracks the local experimental displacement field to within a couple percent of error. Simultaneously, the percent error in the simulation for the load carried by the specimen throughout the test is less than one percent. The enriched calibration data is found to be sufficient to constrain model parameters describing anisotropy that could not be constrained by the global data alone.

Table of Contents

List of Tables xi

List of Figures xii

Chapter 1: Introduction 1

Chapter 2: Deformation and Failure of Al 6061-T6 at Low Triaxiality 6

2.1 Introduction 6

2.2 Experimental Design for Microscopic Observations 8

2.2.1 Design of a Shear-Dominant Specimen 8

2.2.2 Specimen Preparation 11

2.3 Experimental Results 12

2.3.1 Global Response of the Specimen 12

2.3.2 Measurement of the Local Strain Variation in the Specimen 14

2.3.3 Discrete Deformation of the Matrix 16

2.3.4 Fracture and Debonding of the Second Phase Particles 19

2.3.5 Deformation of the Pre-exsting Voids 23

2.3.6 Summary of Observations on Deformation, Debonding, Fracture, and Voids 25

2.4 Discussion 28

2.5 Conclusion 31

Chapter 3: Prediction of Ductile Failure in 15-5 PH Stainless Steel Using a Local Strain-to-Failure Criterion 53

3.1 Introduction 53

3.2 Constitutive and Failure Models 54

3.2.1 Calibration of constitutive model 55

3.2.2 Calibration of failure model 58

3.3 Blind Prediction of the Response of the Challenge Geometry 63

3.4 Additional Experiments Exploring Crack Path Selection 68

3.4.1 Failure path A-C-E 70

3.4.2 Failure path A-D-C-E 72

3.4.3 The competition between failure paths A-C-E and A-D-C-E.....75
3.5 Additional Simulations Exploring Crack Path Selection.....76
3.6 Conclusion 78
3.6.1 Recommendations for Additional Material Testing: 79

Chapter 4: Prediction of Ductile Failure in Ti-6Al-4V using a local strain-to-failure criterion 110
4.1 Introduction.....110
4.2 Constitutive and failure models 112
4.2.1 Calibration of the constitutive model.....112
4.2.1.1 Calibration simulation setup.....116
4.2.1.2 Boundary Conditions.....117
4.2.1.3 Optimization details 118
4.2.2 Calibration of the failure model.....121
4.3 Results of Blind Prediction of the Challenge Problem 123
4.4 Additional Experiments 128
4.4.1 Experimental setup.....128
4.4.2 Load-COD1.....130
4.4.2.1 Ligament failure sequence in the slow-rate tests 131
4.4.2.2 Strain field measurement.....132
4.4.2.3 Microscopy.....134
4.5 Discussion 136
4.5.1 Plasticity.....136
4.5.2 Voids.....139
4.5.3 Failure 140
4.6 Conclusion 141
4.6.1 Recommendation to improve predictive ability.....142

Chapter 5: Extraction of Elastic-Plastic Constitutive Properties from Three-Dimensional Deformation Measurements 166
5.1 Introduction.....166
5.2 Inverse problem in material property characterization 170

5.3 Experiment 174
5.4 Material Model 180
5.5 Numerical simulation of the BVP 185
5.5 Optimization 186
5.5.1 Comparison between experiment and simulation 186
5.5.2 Avoidance of spatial bias in the displacement error 187
5.5.3 The objective function 189
5.5.4 Selection of parameters 191
5.6 Results and Discussion 194
5.7 Conclusion 202
Chapter 6: Conclusion 226
6.1 Summary 226
6.2 Future Work 227
References 229

List of Tables

Table 3.1: Material parameters used in these simulations. Parameters labeled as "modified" were not part of the blind prediction, and were used only after the experimental results were released. 81

Table 4.1: Anisotropic elastic moduli 144

Table 4.2: Inverse calibration simulation details 144

Table 4.3: Plasticity model parameters extracted by the inverse method 144

Table 4.4: Prediction simulation details.....145

Table 4.5: Predicted quantities of interest for the challenge geometry subjected to slow and fast rate loading 145

Table 5.1: The optimized parameters defining the stress strain curve and plastic anisotropy for the load and displacement-optimized cases. Note that there were only two degrees of freedom in the anisotropy, however all the resulting parameters for the yield criterion and the Lankford parameter are listed for completeness. 204

List of Figures

Figure 1.1: The dimpled fracture surface of Ti-6Al-4V.....4

Figure 1.2: Depiction of the (a) initial microstructure with sites of preferable void nucleation, (b) void growth at a subset of nucleation sites, (c) the coalescence of voids, and (d) the material after fracture. 5

Figure 2.1: Strain to failure as a function of triaxiality from three independent investigations for Al 6061-T6. The use of grain level strain measurements has a profound effect on the failure strain.....33

Figure 2.2: Specimen design to create shear dominated deformation between the notches when extension is applied with wedge grips at the specimen ends. The mesh discretization used for FEM is also pictured, to show the very fine mesh used in the vicinity where the notch collapses into a cusp like feature. 34

Figure 2.3: Predicted strain and triaxiality variation on the specimen's surface at three levels of deformation. Note how plastic deformation causes the initially rounded notches to deform into sharp features, and the strong gradient in triaxiality around these features. The triaxiality in the heavily strained region away from the notches is maintained close to zero..35

Figure 2.4: Equivalent plastic strain variation with triaxiality in the specimen from finite element analysis. The center of the specimen undergoes extensive straining with nearly vanishing triaxiality. Some points on the notch surface pass across the cusp tip, while experiencing a rapid increase in both strain and triaxiality. The curve labeled “Cusp 1” corresponds to an element that passes over the cusp tip at a lower level of deformation than the element corresponding to the curve labeled “Cusp 2.” 36

Figure 2.5: The load elongation curve for the specimen. The small disturbances in load seen are the displacement levels where the loading was paused to take high resolution images. The load drift during imaging is likely caused from thermal loading. 37

Figure 2.6: SEM images of the deformation in the sheared region of the specimen in the a) unstrained state and the b) first c) second d) third and e) fourth levels of deformation. The red line shows the displacement predicted by the FEM simulation, which shows reasonable agreement to the experimental result. 38

Figure 2.7: The equivalent plastic strain field at stages D1-D4, determined by tracking approximately 90 particles. (a) Initial positions of the identified points and an example of the Delaunay triangulation that was performed at each stage of deformation. The color map for each Figure 2.has a maximum of (b) 0.35, (c) 0.8, (d) 1.7, and (e) 3. 39

Figure 2.8: Snapshots focusing on the plastic deformation of a grain taken at *D0-D4*. The equivalent plastic strain in the vicinity of the central grain is estimated to be b) 0.13, c) 0.50, d) 1.1 and e) 2.2. The grain boundary is made clearly visible by out of plane grain boundary sliding and is traced by the red dashed line. Extreme deformation and extensive slip is seen on multiple slip systems without any indication of voiding, cracking, or damage within the grain. 40

Figure 2.9: Snapshots of a particle cracking taken at D0-D4. The equivalent plastic strain in the vicinity of the particle is estimated to be b) 0.16, c) 0.32, d) 0.77 and e) 1.3. The particle is seen to have cracked by D2, after the second slip system has been activated. The crack has opened up a void visible in D3, however, no void growth occurs between D3 and D4 and deformation between the particle fragments occurs by slip along the red dashed line. 41

Figure 2.10: Snapshots of a particle cracking taken at D0-D2 and D4. The equivalent plastic strain in the vicinity of the particle is estimated to be b) 0.16, c) 0.39, d) .53, and e) 0.55. Particle cracking is seen to have occurred by D1, where a concentration of activity on the first activated slip system intersects the particle. The crack opens a void that grows up until D3, but does not grow between D3 and D4. 42

Figure 2.11: Snapshots of a small particle cracking taken at D0-D4. The small particle in the center of the image is seen to be cracked in D3 where intersected by a slip trace. All other small particles remain intact; indicating that even small particles can crack, but only if they happen to be intersected by a slip line. 43

Figure 2.12: Snapshots of a particle that remains intact taken at D0, D1, and D4. The equivalent plastic strain in the vicinity of the particle is estimated to be b) 0.21 and c) 0.50. A rather large particle is found in between slip lines in D1. Despite continued deformation of the surrounding matrix material, the particle remains intact and bonded at D4.....44

Figure 2.13: Snapshots of a particle pair with debonding taken at D0-D2 and D4. Interaction between particles is likely, as the lower particle is seen to be partially debonded by D1 to accommodate the growing separation between its neighbor. The debonded length grows by D2, however, by D4 the particle seems to have partially re-embedded into the matrix, as the debonded length is slightly shorter. 45

Figure 2.14: Snapshots of a particle tearing the matrix taken at D0-D4. The equivalent plastic strain in the vicinity of the particle is estimated to be b) 0.22, c) 0.44, d) 1 and e) 1.1. Out of plane deformation is clearly occurring, causing the particle to emerge from the subsurface. This particle may have smaller flaws than most others, allowing it to remain intact despite large concentrations of slip activity intersecting it. Atypical debonding is seen where matrix material that flows past the sharp tip is seen to tear.....46

Figure 2.15: Snapshots of a particle debonding and then cracking taken at *D0-D4*. The equivalent plastic strain in the vicinity of the particle is estimated to be b) 0.15, c) 0.30, d) 1.5 and e) 2.2. A combination of particle debonding (initiated prior to *D1*), and cracking (seen twice, once at *D2* and again at *D3*). The nucleated voids initially grow, however, the one in between particle fragments is seen to partially collapse between *D3* and *D4*.....47

Figure 2.16: Snapshots of a strongly interacting particle pair taken at D0 and D1-D4. A concentration of plastic deformation is seen in between the two central particles in D2. This slip opens up a crack visible in D3. In D4 a crack initiated from the cusp links up to the interior crack, seemingly by coincidence. 48

Figure 2.17: Snapshots of a void at D0-D4. The equivalent plastic strain in the vicinity of the void is estimated to be b) 0.15, c) 0.37, d) 0.66 and e) 0.87. The void is seen to be completely unperturbed by the surrounding plastic deformation occurring on multiple slip systems. 49

Figure 2.18: Snapshots of a void pair deforming taken at D0-D4. These voids are seen to deform modestly in response to extensive deformation of the surrounding matrix.....50

Figure 2.19: Snapshots of a void taken at D0-D4. The equivalent plastic strain in the vicinity of the void is estimated to be b) 0.17, c) 0.37, d) 0.98 and e) 1.6. The central void is seen to show little deformation, at least up to D3. In D4, a crack exists not far to the left of the void and the extreme loading causes considerable shearing of the void. 51

Figure 2.20: Snapshots of a void taken at D0-D3. A large void near the initial notch is seen to be unperturbed by a state of positive triaxiality during D1 and D2. As it passes over the cusp to the side with negative triaxiality, the void is seen to be partially collapsed in D3. 52

Figure 3.1: Nominal stress vs nominal strain variation. Black line corresponds to experimental results from Sandia National Laboratories (Boyce et al., 2014) The red line was obtained from optimized simulations. 'x' marks the point of specimen failure.....82

Figure 3.2: The variation of the true stress with equivalent plastic strain corresponding to the optimized constitutive behavior. Note that the direct measurement–prior to necking–corresponds to strain levels less than about 0.055 (as indicated by the *black line*).....83

Figure 3.3: Overlay of the profile of the neck obtained from the optimized simulation on an image of the necked regions from the tensile experiment (image from Boyce et al. 2014) 84

Figure 3.4: A view of the *C*(*T*) specimen mesh, sectioned along the prospective fracture plane. The initial crack extends from the notch tip at the left to the thick curve that designates the location of the fatigue precrack. 84

Figure 3.5: Equivalent plastic strain in the *C*(*T*) specimen simulation. (a). COD = 0.39 mm (b). COD = 0.58 mm (c) COD = 0.87 mm. This view is sectioned along the prospective fracture plane as well as the specimen midplane.....85

Figure 3.6: Load-COD response of fracture specimen from the experiment and the optimized simulation.....86

Figure 3.7: Calibrated Johnson-Cook failure model with simulated failure paths shown 87
Figure 3.8: Details of the mesh used for the 2012 SFC geometry. A highly refined mesh was used in all areas of possible fracture. The locations I and II correspond to points where failure is most likely to initiate in their ligament.....88
Figure 3.9: Blind prediction of the load-COD response for the 2012 SFC geometry. The results at the marked points are discussed in the text and Figures 3.10 and 3.11.....89
Figure 3.10: Equivalent plastic strain development in the midplane. 90
Figure 3.11: Triaxiality development in the midplane. 91
Figure 3.12: Local strain and triaxiality variation over COD at the critical elements in ligaments *A*-*D* and *A*-*C*. 92
Figure 3.13: Equivalent plastic strain and triaxiality histories of critical elements. The path towards failure on ligaments *A*-*D*, *A*-*C* and *C*-*E* are shown. Failure of the ligament *A*-*C* is denoted by the black 'x' and at this stage the state of ligaments *C*-*E* and *A*-*D* are denoted by the blue and red circular symbols. Failure of the ligament *C*-*E* is identified by the blue 'x'...93
Figure 3.14: Load variation with COD for the blind prediction with the experimental results for specimen **D1**, performed at Sandia's Structural Mechanics Laboratory.....94
Figure 3.15: A close-up image of specimen **S11** prior to testing. The slot placement is within the specifications provided, but due to a machining error for hole *A*, the specimen was out of specification; a clear decrease in the size of the ligament *A*-*D* is evident in this image.....95

Figure 3.16: Experimental set-up. Note the double universal joints, the clevises with flat pin-holes to accommodate pin rolling, and the digital cameras for 3D-DIC image acquisition. 96

Figure 3.17: The load-COD variation for all experiments with crack path *A*-*C*-*E* in comparison with the blind prediction (black line). 97

Figure 3.18: Comparison of the equivalent plastic strain on the surface of the challenge specimen between the blind prediction (top row) and the experimental result from 3D-DIC on specimen **S09** (bottom row). The experimental result shows an overlay of the post processed strain on top of the raw image. The textured appearance of the specimen is from a random speckle pattern adhered to its surface, required to perform DIC. The black dot near the center of ligaments *A*-*C* and *A*-*D* marks the point where strain data for Figure 19 is taken from. (a) COD ~ 1 mm, (b) COD ~ 2 mm, (c) COD ~ 3 mm. 98

Figure 3.19: Variation of the plastic equivalent strain with COD on the surface of two ligaments (*A*-*C* and *A*-*D*) from the experiment (**S09**) compared to the blind prediction at the same locations. 99

Figure 3.20: High magnification image of the fracture surface in the center of ligament *A*-*C* from specimen **S10**. The surface is dominated by equiaxed dimples, but also shows some features significantly larger than the average grain size of ~4.7 μm. 100

Figure 3.21: The load-COD variation for specimen **S11** (black line) compared to Sandia's experiments that failed with the same crack path *A*-*D*-*C*-*E*. **S02** (red line) had the minimum COD at first failure and **S08** (green line) had the maximum COD at first failure. 101

Figure 3.22: High magnification image of the fracture surface in the center of ligament *A*-*D* from specimen **S11**. The surface has both equiaxed dimples and larger features that resemble cascading ledges.....102

Figure 3.23: Micrographs from the midplane of a specimen that was not loaded beyond the first dynamic cracking event. (a) Optical image of the ligament *A*-*D*, after etching. Holes *A* and *D* are located, and the specimen is oriented as pictured in Figure 8. The suspected site of crack initiation is circled in red. (b) SEM image of the suspected initiation site with fine cracks emanating towards holes *A* and *C*. (c) High magnification image of the suspected initiation site, where nearly equiaxed dimples are seen on the unpolished surface. (d) High magnification of the fine crack heading towards hole *D*. Some small voids that tend to form within a band only as wide as a few grains can be seen on the crack flanks. 103

Figure 3.24: The region circled in yellow in Figure 23(a) is shown here with higher magnification SEM images. 104

Figure 3.25: Comparison of the equivalent plastic strain on the surface of the challenge specimen between the experimental results from 3D-DIC on specimens **S09** (left) and **S11** (right). The black dot near the center of ligaments *A*-*C* and *A*-*D* marks the point where strain data for Figure 26 is taken from. (a) COD ~ 1 mm, (b) COD ~ 2 mm.....105

Figure 3.26: Variation of the equivalent plastic strain with COD on the surface of two ligaments (*A*-*C* and *A*-*D*) from specimen **S09** with crack path *A*-*C*-*E* compared to specimen **S11** with crack path *A*-*D*-*C*-*E*. 106

Figure 3.28: The equivalent plastic strain variation with the first 2.5 mm of COD at two selected locations is shown here. The experimental result is from specimen **S11**, the only specimen with crack path *A-D-C-E* for which 3D-DIC data is available. The non-blind simulation result shown here is for the specific geometry of specimen **S06**. 108

Figure 3.29: The load variation over the first 2.5 mm of COD from the experimental result for specimen **S06** and a non-blind simulation is shown here. The non-blind simulation differs from the blind one by taking into account the specific geometry of specimen **S06**, and by using a modified shear coefficient in the yield function. 109

Figure 4.1: The finite element meshes used in the inverse problem to extract constitutive and failure models. (a) Fast-rate tension (b) slow-rate tension, (c) slow-rate shear, (d) fast-rate shear 146

Figure 4.2: Simulated and experimental load elongation curves for the slow-rate calibration experiments. (a) RD tension, (b) TD tension, and (c) VA shear. 147

Figure 4.3: Simulated and experimental load elongation curves for the fast-rate calibration experiments. (a) RD tension and (b) VA shear. 148

Figure 4.4: (a) The strain hardening behavior extracted by the inverse problem. (b) One projection of the yield surface extracted by the inverse problem, compared with the von Mises surface for reference. 149

Figure 4.5: Finite element mesh used for the slow-rate challenge geometry prediction 150

Figure 4.6: Predicted and experimentally observed load-COD1 behavior for (a) slow-rate and (b) fast-rate tests. 151

Figure 4.7: Predicted equivalent plastic strain field on the mid-plane of the challenge geometry for the slow-rate at (a) COD1 = 1 mm, (b) COD1 = 2 mm, (c) COD1 = 3 mm, (d) COD1 = 4.63 mm (ligament *BD* is intact, *DE* is severed by a crack).....152

Figure 4.8: Predicted equivalent plastic strain field on the mid-plane of the challenge geometry for the fast-rate at (a) COD1 = 1 mm, (b) COD1 = 2 mm, (c) COD1 = 3 mm, (d) COD1 = 4.09 mm (ligament *DE* is intact, *BD* is severed by a crack).....153

Figure 4.9: Equivalent plastic strain variation with triaxiality for the most critical elements in ligaments *BD*, *DE*, and *AC*. Solid and dashed lines are for the slow- and fast-rates, respectively.....154

Figure 4.10: Experimental setup showing a challenge specimen mounted in an electromechanical load frame surrounded by four lights and being observed by: a DSLR camera for COD measurements, two CCD cameras for 3D-DIC, and a high speed camera to resolve the crack sequence.....155

Figure 4.11: Load variation with COD1 compared to the results from SNL.....156

Figure 4.12: Three sequential images from the high speed camera with the DIC displacement field overlaid. Positive displacement is downward. (a) Ligaments *BD* and *DE* intact, (b) ligament *BD* intact with ligament *DE* fully cracked, and (c) both ligaments fully cracked.....157

Figure 4.13: Overlay of the principal strain field for sample 13 on the image used for DIC. Data from the three points identified in the ligaments are plotted in Figure 4.14.....158

Figure 4.14: Maximum principal strain variation with COD1 for sample 5 at the locations identified in Figure 4.13. 159

Figure 4.15: Upper side fracture surface of ligament *BD* from sample five. The small dimples visible here are prevalent on the rest of the fracture surface. There is also a region of large dimples adjacent to an area that has been scraped by the opposing fracture surface to become nearly featureless. This pair of features appears at a modicum of other locations. 160

Figure 4.16: Region of the lower side fracture surface of ligament *BD* from sample five that directly opposes the region shown in Figure 4.15. The large dimples correspond to those visible in Figure 4.15. 161

Figure 4.17a: Observation of voids on the mid-plane near the surface of hole *D* from an interrupted test. Inlay shows the unstrained appearance of the surface at the same magnification. 162

Figure 4.17b: Observation of voids on the mid-plane in the ligament *BD*.....163

Figure 4.18: Comparison of the first principal strain fields for the prediction (first column) and those measured with 3D-DIC at (a) COD1 = 1 mm, (b) COD1 = 1.75 mm, and (c) COD1 = 2.0 mm 164

Figure 4.19: Comparison of the maximum principal strain development between the prediction and experimental DIC measurements for ligaments (a) *BD* and (b) *DE*. 165

Figure 5.1: A generic boundary value problem indicating the region of observation for acquiring additional kinematic measurements for use in the inverse problem. 205

Figure 5.2: (a) Drawing of the tensile specimen with dimensions in mm. Note the small curvature over the gauge section and square cross section. (b) Orientation of the tensile specimen relative to the natural directions of texture in the sheet. This is also the perspective that the specimen is viewed from by the stereo imaging system to capture deformation information on two orthogonal surfaces. The shaded area is the region observed by the imaging system. 206

Figure 5.3: Nominal stress strain curve for 15-5 PH in the H-1075 condition. Strain was measured with a DIC-based extensometer, completely spanning the necked region. The first load peak occurs at a strain of about 0.9%, the minimum is reached at a strain of about 1.4%, and the onset of necking occurs at a strain of about 7.6%. Full field strain contours are shown in Figure 4 at the points marked (a)-(d). 207

Figure 5.4: Spatial variation of the maximum true (logarithmic) principal strain field $\varepsilon_1(\mathbf{x})$ as measured from 3D-DIC at stages (a) - (d) marked in Figure 3. The front surface is the one below the corner and the side surface above. The white spaces are where DIC failed to correlate due to proximity to the specimen's corner or local defects in the speckle pattern. No filtering, smoothing, or interpolation have been used in calculating the strain field. 208

Figure 5.5: (a) Spatial variation of the true (logarithmic) strain field $\varepsilon_1(\mathbf{x})$ as measured from 3D DIC just prior to rupture. The maximum true strain measured is around one. The small black and red dots indicate locations along the midline of each surface where the spatial variation of strain is plotted in Figure 5b. The two large black dots are located at the center of necking. At these locations the stress state remains approximately uniaxial throughout the test. Strain data from these two points are used in Figures 5.6 and 5.7.....209

Figure 5.5: (b) Spatial variation of the longitudinal and transverse strains on both surfaces plotted at 30 second intervals for the last three minutes of the test (nominal strain values of 0.106, 0.117, 0.129, 0.142, 0.155, and 0.169). The longitudinal strains on both surfaces remain nearly identical to one another though the duration of the test. Transverse strains accumulate more rapidly on the side surface than the front, indicating a lower stiffness in the short transverse direction than long transverse.210

Figure 5.6: Variation of the transverse strain with respect to longitudinal strain at the deepest point in the neck on the front and side surfaces. The transverse strains develop nonlinearly with continued longitudinal straining, thus indicating that the anisotropy maybe evolving throughout the test. Evolution appears to be the most rapid around a longitudinal strain of 0.14, where the curvature of the lines reaches their maximum magnitude. 211

Figure 5.7: The transverse strains on both surfaces plotted against each other. The variation is nearly linear, with the slope of the line providing one of Lankford's parameters as 0.895. When investigated closely, the Lankford parameter is not constant; it varies most rapidly at the low strain range and then settles to a nearly constant value with increasing strain. This behavior is discernable from the measurements taken in this experiment, but the level of uncertainty is high to investigate this behavior closely. 212

Figure 5.8: Spatial discretization used for the FE model. Two of the three symmetries used are visible. Necking occurs at the symmetry plane on the right, where the refined mesh is located. The smallest mesh dimension is 76 μm. 213

Figure 5.9: Objective function value for the best member of each generation throughout the global optimization procedure. The curve is flat when a lower value for the objective function has not been found from the previous generation. 214

Figure 5.10: Comparison of the nominal stress strain curves produced by both objective functions to the experimental observation. Both of the simulated curves closely follow the experimental result. 215

Figure 5.11: Spatial distribution of the displacement error for the load optimized material just before rupture. The front surface is the lower area and the side surface is the upper area. The center of the neck is located at x=0. The region shown is not the entire surface, but corresponds to $x < 0$, $y > 0$, and $z > 0$. Error is relatively uniform across both surfaces within and beside the necked region. 216

Figure 5.12: Spatial distribution of the displacement error for the displacement optimized material just before rupture. The front surface is the lower area and the side surface is the upper area. The center of the neck is located at x=0. The region shown is not the entire surface, but corresponds to $x < 0$, $y > 0$, and $z > 0$. Error tends to be lower on the front surface and varies along the axis of the specimen. 217

Figure 5.13: Spatial (x-axis) and temporal (y-axis) variation of the displacement error along a line near the midline of the front surface for the load optimized material. Errors that are relatively spatially uniform increase most rapidly during necking. 218

Figure 5.14: Spatial (x-axis) and temporal (y-axis) variation of the displacement error along a line near the midline of the front surface for the displacement optimized material. Errors that are relatively spatially uniform increase most rapidly during necking. 219

Figure 5.15: Out of plane displacement on the midline of the front surface in the necked region. Both load and displacement optimized materials show satisfactory agreement. 220

Figure 5.16: Out of plane displacement on the midline of the side surface in the necked region. The displacement optimized material matches the experimental result much closer than the load optimized material does. 221

Figure 5.17: Strain hardening behavior for load and displacement optimized materials. The displacement optimized material is more compliant at high strains. The tangent modulus of the load optimized material is almost 25% stiffer at a (logarithmic) plastic strain of 0.5.....222

Figure 5.18: (a) Sensitivity of the displacement blind objective function to changes in the model parameters that define anisotropy. Data was produced using the load optimized strain hardening behavior and the values are normalized by the minimum. This objective function is not sensitive to changes in Lankford's value. 223

Figure 5.18: (b) Sensitivity of the displacement aware objective function to changes in the model parameters that define anisotropy. Data was produced using the displacement optimized strain hardening behavior and the values are normalized by the minimum. This objective function is sensitive to both parameters that define anisotropy. 224

Figure 5.19: Variation of the transverse strain with respect to longitudinal strain at the deepest point in the neck on the front and side surfaces. The results from the simulation with the displacement-optimized material parameters are overlaid on the experimental measurement. 225

Chapter 1: Introduction

Avoidance of fracture is one of the most basic requirements for engineering structures. For this reason most structures are stressed to a fraction of what can be endured by the material prior to failure, however, some applications require a structure to be pushed closer to the limit of failure. Such a situation is encountered in aerospace structures, nuclear power generation, and sheet metal forming. Further yet, some structures must be designed to undergo failure while in service, such as an automobile chassis during collision. Finally, failure can be put to constructive use, as it is in the cutting operations by which many machining processes operate. In all of these cases the ability to predict the conditions under which failure will initiate and how it will proceed is extremely valuable.

Current engineering practice is only able to produce reasonable fracture predictions for certain materials under particular loading conditions. Brittle materials under tensile loading are best understood, but as material ductility increases and loading conditions deviate from tensile, the ability to predict failure tends to degrade. Increasing predictive ability for the failure of ductile, polycrystalline metals is of particular importance as these materials are ubiquitous in engineered structures and current design paradigms are too conservative to keep up with the increasing demand for structural efficiency. In particular, failure places engineering limits that are not transparent to designers, and accurate modeling of failure will also allow for better design of failure tolerant structures, less trial and error in manufacturing, and increased collision protection.

Part of the difficulty in predicting ductile failure is that many materials with a rich variety of microstructures exhibit this behavior and a common mechanism between

different materials may have differing levels of importance. As a result, the nature of failure must be studied on a material by material basis to establish an appropriate approach to modeling. Furthermore, a consensus has not yet been reached on the relative importance of many mechanisms, and thus an appropriate modeling approach for even the most commonly used and studied materials is not agreed upon. Many different perspectives and models exist to describe ductile failure due to the complexity of the microstructure in these materials, the variety of mechanisms that occur, the difficulty of observing the initiation and evolution of failure, and then interpreting these observations.

The most common observation made of ductile failure is post-mortem microscopy of the fracture surface. The topography of a fracture surface is craterous and often almost completely covered by adjacent dimples as shown in Figure 1.1. The opposing fracture surface is populated by a complimentary set of such dimples. Thus, it can unambiguously be inferred that immediately before such a dimple on the surface was created, a void in the material existed. An individual surface dimple is the result of a void that ruptures, by merging with a neighboring void. This observation has led to the conclusion that ductile failure occurs through the nucleation, growth, and coalescence of voids, as depicted in Figure 1.2. Although this is undoubtedly the process just preceding material separation, post-mortem analysis cannot reveal the evolution of this process and whether it plays an important role in deformation. It is possible that other mechanisms dominate the progression towards ductile failure, and that modeling the nucleation, growth, and coalescence of voids is not necessary to predict ductile failure.

Another difficulty affecting predictive ability for the failure of ductile metals is that accurately predicting large deformation plasticity is a prerequisite. This subject in and of itself is the focus of extensive research; however, modeling techniques for many materials at the polycrystalline aggregate level are much better established than for

failure. The difficulty in plasticity prediction then lies in the effort required for proper calibration of an appropriate model.

The work in this dissertation is aimed at increasing the predictive ability for ductile failure. This is pursued by three distinct aspects relating to ductile failure to provide a broad perspective covering the mechanisms of failure, appropriate modeling of these mechanisms in predictive exercises, and improvements to model calibration. Chapter 2 investigates failure for a common material, Aluminum 6061-T6, through *in situ* shear dominated loading inside a scanning electron microscope. The goal of these experiments is to directly observe the evolution of the microstructure as the material approaches failure. These observations are then consolidated into a recommended modeling approach which is applied to perform two complete and independent predictions of ductile failure in Chapters 3 and 4. These predictions were made in response to both of the Sandia Fracture Challenges, exercises in which Sandia National Laboratories poses a problem of ductile fracture with an *a priori* unknown solution and collects predictions from an international group of teams. Only after predictions are collected, is the challenge problem "solved" experimentally, making this a truly blind prediction. The results of these exercises motivate the work in Chapter 5, where the use of full field deformation measurements of a tensile specimen are integrated with iterative finite element simulations in order to extract a plasticity model.

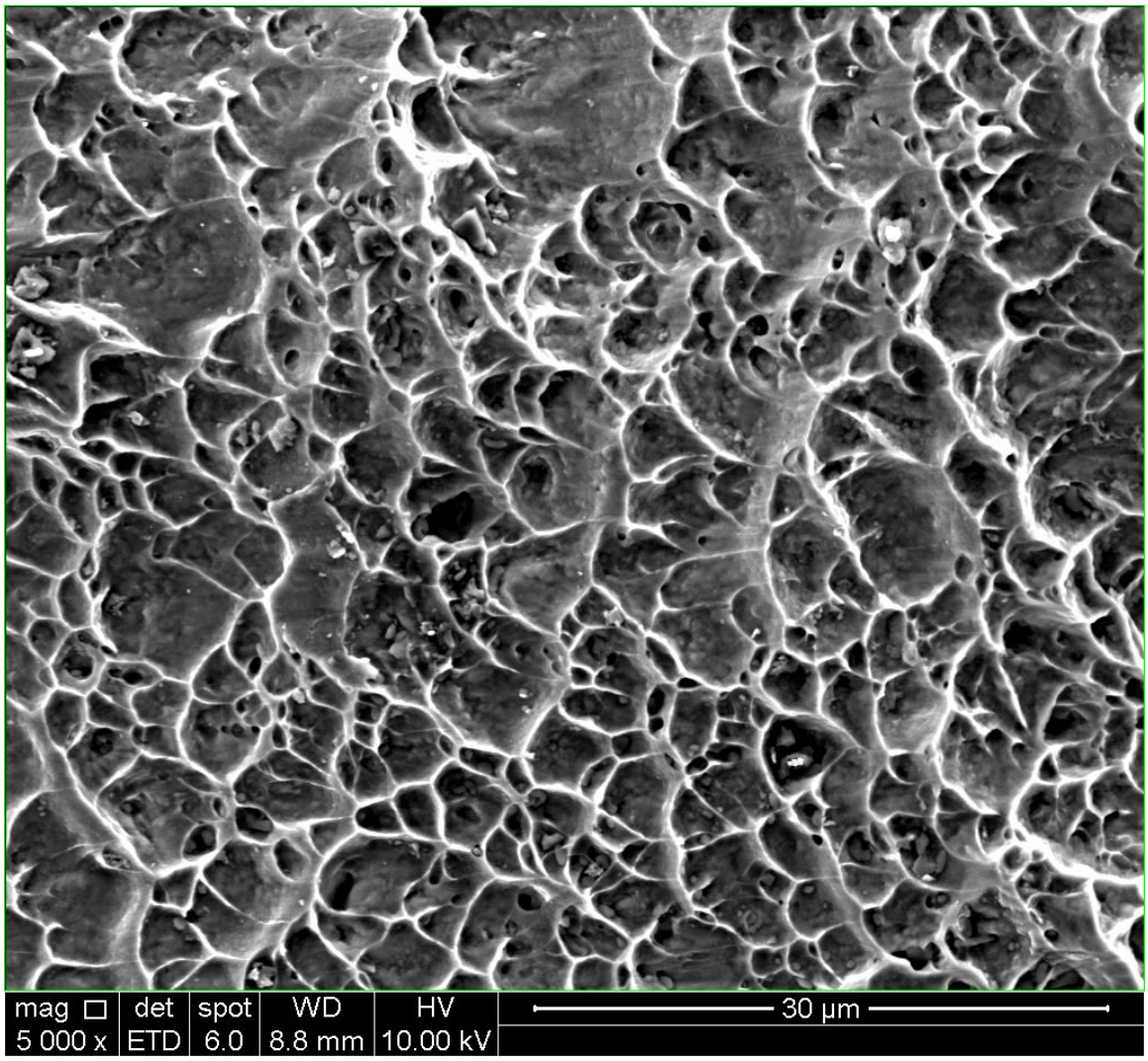

Figure 1.1: The dimpled fracture surface of Ti-6Al-4V.

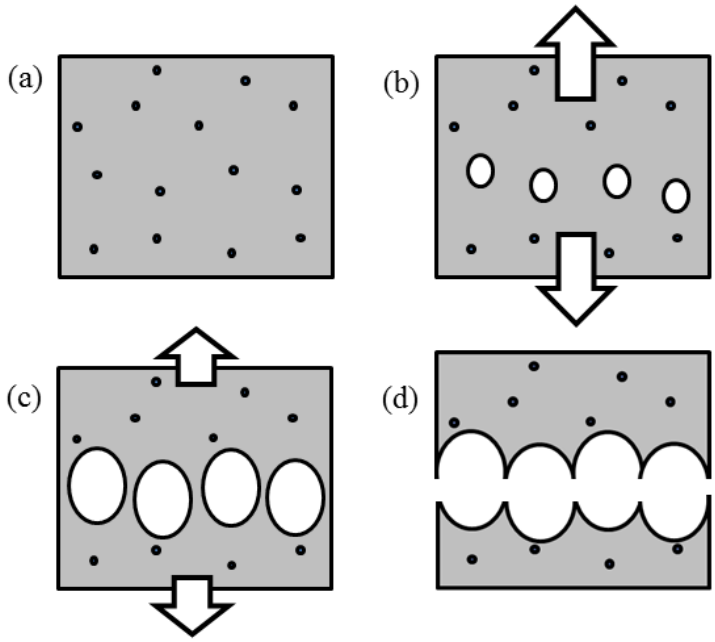

Figure 1.2: Depiction of the (a) initial microstructure with sites of preferable void nucleation, (b) void growth at a subset of nucleation sites, (c) the coalescence of voids, and (d) the material after fracture.

Chapter 2: Deformation and Failure of Al 6061-T6 at Low Triaxiality

2.1 INTRODUCTION

Extensive uncertainty has existed for decades about the nature of failure in polycrystalline metals under states of predominantly shear deformation. Understanding the failure of these materials began with observations correlating hydrostatic stress with ductility, such as that performed by Bridgman (1952). Orowan (1948), Tipper (1949) and Puttick (1960) observed that voids nucleate from second phase particles, then grow and coalesce to cause failure under conditions of positive triaxiality. Subsequent analysis by McClintock (1968) as well as Rice and Tracey (1969) showed void growth to be exponentially related to triaxiality. This led to the development of continuum damage models for these materials such as the Gurson–Tvergaard–Needleman (GTN) model, based on modeling the underlying void growth mechanics. However, in a state of continuing shear deformation, where triaxiality vanishes, this model does not allow for void growth, thus precluding its only measure of damage and failure from departing from its initial value. Modifications, to allow for shear failure have since been proposed (Nahshon and Hutchinson, 2008), but still carry the assumption that void mechanics drive damage and eventual failure.

Separately, several experimental investigations motivated by the work of Bao and Wierzbicki (2004) have been performed in the last decade that seem to indicate significant loss of ductility under shear dominated deformation as opposed to deformation at a higher level of triaxiality. This loss in ductility is thought to occur by a change in mechanism on the microscale from necking of inter-void ligaments to their shearing. In recent papers, Ghahremaninezhad and Ravi-Chandar (2012, 2013) and

Haltom et al. (2013) have observed that remarkably large deformations in Al 6061-T6 are not accompanied by damage in the form of voids. Critically, these measurements used the deformation of grain boundaries to estimate the strain. This is in contrast to more common methods of measurement, that systematically under-estimate the strain. The impact of this more accurate measurement on the calibration of failure models is considerable. The effect is demonstrated in Figure 2.1, where three strain to failure models for Al 6061-T6 calibrated by independent investigations are shown. The most conventional approach is the calibration by Leseur et al. (2001), measuring the strain-to-failure by macroscale techniques to calibrate a Johnson-Cook (1985) failure model. Also plotted is a projection of the modified Mohr-Coulomb failure model calibrated by Beese et al. (2010), where the failure strain in shear was measured with digital image correlation. The final curve is a modified Johnson-Cook failure model produced by Ghahremaninezhad and Ravi-Chandar (2012), where it can be seen that use of the grain-based measurements to calibrate a (lower-bound) strain-to-failure has a profound increase on the failure strain compared to the other two methods.

The purpose of the current work is to determine the mechanisms relating to shear deformation and failure of Al 6061-T6 sheet through *in situ* loading in a scanning electron microscope. The presence of any mechanism leading to a loss in ductility should become apparent with these observations, as well as the strain range over which such mechanisms occur. Of course these observations are only applicable for the material under investigation; however, this is a well-studied alloy, thus maximizing room for comparison to other investigations.

2.2 EXPERIMENTAL DESIGN FOR MICROSCOPIC OBSERVATIONS

2.2.1 Design of a Shear-Dominant Specimen

In order to investigate the deformation and failure mechanisms under low triaxiality or shear-dominated loading a suitable test specimen had to be designed. The main constraint on specimen design is that the remote loading applied is to be extension or compression and along the axis of the specimen, a limitation that arises from the test machine available for use in the Scanning Electron Microscope (SEM). Thus, applying shear through torsion or with a Marciniak-type specimen, such as that used by Yin et al. (2015), would require extensive effort into the design and development of experimental fixturing and was not pursued. Within this constraint, the specimen was designed so as to be as near to zero triaxiality as possible and achieve a maximum amount of straining in the shear-dominated region prior to being disturbed by a change in stress path or failure in the specimen from outside of the shearing region (i.e. from a tensile region that may exist near free surfaces).

The specimen geometry shown in Figure 2.2 was selected for this investigation. This specimen is similar to that used by Peirs et al. (2012); however, the slot geometry just behind the notch radii are altered to have straight notch flanks that are aligned with the opposing notch flank. This alteration permits the application of larger deformations while maintaining low levels of triaxiality in the region of highest deformation, although some small positive component of triaxiality persists as the deformation increases. In order to keep the specimen fabrication simple, further optimization of this geometry was not pursued. If the inner notch flanks are offset farther from the specimen center a decrease in triaxiality (bringing it into the negative regime) will occur between the notches and offsetting the other way has the effect of increasing triaxiality. Through manipulation of this offset, the specimen can be used to examine shear-dominated

loading with varying levels of tension or compression. Both the case of zero offset to cause vanishingly small average triaxiality and a small offset to produce slightly negative triaxiality have been tested and qualitatively show the same overall behavior. In this dissertation, only the case of zero offset – the design that comes closest to pure shear loading while avoiding positive triaxiality – is considered.

Since the main objective of these experiments is to acquire high resolution images across the entire load bearing ligament, the smallest gauge section for the specimen is sought to ensure that the number of images required is reasonably small as to be obtained during pauses in applied load during the test. The minimum size of the specimen is also constrained by the desire to have enough grains in the shearing plane in order to justify modeling the structure as a continuum, thereby bypassing the need for modeling the specific incarnation of the microstructure for each individual specimen tested. To achieve these opposing objectives, the minimum cross sectional area of the specimen was selected to be 400 μm in the plane of observation, and about 2200 μm through the thickness direction. Making use of the mean grain size measurements made by Ghahremaninezhad and Ravi-Chandar (2012) we estimate that approximately 1500 grains occupy the minimum cross section. It is anticipated that the crystallographic orientation of these grains are nearly random, as FCC metals typically do not develop a strong texture during rolling. This grain count is deemed sufficient based on the results of Barbe et al. (2001) and Kanit et al. (2003). Barbe et al. show that the plastic deformation of a representative volume element of 200 randomly oriented grains is sufficient for homogenization. Based on the results of Kanit et al. the current grain count is near the lower bound for which homogenization of the elastic properties is appropriate. Since plastic properties depend on the same underlying crystallographic symmetries, this count is assumed appropriate for slip dominated behavior as well.

The response of this specimen has been simulated using the Abaqus/Explicit FEM package to assess its suitability in achieving a state of nearly vanishing triaxiality during large deformations. A highly refined mesh containing ~200000 linear elements with reduced integration (C3D8R) has been used, as can be seen in Figure 2.2. The elastic-plastic properties used by Ghahremaninezhad and Ravi-Chandar (2012) have been adopted and no failure or damage models are included. The spatial variation of equivalent plastic strain and triaxiality at various levels of deformation are shown in Figure 2.3 as well as the deformation at the notch tips. A band of plastic deformation that is concentrated between the two notch flanks forms initially, and continues to localize over a smaller region as the deformation progresses. As a result, the strain gradient within individual grains is anticipated to be large for this specimen. Note also that the plastic strain as well as triaxiality are not uniform across the line connecting the two notches, but varies significantly; in particular, the triaxiality is close to zero in the central portion between the notches, but is clearly nonzero near the notches, reaching a maximum of about 0.4. As the loading is increased the notches are seen to deform into cusp like features, just from the plastic deformation of the specimen. Thereafter, a process similar to that observed by Ghahremaninezhad and Ravi-Chandar (2013) for Arcan geometry specimens occurs, where material points that are initially outboard of the cusp in the negative triaxiality region move inboard, eventually passing across the cusp into the positive triaxiality region. The triaxiality field has an extremely large gradient near the cusp, along the path that these points follow. Figure 2.4 shows the equivalent plastic strain variation with triaxiality for three points in the model (identified in Figure 2.3a), one in the center of the gauge section and two on the notch surface. Extensive straining at the center of the gauge section occurs with vanishingly small average triaxiality, with most of the straining occurring in a triaxiality range of -0.01 to 0.006. The switch from

negative to positive triaxiality is seen for points on the notch surface, and occurs as they cross the cusp, with some variation in the deformation history depending on when they cross. Specifically, points that traverse the cusp at later states of deformation experience higher triaxiality and more straining than prior points that have passed. Finally, note that the deformation state becomes highly three dimensional in the region of the cusps after they form. The results of the finite element analysis indicate that this specimen is suitable for the purpose at hand: to examine the deformation and failure mechanisms under low triaxiality, if attention is focused on the regions between the two notches.

2.2.2 Specimen Preparation

Specimens based on the geometry discussed above were fabricated from a 2.54 mm thick sheet of 6061-T6 aluminum; these specimens were cut from the same rolled sheet stock used in the experiments of Ghahremaninezhad and Ravi-Chandar (2011, 2012), and hence the grain size statistics (mean grain size in the plane of the sheet of around 39 μm) and specimen material response given in these references are appropriate for the material used in the present work. The notches were cut with wire EDM; in order to prevent damage to the specimens during handling, shims of appropriate thickness were placed between the opposing notch faces. One surface of the specimen was then mechanically polished to a mirror finish, removing ~ 300 μm of material, and the shims were removed; this polishing provides an initially flat surface that is best-suited to reveal the deformation of the material. In addition to allowing clear identification of features such as inclusions and voids within the matrix material, the initially flat polished surface will develop topographic features that are correlated to plastic deformation.

The digital image correlation (DIC) method has been used with SEM images by other investigators, such as Sutton et al. (2006) and Carroll et al. (2013) for determination of strain fields, but is not pursued in this work. This technique is useful for automated acquisition of displacement and strain fields; however, in places where there are strong gradients in the strain field, the measured strain can be strongly affected by image resolution and achieving correlation to provide any measurement at all becomes a challenge. Furthermore, in order to use this method, the native surface of the specimen would have to be masked with a high contrast random speckle pattern. Unfortunately this would obscure, or even completely hide the mechanisms that are of primary interest in this work. Nevertheless, the strain field is interest in this work and will be obtained as an average over a larger gage length by manually identifying physical points on the specimen at different locations and tracking them through the different stages of loading. Averaging in the strain field is unavoidable with any image analysis technique for this work, since deformation appears to occur in discrete slip steps at the current spatial resolution.

2.3 EXPERIMENTAL RESULTS

2.3.1 Global Response of the Specimen

The specimen was loaded in a MTII/Fullam SEM tester with a 1000 lb load frame (with 1000 lb load cell) at a displacement rate of 0.023 mm/min. The load elongation curve is shown in Figure 2.5, indicating an initial elastic response, followed by a plastic response, peak load and eventual failure. The five disturbances observed on the otherwise smooth load-elongation curve correspond to displacement levels at which loading was paused so that high resolution images could be taken. The wandering of the load during

this time period is likely due to preferential heating of the specimen and load frame: the test frame and specimen enter the vacuum chamber of the SEM at room temperature, but the motor dissipates a significant amount of energy as heat during stretching. During pauses in the loading, the specimen heats at a faster rate than the load frame, as the only heat sink in this setup is the connection between the load frame and microscope stage. As a result, the specimen has a larger thermal expansion than the load frame and the load decreases while the crosshead is paused. This process has not been verified with thermal measurements, but is deduced from the load elongation behavior and knowledge that approximately 40° C increase in temperature occurs by the end of the test.

Scanning electron microscopic images were acquired during the loading process at one second time intervals in order to assemble a video of the entire deformation history. This video is available as Supplementary Material SM1 for this dissertation (note that there is one change in magnification shortly after the video begins). Since these images cover the entire region between the two notches, the images are at a relatively low magnification (578 nm/pixel). The events observed in this video generally follow the predictions of finite element analysis, indicating the progressive deformation of the notch tip region, and the formation of a cusp like feature prior to any new surface generation (fracture). The video also shows that failure initiated from the cusp like features that develop from the EDM cut notches, where a higher state of triaxiality than pure shear exists. Initiation and arrest of at least two cracks from the left cusp are seen prior to the final crack that completely severs the specimen. Additionally, it is observed that the final cracking event does not occur through the region of highest shear deformation. The failure of this specimen is clearly not a failure under low triaxiality condition, but one that is driven by the cracks that form at the two notches and propagate towards each other, with the region between the cracks experiencing significant plastic deformation

under low triaxiality. Therefore, a notched specimen could not be used for the determination of the strain-to-failure under low triaxiality conditions. However, the central portions of this specimen do sustain significant shear strains; the high-resolution images obtained at the different stages of loading provide information on the deformation mechanisms that operate during the development of large strains as discussed below.

2.3.2 Measurement of the Local Strain Variation in the Specimen

Prior to loading, and during the first four pauses in loading, a series of images was taken at higher resolution (145 nm/pixel) and stitched together to elucidate the details of deformation during testing. These images are printed with significantly reduced resolution in Figure 2.6, but the full resolution images are available as Supplementary Material SM2a-e. Each global level of deformation at which these high-resolution images were taken will henceforth be referred to as stages D0-D4, with stage D0 referring to the initial state, stage D1 the first level of deformation, stage D2 the second, and so forth. Figure 2.6a shows the microstructure at stage D0. Note that some regions on the specimen appear stained – a light colored region near the right notch, and some dark splotches near the left notch. These regions of discoloration are just surface stains from specimen preparation and are not a part of the microstructure; they do not influence the material behavior. Aside from discoloration, the most dominant feature in this image is the population of second phase particles embedded in the aluminum matrix. Image analysis of multiple optical micrographs of the region identified that about 2% of the surface area is occupied by these particles. There also exists a very small initial void population with some voids near the interface between matrix and inclusion, but the

majority occurring in isolation. Most particles are seen to be intact and bonded to the matrix.

The positions of about 90 particles were tracked *manually* at stages D0-D4 and used as Lagrangian markers to determine the displacement and strain field. While the displacement fields are then readily calculated based on particle positions, the determination of strain requires care. First, as we will see later, substantial deformation gradients and even discontinuities exist within each grain, and thus the identification of strain from the displacement data should be considered as an average measure over the gage length. Second, the strains are calculated using this discretization of the displacement field, Delaunay triangulation, and isoparametric interpolation with a linear basis function. If the connectivity of the Delaunay triangulation of the points was performed obtained in the first image is maintained through all stages of deformation, the mesh becomes extremely distorted in regions of high shearing deformation, requiring rearrangement of the nodal connectivity to maintain triangles of a suitable aspect ratio; the average strain at each particle is then obtained as discussed below. The median area of a triangle in the mesh is about 59 μm^2 with a standard deviation of about 128 μm^2. This yields an average gage length of about 14.8 μm, which is significantly smaller than the grain size (39 μm) in this material.

The Hencky strain was computed for each triangle in order to produce an estimate of the strain in its interior. The equivalent plastic strain of each element was calculated by adding the equivalent plastic strain increment between subsequent stages of deformation to the equivalent plastic strain at the prior stage of deformation. If an element with the same connectivity did not exist at the prior stage of deformation, then the prior equivalent plastic strain was taken as the mean of the three nodal strains for each element. Nodal strains were computed by taking a weighted average of the strain computed for all the

connected elements. Weights were apportioned based on the distance between the node and the centroid of each connected elements. Due to the averaging used to transfer between element and nodal quantities, some smoothing of the equivalent plastic strain field occurs in the remeshing process.

The equivalent plastic strain field at each level of deformation is overlaid on the SEM images in Figure 2.7. Figure 2.7a shows an example of the triangulation that is performed at each level of deformation. At all stages of deformation, the equivalent plastic strain field is seen to be extremely heterogeneous. Heterogeneity is to be expected at this length scale (for an example of the heterogeneity at the higher spatial resolution afforded by DIC see Kammers and Daly, 2013), nonetheless certain trends from the continuum finite element simulation are visible. Namely, that the shear strain is concentrated in between the notch flanks and continues to localize to a smaller region as deformation increases.

Each of the following paragraphs will outline the behavior of a particular feature of the microstructure throughout its deformation history, saving the distillation of the variety of behaviors observed for the following discussion section. When estimates of the strain are available at the location of interest, values are given in the figure caption.

2.3.3 Discrete Deformation of the Matrix

Figure 2.8 shows a higher resolution snapshot of the deformation occurring in the vicinity of a single grain located at the point A in Figure 2.6; the normal direction of the shearing plane is nearly vertical in all of these images. The first image (Figure 2.8a) shows a representative picture of the initial microstructure prior to loading; since this corresponds to the initial polished flat surface of the specimen, there is very little contrast

in the image. The second image corresponding to stage D1, shows some new contrast features that are in the form of parallel lines, but with different orientations in different regions of the image; these are formed by discrete slip events along crystallographic slip planes in different grains that result in out-of-plane displacements, and their formation can be understood by the following argument. Even though the average shear deformation applied to the specimen should result in no out-of-plane displacement, local variations in the grain level deformation are responsible for out-of-plane displacements; the initially flat polished surface develops topographic features that are correlated to plastic deformation in each grain. Since this deformation is concentrated as slip on crystallographic planes that is constrained to occur on a finite number of slip systems, some component of this slip will occur in a direction normal to the polished surface. The surface elevation change from each slip event cannot exceed the length of one Burgers vector (a few angstroms), and therefore individual slip events can only be detected using extremely high resolution techniques such as atomic force microscopy. Comparatively lower resolution instruments, such as the scanning electron microscope (SEM) used in this work, do not directly image activity on the lattice scale; therefore, it can be argued that the observed parallel lines are due to deformation caused by the accumulation of many slip events, on the subgrain, but super lattice level. This implies that even at the grain level, plastic deformation is due to the accumulation of slip events on discrete planes. Such discrete slip will be identified in the next section through tracking of the motion of a particle after fracture. Here, the term slip trace will be used to describe the surface step that is produced by the concentration of activity by a particular slip system onto a single, or tightly bundled group of crystallographic planes. Additionally, the grain boundaries have become visible due to differences in the orientation of the parallel slip traces in each grain and out of plane sliding along the boundaries themselves. The

boundary of the grain labeled A in Figure 2.6 is identified by the red dash-dot line in Figure 2.8b. The slip traces are more visible in Figure 2.8c, an image corresponding to stage D2. It is seen that in some grains the first activated slip system is well aligned with the direction of global shearing, whereas in other grains, such as the central one in this image set, it is not well aligned. Additionally, deformation is clearly visible by the change in shape of the central grain between the first and second levels of deformation. At stage D3, pictured in Figure 2.8d, slip traces from the second activated slip system become just as visible as those from the first. When a second slip system is activated in a grain, it is always well aligned with the global shearing direction. In the fourth and final level of deformation (stage D4, Figure 2.8e), slip traces corresponding to the second activated slip system dominate the image. The central grain is seen to be heavily deformed from its initial shape. Tracking the second phase particles that are at the boundary and within this grain, and using the triangulation described above, the strain in this grain can be estimated to be about 2.2. Additionally, the surface topography in the grain clearly reveals the discreteness of the displacement field. Slip traces that were once smooth, nearly vertical lines, become broken up and exhibit sharp corners where intersected by slip traces running in the horizontal direction. The horizontal slip traces remain smooth curves because appreciable slip on the first system does not occur once slip traces on the second system become visible. Similar observations were made in other parts of this specimen as well as in two other specimens in repeated tests. The material between the two notch regions displays the slip behavior just described and deforms under low triaxiality conditions. The question of whether this material exhibits distributed damage under shear loading and what microstructural aspects lead to final failure/fracture remain to be examined. This will be accomplished through careful examination of the

changes in microstructural features such as voids, second phase particles, slip planes, and grain boundaries through the deformation of the entire specimen.

2.3.4 Fracture and Debonding of the Second Phase Particles

Figure 2.9 tracks the behavior of a single particle throughout the deformation; the location of this particle is identified as P_1 in Figure 2.6. At stage D1 (Figure 2.9b), slip traces on the first activated system are seen to be misaligned with the direction of global shearing. One slip trace appears to terminate at the particle, perhaps because the particle provides a barrier for slip. At stage D2 (Figure 2.9c), slip on the second activated system is visible and the particle cracks; additional slip on the first system is also visible on previously established slip planes. At stage D3 (Figure 2.9d), a slip trace that was faintly visible in stage D2 is now clearly perceptible at the location of particle fracture. Between the stages D2 and D3, the upper and lower fragments of the cracked particle are separated by a plane of active slip and a void develops between them. In Stage D4 (Figure 2.9e), the two particle fragments continue to move farther apart in the presence of extreme plastic deformation. The void between the two fragments shears but does not appear to exhibit any growth. The discrete nature of slip, even on the super lattice scale, is indicated by the red dashed line shown in the figure; it is clear that similar discontinuous slip events occur at each of the parallel slip traces and it is this discontinuous nature of deformation that renders any strain measurement made at this spatial resolution as an averaged or homogenized strain measure, as discussed in Section 2.3.2.

Figure 2.10 tracks another particle throughout the deformation, where again it appears as though a slip trace may be perturbed by the presence of a particle; the location of this particle is identified as P_2 in Figure 2.6. Whether or not the slip trace is affected, it

is clear at stage D2 that the particle cracks where the slip trace intersects it. The final image corresponds to stage D4 of deformation (stage D3 has been omitted due to its similarity to stage D4), where the void resulting from cracking has opened up. In most ways this is quite similar to what happened to the particle P_1 described above, but a couple differences are seen. Particle P_1 was cracked by the slip on the second system (implying at a later loading stage), whereas particle cracking in the current grain has occurred with only one active slip system (at an earlier loading stage). Furthermore, due to the orientation of slip within this particular grain, the void nucleated from the crack opens, rather than shears. If further deformation had continued, it is likely that a second slip system would have been activated in a similar orientation to the global shear direction, and that void shearing similar to what was observed in Figure 2.9 would have ensued.

One final case of particle cracking is to be highlighted, as detailed in Figure 2.11; the location of this particle is identified as P_3 in Figure 2.6. Again, cracking is seen at the intersection of a slip trace and a particle. Here, the clear difference with the prior case is the size of the particle. In the current case, the particle is much smaller, indicating that even small particles can crack, although they are certainly less likely to do so (e.g. the small particle near the left edge of the same Figure 2.does not crack). Also, this particle does not seem to impede the formation of the slip trace. Whereas large particles appear to provide a bit of constraint to slip in their neighborhood (as inferred from the disappearance or deflection of slip traces in their immediate vicinity), the amount of constraint provided by a small particle is not observable at this scale.

While there are ample examples of particle cracking, there are also numerous cases where particles do not crack. Figure 2.12 shows a rather large particle in an area of moderate plastic deformation; the location of this particle is identified as P_4 in Figure 2.6.

At stage D1 (Figure 2.12b), two slip traces straddle the particle. Additional slip planes appear to terminate at the boundary of the particle. Further slip along the same planes occurs, but even at the final level of deformation shown in Figure 2.12c the particle remains intact and bonded to the matrix. In this case slip traces are not seen to intersect the particle, and the particle appears to have arrested two slip traces to its left.

Particle debonding is also observed to occur during deformation, as depicted in Figure 2.13; the location of this particle is identified as P_5 in Figure 2.6. Here, the matrix deformation causes the distance between two nearby particles to increase. In order to accommodate this increase, interface debonding is observed to have occurred at one of the particles by stage D1. As the global deformation increases to stage D2, both the length of the debond and its opening increase. Under continued deformation to the fourth level (the third level has been omitted due to similarity to the fourth), the opening of the debond is seen to increase, however the length actually appears to decrease slightly as the particle partially re-embeds itself into the matrix material.

Another case of debonding is shown in Figure 2.14; the location of this particle is identified as P_6 in Figure 2.6. Here, a particle that appears to emerge from the subsurface between stages D0 and D2 indicates the action of out of plane deformation. The particle separates from the matrix at a location where it has high curvature. At stage D1 there appears to be a void adjacent to the one formed by debonding, and linking of the voids occurs at the second level of deformation. This sequence of events is possible, but since nothing is seen to nucleate the second void, it seems more likely that in this case involving out of plane deformation, that the two voids, are in fact a single cavity that is bridged on the surface. The debonding seen here is slightly atypical, as the interface area of debonding on the particle is minimal, and the particle appears to tear the matrix as it flows past the pointed particle tip. It is interesting to note that despite significant evidence

of plastic deformation in the surrounding matrix, this particle remains intact throughout the deformation; however, this is not always the case.

The particle shown in Figure 2.15 demonstrates that particle cracking and debonding need not happen mutually exclusively; the location of this particle is identified as P_7 in Figure 2.6. The initially intact and well-bonded particle is partially debonded from the matrix at its top before stage D1. By stage D2, the length of the interface debond is static as there is nothing to be gained by driving the interface crack around the particle's corners, but opening of the void is seen. To accommodate additional deformation, the particle cracks again, this time across the middle, and the crack faces move apart while maintaining parallelism. By stage D3 the void from debonding, at the top, has saturated in size, but undergoes mild deformation. One of the particle fragments cracks again, with both of the voids initiated from cracking continuing to grow, and separation between the fragments increasing. By stage D4 the distance between particle fragments continues to increase, however, the voids in between fragments do not grow in area, and are actually seen to partially collapse, with opposing faces coming into contact with one another through shearing of the matrix. One of the particle fragments is unaccounted for in this image. Perhaps it retreated to the subsurface, or the matrix may have flowed over it.

The most complex behavior observed involving particles is shown in Figure 2.16, where a strong interaction exists between two neighboring particles labeled 'L' and 'R'; the location of these particles is identified as P_8 in Figure 2.6. The image at stage D1 is omitted, as there is little change from stage D0. At stage D2 (Figure 2.16b) a strong slip trace is visible between two corners of these particles, but its intensity diminishes outside the inter-particle ligament. Also, it is seen that cusp formation of the notch face is occurring on the surface just to the left of this particle pair. At stage D3 the cusp has been

established directly to the left of these particles. Extensive deformation has brought the corners of the two particles that were once nearly horizontally displaced to each other to be nearly vertically aligned and nearly in contact, again indicating discrete/discontinous slip. In order to accommodate this deformation, cracking along the slip trace occurs in a deformation pattern akin to mode II cracking (deformation is dominated by sliding displacement between crack faces). Indeed, the part of the crack to the left of particle R and below particle L has a modest opening displacement (in addition to the larger sliding displacement) and a length that is nearly identical to that of the slip trace observed at the second level of deformation. Finally, at stage D4 a large crack that is nucleated by the cusp appears to link up to the crack that was initiated between the particles. It is likely that this linking is coincidental, as the crack is initiated from the free surface, and its location set by the position of the cusp. A more convincing case of crack growth influenced by damage and following a voided path would be to see a crack turn slightly to meander from void to void. We reiterate that in the vicinity of the cusp the stress state differs significantly from that of pure shear, but still sliding deformation appears to occur in this neighborhood.

2.3.5 Deformation of the Pre-exsting Voids

We now turn our attention to voids that preexist in the initial state; but before beginning this task, we emphasize that the initial volume fraction of voids is extremely small – 0.06% – suggesting that preexisting voids are indeed a rare occurrence. Figure 2.17 tracks the history of an isolated void in a region of moderate deformation; the location of this void is identified as V_1 in Figure 2.6. The diameter of this void is about 0.8 μm. At stage D1 slip traces corresponding to the first activated system are seen, with

one trace running just to the side of the void. At stage D2, slip traces corresponding to the second activated slip system are visible, and again a slip trace runs near the void, just above but not through it. During stages D3 and D4, we see continued slip on the second slip system. The interesting feature of this image sequence is that no deformation of the void can be perceived at least on the scale of the image, despite continued deformation in the surrounding matrix. In fact, this behavior of preexisting voids appearing completely unperturbed by deformation in the surrounding matrix was commonly observed in this material.

Some voids, such as the ones shown in Figure 2.18 do deform in the presence of matrix deformation; the location of this pair of voids is identified as V_2 in Figure 2.6. The diameters of these voids are about 1.1 μm and 1.0 μm respectively. These two particular voids are closer in vicinity to each other than average and appear to occur in different grains, as indicated by the different pattern of slip traces observed in different regions. Even by stage D1 some shearing of the voids is seen. As more slip develops the voids shear further, however, the deformation is quite small and pales in comparison to what is experienced by voids that are nucleated near second phase particles, which despite sizable deformation, remain quite small. Just a couple of voids located near the cusps are seen to undergo substantial deformation. One such void, located near the left cusp is shown in Figure 2.19; the location of this void is identified as V_3 in Figure 2.6. The diameter of this void is about 1.4 μm. This void experiences minimal distortion during the first three levels of deformation. The fourth level of deformation shows particularly large deformation in the matrix that results in shearing of the void and its near complete closing. Figure 2.20 shows a void very near to the right cusp; the location of this void is identified as V_4 in Figure 2.6. The diameter of this void is about 2.5 μm. This void shears and partially collapses as it passes from the negative triaxiality side of the cusp to the

positive side. It is interesting to note that deformation under a similar stress state, in the vicinity of this void, caused many particles to fragment and/or debond, triggering cavity growth. Yet growth of the void itself does not occur, instead the void is seen to partially close up from the shearing deformation.

2.3.6 Summary of Observations on Deformation, Debonding, Fracture, and Voids

There are a few important observations that are summarized here in order to capture the essence of the results from the *in situ* tests performed.

- First, plastic deformation occurs in a microscopically discrete manner from the very early stages of plastic deformation. Evidence of such discrete plastic deformation is seen from out-of-plane deformation impinging on the polished surface, even in the early stages of deformation (for example in Figure 2.6b, corresponding to stage D1). Many grains located between the two notch flanks of the specimen exhibit a pattern of surface steps, associated with the first activated slip system of each grain. Slip that is visible from surface steps appears to concentrate on a small subset of the crystallographic planes in each grain. This leads to a displacement field that is somewhat discrete with jumps across each of the slip traces. The spacing of the steps is apparently regular within a given grain – somewhere in the range of 2 to 10 μm – but varies widely between different grains. The first activated slip system in some of these grains is oriented in a similar manner to the global shearing deformation, while in other grains it is not. Therefore shearing of the grains occurs through accumulation of discrete slip on these planes in different orientations. As the applied deformation increases to stage D2 and beyond, slip on planes and grain boundaries identified in the

previous loading step continue to accumulate deformation, and additional slip systems are activated in order to accommodate greater strain levels. The discrete accumulation of deformation along differently oriented crystallographic slip traces is the primary deformation mechanism as large shear strains on the order of $\varepsilon_{eq} \sim 2$ are developed in the regions between the two notches. It is expected that this will generate a continued strain-hardening response for the plastic matrix.

- Second, loading from stage D1 through D4 brings about some interaction between the plastic deformation and the larger scale defects such as second phase particles. Most particles remain intact and completely bonded to the matrix in grains where only one slip system is active, while a minority of particles debond or crack, generating a void. Particle cracking becomes more likely in grains with two active slip planes. Particles that crack tend to do so shortly after the activation of the first or second slip system. The result is that particle cracking events are most likely to occur during narrow slices of deformation history, whereas continuation of a particular deformation pattern is unlikely to initiate new particle cracks. Thus, it appears that second phase particles simply break, debond, and/or rotate with the matrix in order to accommodate or facilitate the shearing deformation, instead of acting as sources of damage for the material under shear-dominant loading. The fact that as the deformation progresses to stages D3 and D4, the size of voids initiated from particle debonding and cracking saturates (quite often voids even shrink as a result of matrix flow into these regions) provides strong evidence that the second phase particles do not play a significant role in the deformation and failure under shear loading. Rather, the material shows a matrix-dominated response, which is demonstrated to be strain-hardening in the next section.

- Third, the few voids that are present in the initial microstructure have minimal shape change, and appear to have little if any influence on the surrounding deformation. A couple of large preexisting voids that are near the cusps at the ends of the notch collapse or shear significantly, as stage D4 is approached indicating that these voids do not grow, but close. This behavior is particularly interesting, since it occurs when the shear deformation in these regions is accompanied by a state of positive triaxiality. Therefore, neither the naturally present voids, nor the ones nucleated by particle debonding play a role in the eventual failure of the specimen.
- Finally, while the specimen fails under the "shear loading" applied to the specimen, the sequence of events clearly indicates that damage and/or failure does not occur in the regions with low triaxiality; the central regions of the specimen that are deformed at nearly zero triaxiality strain to equivalent plastic strains on the order of 2.5 without exhibiting any signs of damage, but only shearing discretely along different slip planes.

The observations reported here are from the surface of the specimen. So, one natural question that arises is whether such deformations are possible in the interior of the specimen. Direct examination of this question would require that these experiments be performed in an X-ray tomography system, but even in this case the resolution may not be adequate to resolve some of the features, particularly that associated with discrete plastic slip. However, one can infer that this must occur both from micromechanical arguments and post-mortem examinations of cross-sectional microscopy. The surface topography evolution during deformation simply indicates that in order for a two-dimensional shear deformation to occur in a grain whose crystallographic directions are randomly oriented with respect to the shearing direction, (i) slip must occur through

resolved slip along crystallographic directions resulting in three-dimensional deformation at the grain level and (ii) slip occurs in clusters of slip planes with nearly uniform spacing. It is evident that the first part must be true in the interior as well since this is the only way of accommodating random grain orientations. Evidence for clustering of slip can be found in images of grain boundaries from cross-sectional microscopy. Grain boundaries in the initial microstructure that appeared as linear features at the microscopic scale deform into tortuous lines that arise from the discreteness of the slip processes.

Whether the behavior of particles and preexisting voids on the specimen surface is similar to that in the specimen interior also needs to be considered. The stress state in the interior is slightly different, but the deformation of the surrounding matrix is much the same. Whether different mechanisms occur in the subsurface will depend on how sensitive particles and voids are to the slight increase of negative triaxiality, and a slightly larger Lode parameter that is present in the interior. If the response of particles and voids is dominated by the deformation of the surrounding matrix then behavior in the interior will be quite similar to that observed on the surface. Further consideration of these aspects requires x-ray tomography and other nondestructive tools to provide more detailed picture of the sequence of events.

2.4 DISCUSSION

The fact that crack initiation at the notches occurs prior to reaching the peak load is an important feature of the load elongation behavior of this specimen. This provides direct evidence that no softening behavior of the material could be occurring prior to this point. It is necessary that the flow stress be an increasing function of the strain up to and past stage D3 because the global load is increasing even while cracks propagate from the

notches, thereby decreasing the cross sectional area over which the load is distributed. The peak load corresponds to the balance point at which the stiffness increase of the specimen from the hardening of the material is equal to the stiffness decrease of the specimen from a loss in ligament area from crack extension (or more generally structural stiffness due to crack extension). It is clear that the decrease in load carrying capacity of the specimen is not from intrinsic properties of the material, but rather the specifics of the crack growth for this particular specimen.

Beyond the peak load, while the global load carried by the specimen is decreasing, there can be no direct evidence of increasing flow stress of the material. However, all of the mechanisms that perhaps have the capability to decrease the intrinsic load carrying capability of the material that were observed (that is void growth, particle cracking and debonding) have halted past stage D3. The halting of these mechanisms after peak load may be simply coincidental, but allows for a strong inference to be made: the possibility of material softening can all but be ruled out. There are no observed mechanisms to decrease the intrinsic load carrying capability of the material and the decrease of specimen load can be well explained by the growth of cracks.

Focusing on the behavior of the material itself, while it is interesting to see the variety of mechanisms that occur – lattice slip, brittle fracture of inclusions, interface debonding, and void deformation – it is more important to understand the interactions between these mechanisms and what roles they play in the deformation in order to enable constitutive modeling. The concentration of slip events on a small subset of seemingly identical crystallographic planes is seen to be a characteristic response of the matrix. Discrete plastic displacements are expected at the lattice scale due to dislocation motion, but a discrete displacement field is seen in the present work even at the mesoscale between lattice and grain scales. In some grains the spacing between these active planes

is similar to the size of second phase particles, with the particles sometimes falling in-between active planes and at other locations active planes intersecting the particles. Quite intuitively, cracking of a second phase particle is often correlated with the intersection of one of these active planes. Not all cracked particles have clear evidence of intersection with a highly active slip plane, however not all highly active slip planes are visible as only the out of plane component of slip can be viewed with the SEM imaging.

Considerable attention has been paid to voids and particles in the discussions in this chapter, not because of their importance, but in an effort *to emphasize their relative unimportance*. It is the plastic behavior of the matrix material which is found to dominate the response. No indication of termination for plastic slip is observed in these images obtained as the matrix simply continues to slip to accommodate deformation. The slip is eventually halted simply due to a lack of driving force when cracks that occur outside of the region where shear dominates propagate across the specimen. Interestingly, when the cracks do propagate, they do not propagate through the area of most intense shearing; in fact, cracks propagating into material that has extensive prior shear deformation are seen to be arrested. It is not clear if this is due to an intrinsic property of the sheared material, or simply just a result of this particular specimen configuration. Either way, it suggests that the intensely sheared material has in no way been damaged, or made more likely to fail than it was prior to deformation.

The modeling implications from these observations are fairly simple. Firstly, the need for well-calibrated plasticity models into the range of extremely high strains cannot be overstated. This modeling should not include the possibility for material softening; rather the simpler case of a strain-hardening plastic model is more true to reality, but needs to be calibrated to very large strain levels. The scale and purpose of the model will have an effect on how plasticity should be handled. In order to illustrate this, we show in

Figure 2.6 the deformation of a line computed using FEM with the flow theory of plasticity and Hill's 1948 yield criterion overlaid on the experimental images. The FEM deformation appears to match the overall experimental displacement field quite well at all stages of deformation shown. Calculating strains on the scale of individual grains seems to be the lower limit for this modeling technique, as the subgrain details of slip being concentrated on a small subset of planes, are beyond the capability of this modeling approach. The actual deformation stair-steps along the same smoothly curving trajectory that the model produces. Even modern day crystal plasticity models typically do not capture the behavior of slip concentration that is seen to be prevalent in the plastic flow. Capturing this behavior may prove to be essential for the modeling of failure, and is certainly a requirement to model the cracking of particles. Perhaps most importantly, the experimental observations show that for a large range of strain, modeling of voids or any other damage mechanism is completely unnecessary for this material under shear dominant loading. Even more, these modeling techniques may introduce a nonphysical reduction in flow stress while adding extensive complexity in the calibration of model parameters.

2.5 CONCLUSION

Experiments were performed inside a scanning electron microscope to explore the details of the deformation and possible damage or failure mechanisms of Al 6061-T6 under shear dominated loading. Monotonically increasing stress-strain behavior on the continuum scale is directly observed up to a strain of at least 1.1 and strongly implied for strains in excess of this value. Through high resolution microscopy and particle tracking, it is shown that

- Plastic deformation occurs through the accumulation of discrete slip on slip planes that are spaced between 2 – 10 μm apart within each grain. Average plastic strains on the order of 2 were observed in the interior of the specimen where the triaxiality is nearly zero.
- No evidence for homogenizable damage of the sort required for commonly used continuum damage models was found. In particular, second phase particles broke, debonded or rotated, but these processes occurred while the specimen still exhibited a hardening response.
- Voids present in the initial microstructure have a minimal influence on the deformation and failure of this material. Voids from particle cracking and decohesion are found to be more active, but serve as a deformation mechanism rather than relating to damage or failure. These processes terminate after the initial stages of deformation of the material.
- It was not possible to generate failure under shear in this specimen, because high-triaxiality dominated failure generated from the notches interrupted further progression of shear deformation.

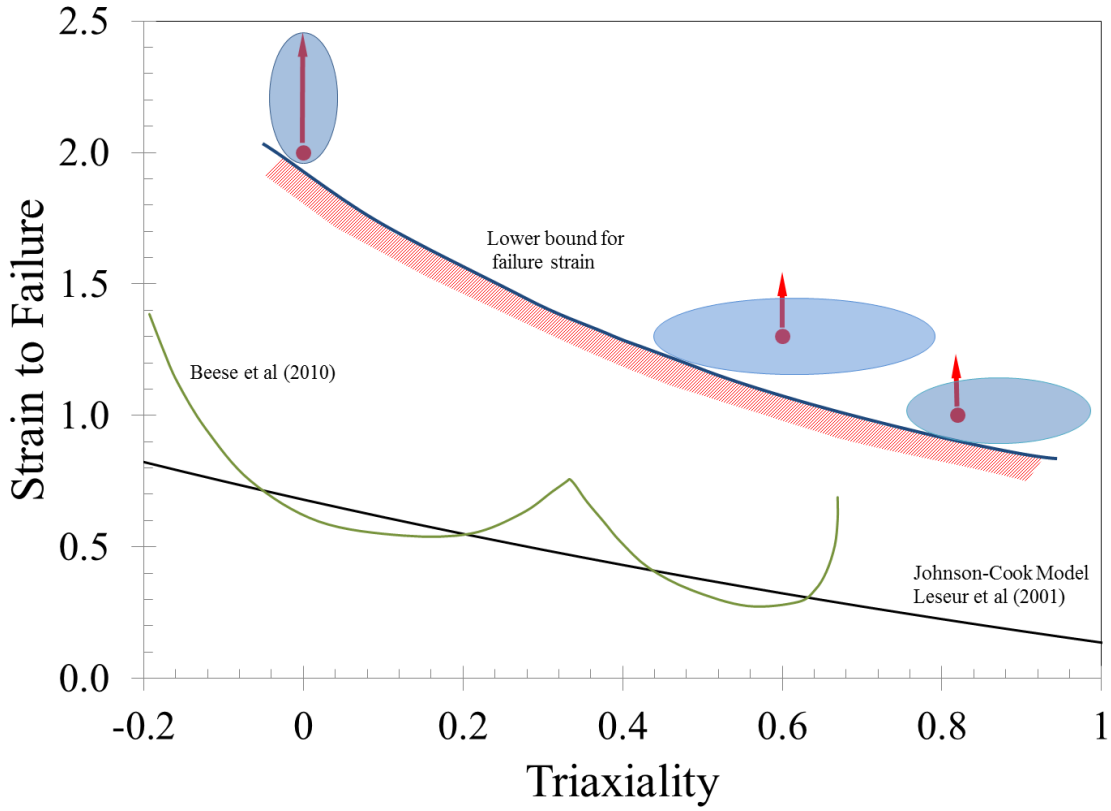

Figure 2.1: Strain to failure as a function of triaxiality from three independent investigations for Al 6061-T6. The use of grain level strain measurements has a profound effect on the failure strain.

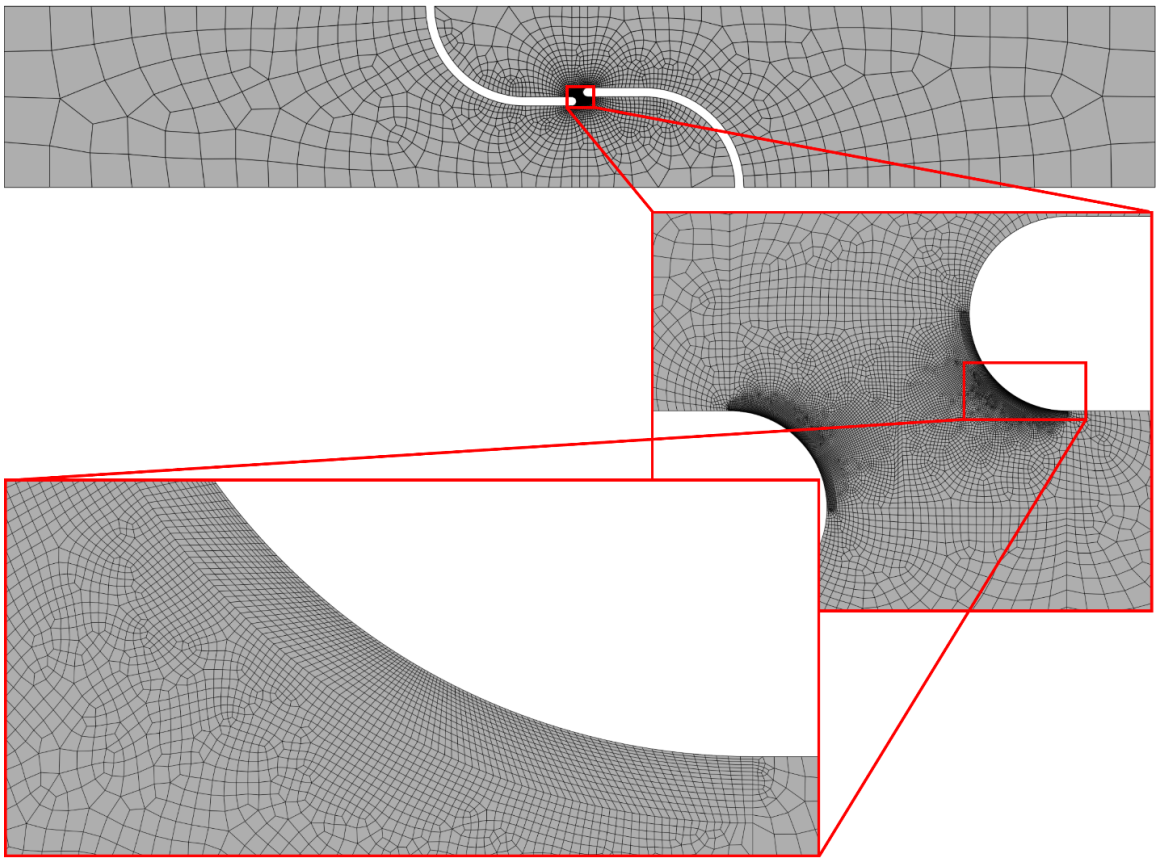

Figure 2.2: Specimen design to create shear dominated deformation between the notches when extension is applied with wedge grips at the specimen ends. The mesh discretization used for FEM is also pictured, to show the very fine mesh used in the vicinity where the notch collapses into a cusp like feature.

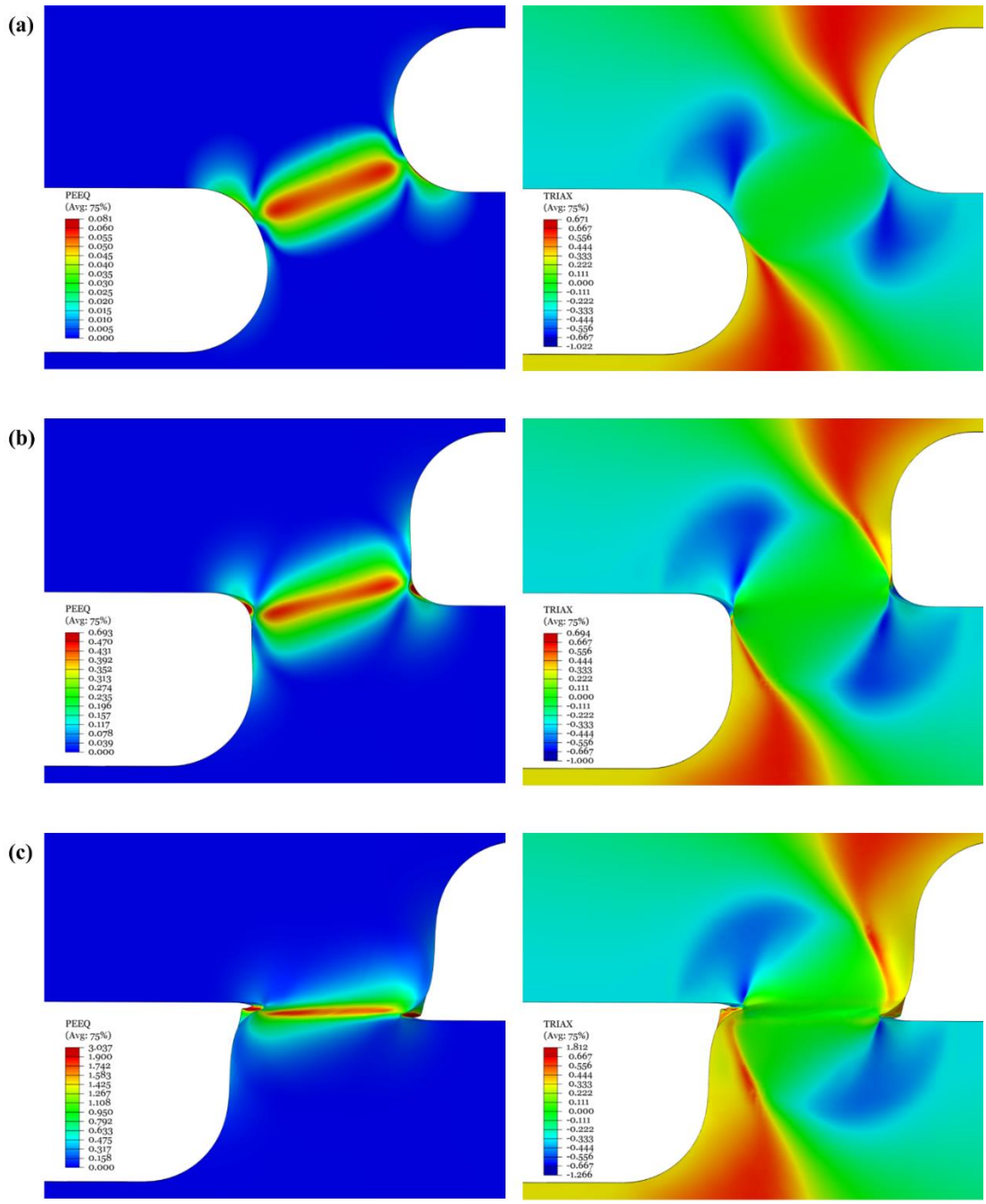

Figure 2.3: Predicted strain and triaxiality variation on the specimen's surface at three levels of deformation. Note how plastic deformation causes the initially rounded notches to deform into sharp features, and the strong gradient in triaxiality around these features. The triaxiality in the heavily strained region away from the notches is maintained close to zero.

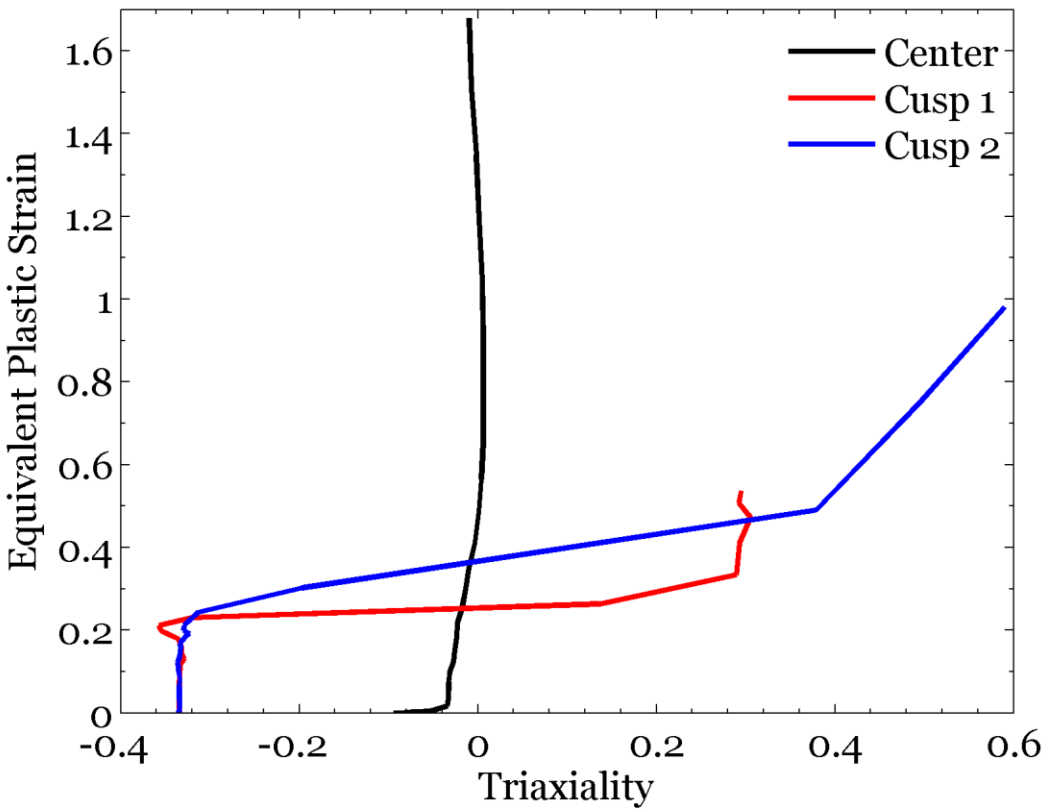

Figure 2.4: Equivalent plastic strain variation with triaxiality in the specimen from finite element analysis. The center of the specimen undergoes extensive straining with nearly vanishing triaxiality. Some points on the notch surface pass across the cusp tip, while experiencing a rapid increase in both strain and triaxiality. The curve labeled "Cusp 1" corresponds to an element that passes over the cusp tip at a lower level of deformation than the element corresponding to the curve labeled "Cusp 2."

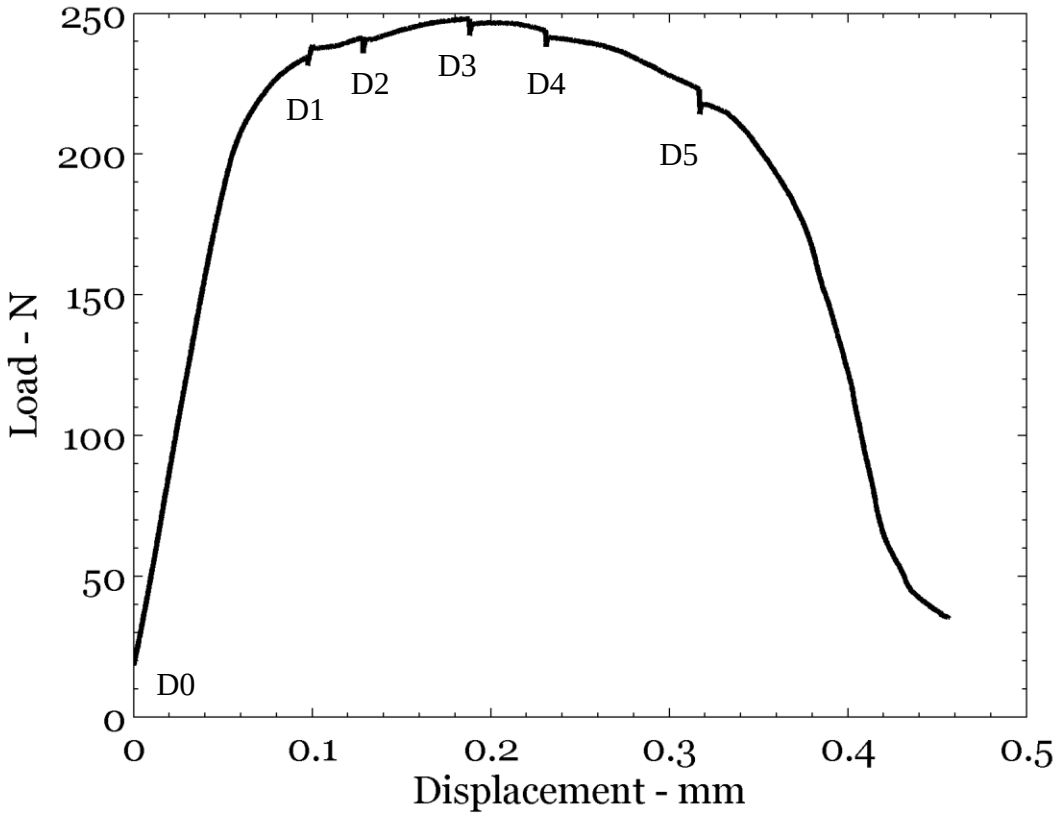

Figure 2.5: The load elongation curve for the specimen. The small disturbances in load seen are the displacement levels where the loading was paused to take high resolution images. The load drift during imaging is likely caused from thermal loading.

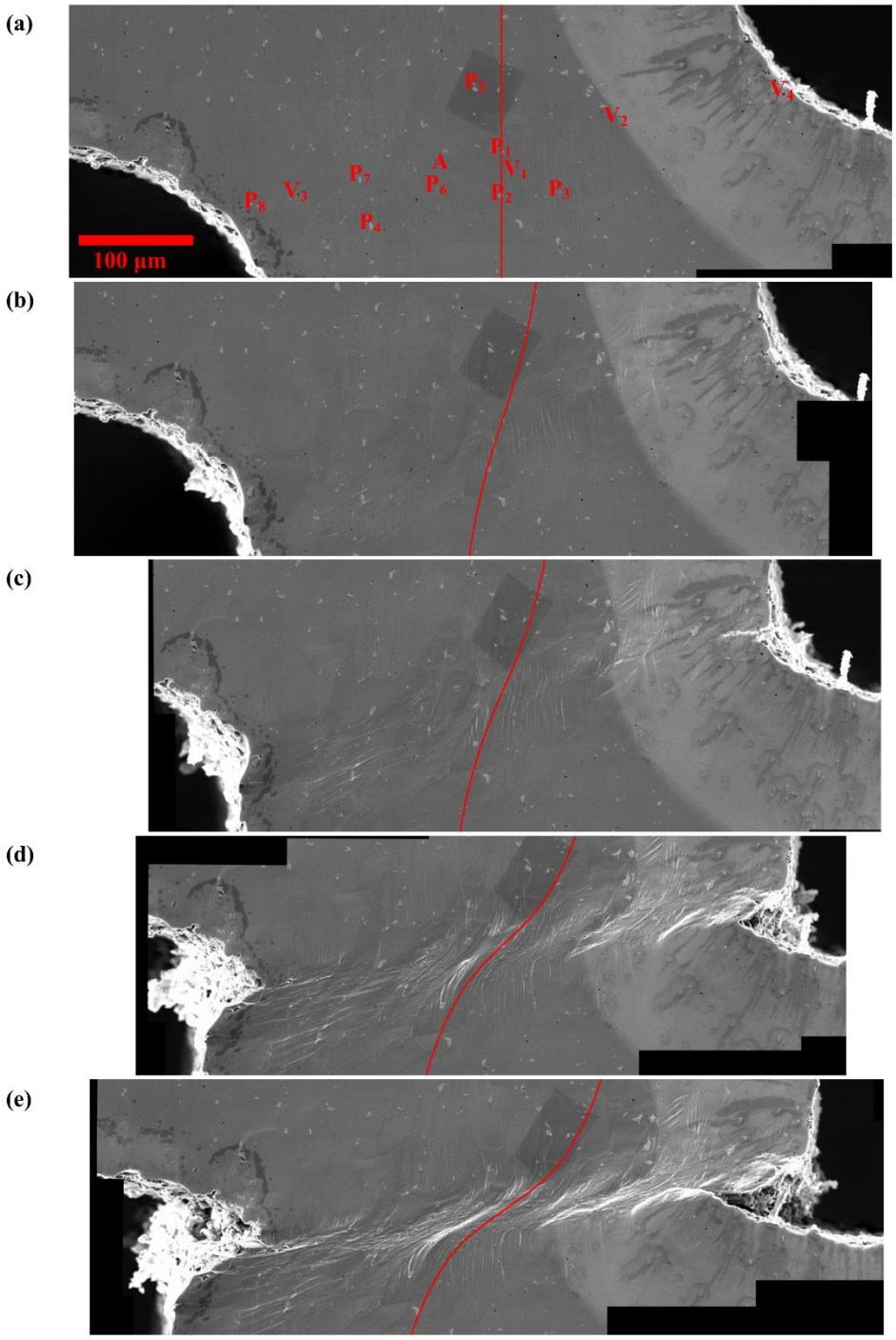

Figure 2.6: SEM images of the deformation in the sheared region of the specimen in the a) unstrained state and the b) first c) second d) third and e) fourth levels of deformation. The red line shows the displacement predicted by the FEM simulation, which shows reasonable agreement to the experimental result.

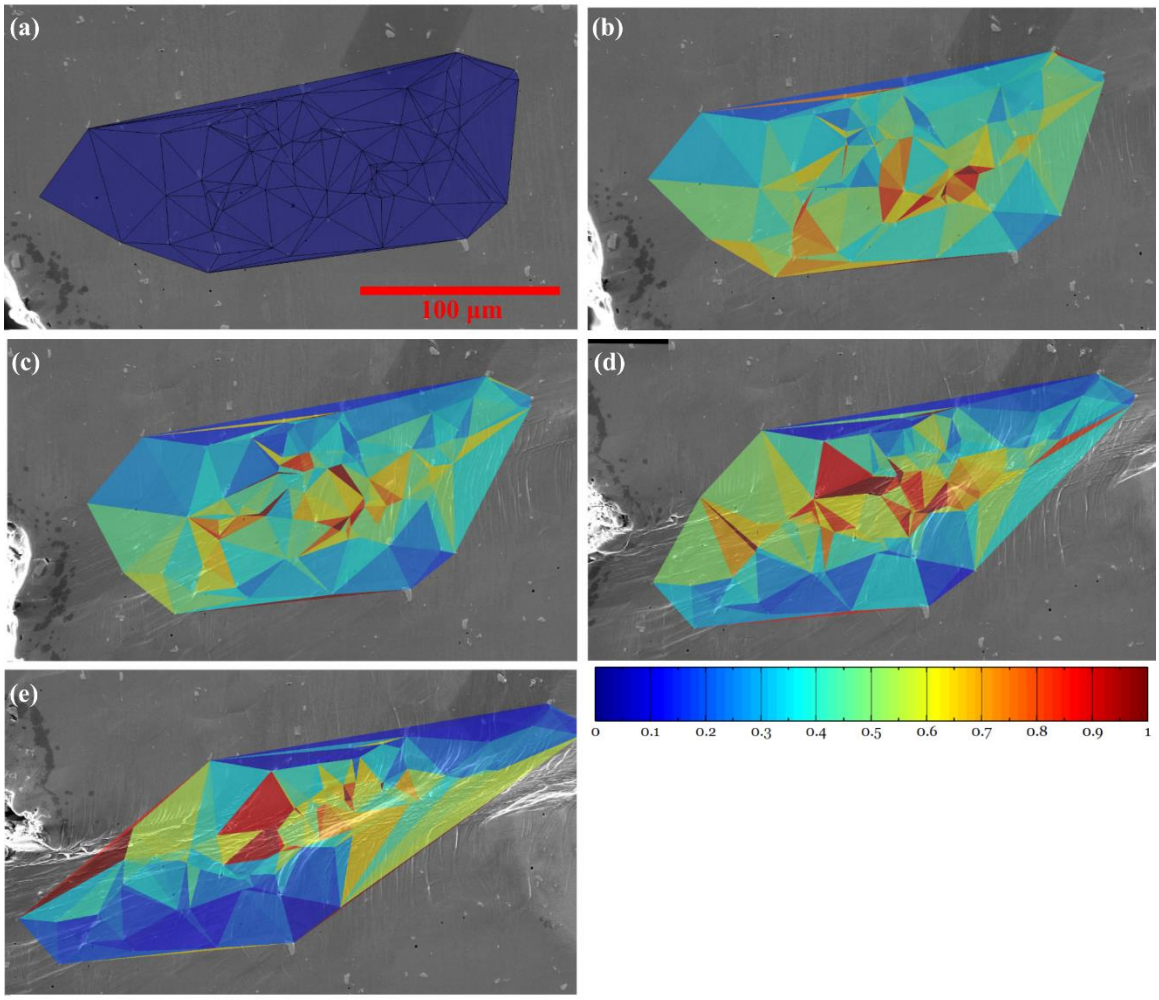

Figure 2.7: The equivalent plastic strain field at stages D1-D4, determined by tracking approximately 90 particles. (a) Initial positions of the identified points and an example of the Delaunay triangulation that was performed at each stage of deformation. The color map for each Figure 2.has a maximum of (b) 0.35, (c) 0.8, (d) 1.7, and (e) 3.

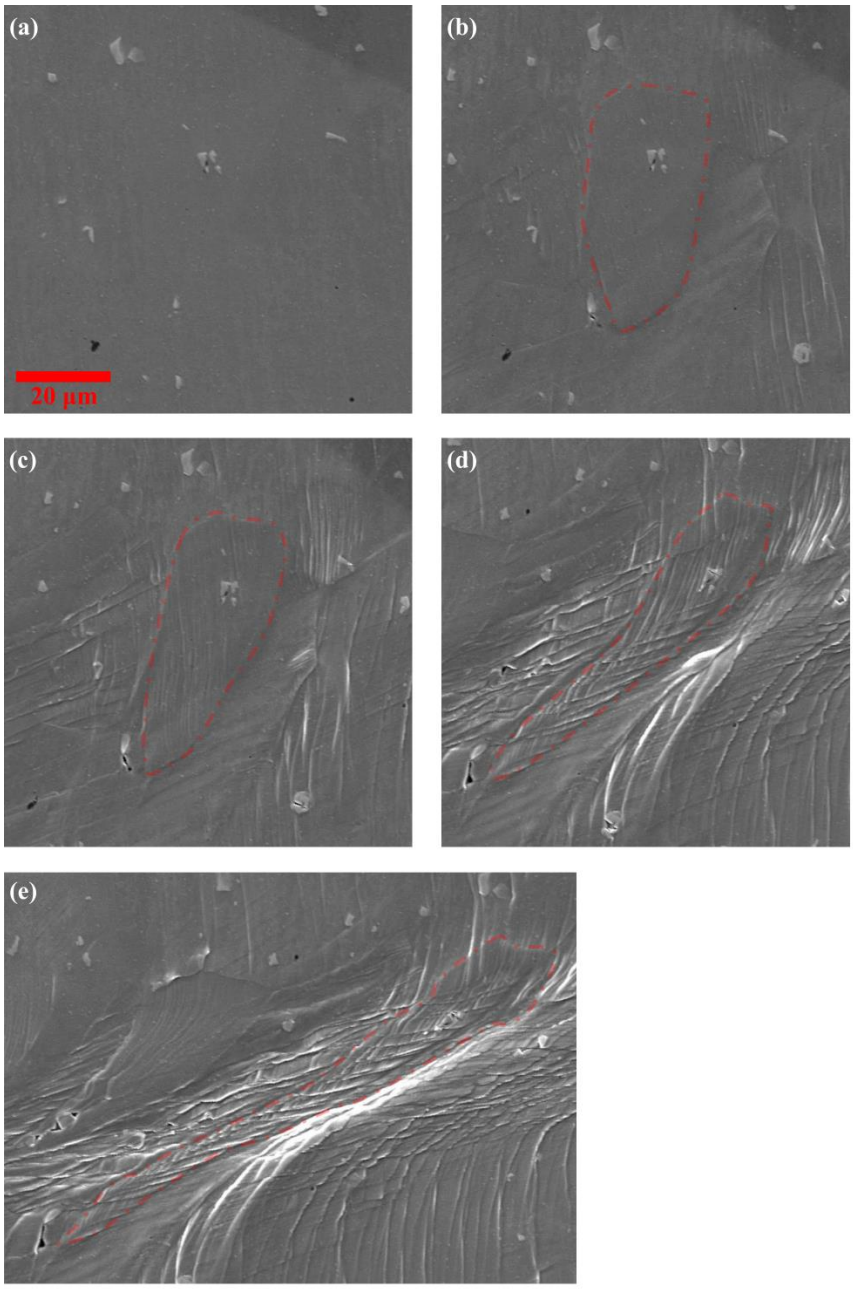

Figure 2.8: Snapshots focusing on the plastic deformation of a grain taken at *D0-D4*. The equivalent plastic strain in the vicinity of the central grain is estimated to be b) 0.13, c) 0.50, d) 1.1 and e) 2.2. The grain boundary is made clearly visible by out of plane grain boundary sliding and is traced by the red dashed line. Extreme deformation and extensive slip is seen on multiple slip systems without any indication of voiding, cracking, or damage within the grain.

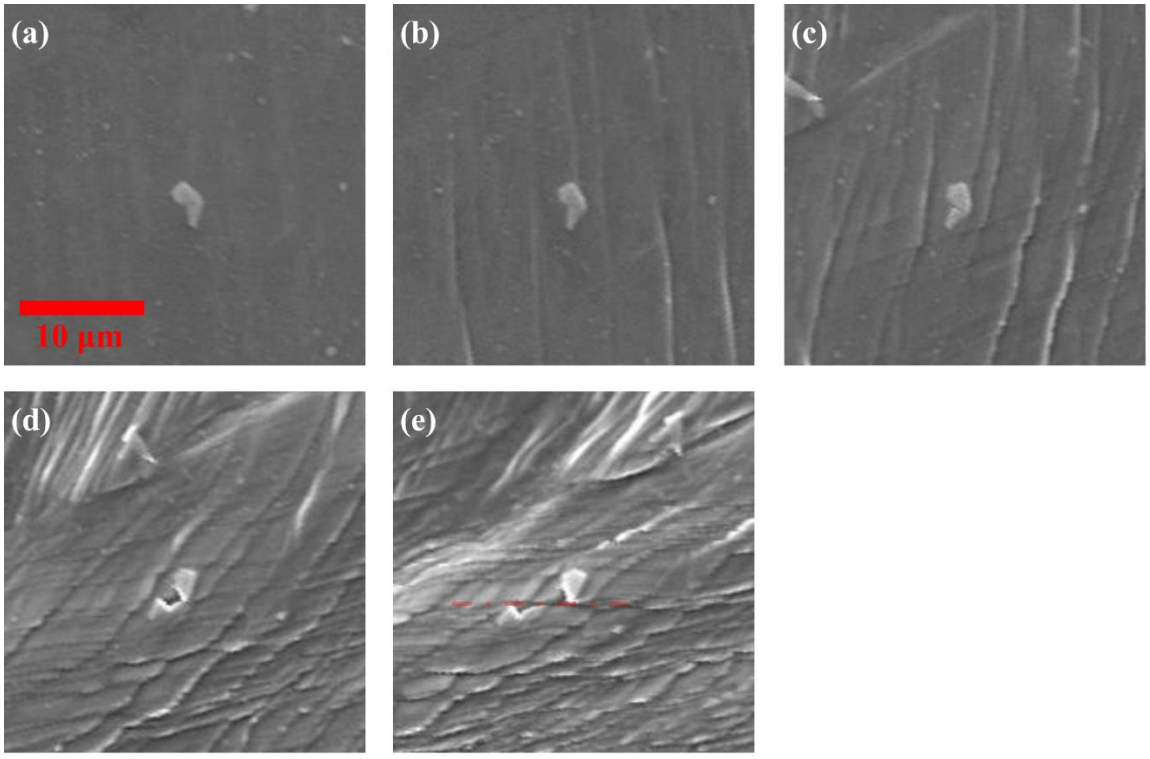

Figure 2.9: Snapshots of a particle cracking taken at D0-D4. The equivalent plastic strain in the vicinity of the particle is estimated to be b) 0.16, c) 0.32, d) 0.77 and e) 1.3. The particle is seen to have cracked by D2, after the second slip system has been activated. The crack has opened up a void visible in D3, however, no void growth occurs between D3 and D4 and deformation between the particle fragments occurs by slip along the red dashed line.

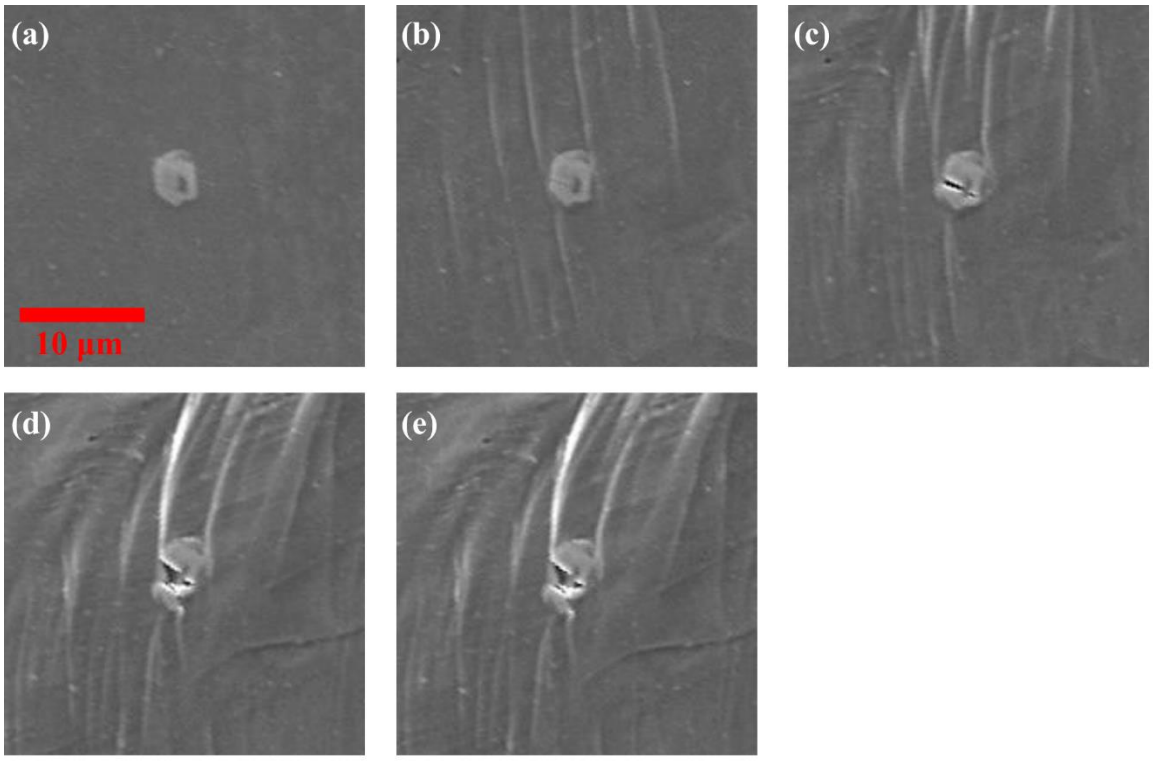

Figure 2.10: Snapshots of a particle cracking taken at D0-D2 and D4. The equivalent plastic strain in the vicinity of the particle is estimated to be b) 0.16, c) 0.39, d) .53, and e) 0.55. Particle cracking is seen to have occurred by D1, where a concentration of activity on the first activated slip system intersects the particle. The crack opens a void that grows up until D3, but does not grow between D3 and D4.

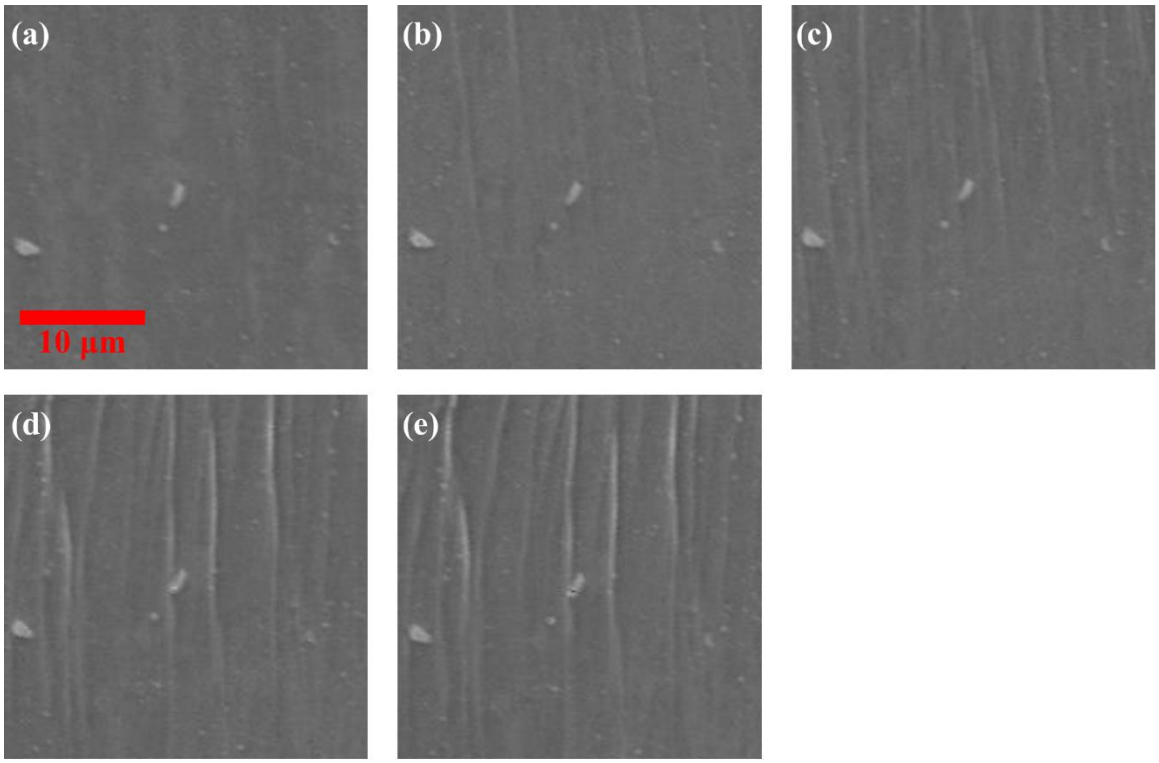

Figure 2.11: Snapshots of a small particle cracking taken at D0-D4. The small particle in the center of the image is seen to be cracked in D3 where intersected by a slip trace. All other small particles remain intact; indicating that even small particles can crack, but only if they happen to be intersected by a slip line.

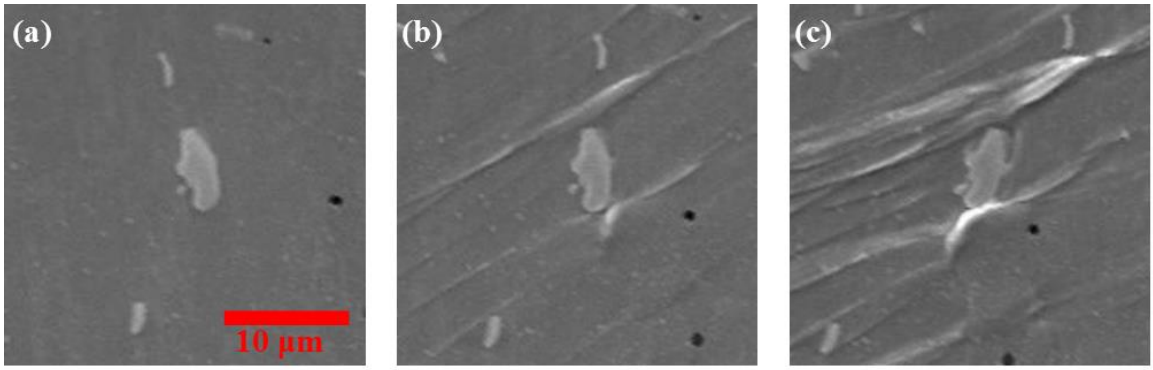

Figure 2.12: Snapshots of a particle that remains intact taken at D0, D1, and D4. The equivalent plastic strain in the vicinity of the particle is estimated to be b) 0.21 and c) 0.50. A rather large particle is found in between slip lines in D1. Despite continued deformation of the surrounding matrix material, the particle remains intact and bonded at D4.

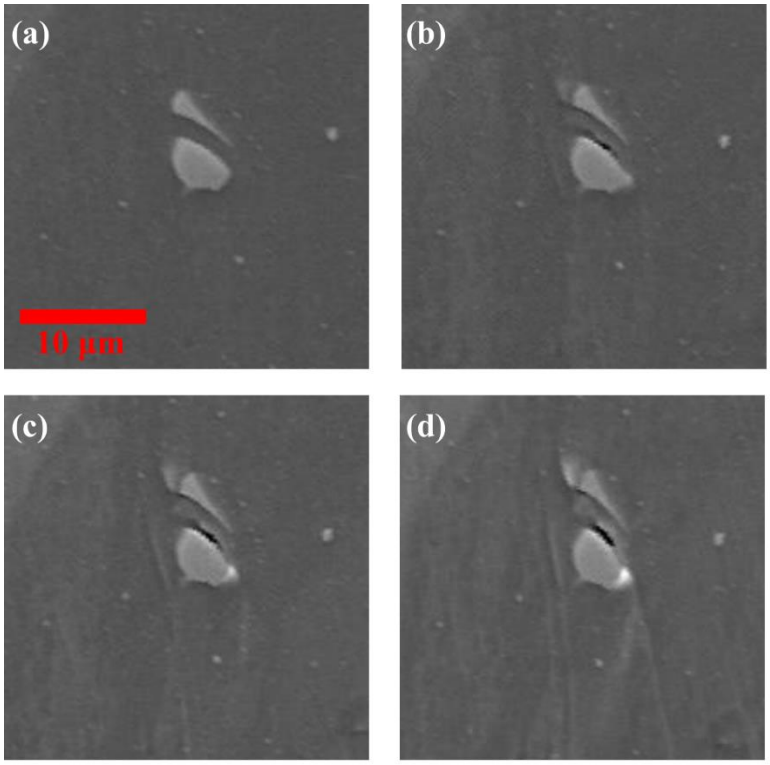

Figure 2.13: Snapshots of a particle pair with debonding taken at D0-D2 and D4. Interaction between particles is likely, as the lower particle is seen to be partially debonded by D1 to accommodate the growing separation between its neighbor. The debonded length grows by D2, however, by D4 the particle seems to have partially re-embedded into the matrix, as the debonded length is slightly shorter.

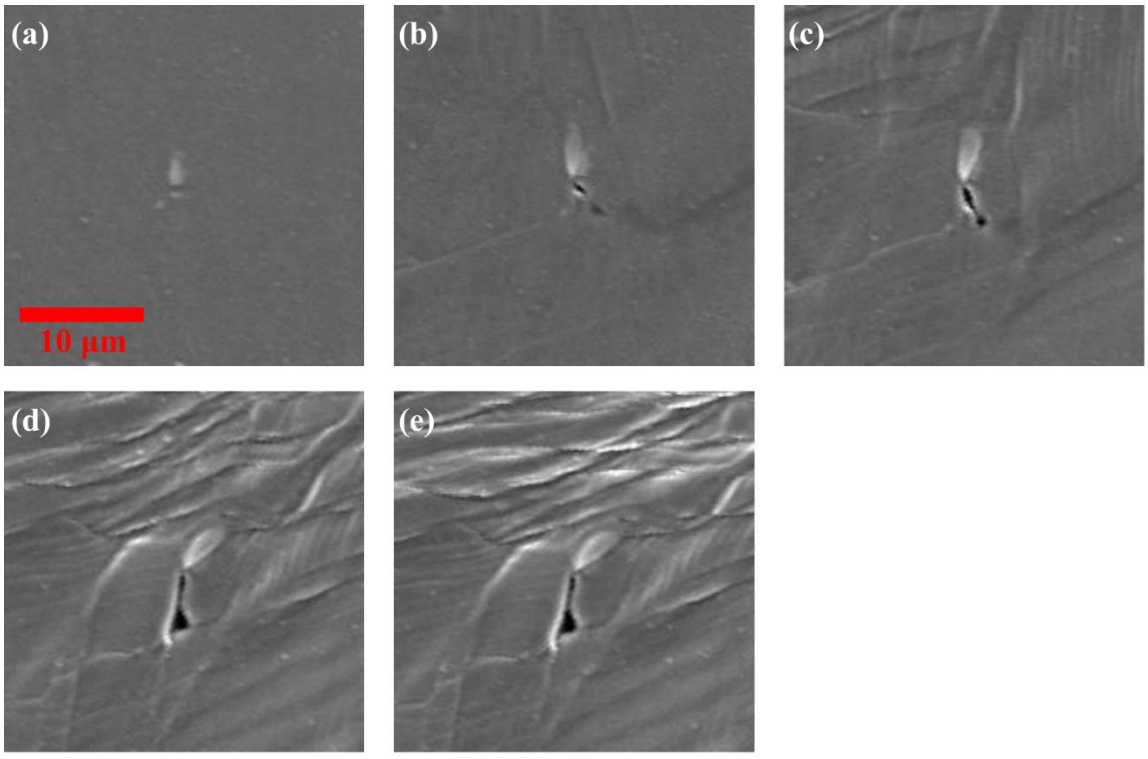

Figure 2.14: Snapshots of a particle tearing the matrix taken at D0-D4. The equivalent plastic strain in the vicinity of the particle is estimated to be b) 0.22, c) 0.44, d) 1 and e) 1.1. Out of plane deformation is clearly occurring, causing the particle to emerge from the subsurface. This particle may have smaller flaws than most others, allowing it to remain intact despite large concentrations of slip activity intersecting it. Atypical debonding is seen where matrix material that flows past the sharp tip is seen to tear.

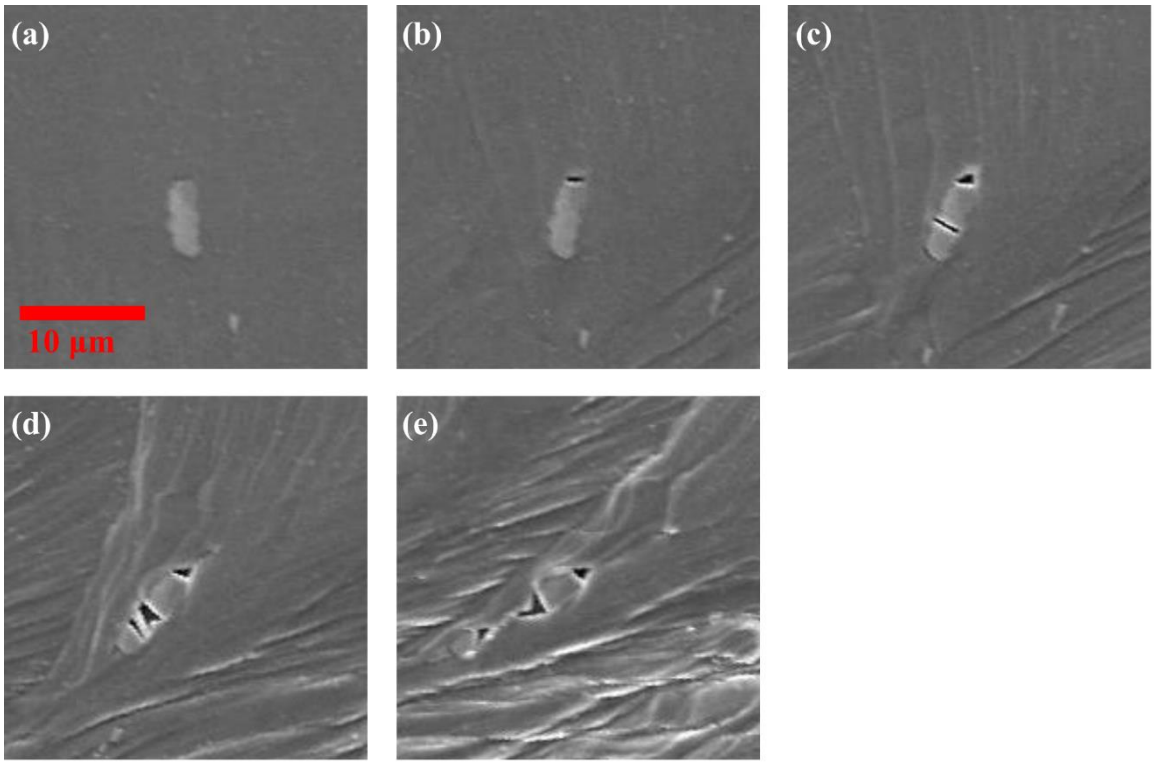

Figure 2.15: Snapshots of a particle debonding and then cracking taken at *D0-D4*. The equivalent plastic strain in the vicinity of the particle is estimated to be b) 0.15, c) 0.30, d) 1.5 and e) 2.2. A combination of particle debonding (initiated prior to *D1*), and cracking (seen twice, once at *D2* and again at *D3*). The nucleated voids initially grow, however, the one in between particle fragments is seen to partially collapse between *D3* and *D4*.

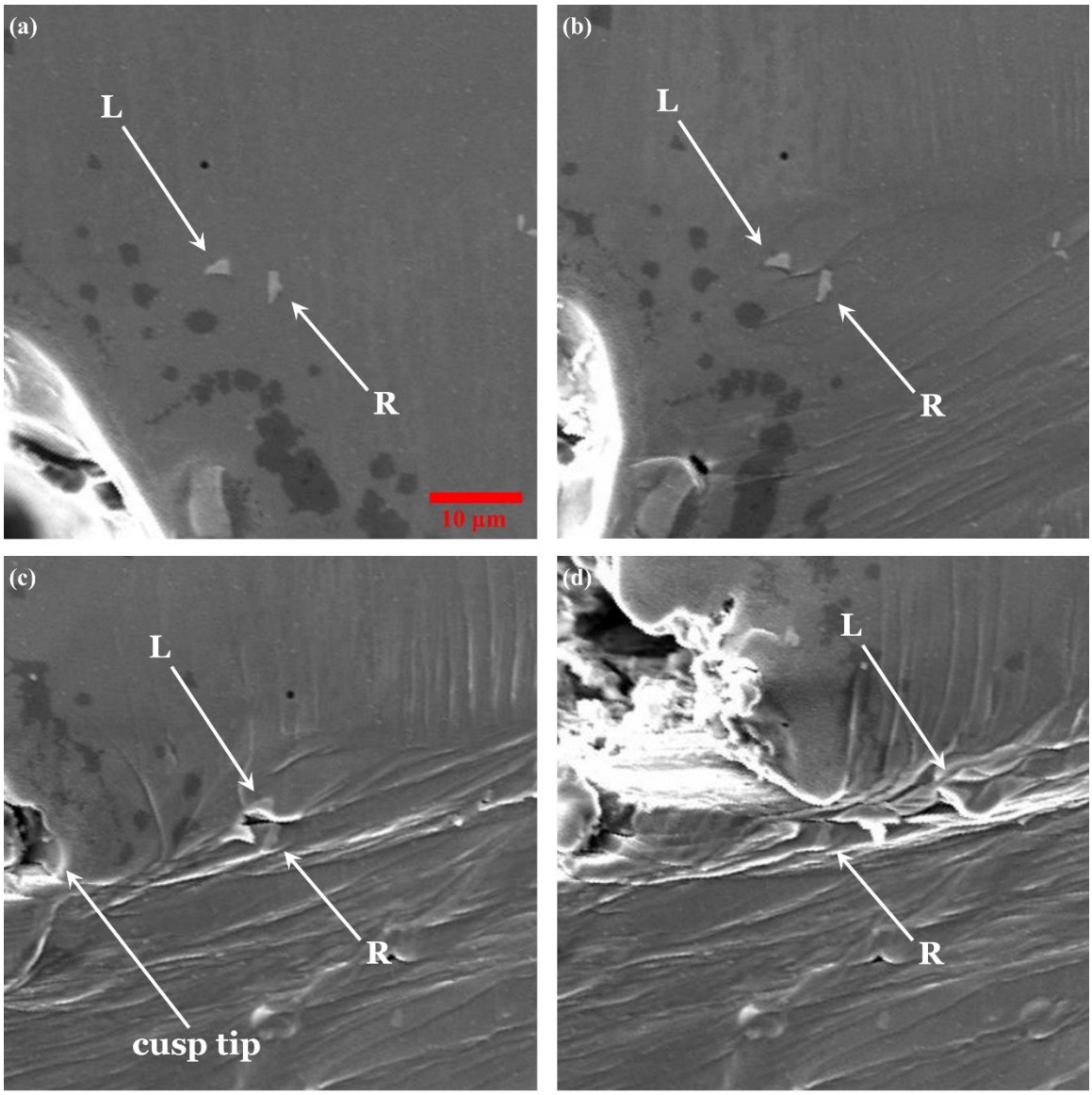

Figure 2.16: Snapshots of a strongly interacting particle pair taken at D0 and D1-D4. A concentration of plastic deformation is seen in between the two central particles in D2. This slip opens up a crack visible in D3. In D4 a crack initiated from the cusp links up to the interior crack, seemingly by coincidence.

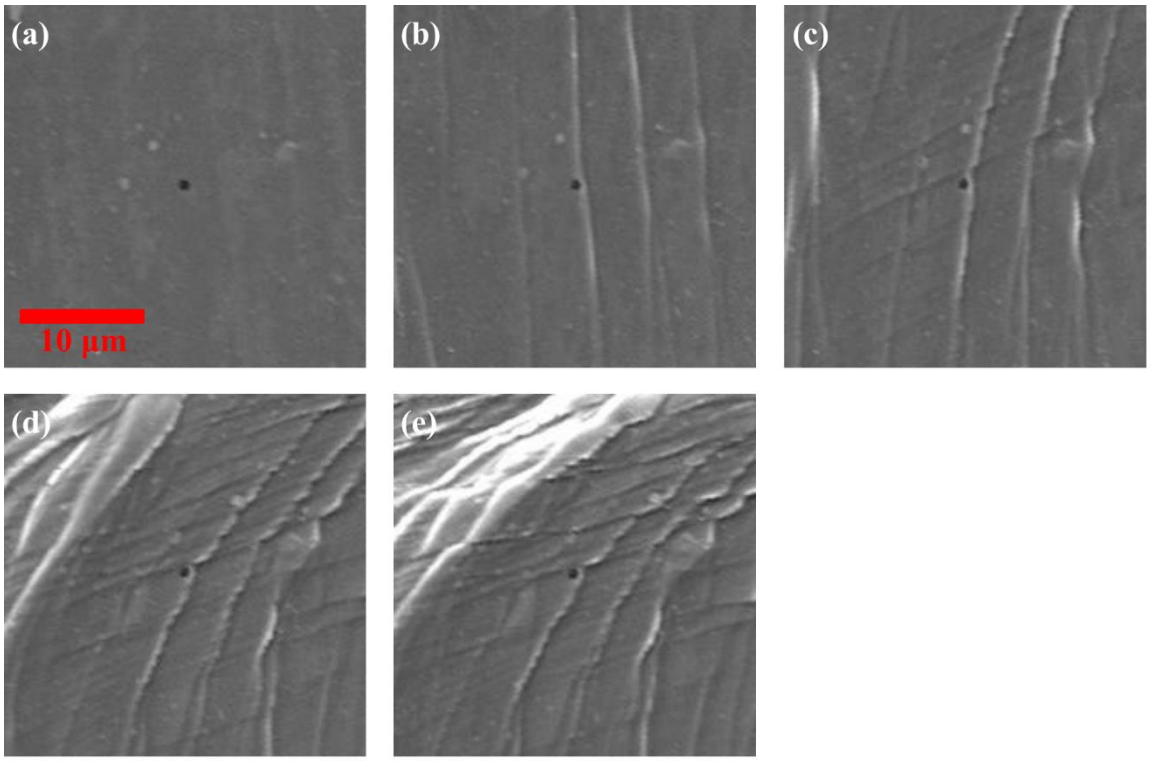

Figure 2.17: Snapshots of a void at D0-D4. The equivalent plastic strain in the vicinity of the void is estimated to be b) 0.15, c) 0.37, d) 0.66 and e) 0.87. The void is seen to be completely unperturbed by the surrounding plastic deformation occurring on multiple slip systems.

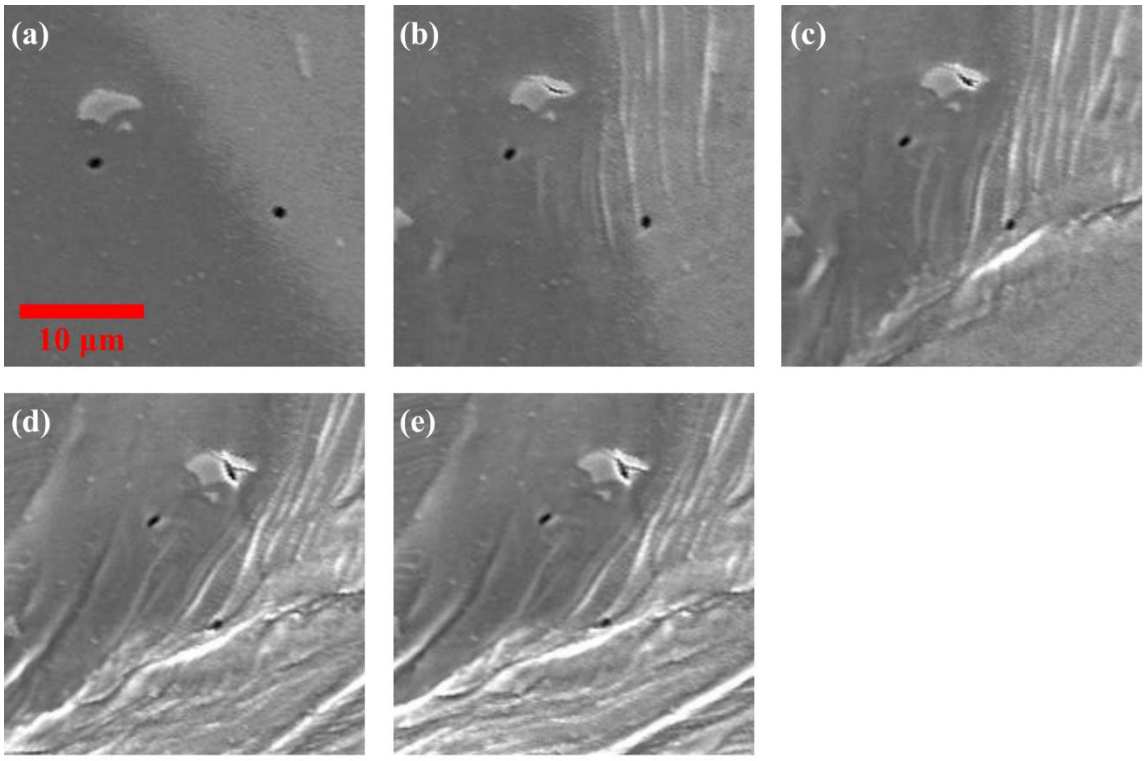

Figure 2.18: Snapshots of a void pair deforming taken at D0-D4. These voids are seen to deform modestly in response to extensive deformation of the surrounding matrix.

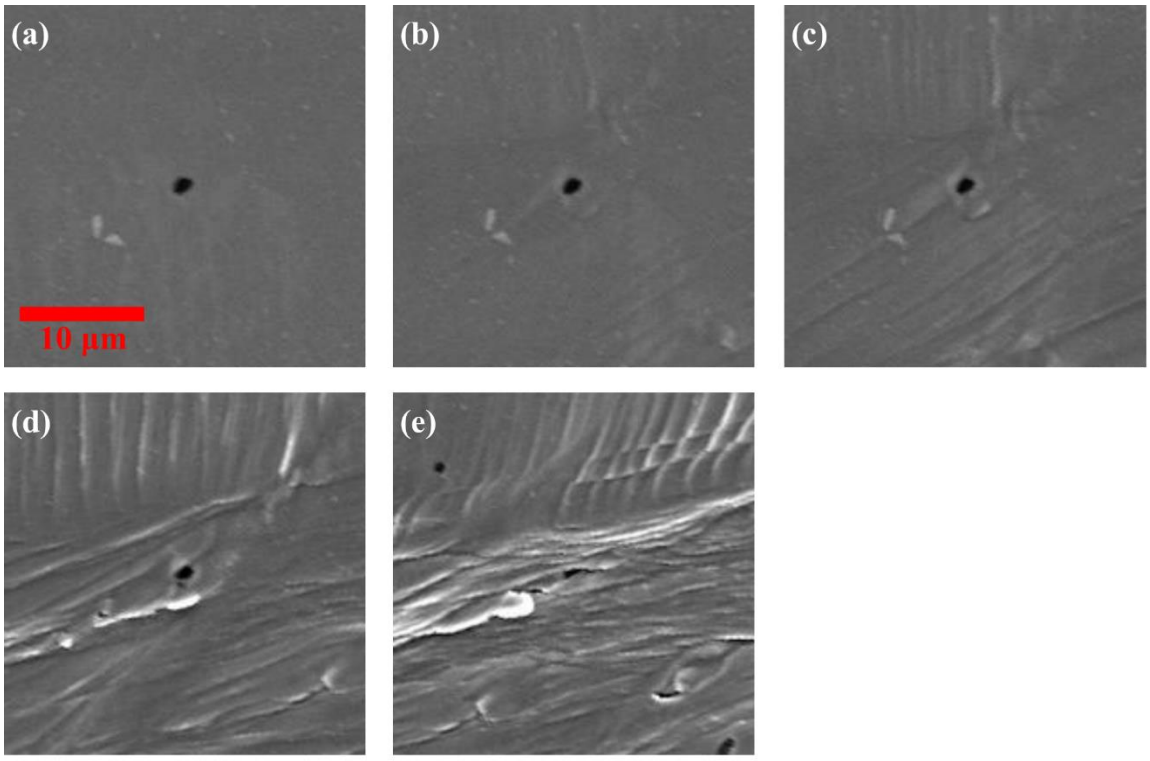

Figure 2.19: Snapshots of a void taken at D0-D4. The equivalent plastic strain in the vicinity of the void is estimated to be b) 0.17, c) 0.37, d) 0.98 and e) 1.6. The central void is seen to show little deformation, at least up to D3. In D4, a crack exists not far to the left of the void and the extreme loading causes considerable shearing of the void.

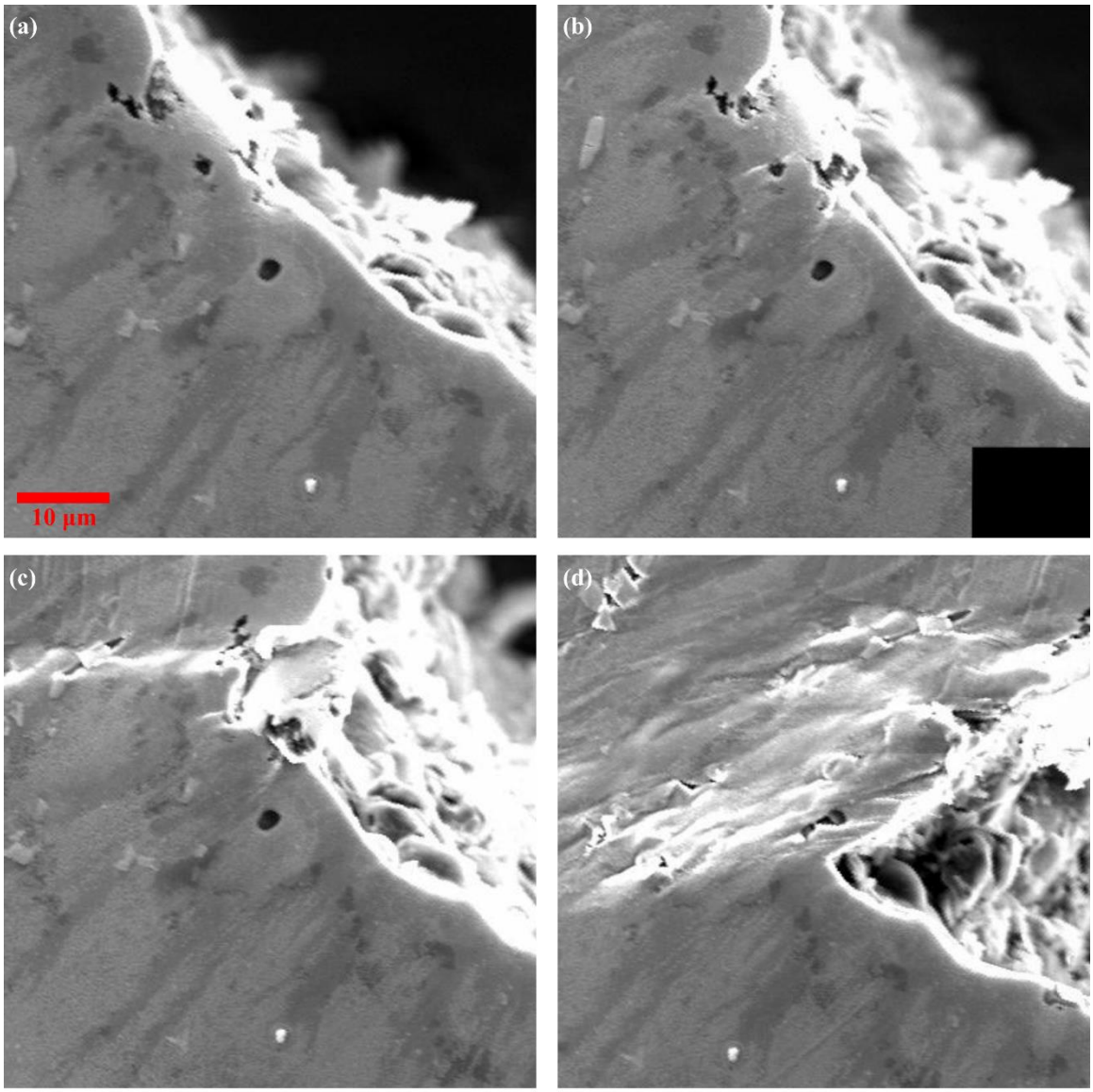

Figure 2.20: Snapshots of a void taken at D0-D3. A large void near the initial notch is seen to be unperturbed by a state of positive triaxiality during D1 and D2. As it passes over the cusp to the side with negative triaxiality, the void is seen to be partially collapsed in D3.

Chapter 3: Prediction of Ductile Failure in 15-5 PH Stainless Steel Using a Local Strain-to-Failure Criterion

3.1 INTRODUCTION

The details of the 2012 Sandia Fracture Challenge (we refer to this challenge as the 2012 SFC) and the outcomes are fully described by Boyce et al., (2014). The main goal of this Challenge was to explore the ability of computational models to predict the onset of ductile failure in a particular structural configuration; such predictions are to be based on calibration of the constitutive and failure properties of the material through a common set of tests and then through independent analysis of the structure, but without prior knowledge of the experimental outcome in order to provide a true indication of predictability. The 2012 SFC also laid out quantities-of-interest (QoIs) that must be compared between the predictions and experiments. Specifically, three QoIs were identified:

(i) What is the force and crack opening displacement (COD) at which a crack first initiates?

(ii) What is the path of crack propagation?

(iii) If the crack does propagate to either holes B, C, or D, at what force and COD does the crack re-initiate out of the first hole?

In addition, the load-COD response data was also requested, not as a primary QoI, but as a collection of the response that could be useful in interpreting the QoIs. In response to this Challenge, we developed a computational model, generated a prediction, and submitted it to Sandia National Laboratories (SNL); the predictions were performed without knowledge of the experimental outcome. The details of calibrating the constitutive and failure models and the prediction of the Challenge problem's response

are documented in this chapter in Sections 3.2 and 3.3. In an attempt to resolve or reconcile the different experimentally observed crack paths, we performed additional experiments on the same lot of specimens that SNL tested. The results of these experiments are reported in Section 3.4. Following up on the experimental results, additional computations were performed in order to identify the underlying reasons for multiple crack paths observed in the experiments; these computations, described in Section 3.5, indicate that geometric defects in the specimen contributed significantly to crack path selection. We conclude in Section 3.6 with a summary of the results of this investigation and a discussion of the prospects for ductile failure modeling.

3.2 CONSTITUTIVE AND FAILURE MODELS

To predict the response of structural materials, the elastic and plastic constitutive properties as well as the failure criteria of the material under consideration are needed. For the 15-5 PH stainless steel, the elastic-plastic behavior can be represented through a standard plasticity model. The details of the calibration of such a plasticity model are given in Section 3.2.1. Based on recent work (Ghahremaninezhad and Ravi-Chandar, 2012, 2013), we conjectured that ductile failure will arise rather abruptly and therefore it is essential to characterize the plastic deformation prior to the onset of failure accurately. To model the sudden change in material behavior during the failure process, a modified Johnson-Cook failure criterion was developed and calibrated as indicated in Section 3.2.2.

The ABAQUS finite element software is used for all modeling reported in this work. All models use explicit time stepping, since this is a requirement in the software to perform element deletion. Non-uniform mass scaling (where the scaled density is

proportional to volume of each element, so that all elements initially have the same stable time step) is used to increase the stable time step enough to make quasi-static simulations feasible on a desktop computer. Three-dimensional continuum linear elements with reduced integration (C3D8R) are used in all models for their computational efficiency and suitability for modeling structural instabilities.

3.2.1 Calibration of constitutive model

The elastic modulus of the 15-5 PH stainless steel under consideration is obtained by fitting the initial linear response and is found to be: E = 199 GPa. In the absence of reported experimental data, the Poisson's ratio was taken to be 0.3; the error associated with this is expected to be negligible since the response of the structure will be dominated by its plastic behavior. The plastic constitutive properties are determined through a calibration procedure that compares the results of iterative simulations to the experimental results provided by SNL (shown in Figure 3.1). Plastic deformation is assumed to be governed by the flow theory of plasticity with isotropic hardening. The slight anisotropy in the initial yield observed from tensile test results reported (see Boyce et al. 2014) in the longitudinal and transverse directions of the sheet is incorporated with the use of Hill's yield criterion (Hill, 1948). These tensile tests indicated that yield occurs at a stress 1.5% lower in the transverse direction than in the longitudinal direction. In the absence of data corresponding to the yield behavior in the thickness direction, normal anisotropy is assumed. The resulting yield criterion is given by:

$$F\left(\sigma_y-\sigma_z\right)^2+G\left(\sigma_z-\sigma_x\right)^2+H\left(\sigma_x-\sigma_y\right)^2+2L\sigma_{yz}^2+2M\sigma_{xz}^2+2N\sigma_{xy}^2=\sigma_0^2 \qquad (3.1)$$

where σ_0 is the yield stress and the parameters characteristic of the anisotropy are given in Table 3.1. In order to determine the strain hardening behavior, the experimentally recorded engineering stress and engineering strain reported by Boyce et al. (2014) are used directly for small strain levels. The engineering stress-strain curve for this material exhibits a local maximum at the end of the elastic regime, and is followed by a short plateau in stress (Figure 3.1). This feature indicates an instability in the experiment; however no mention of this instability or inhomogeneous deformation prior to necking was included with the test results distributed by SNL. From an examination of the full data, it is evident that tensile test results cannot be used directly beyond a logarithmic strain of ~6% because of the inhomogeneity of the deformation that is expected to occur beyond the Considère strain; the images of the failed specimens that were provided clearly indicate that localized necking and additional (nonhomogeneous) strains occurred within the neck. Therefore, the strain-hardening behavior for larger strain levels must be found through an inverse analysis.

For the inverse analysis, the material behavior up to a logarithmic plastic strain of 0.055 is taken directly from the experimental measurement since the deformation is expected to be homogeneous over the gage length of the specimen. Beyond this strain, the material is assumed to be well-described by a general power law of the form:

$$\sigma = C_1 + C_2\left(C_3 + \varepsilon^p\right)^{C_4} \tag{3.2}$$

where ε^p is the equivalent plastic strain, with material constants $C_1 - C_4$ to be determined through the calibration procedure. C^1 continuity is enforced between the inferred and directly observed stress-strain behavior, placing two constraints on the four unknown constitutive parameters. The remaining two coefficients of the power law are

then found through iterative finite element simulations of the tensile test with different trial coefficients.

A MATLAB code was developed to perform the required iterative finite element simulations automatically. This code was used to generate a different trial material for each iteration by specifying the two unconstrained coefficients of the power law. Then the resulting stress-strain behavior is used in an ABAQUS simulation of the tensile test to generate the resulting force-elongation (or nominal stress vs nominal strain) curve. Comparison of the simulated force-elongation curve with that provided by the experimental measurement results in a calculation of the error associated with each trial material. Once the error has been calculated for a set of trial material models, a genetic algorithm is used to choose a set of new trial coefficients and the process is repeated with the goal of minimizing the error. For this code, the nominal strain in the simulation is defined as the change in length over initial length across a 25.4 millimeter span centered on the neck; this strain measure mimics the extensometer reading recorded from the experiments. The error for each trial material is defined as the sum of the squared differences in the net load between its simulation result the experiment at 201 nominal strain values.

This code was first used with a coarse mesh model to quickly approximate the trial coefficients. After convergence of the stress-strain behavior, a fine mesh model was used to finalize the material parameters. To lower the computational cost both models used the three available symmetries in the loading and geometry. The load was applied by an axial displacement on the end of the specimen and varied quadratically over the simulation time. The coarse mesh consisted of 2500 uniformly sized elements that are nearly cubic in shape, with a dimension of 381 μm per side. The fine mesh model had 9520 elements of varying size, the smallest of which were placed at the center of the

necking region with a size of 51 x 227 x 20 μm. The elements were oriented such that the large deformation would reduce their aspect ratio throughout the simulation. After final convergence of this optimization scheme an accurate simulation of the global response of the tensile test was obtained as shown in Figure 3.1. The simulation was terminated based on a criterion discussed in Section 3.2.2. The estimated strain-hardening behavior of the material far beyond the Considère strain is shown in Figure 3.2; note that while the direct measurement of the strain-hardening response terminated at a strain level of 0.055, the inverse procedure extends the calibration to logarithmic strain levels of about 1.3. Another comparison between the simulation and experiment can be obtained by considering the deformed shape of the necked region; this is shown in Figure 3.3 to suggest that the simulated response is reasonably close to the observed deformation, deviating the most in the region of highest strain. The strain-hardening response indicated in Figure 3.2 is used in all further simulations reported in this paper; the calibrated model parameters $C_1 - C_4$ are given in Table 3.1. We note in closing that the calibration has been performed with only global measures introduced in the optimization procedure. The use of local measures, such as the details of the deformation field development during necking, may provide additional constraints on the constitutive characterization and calibration that can be used to model additional features of anisotropy both in yield and strain hardening. Nevertheless, given the limited experimental dataset, the calibration given in Figure 3.2 and Table 3.2 was the most detailed anisotropic model possible.

3.2.2 Calibration of failure model

Ductile failure is most often described by the nucleation, growth, and coalescence of voids across a broad range of strains until failure occurs; micromechanical models

such as the Gurson-Tvergaard-Needleman models have been developed and are commonly used in failure predictions. However, based on recent work (Ghahremaninezhad and Ravi-Chandar, 2012, 2013), and an examination of the microstructure images provided by SNL, we conjectured that damage will begin at much later stages in the deformation of the material with large scale void growth occurring only near the brink of final failure and then progress rapidly. The sudden appearance of damage just prior to failure means that stiffness degradation of the material due to damage can be adequately approximated as a complete loss of stiffness once damage has occurred. Then, all behavior up to failure is completely described by the constitutive relations and a simple equivalent plastic strain-to-failure model suffices to incorporate material fracture. With this in mind, a very simple, modified version of the Johnson-Cook model is used to represent damage. When an element in the finite-element simulations reaches this damage initiation criterion, as implemented through the cumulative damage approach within ABAQUS, its stiffness is set to zero.

The Johnson-Cook failure model (Johnson and Cook, 1985) is commonly used in many applications; for isothermal conditions at small strain rates, it is postulated that the maximum equivalent plastic strain, ε_f, that can be attained at a given level of stress triaxiality can be expressed as:

$$\varepsilon_f\left(\sigma^*\right) = D_1 + D_2 \exp\left(D_3 \sigma^*\right) \tag{3.3}$$

where the triaxiality parameter $\sigma^* = \sigma_m / \sigma_e$ is the ratio of the mean stress, $\sigma_m = \sigma_{kk}/3$, to the effective stress, $\sigma_e = \sqrt{\frac{3}{2} s_{ij} s_{ij}}$, and $s_{ij} = \sigma_{ij} - \frac{1}{3}\sigma_{kk}\delta_{ij}$ is the deviatoric stress. $D_1 - D_3$ are material constants to be determined through calibration experiments. Since the underlying motivation for such a failure model is the rapid growth of voids in a

localized region, the exponential dependence of the failure strain on triaxiality may be motivated by the void growth analysis of McClintock (1968) and Rice and Tracey (1968). In the present work, while we use failure criterion in the form of Eq. (3), a significant and crucial departure occurs in the calibration of the model: while the traditional calibration of the Johnson-Cook failure model is obtained through macroscopic measurements of strains at gage lengths that correspond to specimen dimensions, we recognize that the local strains at the level of a few grains prior to final failure could be quite high. In previous studies on Al 6061-T6, Ghahremaninezhad and Ravi-Chandar (2012, 2013) showed that while the Johnson-Cook model calibrated through macroscopic measurements (for example as given in Lesuer et al. 2001), indicated quite low strain-to-failure, local measurements based on grain level measurements on a scale of about 20 μm indicated significantly greater local strains. Since the 15-5 PH stainless steel is a very fine grained material, with average grain size ~ 4.7 μm, we estimated that the local strain to failure could be quite large.

For calibration of the failure criterion, we have two kinds of experimental results provided by the SNL Structural Mechanics Laboratory. Therefore, two restrictions can be placed on the coefficients $D_1 - D_3$ from the experiments; the first constraint is obtained from the tensile test and the second constraint arises from the fracture test performed on the compact tension ($C(T)$) specimen. In our calibration procedure, the optimized strain-hardening response found in Section 3.0 is used in a simulation of the full tensile specimen. This simulation is continued until the nominal strain across the 25.4 mm gage length reaches the average rupture strain reported from the two tensile experiments tested in the longitudinal direction of the sheet. Then the equivalent plastic strain and triaxiality at the central element, the location where both quantities reach their maxima, are taken to be those corresponding to failure, resulting in a constraint on the failure model. Thus,

information about the failure of the material is deduced without implementing the failure model in simulations. Simulating the uniaxial tension experiment with the optimized strain-hardening response using the above conditions for failure resulted in a stress triaxiality of ~0.9 at the center of the neck and a local equivalent plastic strain of ~ 1.3 just before failure. Performing the tension test simulation with inclusion of this failure criterion is merely used as a check and yields the simulation result shown in Figure 3.1.

The second constraint placed on the failure model is obtained from matching the global load-displacement response of the *C*(*T*) specimen, since this is the only dataset provided by SNL for comparison. From this response, it is evident that the specimen exhibited slow stable crack growth; modeling this requires the inclusion of the failure model in simulations. However, calibration of the failure model is the objective of the simulations; therefore, these simulations are run iteratively, varying failure parameters of the modified Johnson-Cook model within the constraint found from modeling the rupture of the tensile specimen with the goal of replicating the load-COD response of the *C(T)* specimen. It is noted that parameter D_1 in Eq.(3) is the most significant parameter in this process, since it has the greatest influence at high triaxialities, and least at low triaxialities. Seven iterations were performed with different damage parameters selected by the investigator; automation was not pursued due to the large computational cost of this simulation. During this calibration process, it was determined that inclusion of the through-thickness curvature of the fatigue precrack is critical to successfully simulate the crack growth response of the *C*(*T*) specimen. The crack profile resulting from the fatigue precracking procedure was approximated using the specification for precrack length measurement in ASTM E399, as the details of the exact shape were not available. Figure 3.4 shows the details of the mesh and the geometry of the crack tip region; this view is sectioned along the prospective crack plane. Figure 3.5 is additionally sectioned on the

specimen midplane. The curvature of the precrack is visible in Figure 3.5a corresponding to a loading stage prior to crack extension; the characteristic shape of the plastic zone can be identified easily in this figure. Figures 3.5(b) and 3.5(c) show the growth of the crack; the initial parabolic shape of the crack front is seen to lead to a significantly tunneled crack front as crack extension continues. At the crack tip high triaxialities are developed, with the level of triaxiality being sensitive to the mesh size. Additionally, the equivalent plastic strain is mesh dependent near the crack tip. For these two reasons, once the failure model is calibrated it is tied to the mesh size used in modeling the $C(T)$ specimen. For this work, elements with planar dimensions of 31.75 x 31.75 μm were used in all areas where fracture is a possibility; this is roughly 10 times the grain size in the material. Since data on crack extension was not provided, comparison between simulations and experiments can be performed only with respect to the load-COD variation as indicated in Figure 3.6. The agreement between the simulation and experimental load-COD variation shown in Figure 3.6 is considered to be adequate for obtaining an estimate for the strain-to-failure corresponding to the triaxiality state at the crack tip. This is mainly because we anticipated that the triaxialities in the Challenge geometry are likely to be significantly lower during the crack initiation stages. From this calibration procedure, we took the strain-to-failure at a triaxiality of ~1.9 to be ~0.26.

After exhausting the experimental results provided, one degree of freedom in the failure model is left unconstrained. Since the failure strain at low triaxialities is not provided by any given experimental results, an approximation is made based on prior knowledge of other materials. Considering that it is very difficult to damage most materials under pure shear[1] (with low triaxiality), we set $\varepsilon_f\left(\sigma^* = 0\right) = 3.9$. The final

[1] A number of experimental investigations have indicated that it is quite difficult to trigger failure under pure shear; in recent work Ghahremaninezhad and Ravi-Chandar

failure model parameters $D_1 - D_3$ are listed in Table 3.1. The modified Johnson-Cook failure model for the 15-5 PH stainless steel is shown in Figure 3.7. The variation of the triaxiality and equivalent plastic strain for the critical element in the uniaxial tension test and a characteristic element in the $C(T)$ test are also indicated in Figure 3.7. While we have calibrated a modified Johnson-Cook model for the purposes of this Challenge problem, we note that the experimental information provided is insufficient to characterize the failure criterion completely; additional experiments corresponding to low triaxiality conditions as well as additional measurements in the tension and fracture tests would provide a richer dataset on which the constitutive and failure models for the material can be calibrated.

3.3 BLIND PREDICTION OF THE RESPONSE OF THE CHALLENGE GEOMETRY

This simulation was performed without utilizing the available symmetry. Discretization of the challenge geometry is shown in Figure 3.8; eight-noded linear elements with reduced integration and hourglass control were used. Thirty-one elements were used across the thickness and the smallest elements had in plane dimensions of 31.75 x 31.75 μm in keeping with the element size used in the failure calibration. A uniform and highly refined mesh is used in the vicinity of the holes *A*-*B*-*C*-*D* in regions of anticipated strain localization. These small elements were used uniformly in all areas where strain localization and subsequent fracture was a possibility; examination of the

---

(2011, 2012, 2013) have shown that in pure oxygen free high conductivity copper and Al 6061-T6 the lower-bound for the equivalent plastic strain at failure could be in the range of 2 to 4. These studies also indicated that failure really nucleates at locations where positive triaxiality develops in specific regions of the specimen. Based on this experience, we expect that for the 15-5 PH stainless steel the equivalent plastic strain at failure under pure shear could be in this range as well.

specimen geometry clearly indicates that failure may occur along the thin ligaments across segments *A-D*, *A-C*, *A-B*, *D-C*, and *C-E*. A total of 2.25 million elements with seven million degrees of freedom were used; computations were performed in a Linux machine utilizing seven cores and typically required about 2000h of CPU time (280 hours of wall time with 7 cores). The constitutive and failure properties of the 15-5 PH stainless steel, calibrated as indicated in Section 3.2, were used to obtain a blind prediction to the response of the 2012 SFC challenge specimen. The loading pins were included as rigid, frictionless bodies; the pin nearest to hole D was kept stationary and the other pin was moved quadratically over the simulation time to apply the load. The applied load is reported from the reaction at the stationary pin.

A graphical illustration of the results from the simulation is shown in a movie included as Supplementary Material SM3 to this dissertation. The predicted variation of the load with the COD is shown in Figure 3.9. In order to track the evolution of deformation and constraint in the specimen, the spatial distributions of the equivalent plastic strain and the triaxiality on the middle plane of the specimen at load steps marked as 1 – 6 in Figure 3.9 are shown in Figures 3.10 and 3.11, respectively. The variation with the COD of the equivalent plastic strain and triaxiality at critical elements (the elements that are approaching the failure criterion more quickly than any other in the same ligament) in the ligaments *A-D* and *A-C* near points labeled I and II in Figure 3.8 is shown in Figure 3.12. The variation of the equivalent plastic strain with triaxiality at the critical elements in ligaments *A-D*, *A-C*, and *C-E* is plotted in Figure 3.13, along with the failure curve in order to indicate the progression towards failure. The following features of the predictions are noted:

- The load-COD diagram indicates an initial elastic region followed by a nonlinear response in the plastic region. From Figure 3.10, it is clear that during the early

stages of the loading (steps 2 and 3), plastic deformation accumulates more rapidly in the ligament *A*-*D* than in any other ligament. The triaxiality in this ligament is quite low (see Figure 3.11) and hence failure is not imminent.

- A limit load is reached corresponding to a COD ~ 2.3 mm (state 3). From an examination of Figures 3.10 and 3.11, it is clear that this corresponds to the formation of a mechanism for accommodating plastic flow across ligaments *A*-*D*, *D*-*C*, and *A*-*C*. Following the limit load, a structural softening occurs. When the limit load is reached, the ligament *A*-*D* still carries the highest strain; however at this point thinning localization initiates in ligament *A*-*C*.
- After the peak load, strain accumulation in ligament *A*-*D* tapers off quickly and the equivalent plastic strain reaches a constant value, well below the failure strain level for the triaxiality in this ligament (see the red lines in Figures 3.12 and 3.13). Meanwhile ligament *A*-*C* experiences a rapid increase in strain as well as triaxiality until it fails (see the black lines in Figures 3.12 and 3.13). The ligament *A*-*C* failed first eventually crossing the modified Johnson-Cook failure line at a triaxiality of about one.
- The failure of the ligament *A*-*C* occurs over a small increase in COD in the simulation, raising the possibility of a dynamic event in the experiment. Due to the artificially increased mass, the simulation cannot capture dynamic events. Therefore, this simulation does not provide a confident prediction just after the fracture of ligament *A*-*C* begins.
- The integrity of the simulation resumes shortly thereafter (at a COD increment of 0.25 mm after first initiation), and shows a nearly constant load maintained over a large range of COD. In this region, deformation is localizing on the surface of hole *C*, on the large ligament *C*-*E*. The final fracture is then initiated just off the

surface of hole *C* and is accompanied by a rapid drop in load. With continued loading, the crack propagates towards the back edge of the specimen until the simulation is stopped. In summary, the simulations indicated a failure path along *A*-*C*-*E*, and the load-COD variation indicated in Figure 3.9.

– The approach to failure is tracked by following the variation of the equivalent plastic strain and triaxiality with loading in Figure 3.13. The ligament *A*-*C* starts at a triaxiality of ~ 0.5, but quickly increases to about one and failure of the ligament occurs at the state indicated by the black 'x' in the figure. At this stage, the ligaments *A*-*D* and *C*-*E* are at a strain level of ~ 0.5, at smaller triaxialities, and far from failure as indicated by the circular symbols on the red and blue lines. Once ligament *A*-*C* breaks, the ligament *A*-*D* stops straining further and all strain accumulation is in the vicinity of the ligament *C*-*E*, which eventually fails at a strain level of ~ 1.25.

The results described in this section are the main results of the blind prediction. We now turn to a comparison to the experimental results; a complete description of the experiments performed by SNL can be found in the article by Boyce et al. (2014). As described by Boyce et al. (2014), in a majority of the experiments performed, the crack followed the path *A*-*D*-*C*-*E*. However, two experiments – one each from the Structural Mechanics Laboratory and the Materials Mechanics Laboratory – showed fracture along the path *A*-*C*-*E*. Here we provide a comparison of our prediction only to the experiment **D1** that exhibited the crack path *A*-*C*-*E*, as this response is distinct from the result for the other crack path. We will follow this up in Sections 3.4 and 3.5 with an additional investigation to discern the reasons for the experiments exhibiting two different paths.

The load-COD variation from the blind prediction of the present work is overlaid with the experiment **D1** in Figure 3.14. Overall, the prediction from this modeling effort

is in very good quantitative agreement with the experimental results reported by SNL *for the specimens that followed the crack path A-C-E*; see the article by Boyce et al. (2014) for a quantitative comparison of the scalar QoIs. Specifically, the loading sector prior to the onset of localization, the limit load, the onset of failure in the ligament *A-C*, the plateau load beyond the first failure of the ligament *A-C*, and the rate at which load drops after both failures are initiated, *all show excellent agreement between the simulation and experiment*. The COD of second initiation in the ligament *C-E* is the weakest part of the prediction. We attribute this shortcoming to the fact that the triaxiality of the initiation site is much lower than any experimental result used to calibrate the failure model and consequently falls outside the region where the failure model is best matched to the material. As shown in Figure 3.13, the location in the ligament *A-C* that failed first follows the path in triaxiality-strain space shown by the black line, beginning at very low triaxiality at the early stage of loading and eventually crossing the failure line at a triaxiality of about one. At this stage, the triaxiality in the critical element of ligament *C-E* is about 0.6 (indicated by the blue circular symbol in Figure 3.13); with further loading, the triaxiality remains nearly constant as the strain increases towards the failure threshold; however, this triaxiality is outside the range of values used in the calibration of the failure criterion. Additional calibration data for lower triaxiality levels is needed in order to bring the second crack nucleation prediction closer to the experimentally observed range.

We close by summarizing that the blind prediction for the 2012 SFC using a well-calibrated continuum plasticity model, augmented with a simple triaxiality-dependent strain-to-failure model is capable of providing predictive simulations of ductile failure; the need for additional calibration experiments that can provide failure data at lower triaxiality conditions has also been identified. Nevertheless, some additional questions

remain: the most serious of these are as follows: (i) why did the majority of the experiments performed by SNL follow the path *A-D-C-E*? (ii) could the two different paths followed in the experiments be reproduced in the simulations by proper accounting of the underlying reasons? These issues are addressed in the following two sections through additional experiments and simulations.

3.4 ADDITIONAL EXPERIMENTS EXPLORING CRACK PATH SELECTION

The observation of multiple crack paths from SNL's experiments gave rise to uncertainties about the testing conditions and how they could affect the test outcome. Furthermore, the excellent agreement demonstrated above between the predictions described in Section 3.0 and the specimen **D1** that failed with crack path *A-C-E* provided strong evidence that some unreported and/or possibly unknown factor in these experiments determined their final outcome. Initially we hypothesized that misalignments in specimen loading may be a driving force to encourage localization in ligament *A-D*, since it is the site of substantial strain accumulation prior to the localization and subsequent failure of ligament *A-C* in the blind prediction. It is with this perspective that additional testing of the 2012 SFC challenge geometry was explored. SNL provided three samples (**S09**, **S10**, and **S11**) from the original lot of challenge specimens for this testing. Specimens **S09** and **S10** were fully machined and ready for testing, but specimen **S11** was not fully prepared on delivery. This specimen had the four holes drilled (*A*, *B*, *C*, and *D*), but the slot connecting hole *A* to the specimen's edge had not been cut. The notch was cut at the University of Texas using wire EDM. The slot was placed as specified in the drawing, but after cutting it was clear that hole *A* was misplaced in such a way as to reduce the thickness of ligament *A-D* as can be seen in Figure 3.15.

The experimental setup shown in Figure 3.16 was designed to minimize loading misalignments and to quantify any remaining misalignments using an ARAMIS three dimensional digital image correlation system (3D-DIC). Both clevises were anchored to the loading frame through a universal joint. The extra degrees of freedom from the joints compensate for both in-plane and out of plane misalignments in the loading fixture. However, due to anticipated specimen rotation during the test, the universal joints are not sufficient to eliminate all unwanted in-plane loads. In order to accommodate this rotation, the clevis is flat where contact with the specimen loading pins occurs, as specified in ASTM standard E399 for fracture tests. This allows the loading pins to freely rotate throughout the test, significantly reducing unwanted in-plane transverse loads. The need for and use of this degree of freedom is clearly observed in images taken during the test and can be seen in the experimental videos included as Supplementary Materials SM4 and SM5 for this dissertation. Loading was applied with a 100 kN capacity Instron Model 5582 electromechanical universal testing machine. The load was measured by an Instron Model 2525 100 kN load cell. This sensor was self-calibrated and is specified to have an uncertainty of 25 N. The tests were carried out at a crosshead rate of 12.7 μm/s, the same rate at which the SNL Structural Mechanics Laboratory tests were conducted. Load was sampled at a rate of 10 Hz and images were taken once every second. Displacements were tracked with two 2.5 MP cameras with a spatial resolution of 18 μm per pixel. The field of view of these cameras can be seen in the Supplementary Material files SM4 and SM5 for this dissertation. For these tests the uncertainty in displacements was found to be 10 μm and the uncertainty in strain is 1000 microstrain. The COD was measured by taking the difference in displacement between two points tracked with DIC. Since DIC does not provide results near specimen edges, the points chosen for the COD measurement were offset about 1 mm from the knife edge (where clip gauge

measurements are taken), toward the center of the loading hole. In order to quantify the amount of out-of-plane deformation, a plane was fit to points with DIC measurements on the notch flanks where plastic deformation does not occur. Between all three specimens, the maximum deviation between this plane and any experimentally observed point did not exceed 17 μm prior to failure of ligament *C-E*, and the standard deviation between the plane and points never exceeded 4 μm. Typically the maximum deviation remained less than the uncertainty in displacement measurements, thus verifying that out-of-plane loading was negligible for these experiments.

3.4.1 Failure path A-C-E

Both specimens **S09** and **S10** failed along the crack path *A-C-E*. A video file containing the development of equivalent plastic strain as obtained from the 3D-DIC for specimen **S09** is included as the Supplementary Material SM4 for this dissertation. The load variation with COD for both tests can be seen in Figure 3.17 and show agreement with SNL's specimen **D1** that failed along the same crack path. The sharp load drop is accompanied by an audible 'pop'; the development of the crack penetrating the surface was not captured due to the limited spatial and temporal resolution of the stereo visions system used. The only noteworthy difference between the results from the present tests and the specimen **D1** from SNL is that failure initiated at a greater COD in the present tests. The factors that may influence this observation are variations in specimen-to-specimen material properties, geometry, or the slightly different loading conditions applied in the two labs. Decoupling the effects of these influences is not the focus of this work, however it is noted that experimental boundary conditions must be implemented with great scrutiny to ensure that the intended loading is imparted and so that

observations are repeatable in different labs. It is also noted that an analysis of the dimensional tolerances for the specimens **S09-S11** is given in Boyce et al. (2014); specimens **S09** and **S10**, along with **D1** had the smallest deviation from the specifications in the ratio of the ligament lengths between *A-D* and *A-C*.

Agreement with global quantities such as the variation of load with respect to COD does not always assure that a model accurately captures the conditions of failure initiation and propagation. Specifically, failure in this structure is always preceded by localization, regardless of crack path; during localization the strain field in the localized area changes rapidly with COD. Thus, even if the COD reported for failure in the model is close to the experimental value, the local state under which failure occurred in the model could have large errors. The local strain information obtained from using 3D-DIC in these experiments provides an additional assessment of the blind prediction offered in Section 3.0. Figure 3.18 shows the local equivalent plastic strain contours observed in the specimen **S09** compared to those calculated in the blind prediction at three different COD levels. A quantitative comparison of the variation with COD of the measured equivalent plastic strains at two points in the ligaments *A-D* and *A-C* of Specimen **S09** is shown in Figure 3.19 compared with the corresponding results from the blind predictions reported in Section 3.3. The simulation captures the correct overall trends in the strain evolution on the surface of the specimen as well as the details in all the ligaments where substantial straining occurs. Even further, the local strain at failure on the ligament *A-C* is nearly identical in the experiment and blind prediction, implying that the calibration of the failure model for this range of triaxiality is quite good.

The failure surface of the ligament *A-C* was examined through microscopy; the overall appearance was similar to that observed by Boyce et al. (2014; see Figure 3.16). Significant thinning of the ligament was clearly observed; measurements of the thickness

change performed on a micrograph of the specimen near the notch *A* indicated a strain of about 0.28. This is clearly supported by the softening behavior seen in the load-COD variation. A high magnification image of the fracture surface in the middle portion of the ligament *A-C* is shown in Figure 3.20. This region has a dimpled surface suggesting that the failure occurred under high triaxiality through void growth and coalescence. There were some regions where the size of the fracture surface features were quite large, suggesting that the path possibly meandered through the stringers observed in the microstructure.

3.4.2 Failure path A-D-C-E

Specimen **S11** failed with crack path *A-D-C-E*; a video file containing the development of equivalent plastic strain as obtained from the 3D-DIC for specimen **S11** is included as Supplementary Material SM5 for this dissertation. The load variation with COD is shown in Figure 3.21 and shows agreement with SNL's tests that failed with the same crack path; data from SNL tests **S02** and **S08** are plotted in the same figure, because their COD at first initiation bound all other results. The first failure of the ligament was accompanied by an audible 'pop' as reported by SNL; this was due to an internal crack, as confirmed from further tests reported below. Subsequent loading caused this crack to propagate across the ligament *A-D*, and then triggered another audible 'pop' as the ligament *C-D* failed. Each audible sound was accompanied by a sharp load drop. This agreement between the failure behavior of **S11** and SNL's testing, as well as the fact that **S11** had a geometrical defect in the ratio of the size of ligaments *A-D* to *A-C* that was out of specification, suggests that geometric defects similar to the one observed in specimen **S11** might have existed in the specimens that failed with crack path *A-D-C-E* at SNL.

This was indeed confirmed by an examination of the geometric imperfections as reported by Boyce et al. (2014). The task of identifying the role of these geometric imperfections in the selection of paths *A-C-E* and *A-D-C-E* still remains; we will explore this, first by considering the experimental results of **S09** and **S11**, and then through numerical simulations.

The failure surface of the ligament *A-D* was examined through microscopy; the overall appearance was similar to that observed by Boyce et al. (2014; see Figure 3.16). Similar to the ligament *A-C* of specimen **S09**, thinning of the ligament *A-D* was significant; measurements of the thickness change performed on a micrograph of the specimen across the fractured surface indicated a strain of about 0.2. Although deformation is dominated by shear in this ligament, there must be significant stretching in order to cause such thinning. A high magnification image of the fracture surface in the middle portion of the ligament *A-D* is shown in Figure 3.22. This region presented a mixed appearance: some regions show a dimpled surface suggesting that the failure occurred through void growth and coalescence, but other regions appear as a cascade of ledges, with individual features on different planes. The mechanism of fracture is not readily apparent from these images. Additionally, regions away from the center of the ligament *A-D* were damaged significantly by contact and sliding of the two mating fracture surfaces resulting in a grooved appearance. In order to explore the failure along *A-D* more carefully, tests was performed on additional specimens fabricated from a different batch of material.[2] Two of the specimens that indicated eventual failure along the path *A-D* were interrupted: one test was halted and the specimen unloaded as soon as

[2] These specimens were made from another sheet of the 15-5 PH stainless steel purchased from AK Steel (West Chester, Ohio). We are grateful to Dr. Brad Boyce of Sandia National Laboratories for heat-treating these samples to the same protocol as the SFC 2012 samples.

the audible pop was heard corresponding to the initiation of a crack along *A*-*D*. Examination of the front and back surfaces of the specimen did not reveal a surface breaking crack, even though the load dropped by 1150 N. The surfaces of the notch *A* and the hole *D* could not be observed at high magnification due to geometrical constraints. The specimen was then mounted in an epoxy holder and polished down to the mid-plane and etched with Vilella's reagent in order to examine the crack that was nucleated in the ligament *A*-*D*. A composite image of this ligament at a high magnification is shown with reduced resolution Figure 3.23a. The full resolution image is available as Supplementary Material SM6 for this dissertation. The region of suspected crack nucleation is indicated by a red circle in this figure, and is roughly near the center of the ligament *A*-*D*. It is also clear that while the crack did not break through the front or back surfaces, it did grow all the way to the surface of the notch region *A* and the surface of the hole *D*. The tortuous path of the crack is an indication that this growth may have occurred under significantly mixed-mode loading. A high magnification scanning electron microscope image of the suspected nucleation site is shown in Figure 3.23b, with an additional high magnification image in Figure 3.23c. The surface of the fracture has nearly equiaxed dimples, clearly indicating that the nucleation was triggered through void nucleation and growth, even though the ligament *A*-*D* is under a macroscopic shear loading; however, we will show later in Section 3.5 that numerical simulations indicate that there is a region of high triaxiality within the ligament *A*-*D* in the neighborhood of where the crack nucleated. The high magnification image in Figure 3.23d shows connections between different open cracks by a very thin crack. Farther away from the nucleation site, there is evidence of large shear deformations. High magnification SEM images of the region highlighted by the yellow circle in Figure 3.23 are shown in Figure 3.24: a few features of the damage development are evident. First, in comparison to the initial grain structure, there is

significant shear deformation in the vicinity of the cracks that exhibit very little opening pointing to a shear mode of cracking/failure. Second, there are numerous voids, predominantly in the grain boundaries, but only over a region very close to the eventual fracture plane. Third, multiple open cracks separated either by a sheared region or sheared crack are observed. Finally, parallel sets of cracks are observed suggesting possible break-up of the growing crack due to the mode-III shear that is likely to form as the interior crack grows out towards the free surfaces of the specimen. These observations point to a complex mechanism or collection of mechanisms that coexist in these areas.

3.4.3 The competition between failure paths A-C-E and A-D-C-E

The experimental results allow us to make a comparison of the strain evolution between specimens that followed crack paths *A-C-E* and *A-D-C-E* and gain further insight into the cause of the different observed cracking paths. Contours of equivalent plastic strains on the surfaces of specimens **S09** and **S11** at two different values of COD are shown in Figure 3.25. The equivalent plastic strain variation with COD at two points in the ligaments *A-D* and *A-C* is compared between **S09** and **S11** in Figure 3.26. It is clear from these figures that even after a COD of only about 0.5 mm – well before any failure processes are activated and during the portion when all that governs is the plastic response of the material – there is a significant deviation in the local strain fields between specimens that fail with different crack paths. This deviation occurs well before localization of any ligament, and at this COD the strains in the specimen are relatively small, not exceeding a logarithmic strain of 0.07. The implication is that the crack path has been determined by the evolving plastic deformations early in the deformation history

when the material can be well described by continuum plasticity alone, without invoking any damage. This basic finding isolates the mechanisms involved in selection of the crack path and sets the boundaries on modeling efforts to replicate both experimentally observed crack paths – imperfections in the geometry and details of the plastic constitutive model must be the primary determinants rather than the failure model.

3.5 ADDITIONAL SIMULATIONS EXPLORING CRACK PATH SELECTION

There are two questions regarding the path selection that require further discussion: first, is there a bifurcation in the solution? i.e., for nominally the same boundary value problem posed in the original challenge, is there a bifurcation to two solutions corresponding to paths *A-C-E* and *A-D-C-E*? Second, can the two crack paths observed in the experiments be understood/replicated by simulations including the specific geometric imperfections, but with the same constitutive and failure model? The experimental observations suggest that there is no bifurcation in the solution: if one exists, then crack path *A-D-C-E* corresponds to the lower energy state and therefore this should be the only experimentally observed path; however, a significant number of specimens within some range of imperfections followed the crack path *A-C-E*. This suggests that the ideal geometry of the challenge problem lies near the boundary of two neighboring families of problems – one family that fails with crack path *A-C-E* and the other with *A-D-C-E*. The ideal geometry falls within the former family, and the geometric defects present in most of the test specimens cause them to lie within the latter. Both families of problems follow characteristic patterns of deformation that are clearly distinct from each other shortly after plastic deformation occurs, as discussed in Section 3.4. The distinction between each family continues to become more pronounced with increasing

deformation, and it is not observed that a switching between deformation patterns can occur – as it would from bifurcation. The recognition that a bifurcation is not present makes clear that the crack path *A-D-C-E* is not more common due to it being a lower energy path, but due to bias error in the placement of holes during specimen fabrication.

A set of numerical simulations were performed in which the material model described in Section 3.2 for the blind predictions was kept unchanged and a range of imperfections spanning the observed variations in specimen geometry were introduced into the geometric model; additionally loading imperfections were also introduced. In all cases, the model predicted the path *A-C-E*. Since it was difficult to trigger first failure along the ligament *A-D* with just geometric perturbations, a second pair of simulations was performed in which the shear coefficient in the yield criterion was modified; specifically, by setting $2N = 3.47$ instead of 3 in Eq.(1), it was possible to continue concentrating strain along the ligament *A-D*, and prevent localization in the ligament *A-C*. This change in constitutive behavior only triggered crack path *A-D-C-E* for geometry with initial defects, and did not greatly alter the simulation results for the ideal geometry. The fact that such a small change in the yield condition makes a dramatic difference in strain accumulation points to the need for better characterization of the material even before the onset of damage. The results of this simulation, corresponding to the dimensions of specimen **S06** (the specimen that has the median defect size for the ratio of ligament lengths *A-D* to *A-C*), show that although the overall deformation in the ligament *A-D* appears to be shear-dominant, the local levels of triaxiality increase with COD to ~ 0.7 in the center of the ligament, where nucleation of the interior crack illustrated in Figure 3.23 occurs. These simulation results capture the early response of specimens failing with crack path *A-D-C-E*, as can be seen when comparisons to the experimental are made. The contours of equivalent plastic strain at two different COD values are

shown in Figure 3.27 from the experimental measurement of **S11** and numerical simulation of **S06**. The equivalent plastic strain variation with COD at two points in the ligaments *A-D* and *A-C* is compared between the experiment **S11** and the simulation **S06** in Figure 3.28. The agreement between the simulations of **S06** and the experiments on **S11** is extremely good until a COD of ~ 1.25 mm and reasonable up to a COD of ~ 2 mm, when the experiment indicated a significant departure shortly before fracture. The load variation with COD is shown in Figure 3.29 for specimen **S06** (obtained from the SNL results) and compared with the simulation of **S06**. While we have succeeded in nudging the development of strain accumulation along the ligament *A-D* ahead of ligament *A-C*, there is still significant discrepancy in the load-COD behavior and the onset of failure. This points to the need for additional material characterization, both with respect to the plastic response (anisotropy, shear effects, etc) and with respect to failure, particularly under low triaxiality – high shear conditions. It is suggested that such additional characterization would indeed provide a predictive framework for ductile failure.

3.6 CONCLUSION

The details of the simulations and experiments performed by the University of Texas team in response to the 2012 Sandia Fracture Challenge (SFC 2012; see Boyce et al. 2014) are presented in this chapter. The tension test and fracture test data were used to generate a power-law hardening model for characterizing the plastic behavior and a modified Johnson-Cook model for material failure. These were used to generate a blind prediction of the challenge specimen. Our predicted response indicated the path *A-C-E* and agreed quantitatively extremely well with specimen **D1** of the experiments reported

by Sandia. Based on the confidence in our simulations we requested testing of additional specimens with different gripping conditions and additional measurements using 3D-DIC measurements of the strain field on the specimen surface. These experiments were performed at the University of Texas and indicated that geometric imperfections may have resulted in the alternate observed crack path. Some aspects of the effects of imperfections are confirmed in the article by Boyce et al. (2014). The experiments also provided a wealth of data for comparison both to the blind predictions and to additional simulations. Specifically, first, the comparison of the load-COD and strain evolution in the ligaments *A-C* and *A-D* for specimen **S09** matched the blind predictions extremely well. Second, comparison of the experimental measurements of the load-COD and strain evolution in the ligaments *A-C* and *A-D* for specimens **S09** and **S11** indicated that the selection of the path *A-D-C-E* occurred very early in the deformation history, at a stage when the response was dictated by plasticity and not damage. Third, a simple modification to the parameters of the calibration of the constitutive model was adequate in switching the failure path from *A-C* to *A-D* when appropriate geometric imperfections were introduced in the numeric discretization to replicate the actual geometric imperfections. Lastly, it should be emphasized that the experiments and simulations presented here point to the ability of a simple constitutive and failure model to capture ductile failure when proper calibration of the material models is undertaken.

3.6.1 Recommendations for Additional Material Testing:

Both the constitutive and failure models used in the present simulations can be improved through a small increase in the experimental work. First, the plasticity model was calibrated from just one set of experiments in which the only real input was the load-

elongation diagram from a tensile test. Minor accommodations were introduced to account for anisotropy. A full set of experiments to characterize the anisotropic material response is essential in order to extract an appropriate plasticity model. The full integration of detailed three-dimensional kinematic measurements (using DIC or other full-field methods) with load-elongation measurements and numerical simulation is essential for this material calibration to be accomplished. The largest improvement to be gained will come from additional tests under shear-dominated loading. Strain-to-failure at such a low triaxiality will allow for more thorough determination of the damage parameters across a wide range of triaxialities. Finally, high spatial resolution of strain measurements near fracture surfaces can supplement the failure data already used to create a more robust failure model.

Table 3.1: Material parameters used in these simulations. Parameters labeled as "modified" were not part of the blind prediction, and were used only after the experimental results were released.

Hardening Parameters	C_1 (MPa)	C_2 (MPa)	C_3	C_4		
	755.4	818.1	0.05674	0.2889		
Failure Parameters	D_1	D_2	D_3			
	0.1000	3.810	-1.847			
Lankford Coefficients	r_0	r_{45}	r_{90}			
	1.000	0.9537	0.9402			
Hill's Coefficients	F	G	H	L	M	N
	0.5328	0.5000	0.5000	1.500	1.500	1.500
Modified Lankford Coefficients	r_0	r_{45}	r_{90}			
	1.000	1.1808	0.9402			
Modified Hill's Coefficients	F	G	H	L	M	N
	0.5318	0.5000	0.5000	1.500	1.500	1.734

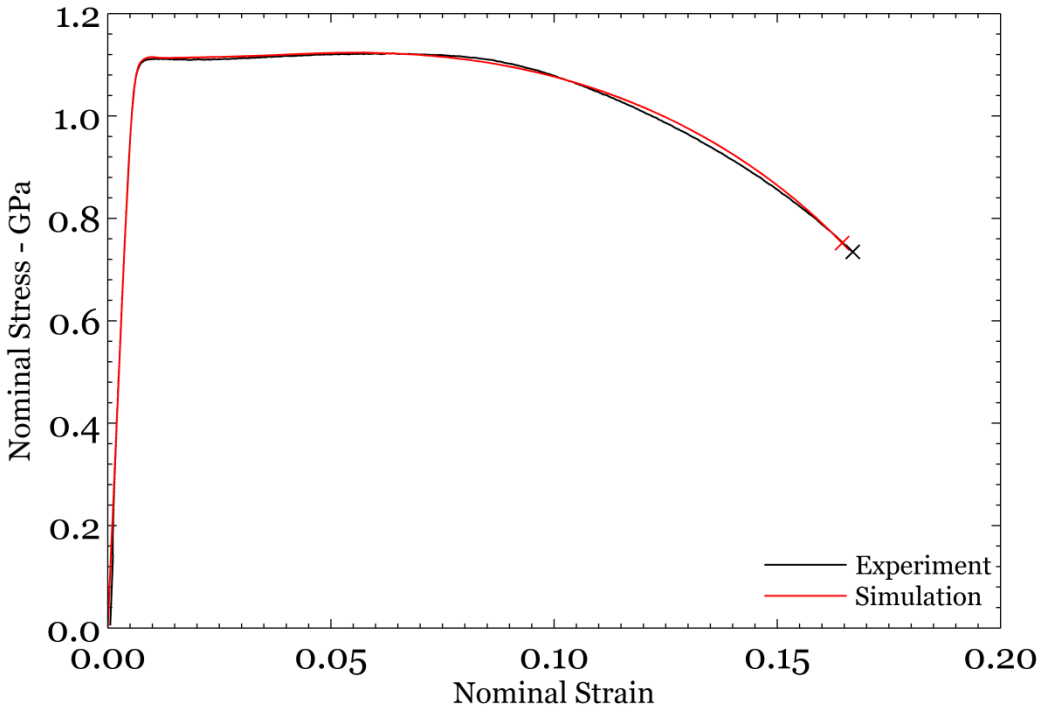

Figure 3.1: Nominal stress vs nominal strain variation. Black line corresponds to experimental results from Sandia National Laboratories (Boyce et al., 2014) The red line was obtained from optimized simulations. 'x' marks the point of specimen failure.

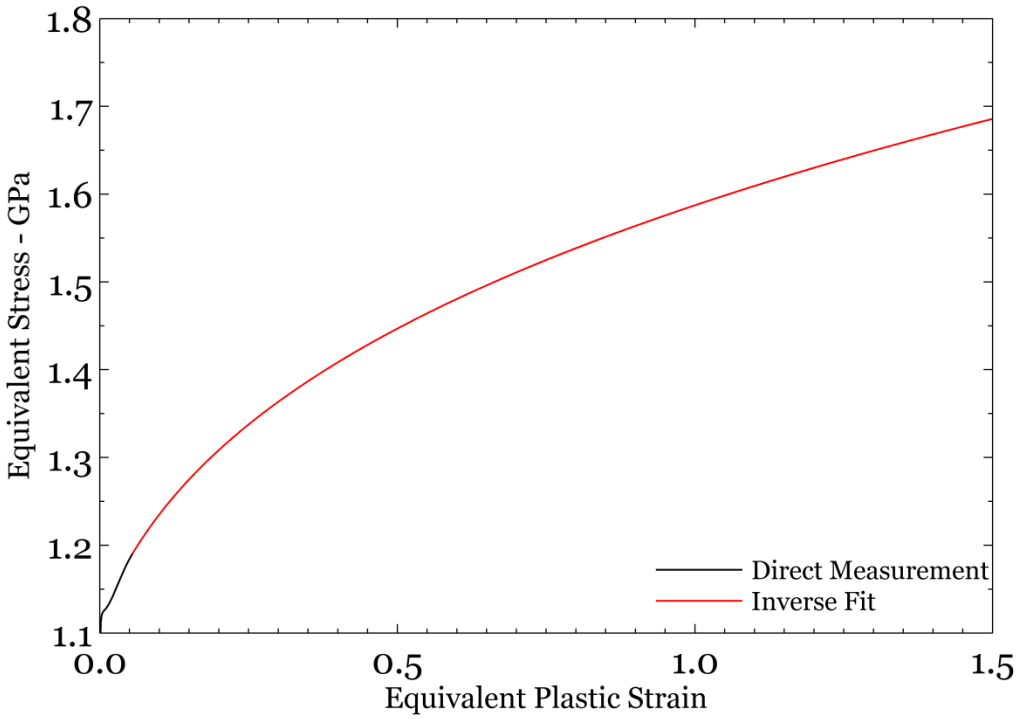

Figure 3.2: The variation of the true stress with equivalent plastic strain corresponding to the optimized constitutive behavior. Note that the direct measurement–prior to necking–corresponds to strain levels less than about 0.055 (as indicated by the *black line*)

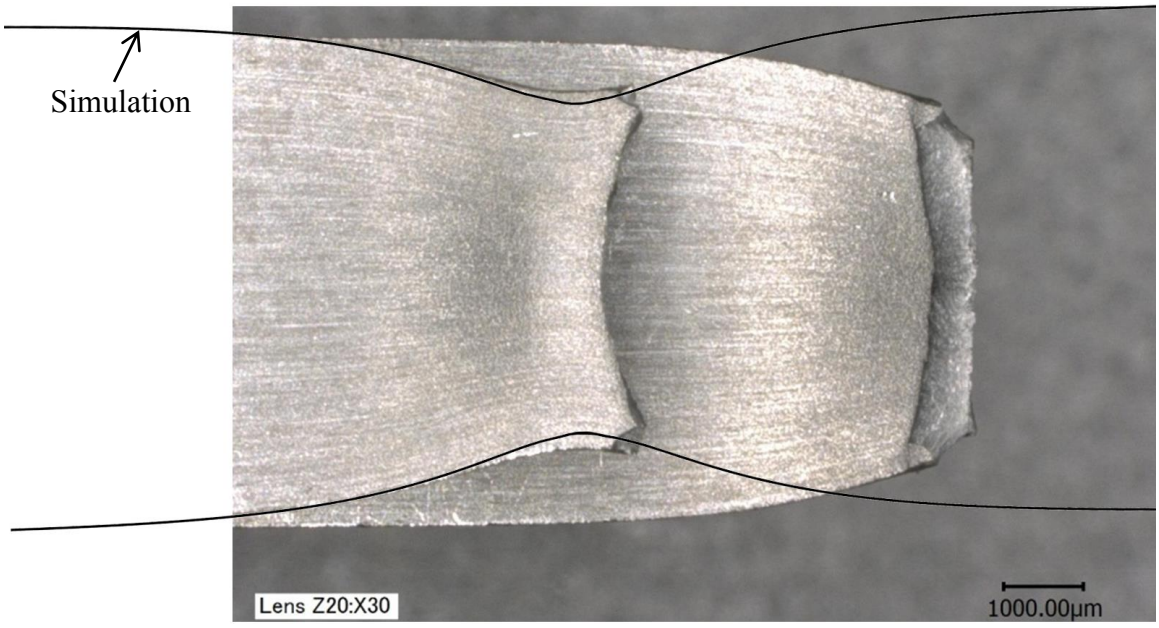

Figure 3.3: Overlay of the profile of the neck obtained from the optimized simulation on an image of the necked regions from the tensile experiment (image from Boyce et al. 2014)

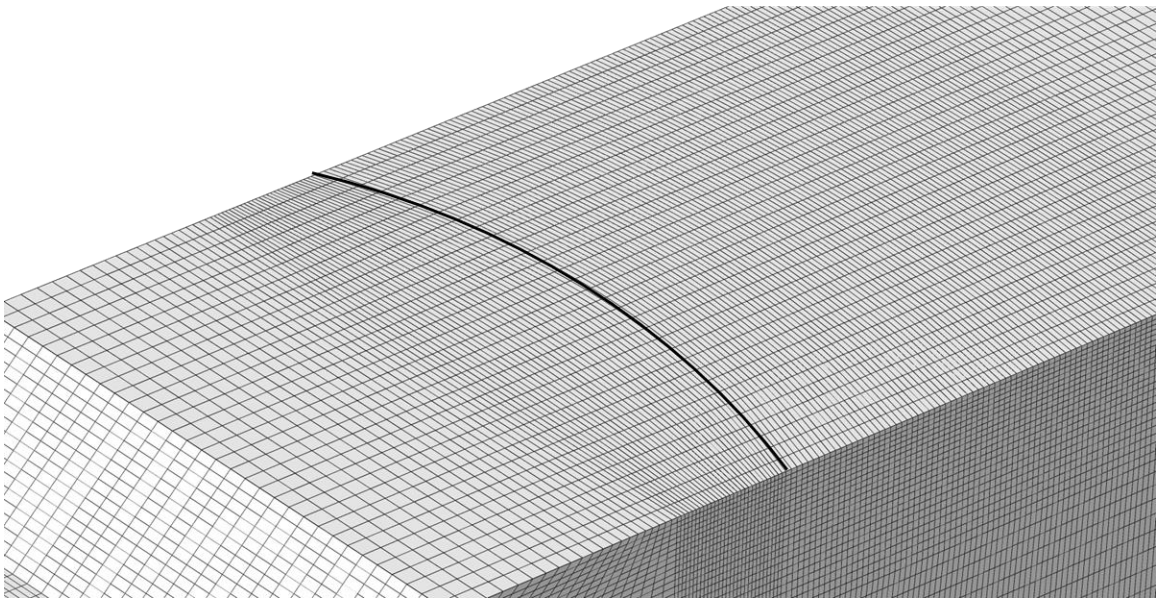

Figure 3.4: A view of the $C(T)$ specimen mesh, sectioned along the prospective fracture plane. The initial crack extends from the notch tip at the left to the thick curve that designates the location of the fatigue precrack.

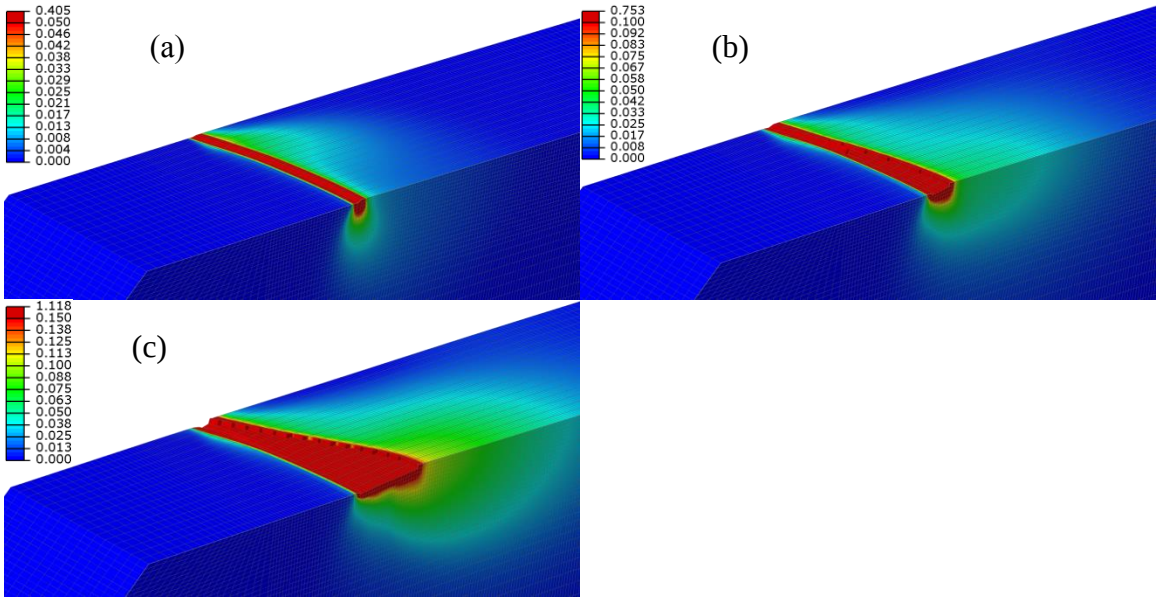

Figure 3.5: Equivalent plastic strain in the $C(T)$ specimen simulation. (a). COD = 0.39 mm (b). COD = 0.58 mm (c) COD = 0.87 mm. This view is sectioned along the prospective fracture plane as well as the specimen midplane.

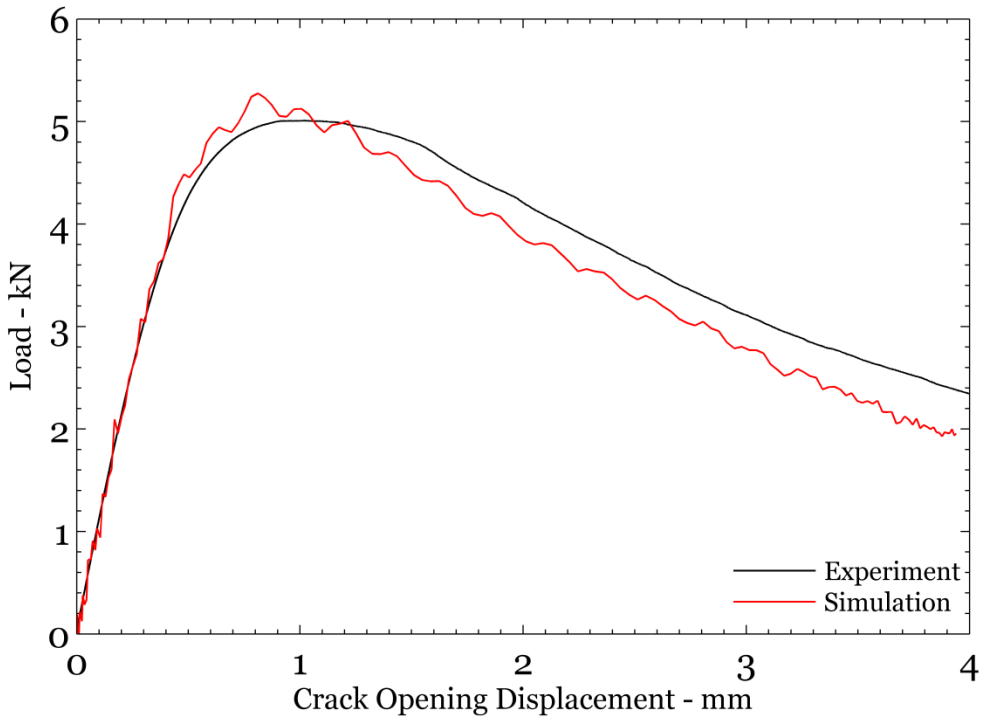

Figure 3.6: Load-COD response of fracture specimen from the experiment and the optimized simulation.

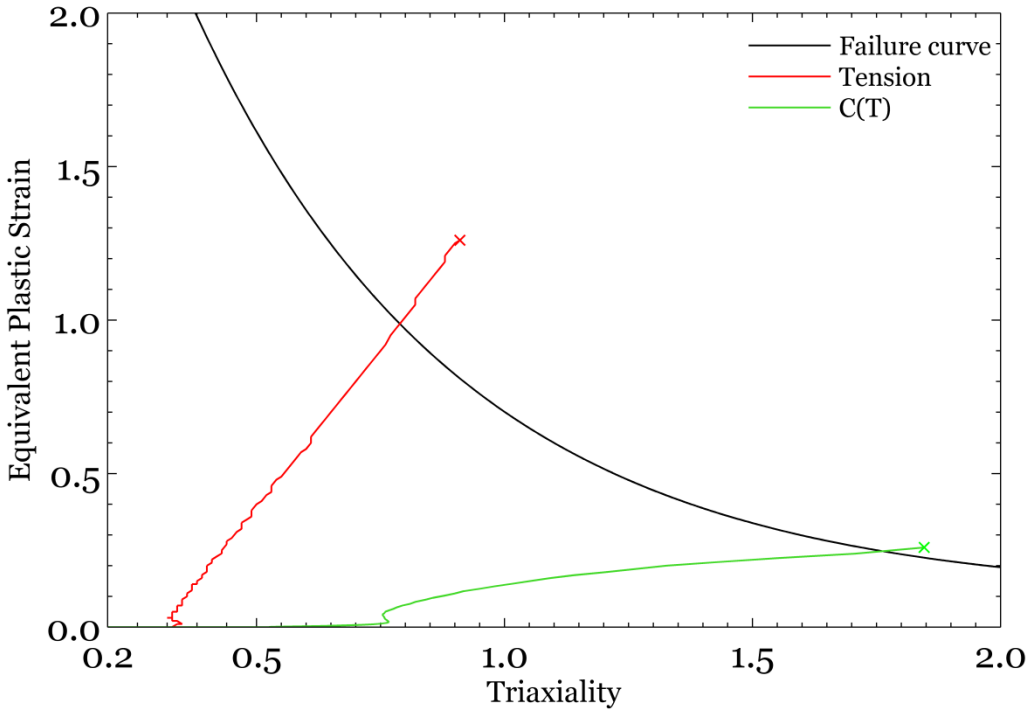

Figure 3.7: Calibrated Johnson-Cook failure model with simulated failure paths shown

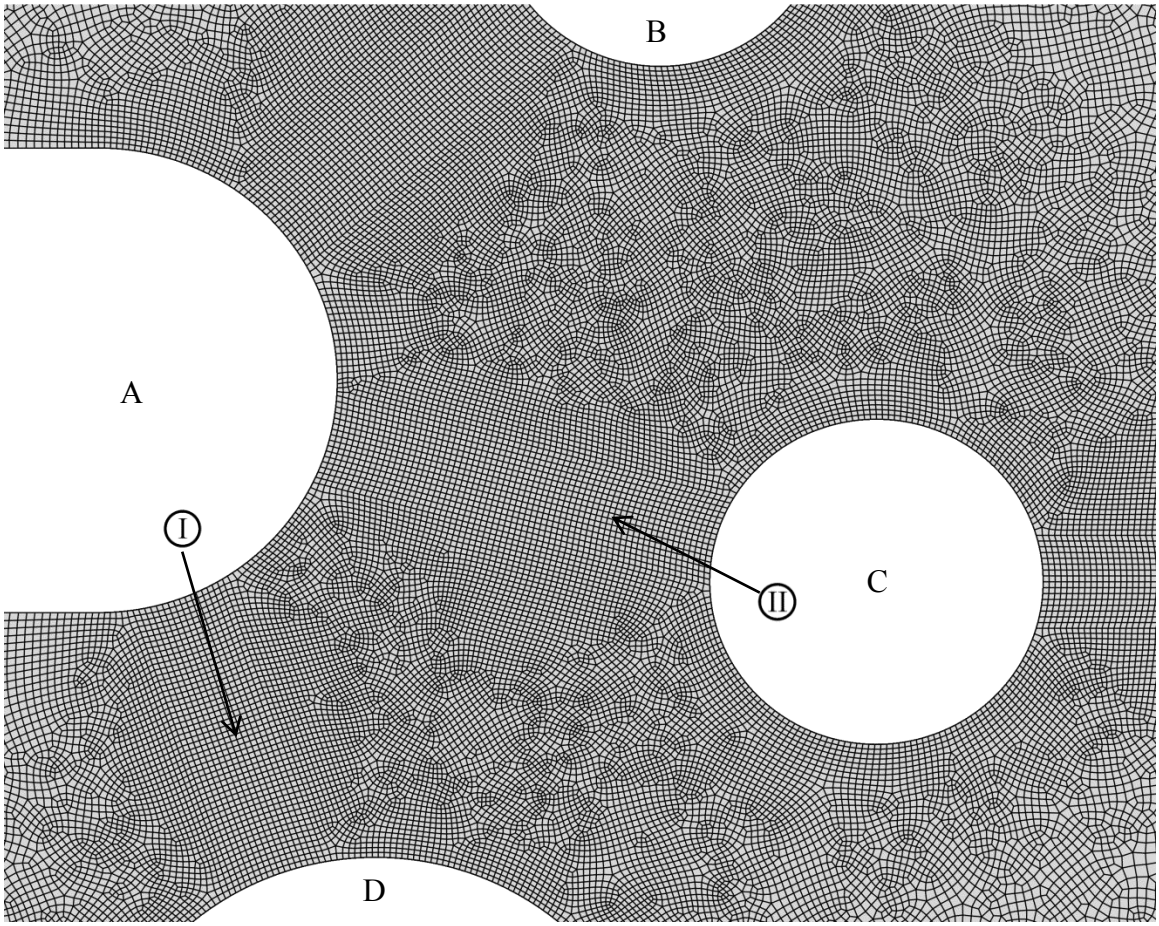

Figure 3.8: Details of the mesh used for the 2012 SFC geometry. A highly refined mesh was used in all areas of possible fracture. The locations I and II correspond to points where failure is most likely to initiate in their ligament.

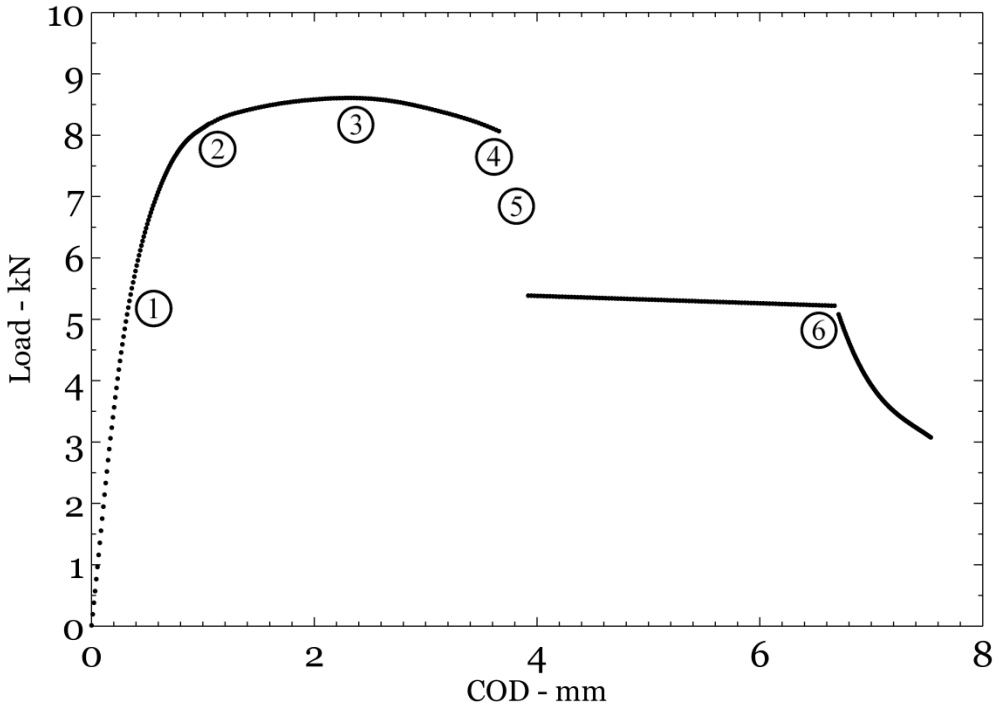

Figure 3.9: Blind prediction of the load-COD response for the 2012 SFC geometry. The results at the marked points are discussed in the text and Figures 3.10 and 3.11.

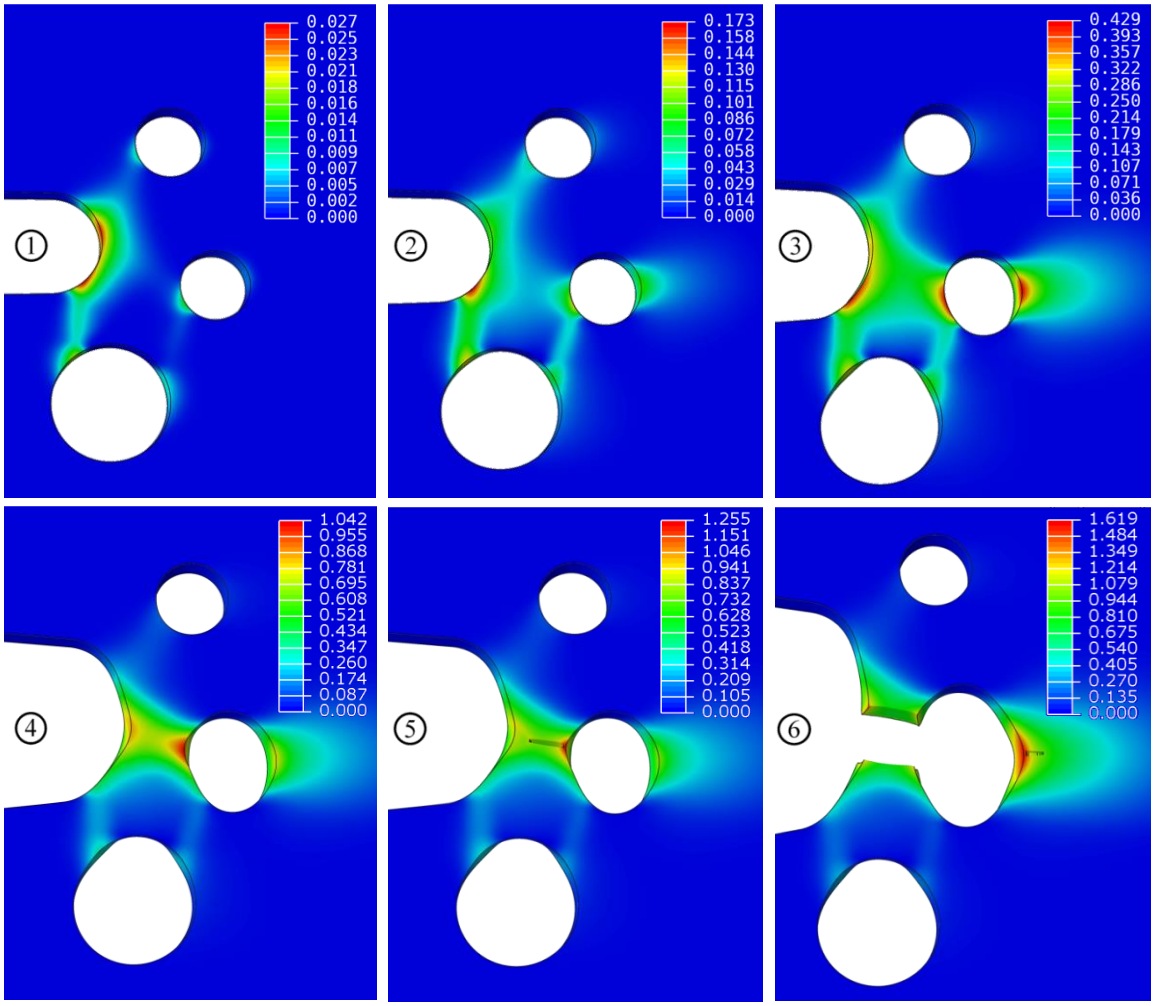

Figure 3.10: Equivalent plastic strain development in the midplane.

① COD=0.33 mm
② COD=0.93 mm
③ COD=2.29 mm
④ COD=3.66 mm
⑤ COD=3.71 mm
⑥ COD=6.75 mm

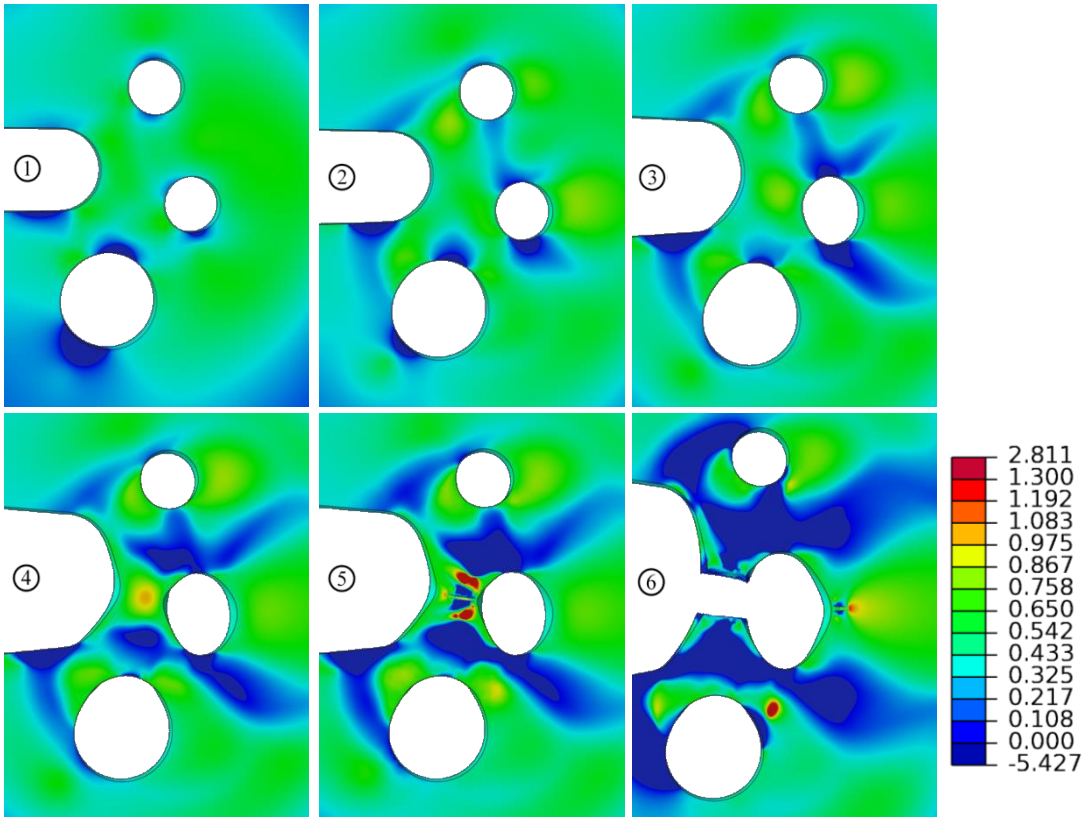

Figure 3.11: Triaxiality development in the midplane.

① COD=0.33 mm
② COD=0.93 mm
③ COD=2.29 mm
④ COD=3.66 mm
⑤ COD=3.71 mm
⑥ COD=6.75 mm

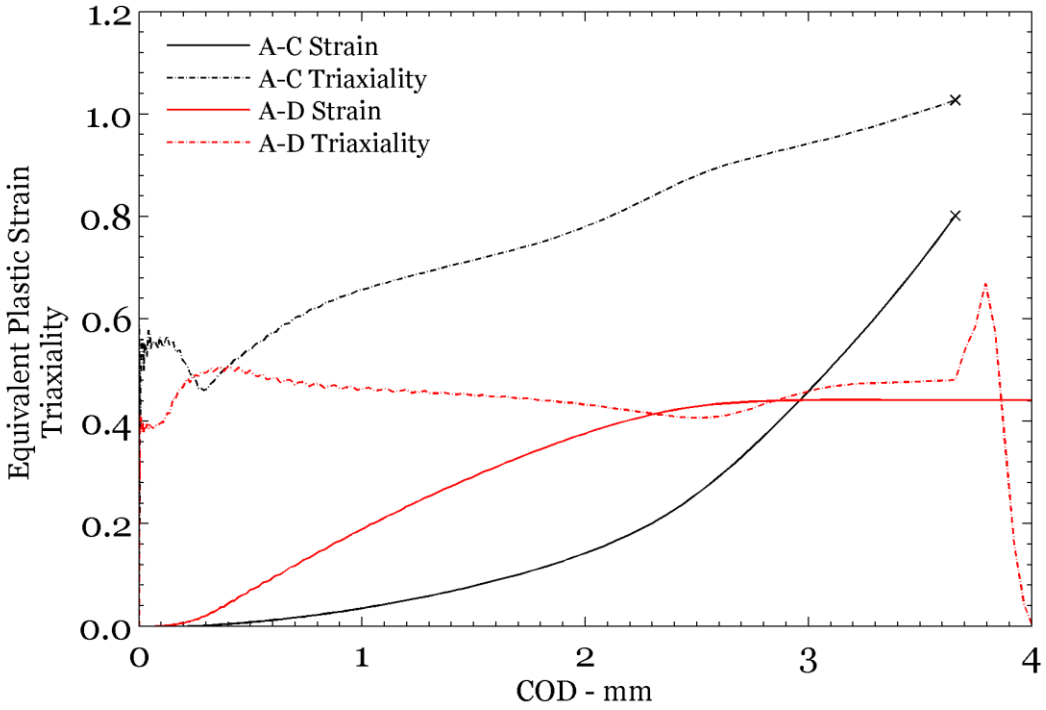

Figure 3.12: Local strain and triaxiality variation over COD at the critical elements in ligaments *A-D* and *A-C*.

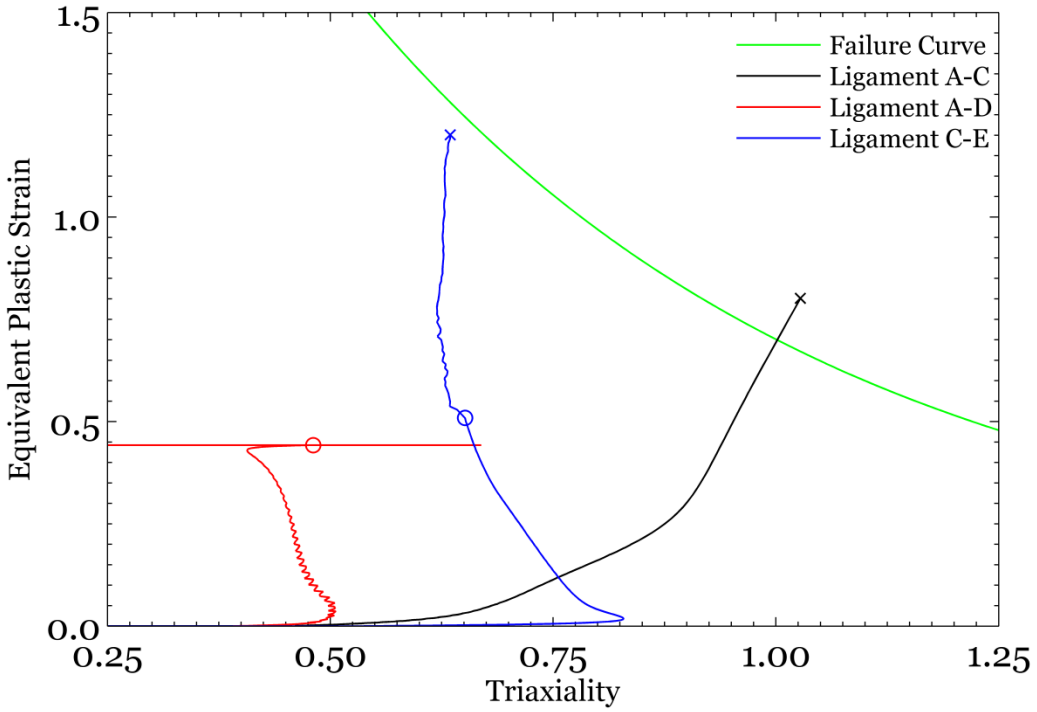

Figure 3.13: Equivalent plastic strain and triaxiality histories of critical elements. The path towards failure on ligaments *A-D*, *A-C* and *C-E* are shown. Failure of the ligament *A-C* is denoted by the black 'x' and at this stage the state of ligaments *C-E* and *A-D* are denoted by the blue and red circular symbols. Failure of the ligament *C-E* is identified by the blue 'x'.

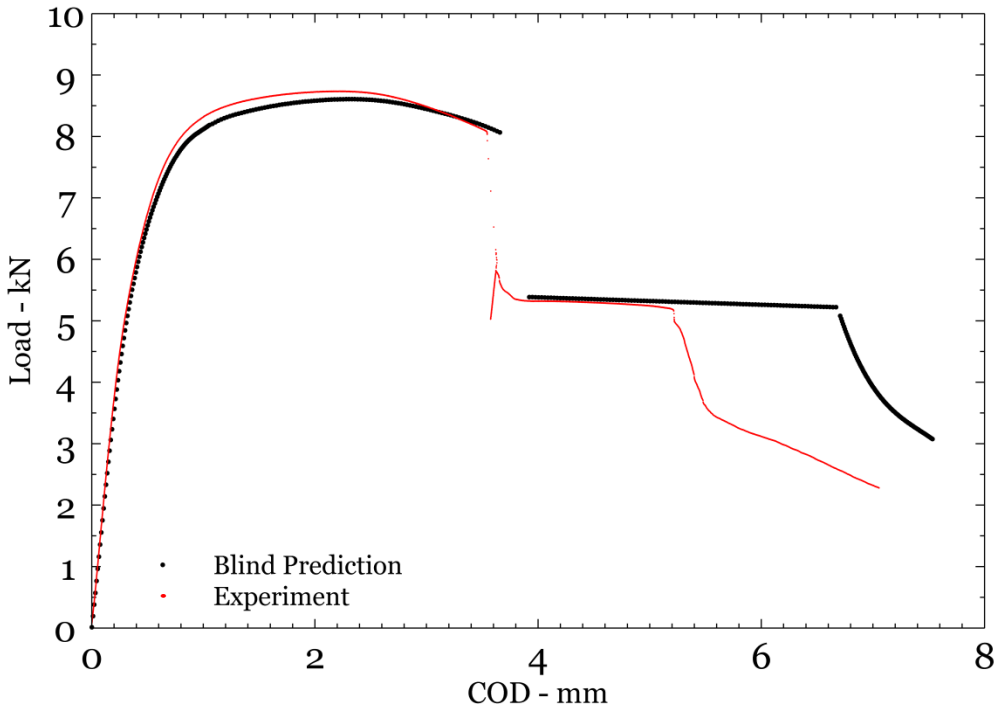

Figure 3.14: Load variation with COD for the blind prediction with the experimental results for specimen **D1**, performed at Sandia's Structural Mechanics Laboratory.

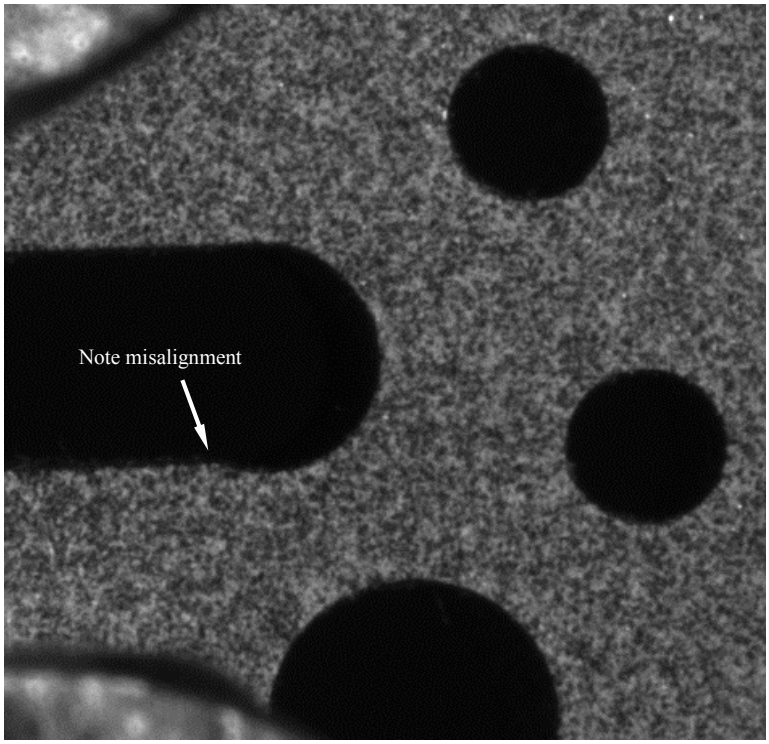

Figure 3.15: A close-up image of specimen **S11** prior to testing. The slot placement is within the specifications provided, but due to a machining error for hole *A*, the specimen was out of specification; a clear decrease in the size of the ligament *A*-*D* is evident in this image.

Figure 3.16: Experimental set-up. Note the double universal joints, the clevises with flat pin-holes to accommodate pin rolling, and the digital cameras for 3D-DIC image acquisition.

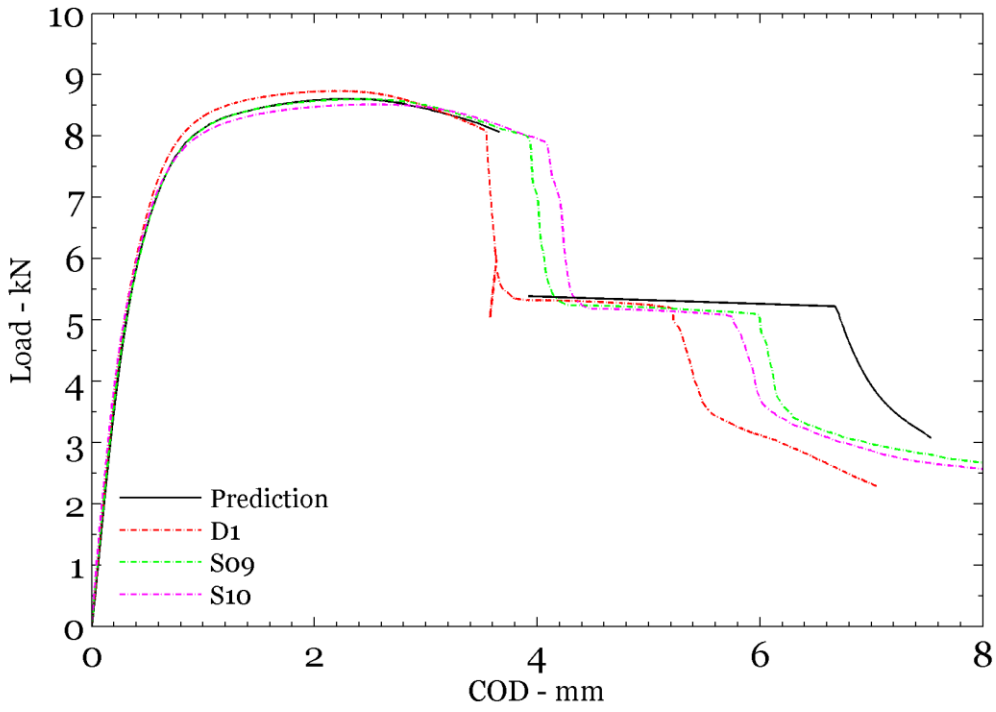

Figure 3.17: The load-COD variation for all experiments with crack path *A-C-E* in comparison with the blind prediction (black line).

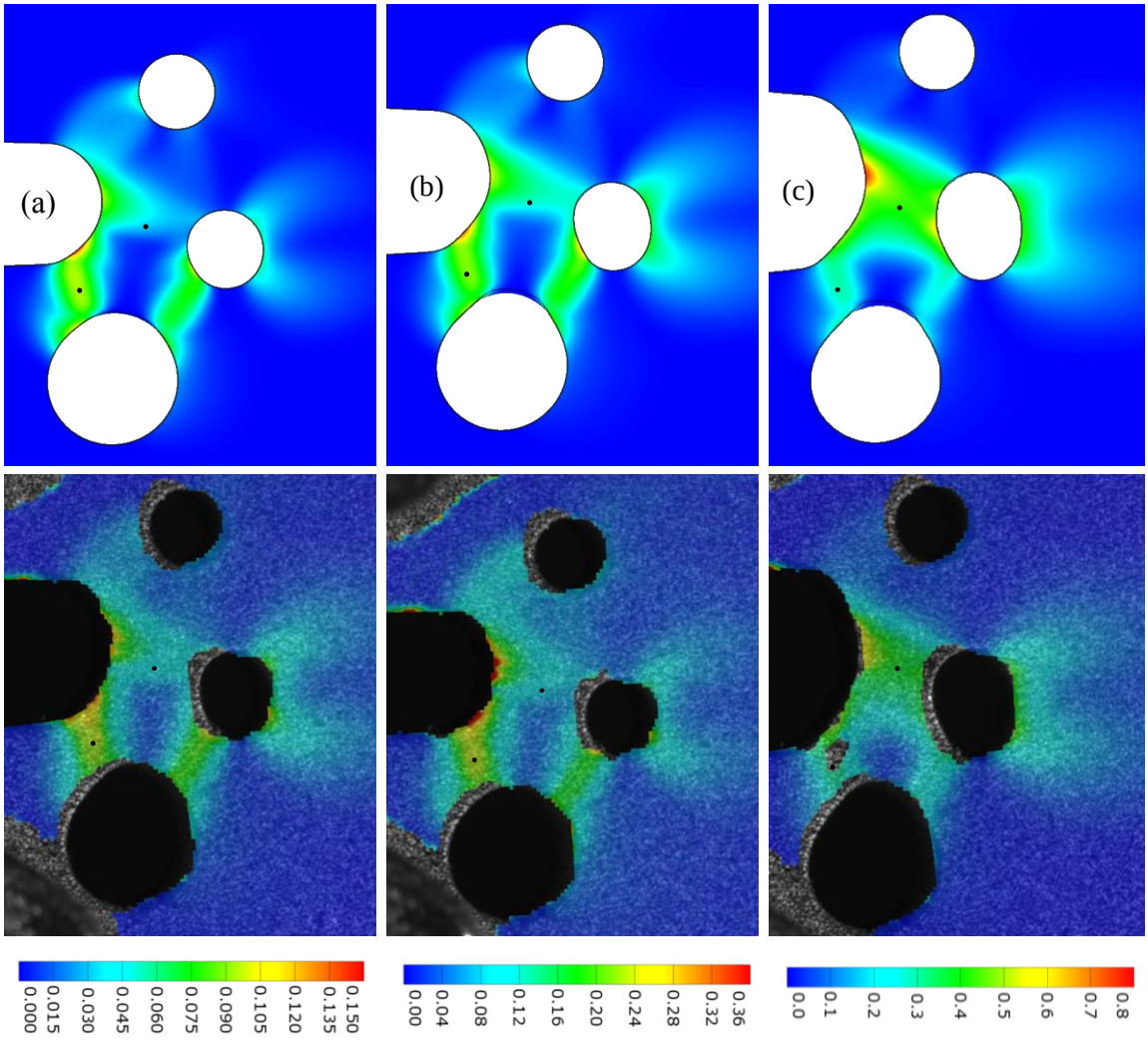

Figure 3.18: Comparison of the equivalent plastic strain on the surface of the challenge specimen between the blind prediction (top row) and the experimental result from 3D-DIC on specimen **S09** (bottom row). The experimental result shows an overlay of the post processed strain on top of the raw image. The textured appearance of the specimen is from a random speckle pattern adhered to its surface, required to perform DIC. The black dot near the center of ligaments *A*-*C* and *A*-*D* marks the point where strain data for Figure 19 is taken from. (a) COD ~ 1 mm, (b) COD ~ 2 mm, (c) COD ~ 3 mm.

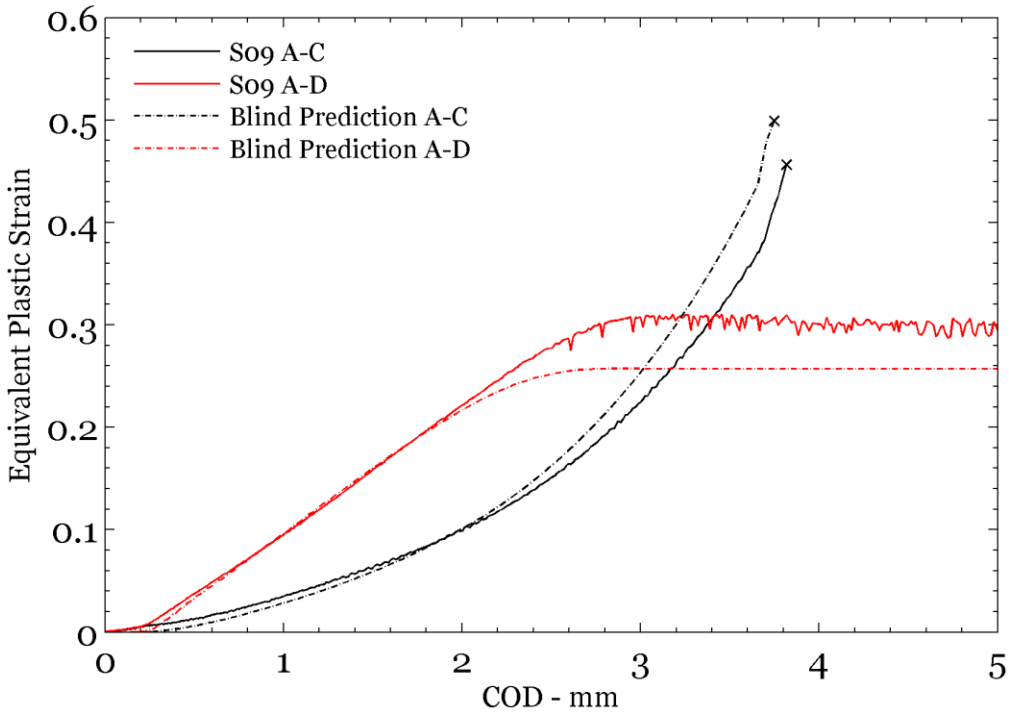

Figure 3.19: Variation of the plastic equivalent strain with COD on the surface of two ligaments (*A-C* and *A-D*) from the experiment (**S09**) compared to the blind prediction at the same locations.

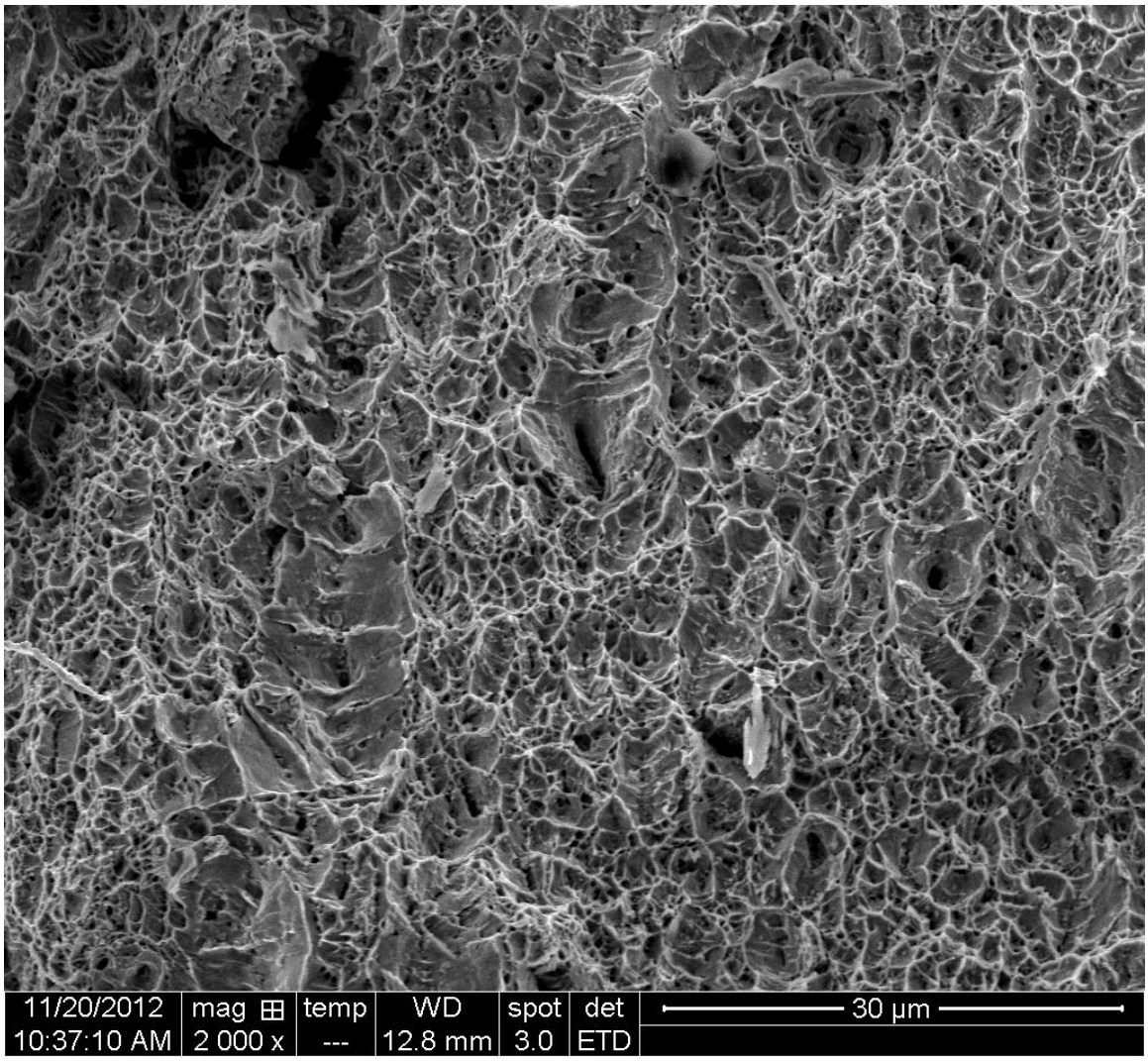

Figure 3.20: High magnification image of the fracture surface in the center of ligament *A-C* from specimen **S10**. The surface is dominated by equiaxed dimples, but also shows some features significantly larger than the average grain size of ~4.7 µm.

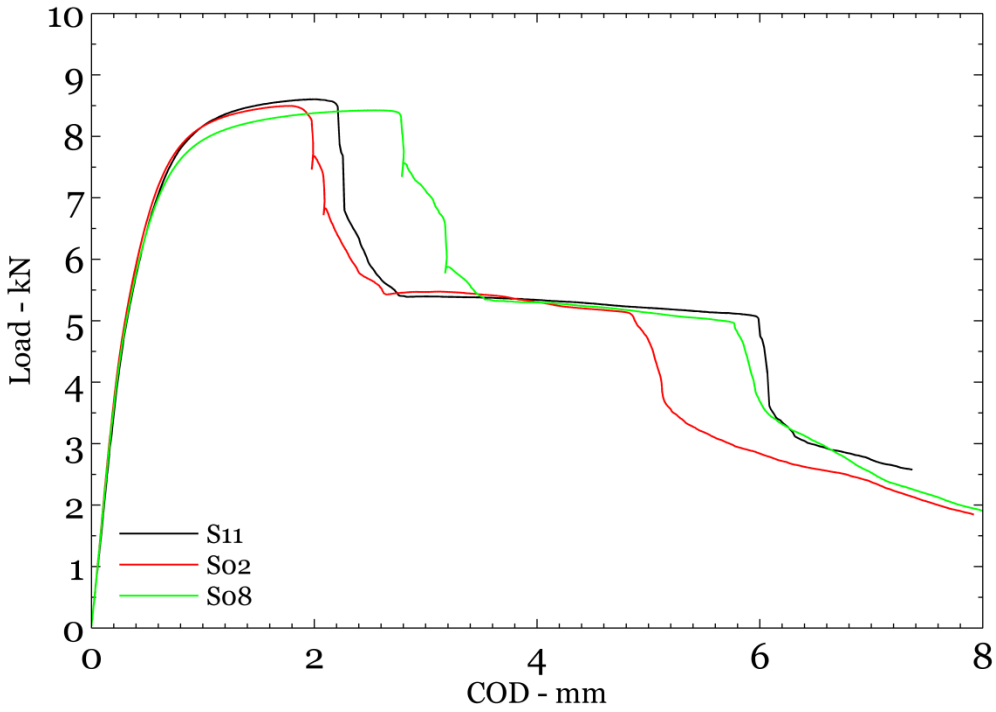

Figure 3.21: The load-COD variation for specimen **S11** (black line) compared to Sandia's experiments that failed with the same crack path *A*-*D*-*C*-*E*. **S02** (red line) had the minimum COD at first failure and **S08** (green line) had the maximum COD at first failure.

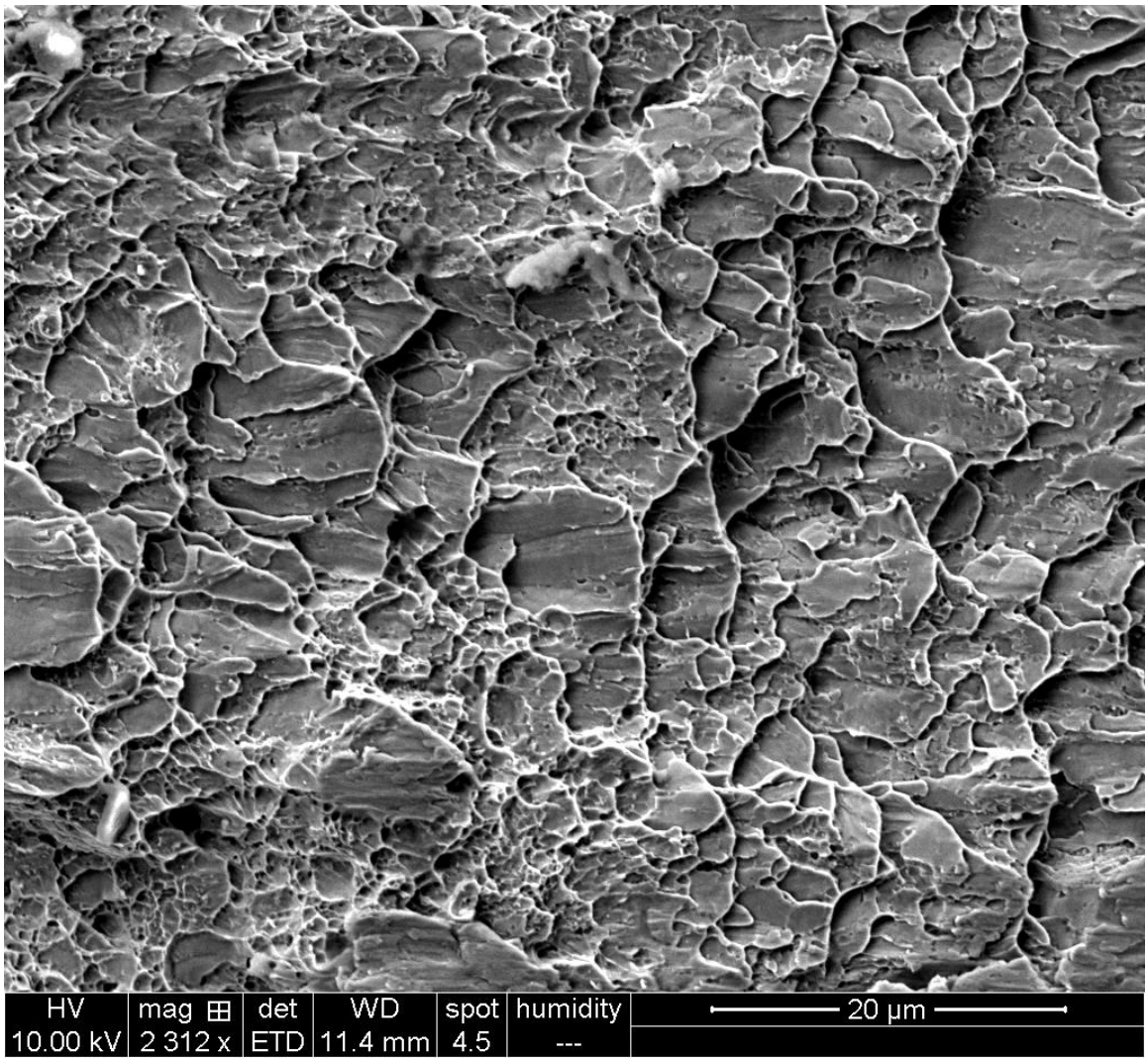

Figure 3.22: High magnification image of the fracture surface in the center of ligament *A-D* from specimen **S11**. The surface has both equiaxed dimples and larger features that resemble cascading ledges.

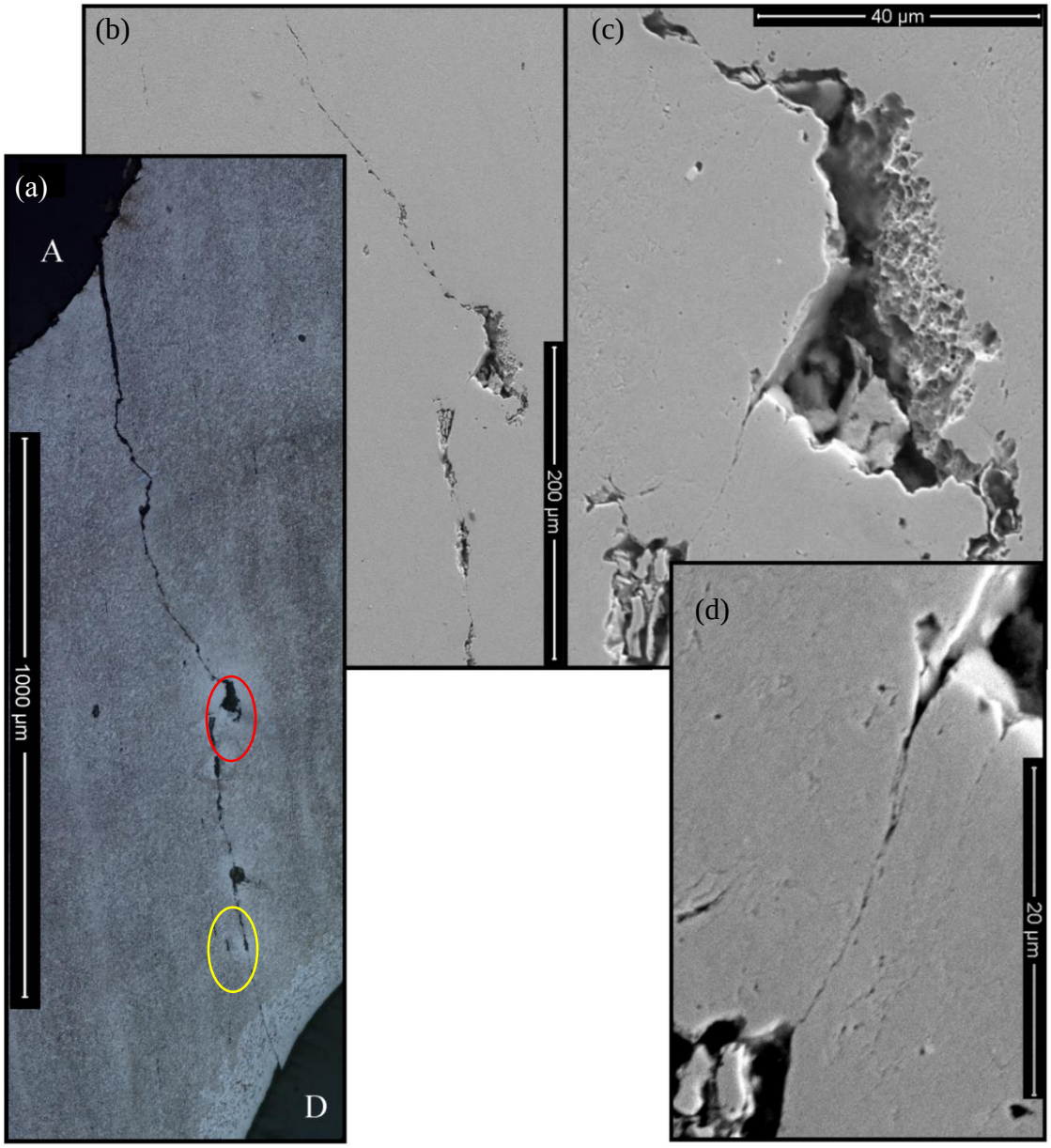

Figure 3.23: Micrographs from the midplane of a specimen that was not loaded beyond the first dynamic cracking event. (a) Optical image of the ligament *A*-*D*, after etching. Holes *A* and *D* are located, and the specimen is oriented as pictured in Figure 8. The suspected site of crack initiation is circled in red. (b) SEM image of the suspected initiation site with fine cracks emanating towards holes *A* and *C*. (c) High magnification image of the suspected initiation site, where nearly equiaxed dimples are seen on the unpolished surface. (d) High magnification of the fine crack heading towards hole *D*. Some small voids that tend to form within a band only as wide as a few grains can be seen on the crack flanks.

Figure 3.24: The region circled in yellow in Figure 23(a) is shown here with higher magnification SEM images.

(a) Parallel cracks are seen running side by side for a small length of the ligament. Note that there is no appreciable void growth between the two cracks.

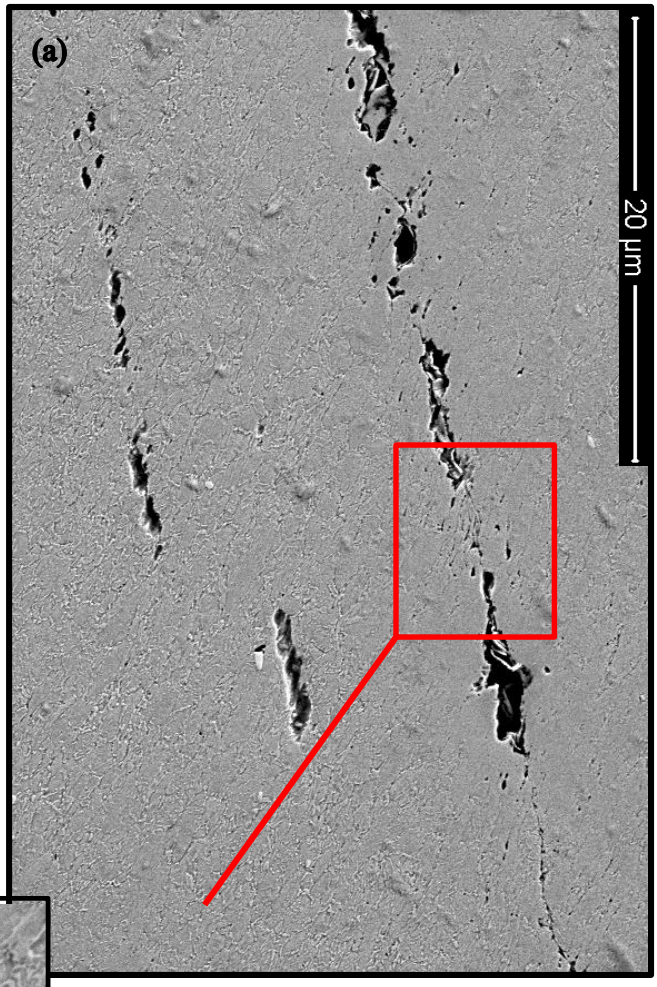

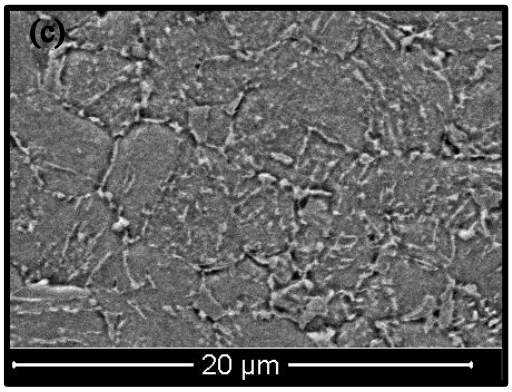

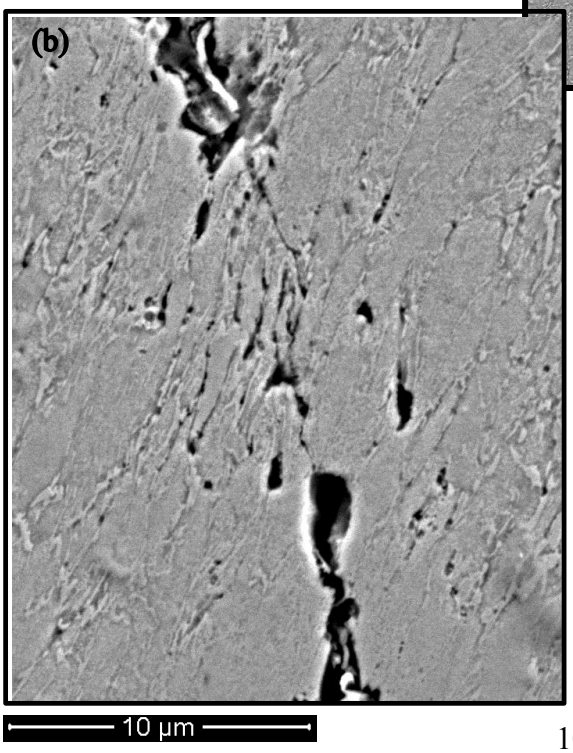

(b) High magnification image where many grain boundaries are visible. The material near the crack has undergone large shearing deformation, apparent from the large aspect ratio of the initially equiaxed grains. The fine crack appears to be meandering along grain boundaries. This region has larger than typical void growth on the crack flanks. The voids appear to be the product of grain boundary decohesion.

(c) Undeformed microstructure.

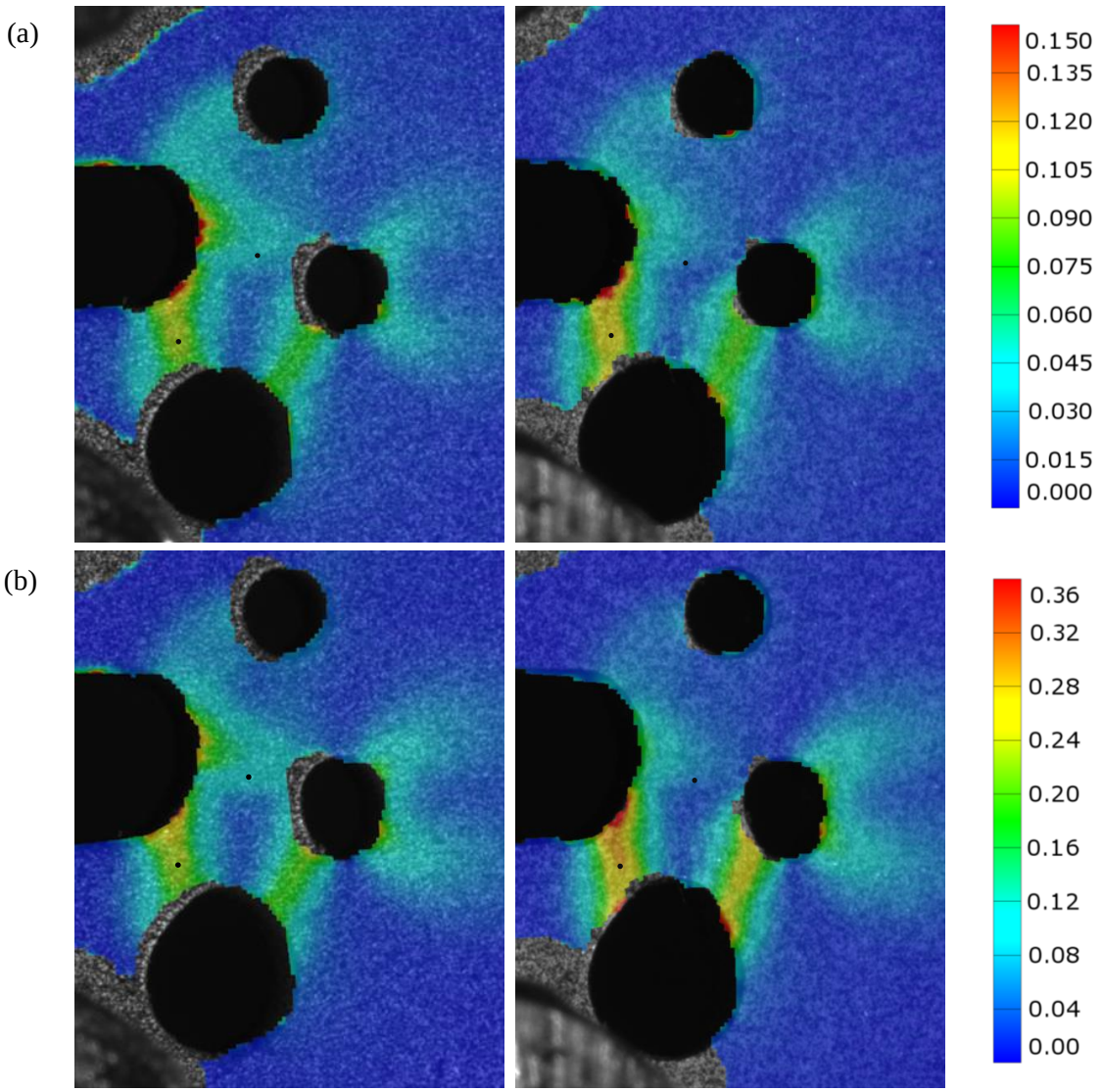

Figure 3.25: Comparison of the equivalent plastic strain on the surface of the challenge specimen between the experimental results from 3D-DIC on specimens **S09** (left) and **S11** (right). The black dot near the center of ligaments *A*-*C* and *A*-*D* marks the point where strain data for Figure 26 is taken from. (a) COD ~ 1 mm, (b) COD ~ 2 mm.

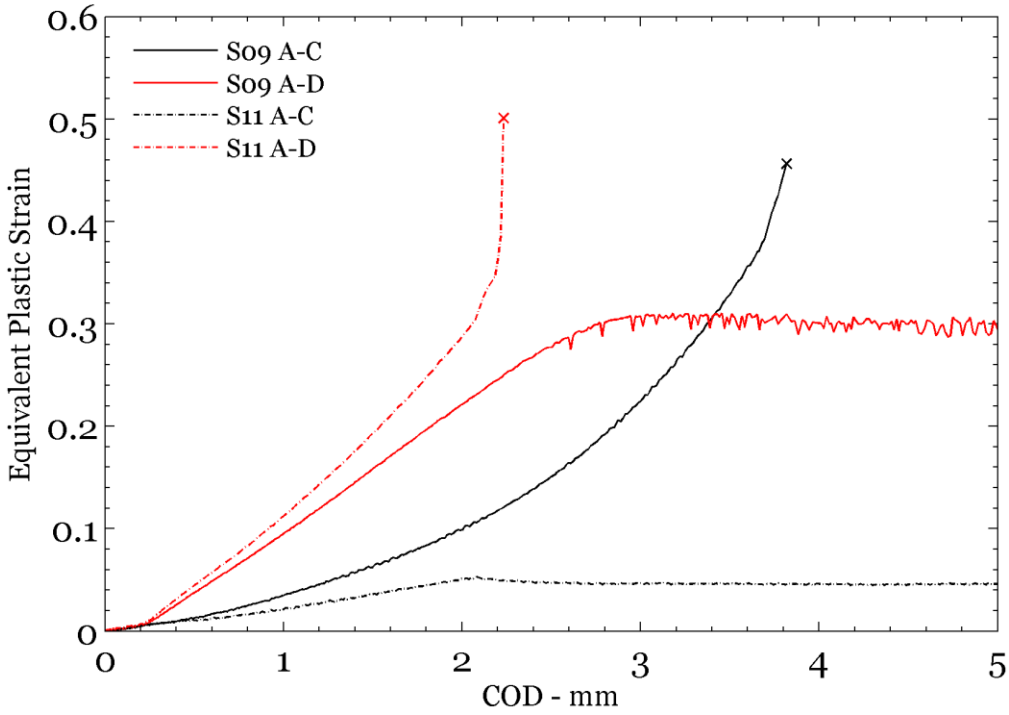

Figure 3.26: Variation of the equivalent plastic strain with COD on the surface of two ligaments (*A-C* and *A-D*) from specimen **S09** with crack path *A-C-E* compared to specimen **S11** with crack path *A-D-C-E*.

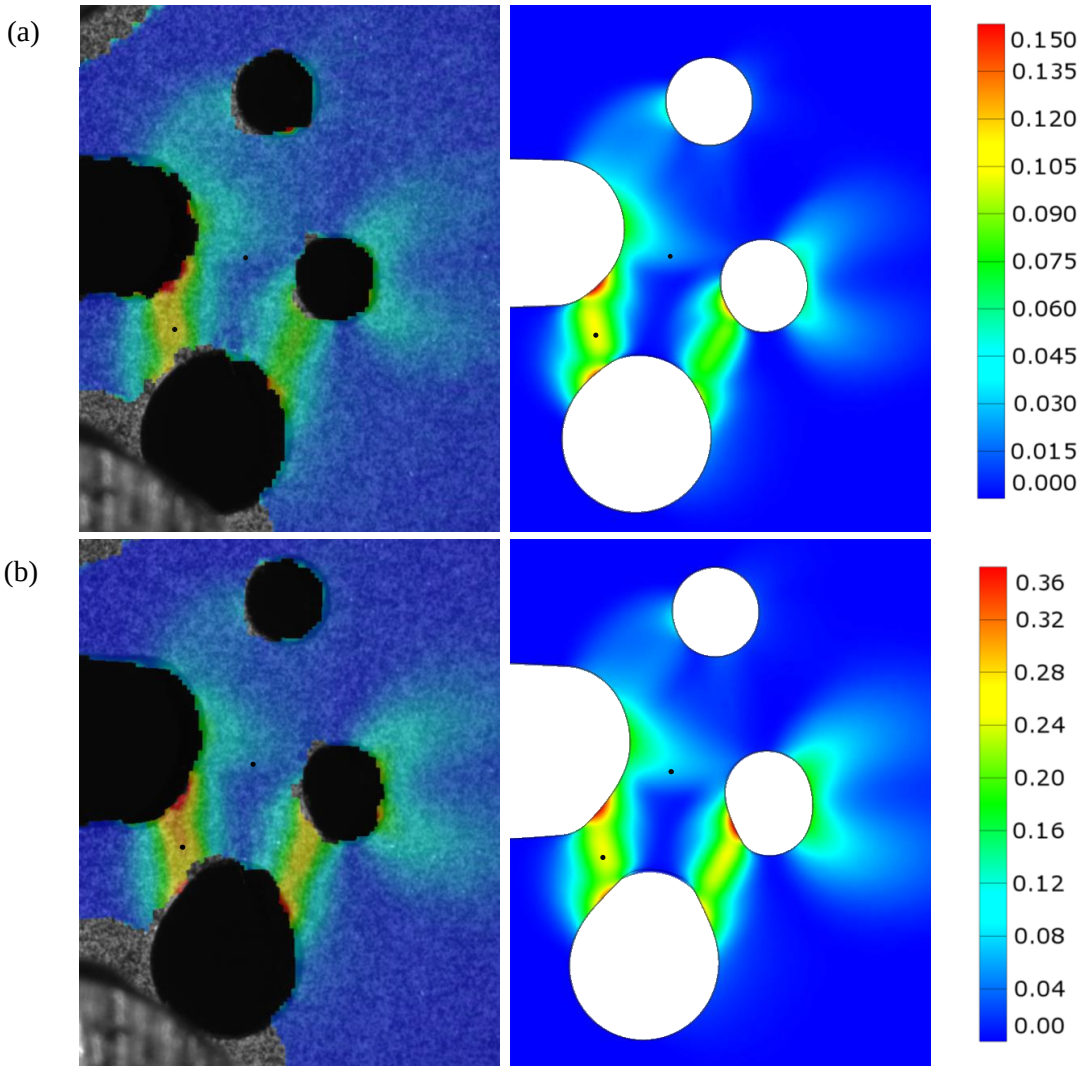

Figure 3.27: Comparison of the equivalent plastic strain on the surface of the challenge specimen between the experimental result from 3D-DIC on specimen **S11** (left) and a non-blind simulation using the geometry from specimen **S06** with a modified shear potential in the plasticity model (right). The black dot near the center of ligaments *A*-*C* and *A*-*D* marks the point where strain data for Figure 28 is taken from.

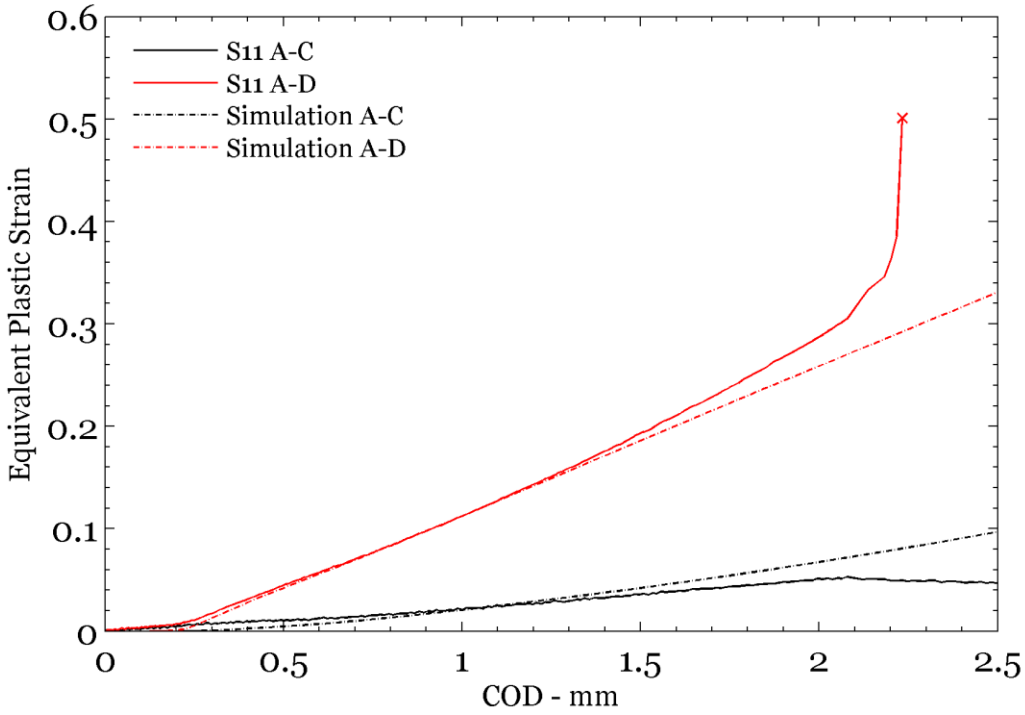

Figure 3.28: The equivalent plastic strain variation with the first 2.5 mm of COD at two selected locations is shown here. The experimental result is from specimen **S11**, the only specimen with crack path *A-D-C-E* for which 3D-DIC data is available. The non-blind simulation result shown here is for the specific geometry of specimen **S06**.

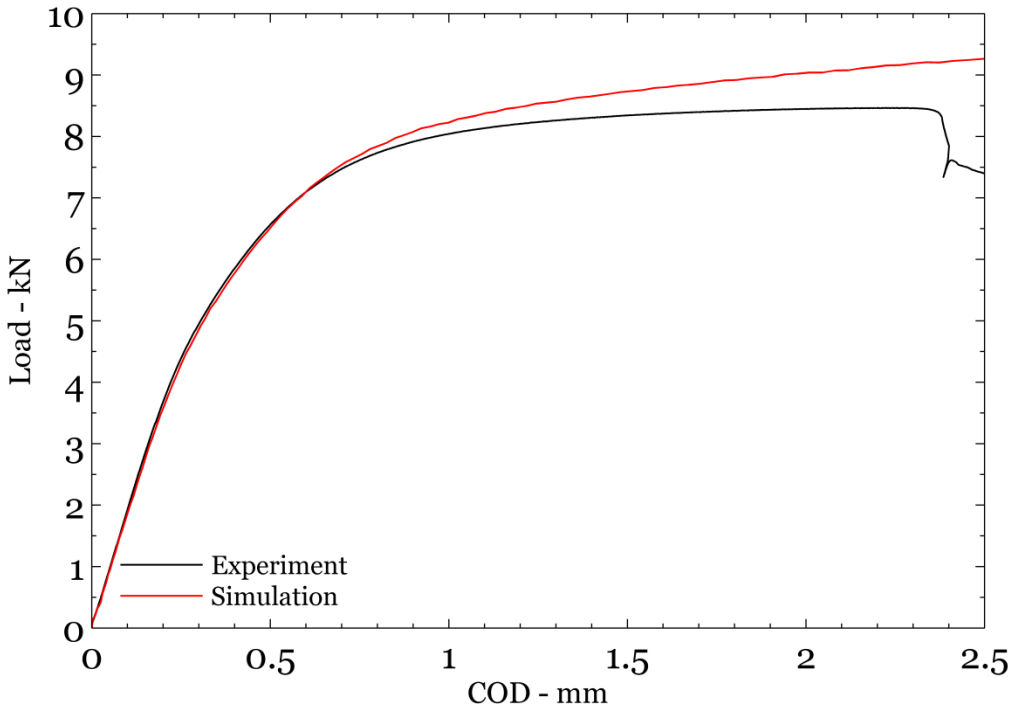

Figure 3.29: The load variation over the first 2.5 mm of COD from the experimental result for specimen **S06** and a non-blind simulation is shown here. The non-blind simulation differs from the blind one by taking into account the specific geometry of specimen **S06**, and by using a modified shear coefficient in the yield function.

Chapter 4: Prediction of Ductile Failure in Ti-6Al-4V using a local strain-to-failure criterion

4.1 INTRODUCTION

Sandia National Laboratories (SNL) issued the second Sandia Fracture Challenge (SFC2) in May of 2014. The details of the challenge itself and the overall outcomes are described by Boyce et al. (2015). This challenge is the second in a series of problems posed by SNL with the purpose of exploring and refining methods for predicting the failure of ductile metals. In this challenge, participating teams were invited to predict the behavior of a specially designed specimen geometry that will experience multiple cracking events during testing. To facilitate the prediction, SNL also provided data from a set of material characterization tests from which suitable constitutive and failure models for the material of interest could be calibrated. These constitute truly blind predictions because only after the participating teams submitted their predictions was the testing of the challenge specimen performed, ensuring that all predictions were made without any knowledge of the actual experimental result. A time-line was followed for the whole procedure as discussed in Boyce et al. (2015) that allowed about four months for the efforts associated with material calibration and prediction of the response of the challenge problem. In this challenge, both the calibration tests and the challenge tests were performed at two specific cross-head displacement rates – of 0.0254 in/min and 25.4 in/min – in order to introduce strain-rate dependence. In this chapter, we will refer to those tests or simulations performed at 0.0254 in/min as the "slow-rate" and those performed at 25.4 in/min as "fast-rate".

For completeness, the quantities of interest (QoIs) that were requested from SNL to compare prediction to experimental results are summarized here:

i. What is the load when the crack opening displacement (COD) of notch B (referred to hereafter as COD1, and the COD at notch A is hereafter called COD2) is equal to 1 mm, 2 mm, and 3 mm?

ii. What is the peak load?

iii. What are the COD1 and COD2 values when the load is 90% and 30% of the peak load?

iv. What is the crack path?

v. What is the complete load variation with COD1 and COD2?

After predictions were made and testing of the challenge geometry was performed, QoI iii was discarded and the following additional QoIs were posed:

vi. Is crack growth stable or unstable?

vii. What is the load at which an unstable crack is initiated?

viii. What is the COD1 at which an unstable crack is initiated?

This chapter provides the details of the effort from the University of Texas team both in the predictions for this challenge, as well as the experimental results performed as a follow-up exercise to identify additional local features of the response of the challenge geometry. The methods used here are quite similar to those used previously by the same authors in the previous SFC (Gross and Ravi-Chandar, 2014), but have been adapted for the change in material, available characterization data, and testing conditions. The details of calibrating the constitutive and failure models and the use of these models to generate a prediction are contained in Sections 4.2 and 4.3. Additional experiments performed on the challenge specimens with detailed observations of the material behavior is documented in Section 4.4. These observations are then used for assessing the modeling techniques used in the challenge in Section 4.5. A summary with concluding remarks and

recommendations on efforts to improve predictive ability for problems of ductile failure is given in Section 4.6.

4.2 CONSTITUTIVE AND FAILURE MODELS

In order to predict the response of structural materials, the elastic and plastic constitutive properties as well as the failure behavior of the material under consideration are needed. In this work, models for both of these behaviors were selected based on knowledge of the underlying physical mechanisms, the nature of the calibration data provided by SNL, past experience, and availability in the numerical tools used. ABAQUS finite element software was used for all modeling reported in this work. Some simulations were performed with implicit time stepping and others with explicit as described below. In the explicit simulations, fixed mass scaling (where the scaling factor for density is constant for each element, regardless of their initial mass) was used to increase the stable time step enough to make the simulations feasible on a desktop computer. Three-dimensional continuum linear elements with reduced integration (C3D8R and C3D8RT for models with thermal degrees of freedom) were used in all models for their computational efficiency and suitability for modeling large plastic deformations.

4.2.1 Calibration of the constitutive model

The anisotropic elastic moduli for Ti-6Al-4V shown in Table 4.1 were obtained by fitting the initial linear response for each of the calibration experiments. For the shear testing, this required performing a FEM simulation of the experiment (as no analytical solution exists for this problem) and matching the load vs. strain curves. In the absence of

experimental data, Poisson's ratio was taken to be 0.34; the error associated with this assumption was expected to be negligible since the response of the structure was expected to be dominated by its plastic behavior.

Ti-6Al-4V is a dual phase alloy with a hexagonally close-packed (HCP) α phase and a body-centered cubic β phase. As a consequence, *a priori* confidence in plasticity models developed for face-centered cubic polycrystals is lowered, and the plasticity models developed specifically for HCP metals by some investigators may be more appropriate. Despite the greater uncertainty of using a standard plasticity model, this choice was made due to the absence of models designed specifically for HCP metals in ABAQUS. The Hill-48 yield criterion was selected and the four parameters governing anisotropy of the normal and in-plane shear stresses were subject to calibration. The hardening behavior for plastic strains less than ~0.04 was represented by directly fitting to the experimental data a monotonically increasing spline of the form discussed in Gross and Ravi-Chandar (2015). For higher strain levels, the spline was extended with 7 knot points, whose locations were subject to calibration. For modeling of the experiments performed at the faster of the two loading rates, Johnson-Cook temperature and rate sensitivity model were used to modify the base stress-strain curve that was first found from the slower loading rate experiments.

Selection of parameters for these models followed an inverse procedure nearly identical to that performed by Gross and Ravi-Chandar (2014) and is summarized as follows: FEM simulations of the calibration experiments were run with trial model parameters. The resulting load-elongation curves were compared to the experimental results and deviations were penalized in an optimization scheme. This process was automated and iterated until the deviations were satisfactorily low. It is important that all of the slow-rate calibration experiments that were selected for fitting were considered

simultaneously in order to obtain material parameters that are suitable for all the test data. That is, the parameters defining strain hardening and anisotropy that minimizes the sum of the errors between simulation and experiment for the rolling direction (RD) tensile, transverse direction (TD) tensile, and shear (VA; this orientation has the RD in the plane of shear) was sought. After calibration of the anisotropy and stress-strain curve from the slow-rate tests was completed, the parameters for temperature and rate sensitivity were found using the fast-rate RD tensile and VA shear tests with the same inverse procedure. TD tension test data was not used because temperature and rate sensitivity were expected to be isotropic, and thus its inclusion was not worth the extra computation time. The two fast-rate tests used for calibration were chosen because they were dominated by different strain rates and temperature ranges.

Some of the data provided by SNL, such as the VP shear data (this orientation has the RD normal to plane of shear), were not used. The chosen constitutive model does not allow for anisotropy in pure shear loading between the VA and VP orientations. As a result, simulations of the two orientations only differ slightly, due to the change in orientation of the normal stresses that are present in the test geometry (which the constitutive model is sensitive to). Since the load elongation curve of both orientations could not be reproduced by the model; VA shear was used exclusively for model calibration as it corresponds to the dominant orientation of shear loading in the challenge geometry.

Other experimental data were left out due to large scatter, which was handled indirectly because time only allowed for a deterministic model calibration. As a result, tensile test data that were distinctively more compliant than the stiffest observation were discarded based on the following argument. Because the tensile test samples a large volume of uniformly deformed material, and necking occurs at the weakest section of the

specimen, the post-necking load elongation behavior will be dominated by the largest defect (understood to be either geometric or perhaps an unfavorable orientation of the microstructure). In contrast, the volume of highly strained material in the challenge geometry is significantly smaller, and is significantly less likely to contain a defect of equal severity. Separately, one of the fast-rate RD tensile tests (RD4) was discarded as it was clear from the post-mortem photographs supplied that necking occurred partially outside the gauge length of the extensometer. The tensile test data used for calibration was RD 2 and 5 for slow-rate RD, TD 2, 3, and 4 for slow-rate TD, and RD10 for high-rate RD. For tests where more than one specimen was chosen, the mean response was taken. The scatter for the shear tests was much smaller. VA1 was chosen for the slow-rate and VA4 for the fast-rate shear data for the calibration.

Despite these efforts to distill the calibration experiments into a body of data that appropriately matched the limitations of the chosen plasticity model, there still existed one feature in this reduced dataset that is beyond the ability of model. The load-elongation curves for tension in the RD and TD directions have distinctly different shapes prior to necking. The chosen plasticity model can only multiplicatively shift the stress strain curve to capture anisotropy, and not change the shape of the curve. We speculated that the shape of the stress strain curve in the high strain regime also differs for the two orientations; however, direct evidence of this is obscured by necking, and the influence of such a shape difference is left as an unknown. Additionally, there is some instability at the end of the elastic regime for both orientations; it is much more pronounced for the tension test in the TD. Understanding the nature of this load drop requires additional kinematic data that was not available. We conjectured that the importance of this instability would fade with strain as it occurs only in the very small plastic strain regime; however, due to the history dependence of plasticity, further propagation of error cannot

be ruled out. In summary, a model that allows for unique stress strain curves and/or anisotropic growth of the yield surface is most appropriate for this material, however due to an insufficiency of data to properly calibrate such a plasticity model and its unavailability in the numerical tools used, the simpler Hill-48 model was adopted.

4.2.1.1 Calibration simulation setup

The simulations of the slow-rate tests were performed for calibration of the strain hardening curve and yield surface using implicit time stepping. The effect of heating from plastic dissipation was not included in these simulations. All three available planes of symmetry were used in the tension test simulations while the shear simulations used just one symmetry plane in the thickness direction. A mesh convergence study was performed to find efficient meshes for both geometries and the "as-measured" thickness of the experimental specimens was used. The discretization details are listed in Table 4.2 and the mesh details can be seen in Figure 4.1.

The simulations of the fast-rate tests were performed for the calibration of rate and temperature effects using explicit time stepping. Mass scaling was used to increase the stable time step to 2 microseconds for both tensile and shear simulations. A Taylor factor of 0.9 was used in converting plastic work to heat in the simulations. Temperature dependent elastic moduli scaling, thermal conductivity, coefficient of thermal expansion, and specific heat were used from the works of Fukuhara and Sanpei (1993) and Zhang et al. (2001), respectively.

The fast-rate tensile and shear simulations used only the through thickness symmetry; this choice was made so as to allow for localized necking to occur in the tensile simulation, as observed in the experiment. It was verified prior to fitting the

calibration experiments that the simulation would in fact exhibit localized necking if a small defect was included (0.015% reduction of the flow stress for 8 elements) and the effect of thermal softening was large. Once again, a mesh convergence study was performed to find efficient meshes for both geometries. The mesh size required to allow for thermally triggered localization was found to be smaller than the size used for slow-rate simulations. As a consequence, the fast-rate simulations have many more degrees of freedom than the slow-rate. The mesh is sufficiently fine so that mesh dependency of localized necking induced by thermal softening was combatted by the rate of heat diffusion between elements. Further refinement did not have a profound effect on the global load-elongation behavior. Despite the effort made to allow for thermal softening triggered localization, the calibrated material model did not exhibit this behavior for either the tensile or shear geometry.

4.2.1.2 Boundary Conditions

Care was taken to replicate the experimental conditions as closely as possible in the simulations used in the inverse problem. For modeling of geometry, this is as simple as using the dimensions from the machine drawings, but using the measured specimen thickness for the data particular test data chosen for calibration (or the average thickness if multiple curves were averaged). The application of proper boundary conditions required more effort.

For shear testing at both loading rates, a local displacement measurement on the specimen was not supplied. As a result, to make the load vs. crosshead displacement curve useful, the slip correction suggested by SNL was used with an additional correction factor for grip compliance. The grip compliance was estimated by performing simulations

of the strain-gauged titanium compliance bar testing performed by SNL. The compliance correction was taken to be the difference in grip displacement between the experiment and simulation at a given level of load. This produced a nonlinear, elastic compliance curve that was used to shift the shear data. Unfortunately, application of this compliance correction to the shear specimen load-elongation data did not produce agreement between the simulated and compliance-corrected experimental curves in the elastic regime. The compliance curve was then scaled by a non-negligible factor to bring the simulations and experiments into agreement. This scaling factor sheds some doubt on the load elongation behavior of the shear specimens used, but without any displacement measurement made directly on the shear specimen, no better alternative was available. The uncertainty in this process points to the inadequacy of relying on displacement measurements that are not local to the specimen itself.

Additional consideration is required for the applied boundary condition in the fast-rate tension test. The rate of load application in the tension test was inferred from the time variation of the extensometer measurement. The fast-rate tensile test simulation had displacement boundary conditions applied on the shoulders in such a way that caused the time variation of a virtual extensometer measurement on the simulation to match the nonlinear variation that was measured in the experiment. Of course the virtual extensometer measurement is dependent on the particular values chosen for the parameters of the constitutive model, so several iterations of boundary loading rates were required as the value of these parameters evolved throughout the calibration process.

4.2.1.3 Optimization details

The objective functions used for the slow- and fast-rate inverse procedures are:

$$\Phi_S = \varphi_{RD} + \varphi_{TD} + \varphi_{VA} \quad (1)$$

$$\Phi_F = \varphi_{RD} + \varphi_{VA} \quad (2)$$

$$\varphi = \sum_{i=1}^{n} \frac{\left|F_i^{exp} - F_i^{sim}\right|}{F_i^{exp}} \quad (3)$$

where Φ_S and Φ_F are the objective function values for the slow- and fast-rate optimization procedures, respectively. φ_{RD}, φ_{TD}, and φ_{VA} are the relative error between experiment and simulation for RD tension, TD tension, and VA shear, respectively, and taken at the appropriate loading rate. Equation (3) defines the relative error, where F_i is the load at the i^{th} level of deformation, and n, the number of levels of deformation considered was set to be equal to 100.

The genetic algorithm as implemented in MATLAB was the main tool used for minimization. Population sizes of 40 and 51 were chosen for the slow- and fast-rate optimization runs respectively. Thirty-one generations were completed for the slow-rate and eleven generations for the fast-rate. Latin hypercube sampling was used to generate the initial parameters used for both anisotropy and thermal/rate effects that were then used to seed the optimization runs. Due to the difficulty of using this same method to create constrained parameter sets, a large pool of initial flow curves was randomly generated and the curves that were not monotonically increasing or did not have a decreasing tangent stiffness were rejected. The relative difference between each of the remaining curves with respect to all the others was then calculated and the mean of all the relative differences for each curve was found. Finally, a diverse set of curves was made by selecting curves that spanned the range of mean relative difference. These curves made up the initial population for the genetic algorithm used in the slow-rate inverse procedure, and convergence to a minimum of the objective function was found. The best individual was then used to start the pattern search algorithm in MATLAB to reduce the

objective function further, although significant reduction was not achieved. The fast-rate optimization was performed with the genetic algorithm and no subsequent effort was made to reduce this value further.

The load variation with applied displacement for the three slow-rate calibration tests are shown in Figure 4.2. It is seen that the simulated responses very closely match the experiments for all three tests. The average error between simulation and experiment for all three tests is only 1%. Within this minor error, the largest discrepancy occurs for the early part of the TD tension curve. As anticipated, the load drop just after the elastic regime was not captured by the model, leading to a reduced prediction in the TD yield stress. The next largest error occurred in the shear test, where matching of the load-elongation curve degrades slightly with increasing deformation. The simulated response shows slightly stiffer behavior for a displacement in excess of 1.4 mm, when the average strain between the notches exceeds a value of about 0.2. These minor deviations in the load elongation behavior are interrogated in detail because it is possible that a minor error in this curve is evidence of a larger error in the local fields. However, little room for improvement is possible with the given information, and this calibration is deemed sufficient to move onto the calibration of model parameters controlling temperature and rate sensitivity.

The load variation with applied displacement for the two fast-rate calibration tests are shown in Figure 4.3. The agreement between simulation and experiment is seen to be adequate, although not as good as the results at the slow-rate. The average error between simulation and experiment for these two tests is 2.3%. The cause for higher error is likely due to the minimization scheme being diverted by a local minimum and searching for parameters in its vicinity, and thus missing the global minimum for the objective function. To be clear, it is anticipated that the Johnson-Cook thermal and rate dependence

is able to describe the material more accurately than demonstrated here. A better calibrated parameter set for this model was not pursued due to time constraints. With the final set of calibrated model parameters, simulations of the two calibration experiments indicate structural response that does not soften as much as the experiment at high levels of deformation. This likely means that the actual constitutive properties are slightly more temperature dependent than the calibrated model.

The extracted constitutive parameters underlying these load-elongation curves are given in Table 4.3. The slow-rate stress-strain curve is plotted in Figure 4.4a, and shows continued strain-hardening throughout the strain range explored. One projection of the calibrated Hill 48 yield surface is compared to von Mises yield surface in Figure 4.4b. The largest difference between these surfaces occurs in the biaxial stress regime, where anisotropy is seen to significantly delay yielding.

4.2.2 Calibration of the failure model

Ductile failure is most often described by the nucleation, growth, and coalescence of voids across a broad range of strains until failure occurs; micromechanical models such as the Gurson–Tvergaard–Needleman models have been developed and are commonly used in failure predictions. However, based on recent work (Ghahremaninezhad and Ravi-Chandar 2012, 2013, Haltom et al. 2013), and prior knowledge of the microstructure of the Ti-6Al-4V, we conjectured that damage will begin at much later stages in the deformation of the material with large scale void growth occurring only near the brink of final failure and then progress rapidly. The sudden appearance of damage just prior to failure means that stiffness degradation of the material due to damage can be adequately approximated as a complete loss of stiffness once

damage has occurred. Then, all behavior up to failure is completely described by the constitutive relations and a simple equivalent plastic strain-to-failure model suffices to incorporate material fracture.

The failure strain, ε^f, is chosen to be dependent exclusively on stress triaxiality. When an element in the FEM simulations accumulates a damage parameter equal to unity according to the rule: $\int \frac{d\varepsilon^p}{\varepsilon^f}$, its stiffness is set to zero, where $d\varepsilon^p$ is the plastic strain increment. The failure strain was calibrated by using the optimized RD tensile and VA shear simulations.

For tension, the central element in the neck has both the highest triaxiality and strain. Since rupture of the specimen occurs rapidly, it corresponds to failure of this central element. By matching the experimental elongation at rupture in the simulation, the central element in the neck provides a strain-to-failure estimate under moderate levels of triaxiality. Anisotropy in fracture properties is certainly a possibility, so the same calculation was also performed for TD tension, however the failure strain was found to be much higher. Seeing this discrepancy as more likely to be a plasticity modeling error than to actually describe the behavior of the material, the failure strain calculated from TD tension was simply ignored.

Strain-to-failure estimation in the shear specimen is based on past experimental experience indicating that the peak load in the test corresponds to the formation of a crack at one of the notch tips. Then the grip displacement at peak load in the experiment corresponds to global deformation state where the element at the current notch tip in the simulation must fail. This provides an estimate on the strain-to-failure under negative triaxiality conditions. After crack initiation, stable growth occurs in the experiment and could be used to perform a more detailed failure calibration. Due to time constraints this data was not used. It was found that the strains to failure over the large range of triaxiality

spanned by these two tests were nearly identical (0.79 from tension and 0.82 from shear), so the strain-to-failure between them was simply interpolated linearly. For triaxialities in excess of those in the tensile test, a conservative strain-to-failure curve that is motivated by the exponential behavior first suggested by McClintock (1968) was adopted.

4.3 RESULTS OF BLIND PREDICTION OF THE CHALLENGE PROBLEM

Prior to performing the final prediction for the challenge geometry, a number of exploratory simulations for the slow-rate loading were performed. Firstly, a simulation with implicit time stepping and the exclusion of a failure model was used to investigate where on the specimen plasticity would cause localization of the deformation. Localization was found to occur first in ligament *BD* closesly followed by ligament *DE*. The model parameter controlling shear anisotropy was then varied to see if switching of localization to the ligament *AC* was possible. It was found that setting the parameter *N* in Hill-48 to be greater than or equal to 0.92 did in fact cause this change in the localization behavior. This critical value is sufficiently far from the calibrated value to preclude the chance of localization occurring in ligament *AC* in the slow-rate simulation, but close enough that both paths should be considered when the loading rate is changed.

For the final prediction, the challenge geometry was modeled in full without using the available symmetry plane in the thickness direction. The loading pins were included as separate, rigid bodies from the challenge specimen. Frictionless contact was assumed between the pins and the specimen. The top pin was held stationary and for the slow-rate simulation the bottom pin was displaced downward at a quadratic rate. The rate of application for the slow-rate simulation is unimportant, as the material model does not include any time dependent behavior (e.g. viscoplasticity or heat diffusion). For the fast-

rate simulation, the bottom pin was displaced downward at a quadratic rate during elastic deformation, reaching the target displacement rate of 25.4 mm/s just prior to the onset of plastic deformation, and continuing for the rest of the simulation at this constant rate.

The challenge geometry was meshed as shown in Figure 4.5 for the slow-rate prediction. The inset shows the fine level of discretization used in the areas where fracture was expected. The mesh used for the fast-rate prediction is quite similar, but with refinement along the possible failure path through ligaments *AC* and *CE*. The discretization was chosen to be fine enough to ensure that plastic deformation is accurately modeled, yet without an undue number of elements so that the simulations could still be solved on a desktop computer. The details of the spatial and temporal discretization used for both loading rates are given in Table 4.4.

The load-COD response for the slow-rate prediction is shown in Figure 4.6a and contours of the equivalent plastic strain development on the mid-plane are shown in Figure 4.7. The load-COD curve shows initial elastic behavior up to a load of ~10 kN at ~0.56 mm of crack opening displacement at the lower notch (COD1). After this point, the curve becomes nonlinear, and the initial accumulation of plastic strain occurs most rapidly in the ligament *AC*, as seen in Figure 4.7a. By about 2 mm of COD1, the plastic strain in ligaments *DE* and *BD* surpasses that in ligament *AC* (Figure 4.7b), and maintains this lead for the rest of the deformation. At 3 mm of COD1 the maximum strain in the simulation is still well below the failure strain for the material and the load is still increasing with additional pin displacement. It is only just after the onset of structural instability (50 μm of additional COD1 after the peak load), that failure occurs. The failure occurs on these two ligaments in rapid succession, appearing as a single and sudden drop on the load vs. COD1 curve.

The first failure is predicted to initiate on the surface of hole *D* and exhibit unstable growth towards hole *E*. Just following this break, another failure event is predicted to initiate on the surface of notch *B* and exhibit unstable growth towards the hole *D*. Figure 4.7d shows the strain field in between these two cracking events, with ligament *DE* severed, but ligament *BD* intact. Initiation of both cracks occurs on the specimen mid-plane. After both of these ligaments have been severed, the specimen can accommodate a large rotation and will return to near zero load without being completely broken into two pieces (it is anticipated that in the experiment the load may not return to zero if there is significant load train compliance). Ligament *EA* is still intact at this point, but it is obvious that further loading will cause this ligament to eventually fail. All QoIs are thus known at this level of deformation and the simulation is halted.

The crack path is reported as *D*-*E*;*B*-*D*;*EA*; indicating that first cracking will occur from hole *D* to *E*, a separate crack from hole *B* to *D*, and finally *EA* will break, but no prediction is supplied as to where this last crack will initiate. Greater specificity could not be given confidently for this final cracking event for two reasons: Firstly, part of ligament *EA* is undergoing compression, but the calibration data supplied did not probe material behavior in compression (which is known to be different than the tensile behavior for this metal). Secondly, the simulation used mass scaling and the effect of this during, and especially after dynamic cracking of the first two ligaments is not accounted for.

The trends for the fast-rate simulations are very similar to that for the slow-rate simulations. The load-COD curve is shown in Figure 4.6b and the strain contours on the mid-plane in Figure 4.8. The strain paths of three points, one each in the ligaments *BD*, *DE* and *AC* are tracked in Figure 4.9 where the values of the equivalent plastic strain is plotted as a function of the triaxiality for later discussion. The largest difference in the fast-rate load-COD behavior from the slow-rate loading is that the structure is predicted

to reach a limit load well before failure occurs. This is a consequence of thermal softening on the structure, as substantial heating occurs in the ligaments between holes. After peak load, straining still occurs at a slow-rate on ligament *AC*, indicating that the structural softening is due to material effects and not geometric effects. When failure occurs, it is again with unstable crack growth in the ligaments *BD* and *DE*, however, the order is opposite from that in the slow rate loading. Again, the load is predicted to drop near zero when ligament *EA* is the only ligament left intact along the cracking path, and the simulation is halted for the same reasons as before. The crack path for the fast-rate prediction is the same as the slow-rate, however the sequence of cracking is different and was reported as *B-D-EA*.

The complete table of QoIs for both loading rates that was extracted from these blind predictions and submitted to SNL prior to challenge deadline are presented in Table 4.5. The upper and lower bounds for the predictions of load at the specified levels of COD1 were formed by the following simple, *ad hoc* method: The largest average strain in any of the ligaments on the challenge geometry was computed and correlated to the average strain in the minimum cross section of the neck in the (slow rate RD and TD) tensile calibration experiments. The range between upper and lower bound in the prediction was taken to be the same as the range in load observed between the tensile experiments at the same level of strain, with the simulation results assumed to be the mean response. Bounds for the COD predictions at the specified levels of load were formulated by maintaining that the load drop through this load range will be sudden. The range for the failure strain was assumed to be quite large (around 20%) causing about a 1 mm window of COD over which failure was possible, with the simulated response again taken as the mean response. Given the constrained timeline that predictions had to meet,

the limited time available was dedicated to finding the mean response, only leaving time for a coarse method of bounding that mean response such as described above.

We turn now to a comparison of the predictions to the experiments performed by SNL. A detailed description of these experiments can be found in Boyce et al (2015). The experimental load-COD curves for both loading rates are shown in Figure 4.6. Excellent agreement between the prediction and experimental results is found from the initial elastic response up to a COD1 level of about 1.75 mm for both the slow- and fast-rate cases (4.8% and 2.3% relative error for slow- and fast-rate cases, respectively). A significant contribution to this error is from the elastic regime, where synchronization error between experiment and simulation can have a large effect. Relative error for the COD1 range of 1 – 1.75 mm is 3.3% and 0.4% for slow- and fast-rate cases, respectively. For COD1 levels beyond this, the predicted load-COD1 curves are slightly stiffer than the experimental result. The effect of this stiffness discrepancy causes continuously increasing deviation from the predicted and observed load as COD1 increases. The fast-rate simulation correctly predicts the presence of a limit load; however, it is predicted to occur at a larger COD1 than observed in the experiments. At both loading rates, the specimen is found to fail at a lower level of COD1 than predicted; however, the nature of failure occurs as predicted, with a sudden load drop caused by unstable propagation of cracks across the ligaments *BD* and *DE* occurring almost simultaneously (appearing completely simultaneous at the temporal resolution of the current measurements). As a whole, the major features of the experimental load-COD1 curves were predicted, but were spread out over a larger range of COD1 than observed in the experiment. In terms of the quantities of interest, all scalar measures except the COD1 at fracture were predicted to within 12%, and the presence of unstable fracture was identified. The only feature lacking in the predictions was a limit load for the slow-rate case prior to failure.

To probe the cause of these forecasting errors, experiments with additional diagnostic measurements were performed on the same material as the experiments performed at SNL.

4.4 ADDITIONAL EXPERIMENTS

Additional experiments of the challenge geometry were performed after the predictions of all participating teams and the results of experiments by two different groups within SNL had been distributed. These samples were provided by SNL with the sample designation 2, 5 and 31, and obtained from the same manufacturing lot as the samples tested at SNL. Due to the limited number of samples, only experiments at the slow-rate were performed. Additional measurements of the evolution of the three-dimensional displacement fields on one surface of the specimen were taken in order to produce a complimentary set of data to those already compiled by the two Sandia laboratories. The two main goals of these experiments are (i) to provide greater details of local deformation fields in the specimen that can enable a careful assessment of the capabilities and difficulties in the modeling efforts and (ii) to reveal the crack sequence for the slow-rate experiment.

4.4.1 Experimental setup

The experimental setup used is shown in Figure 4.10. The experiments utilized a 100-kN Instron electromechanical load frame, with a 100-kN load cell ($\pm 0.25\%$ uncertainty of the measured value) at ambient temperature. The level of noise in the load signal was measured to be 2 N. The crosshead rate was maintained at 0.0254 mm/s, as prescribed in the challenge. Two universal joints were placed, one each at the upper and

lower grips in order to minimize the effect of loading misalignments. In addition, the same clevises used by SNL were used. Instead of using COD gages to measure the displacements at the notch mouths an optical measurement was made. This was made possible by affixing small fiducial patches with a speckle pattern to the four notch roots on the specimen, extending beyond the location of the knife edge features intended for contact COD measurements to provide features that could be used to obtain a DIC displacement measurement at the same location. A digital single-lens reflex (DSLR) camera was used to view the entire specimen and to capture the images needed for this measurement. The pixel resolution of this camera was 133 μm/pixel and frames were down sampled at a rate of 8 Hz. The DIC used a sub-image size of 40 pixels with a step of 10 pixels between sub-images. The resulting measurement of COD has an uncertainty of 0.02 mm. For one specimen (sample number 2) this camera was configured differently to have increased spatial resolution at the cost of sampling at a rate of one image every 5 seconds.

Images from two CCD cameras focused on the region between the notches were used to perform 3D-DIC measurements and determine the three-dimensional kinematic fields in the regions of highest deformation and eventual failure. A high contrast random speckle pattern was applied to the specimen in this region. The cameras captured images with a spatial resolution of 17.8 μm/pixel and at a rate of once every second. DIC was performed with a sub-image size of 20 pixels and a step size of 10 pixels between sub-images. The effective gauge length for strain measurements is then 356 μm and strains were measured with an uncertainty of 1000 με.

A Photron SA1 camera, with high frame rate capability, was positioned to view the ligaments B-D and D-E and resolve the order in which these ligaments failed. This camera was placed on the back side of the specimen so that the bright lighting that is

required for fast-rate imaging could be focused on these two ligaments without disturbing the images taken by the other three cameras. A fan was used to cool the specimen so that the lights did not cause substantial heating during the test. To ensure that cracks on the specimen are as visible as possible, no speckle pattern was applied to the specimen, however, the specimen has a natural surface texture that is adequate for use in performing DIC measurements of the in-plane displacements. Images were captured with a spatial resolution of 37 μm/pixel at a rate of 20000 and 40000 frames per second for samples 2 and 5, respectively. This camera was triggered with the load-drop corresponding to unstable crack initiation, with images recorded for half-second prior and half-second post trigger time; this permitted capturing the dynamic events associated with the failure of the ligaments *DE* and *BD*.

4.4.2 Load-COD1

Confirmation of the load-COD1 results observed at SNL is shown in Figure 4.11**Error! Reference source not found.**. Sample 2 failed at a slightly higher level of OD1 than shown in this figure; the exact COD is not known precisely due to the coarser image capture rate used for COD measurements on this sample. Additionally, sample 31 was not loaded until failure; loading was interrupted just after localization to preserve this sample for microscopic examination. Samples 2 and 5 failed along the same crack path (*DE;BD;EA*); failure occurred in ligaments *BD* and *DE* almost simultaneously. Although loading on sample 31was halted prior to cracking of these ligaments, it is clear that failure would have occurred there if further loading was applied.

4.4.2.1 Ligament failure sequence in the slow-rate tests

For the two samples loaded until failure, unstable fast fracture occurred in ligaments *BD* and *DE* nearly simultaneously. However, the image sequence showing three subsequent frames captured by the high speed camera at the time of failure for sample 2 shown in Figure 4.12 is able to resolve the actual failure sequence. The overlaid color contours indicate the vertical displacement field calculated with DIC from the high speed images. The first image shows the state of the sample just before cracking of any ligament, the second image shows ligament *BD* intact with ligament *DE* completely severed, and the final image shows both ligaments fully broken. Identification of cracking in the in the ligament *DE* second image is made by observing a displacement field consistent with the elastic recovery expected after release of tractions across the broken ligament. A high speed video with more frames for this sample and without DIC processing is included as Supplementary Material SM7 for this dissertation. Despite increasing the frame rate for sample 5, only three subsequent frames capture the same behavior observed for sample 2. Sufficient temporal resolution to determine the location of crack initiation in each ligament was not pursued. Thus, the greatest specificity that can be given for the cracking sequence of these two specimens is that ligament *DE* failed first, closely followed by the failure of ligament *BD* within the next 50 μs. It is clear that any modeling effort to capture the final failure of ligaments *DE* and *BD* must account not only for initiation of cracks, but also for their dynamic growth with inertial effects. After continued loading ligament *EA* is expected to fail as observed in the experiments performed by SNL.

4.4.2.2 Strain field measurement

The strain field for sample 5 just prior to fracture is overlaid on the raw image used for the DIC measurement in Figure 4.13. Since ligament *AC* was not of interest it was not completely contained in the field of view in order to increase the spatial resolution on the eventual path of failure. Despite this restricted field, at the state of deformation shown here it is likely that the strain gradient is too strong to be insensitive to the effect of gauge length. The DIC strain values should be interpreted with this in mind, and seen as lower bound for the actual strain, especially at larger levels of strain. The strain accumulation with COD1 at the points identified in Figure 4.13 (points of maximum principal strain measured within each of the ligaments) are plotted in Figure 4.14. In spite of not capturing the location of maximum strain in ligament *AC* in the field of view, the point of maximum strain within the observed region still shows more strain accumulation in ligament *AC* than any other for COD1 values less than about 1 mm. After this level of COD1, strain accumulation in ligaments *BD* and *DE* accelerates until failure. This acceleration is gradual and continuous, with no indication of an abrupt localization into these ligaments apparent in the local strain field. This could again be due to strong gradients in the strain field, or because development of the localization is interrupted by failure before it has too much of a strain concentrating effect. Regardless of the reason, it is interesting to note that the global load measurement is able to reveal some detail of the strain development that is imperceptible with the DIC measurement.

In seeming contradiction to the sequence in which cracking occurs, the maximum strain measured on the surface in ligament *BD* is larger than that measured in ligament *DE*. This can be explained by any combination of the following possibilities:

- Ligament *DE* may have a stronger strain variation through its thickness than ligament *BD*; thus the strain on the mid-plane (where failure develops) may actually be larger for this ligament.
- The location of maximum strain in one or both ligaments may be on the edge of the hole, where DIC cannot provide a strain measurement. This unknown strain may be larger for ligament *DE* than *BD*.
- The strain gradient across ligament *DE* may be stronger than that across ligament *BD*, thus causing the DIC measurement to underestimate the strain in this ligament more severely than in ligament *BD*.
- The strain in ligament *DE* may actually be less than that in ligament *BD* and some other factor (e.g. a difference in stress triaxiality or lode angle) causes ligament *DE* to fail first.

Since failure is likely initiated on the mid-plane of the specimen, it is useful to discuss the deformation history on this plane. Experimental strain measurements are not available on the mid-plane only the surface strains can be measured. The strain in the interior can be estimated by correlating the surface strain between simulation and experiment, and then investigating the interior strain in the simulation. This method can only be as accurate as the simulation. The stiffer response observed in the simulation is likely to underestimate the increase in strain experienced on the interior; this underestimation coupled with the underestimation of the strain from DIC places a very conservative lower bound on the failure strain as 0.6 for a triaxiality of 0.4. A better methodology for obtaining a tighter lower bound for the failure strain would be the tracking of microstructural deformations directly. Such a study was not pursued.

4.4.2.3 Microscopy

The fracture surfaces of sample 5 were examined with a scanning electron microscope (SEM). Figures 4.15 and 4.16 show the upper and lower sides of the fracture surfaces along the ligament *BD*. The upper side refers to the part of the sample after failure along *B-D-E-A* that contains hole *C*. The fracture surfaces along ligament *DE* are nearly identical in all its features and hence is not shown. Most of the surface for both ligaments *BD* and *DE* is found to be dominated by uniformly distributed small dimples, with a typical equivalent diameter of about 3 μm. These dimples are indicative of the ductile failure mechanism that is operative in the fracture of the ligaments. However, some localized regions exhibited larger dimples (of equivalent diameter ~ 12 μm which is greater than the mean grain size in the material) as seen in the central portion of Figures 4.15 and 4.16. Such a region of large dimples surrounded by the more prevalent small dimples is clearly identifiable on the failure surfaces of ligaments *BD* and *DE*. Due to the infrequency and isolation of such large dimples in comparison to more homogeneous distribution of the smaller dimples, it is thought that the regions of large dimples exhibited growth separately from the formation and growth of the fracture.

Another feature of interest in Figures 4.15 and 4.16 is a nearly smooth region in the neighborhood of the region with the large dimples. Investigating five other locations on this same fracture surface revealed that such featureless regions always accompany the region with large dimples. By performing a comparison of the upper and lower fracture surfaces, it is clear that the regions with large dimples mate with each other (note the mirror symmetry about the horizontal axis since we are viewing the mating fracture surfaces), but the smooth regions do not mate each other! On the upper fracture surface the featureless region is always to the right (towards hole *D*) of the large dimpled region, while it is always to the left (towards notch *B*) of the large dimples on the lower fracture

surface. Furthermore, what would have been the mating surfaces of the featureless regions on the opposite fracture surface are fully dimpled with fine scale dimples. It is apparent that after the cracks had propagated across the ligament, a large sliding displacement between the opposing crack faces occurred, and the contact of opposing faces scraped off the dimples on either side of the region with the large dimples, leaving the featureless surfaces.

Sample 31, the sample that was halted just after the limit load was reached, was examined in the scanning electron microscope (SEM). From the DIC calculation, the lower bound for the plastic strain in the ligaments *BD* and *DE* corresponding to the load-interruption is in the range of 0.5, with a triaxiality in the range of 0.43, as found from the simulation. This sample was prepared for microscopy by extracting the material in the vicinity of the prospective crack path. The extracted piece was mounted and mechanically polished until the mid-plane was reached; it was then etched with Kroll's reagent to reveal the grain boundaries. A SEM image near hole *D*, in the ligament *DE* is shown in Figure 4.17a along with an inlay showing the appearance of an unstrained region. The unstrained material was inspected over a broad area and no initial porosity was detectable at this spatial resolution. The presence of voids in the strained material is clearly observed and occurs over a broad region that extends beyond the edges of the image. The area fraction of voids in this image is approximately 1% and the mean ligament length between voids is about 22 μm. The largest void is elliptical in shape with major and minor axes of about 9 μm and 4 μm, respectively. The presence of voids is also observed in ligament *BD* in this same sample. Figure 4.17b shows how the state of porosity varies across the width of the ligament. The full resolution image is included as Supplementary Material SM8 for this dissertation. The voids are mostly concentrated in a band about 300 μm wide. Within this band the area fraction of voids is approximately

0.9% and the mean ligament length between voids in the band is about 24 μm. The largest void is elliptical in shape with major and minor axes of about 8 μm and 4 μm, respectively.

These observations of voids made during the interrupted test are consistent with the images of the fracture surface for sample 5 and the images taken by Boyce et al. (2015) of the fracture surface for other challenge geometry specimens. Specifically, the larger than typical dimples that are seen on the fracture surface are thought to be the result of continued growth by voids like those found in the interior of the interrupted test. The size and location of the voided region and the size of the individual voids themselves observed in the interrupted test appears to be compatible with the features observed on the fracture surface. Finally, sample 31 was polished further and no voids were seen upon reexamination; the fact that voids do not exist on the newly exposed surface is also consistent with the observations made on the fracture surface that regions with larger than typical voids do not span more than a few hundred micron across the thickness.

4.5 DISCUSSION

4.5.1 Plasticity

An important prerequisite to the ability to predict ductile failure is the ability to make an accurate prediction of the plastic behavior. The deformation leading up to the eventual failure of this material occurs through the continuing development of slip and twinning mechanisms at the crystallographic level that are readily modeled as plastic flow at the polycrystalline aggregate level through a phenomenological model. Assessment of the continuum plasticity model used for the blind prediction is then the starting point to assess the failure prediction. Figure 4.18 shows a comparison of contours

of the maximum principal strain between the blind prediction (left column) and the experimental measurement (right column) corresponding to different COD1 levels. Figure 4.19 shows a quantitative comparison of the variation with COD1 the maximum principal strains in the ligaments *DE* and *BD* between simulation and experiment. Note that the strain from the prediction is taken as the average of 64 neighboring elements, spanning the same area that is used for DIC strain calculation. The predicted strain in the ligaments tracks the measured values until the maximum principal strain is about 0.18 in ligament *BD*, at a COD1 of 1.8 mm. The maximum equivalent plastic strain in the simulation at this state is 0.22 at a location where the triaxiality is 0.44. Recall that the load-COD1 curve was also well predicted up to this level of COD1. Beyond this point, the predicted strain underestimates the measured value. It is anticipated that if a shorter gauge length were available for comparison, then the deviation between prediction and measurement would be even larger for strains beyond this level.

The local strain comparison provides additional insight to validate the prediction up to a COD1 level of about 1.8 mm, and also elucidate what aspect of modeling needs improvement at higher levels of deformation. Matching of not only the global response, but also the local strain development in the ligaments demonstrates a much stronger correlation between simulation and experiment than matching just the global response. Essentially identical load-COD1 curves can be produced from different local fields, therefore a good match in global behavior can still hide discrepancies in the modeling. If matching of the local field at its most critical locations occurs as well, little room is left for such discrepancies in the models. Even better would be to match the local field over an area or volume rather than just at a point; however, producing a suitable metric to quantify the matching over such a region is still a work in progress. In the slow-rate prediction considered here, matching at the only two points in the local field that were

interrogated and the global response is found for COD1 values under 1.8 mm. This strongly suggests that the plasticity model used is well-suited to describe the material behavior for the strain range where matching occurred (0-0.22), in the region of stress space activated by this particular challenge geometry.

The loss of agreement beyond an equivalent plastic strain of 0.22 is undoubtedly from an error in the extracted plasticity model. As seen by the microscopy performed on the interrupted test, voiding of the material does occur; although a tight lower bound cannot be placed for the strain on which it occurs for the loading history in ligaments *BD* and *DE*, an extremely conservative lower bound of 0.45 can be inferred from the DIC measured strain field. Even this inaccurately low bound for the onset of voiding is far above the strain level at which the prediction departs from the experiment. Thus, damage does not play a role in the departure of the prediction.

This departure beyond a strain level of 0.22 indicates that some modification must be made to the plasticity model to improve overall predictive ability; however, the need for such a modification was not obvious from the suite of calibration data provided. The load-elongation curves, particularly for the slow-rate loading calibration experiments, were well replicated by the Hill-48 anisotropic plasticity model used in the calibration exercise. The ability to fit the plasticity calibration data well, yet not capture the correct plastic deformation throughout the prediction indicates a deficiency in the set of calibration data. One possible shortcoming of the calibration data is the aforementioned lack of sensitivity of global structural response to changes in the local fields. This will allow errors in the local fields to go undetected and propagate into error of the extracted model.

Another weakness of the calibration data is the scarcity of stress paths explored. The majority of deformation in the challenge geometry occurs in stress states not

explored by the calibration experiments. Significant interpolation of the yield surface is then relied upon in the prediction, eroding confidence in predictive ability, and in this case even leading to a breakdown of predictive ability. Some amount of interpolation of the yield surface will always be required, but should either be performed over much smaller changes in stress state, or for a material where a particular interpolation strategy (e.g. choice of a particular yield surface shape) has been validated through extensive past examination. Reliance on calibration data that has a sparse exploration of stress space and does not include any local deformation information nearly precludes any systematic advantage that could be gained by using a sophisticated plasticity model that has more freedom in yield surface shape, anisotropic growth, and non-associated flow. Such a model requires a significantly larger set of calibration data to be well constrained.

More calibration data could be provided through conventional methods, such as tensile testing in additional orientations and dimensional measurements to calculate Lankford's parameters. Another route to enrich the calibration data would be to make local measurements of the deformation in addition to the conventional global measurements. This local deformation data can be used to turn the under constrained minimization problem of constitutive property extraction to an over constrained minimization problem. No matter the specifics of how calibration data is enhanced, predictive ability relies squarely on the suitability of models employed, and thus on the robustness of the experimental data used to calculate those models.

4.5.2 Voids

The presence of a dilute void population in the interrupted test of the challenge geometry (at equivalent plastic strains in excess of ~0.5 and a triaxiality of ~0.43) opens

the possibility that void growth models such as the GTN model may be of use for simulating this material; however, an experimental investigation to further understand the void mechanics is necessary before such a recommendation is made. Answers to the following questions are needed in such an investigation:

- What are the conditions associated with the initiation of a measurable concentration of dilute voids?
- How broad or narrow is the strain range where the presence of voids is detectable?
- What is growth rate of voids with continued loading down the same stress path?
- What level of porosity causes the material to exhibit a significantly decreasing tangent modulus?

Experimental answers to these questions would determine if the effect of porosity is important to include in the material model. If so, the void model should finally be tested in a mode similar to the SFC to verify that it is of utility in creating predictions of ductile failure. Additionally, if porosity is found to have a non-negligible effect on the material, its inclusion in modeling may only be important for certain loading histories. What is certain is that more quantitative experimental results are needed to infer successful modeling techniques and that the material considered in this work seems well suited for such experiments.

4.5.3 Failure

Although the COD1 at failure was over predicted, the local state of deformation in the ligaments *BD* and *DE* is quite similar between the simulation and experiment when failure does occur. It is noted that the lower bound strain measurements made just before

failure with DIC are compatible with the failure strain used in the model. Further specification of the actual failure strain and its dependencies is not possible with the current set of experimental observations. Therefore, at the current level of investigation, no deficiency is found with the failure model used. In fact, all of the observed features of cracking in the experiment were correctly predicted. Specifically:

- The crack path was predicted correctly
- The cracking sequence of ligaments was predicted correctly (verified only for slow-rate loading)
- Unstable propagation of initiated cracks was correctly predicted

Predicting the correct crack path is mostly a consequence of the plasticity model being successful enough to correctly predict the location of maximum strain when failure is being approached. Indication of the correct crack sequence should not be given too much weight, as remaining deficiencies in the plasticity model are likely to play a larger role on the sequence than the failure model itself. The best indication that the failure model used is appropriate is that failure was predicted to occur in the correct strain range, and that failure was correctly predicted to cause the sudden and complete loss in load carrying ability of the challenge geometry.

4.6 CONCLUSION

The details of the simulations and experiments performed by the University of Texas team in response to the second Sandia Fracture Challenge are presented in this chapter of the dissertation. An adaptation of the same strategy that was successful in the first challenge was used. Specifically, calibration of a stress-strain curve, Hill 48 yield surface, and Johnson-Cook rate and temperature dependence were performed with the

load elongation data from tensile and shear testing at both loading rates. A strain-to-failure model was used and was calibrated by considering the loading and deformation history of the first element to fail in the simulations of the calibration experiments. These models were used to generate a blind prediction of the challenge specimens. The load elongation behavior of the challenge specimen was accurately predicted for approximately the first 60% of crack opening displacement, but thereafter the prediction departed from the experimental result. The correct crack path and sequence of cracking events were predicted, as well as the occurrence of unstable crack growth. All the scalar measures except the COD1 at fracture were predicted to within 12%, and the presence of unstable fracture was identified. The only feature lacking in the predictions was a limit load for the slow-rate case prior to failure. Additional experiments performed on the challenge specimens included 3D-DIC and microscopy of an interrupted test. The strain field measurements from 3D-DIC revealed that the cause of departure of the prediction from the experiment is due to insufficient information about the plastic behavior of the material. Microscopy revealed that a dilute dispersion of voids occurs in this material prior to unstable crack growth. Attention to improving the methods and experimental data used for plasticity model calibration is seen as the most critical aspect to improving the ability to predict ductile failure.

4.6.1 Recommendation to improve predictive ability

The largest barrier to producing a successful prediction of ductile failure is still that of extracting an accurate model for plasticity from a set of calibration experiments. It is understood that a large experimental program for this purpose is unattractive, so it is suggested that the number of calibration experiments performed in the current work is

maintained, but that each experiment cause the material to deform over a large region of stress space. Such experiments need not have accompanying analytical solutions, as an inverse method for constitutive property extraction is seen as the best means for calibration of model parameters. Finally, the calibration experiments should include full field measurements of the deformation (e.g. from DIC) to supply enough data to properly constrain the inverse problem, and assure that each parameter in the constitutive model has sensitivity to the calibration data set.

Table 4.1: Anisotropic elastic moduli

E_1 (GPa)	E_2 (GPa)	E_3 (GPa)	ν	G (GPa)
112	120	120	0.34	39.7

Table 4.2: Inverse calibration simulation details

	Number of elements	**Degrees of freedom**	**Smallest element size (μm)**	**Elements through thickness**
QS tension	1152	4995	150 × 397	4
QS shear	1902	9108	178 × 57	2
HR tension	8576	45900	100 × 397	4
HR shear	6648	40992	49 × 48	2

Table 4.3: Plasticity model parameters extracted by the inverse method

Flow Curve		**Yield Surface**		**Rate and Temperature Dependence**	
Strain	**Stress (GPa)**				
0.05	1130	F	0.431	m	0.8010
0.10	1186	G	0.379	C	0.0278
0.15	1239	H	0.621	$\dot{\varepsilon}_0$	0.0582
0.30	1327	N	1.901		
0.50	1422				
0.80	1522				
1.30	1563				

Table 4.4: Prediction simulation details

	Number of elements	Degrees of freedom (millions)	Smallest element size (μm)	Elements through thickness
Slow-rate	697382	2.22	29.2 × 46.4	22
Fast-rate	698526	2.96	29.2 × 46.4	22

Table 4.5: Predicted quantities of interest for the challenge geometry subjected to slow and fast rate loading

Slow Rate	Force (N) at COD1 =1mm	Force (N) at COD1 =2mm	Force (N) at COD1 =3mm	Peak Force of Test (N)	COD1@90 % of peak force (mm)	COD2@ 90% of peak force (mm)	COD1 @30% of peak force (mm)	COD2@ 30% of peak force (mm)	Crack Path
Upper Bound	15630	20260	21580	22180	5.128	4.573	5.128	4.573	D-E;B-D;EA
Expected Value	15530	19860	20950	21570	4.628	4.073	4.628	4.073	D-E;B-D;EA
Lower Bound	15430	19460	20320	20950	4.128	3.573	4.128	3.573	D-E;B-D;EA

High Rate	Force (N) at COD1 =1mm	Force (N) at COD1 =2mm	Force (N) at COD1 =3mm	Peak Force of Test (N)	COD1@90 % of peak force (mm)	COD2@ 90% of peak force (mm)	COD1 @30% of peak force (mm)	COD2@ 30% of peak force (mm)	Crack Path
Upper Bound	16000	21060	21700	21720	4.587	4.143	4.587	4.143	B-D-EA
Expected Value	15900	20650	21070	21090	4.087	3.643	4.087	3.643	B-D-EA
Lower Bound	15800	20240	20440	20460	3.587	3.143	3.587	3.143	B-D-EA

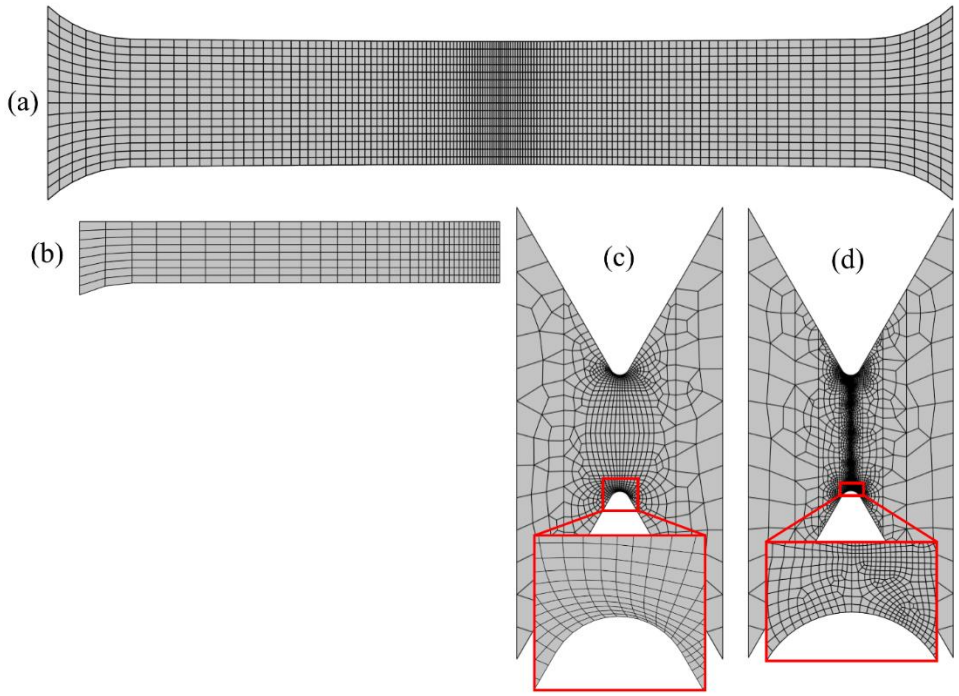

Figure 4.1: The finite element meshes used in the inverse problem to extract constitutive and failure models. (a) Fast-rate tension (b) slow-rate tension, (c) slow-rate shear, (d) fast-rate shear

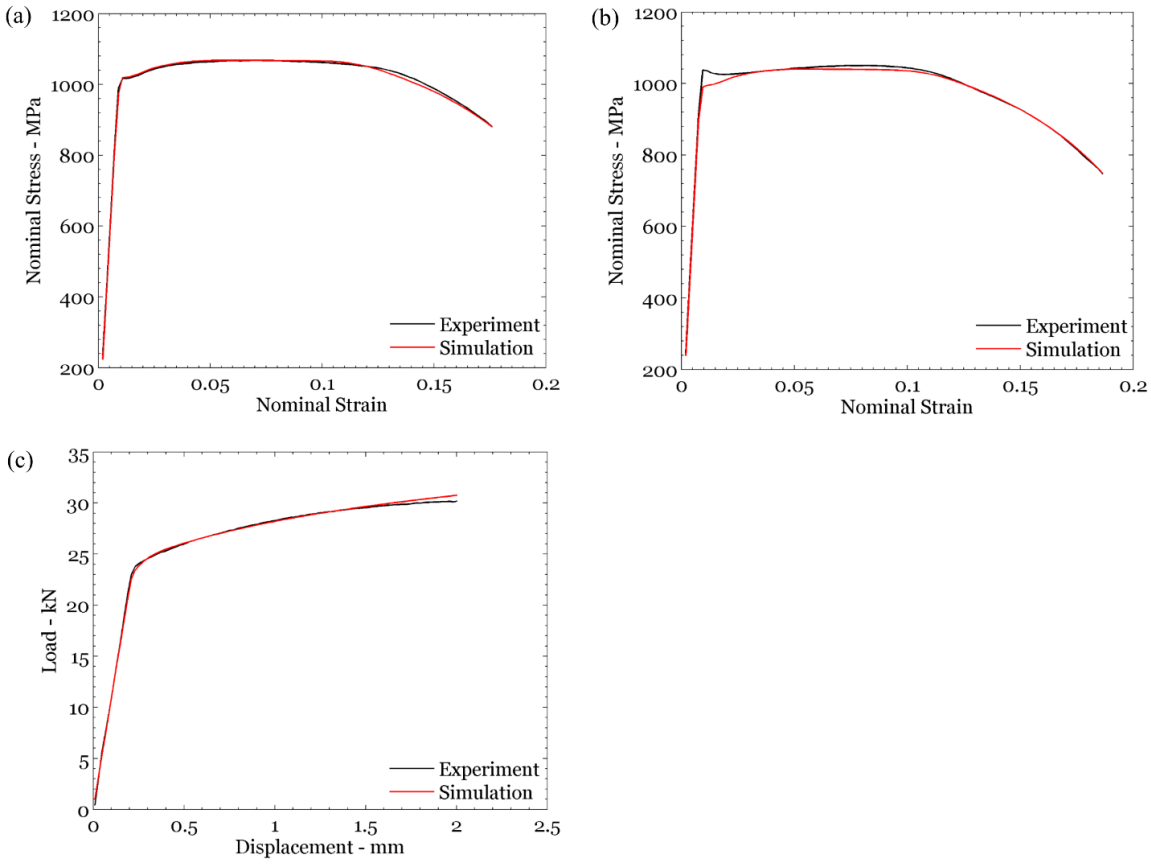

Figure 4.2: Simulated and experimental load elongation curves for the slow-rate calibration experiments. (a) RD tension, (b) TD tension, and (c) VA shear.

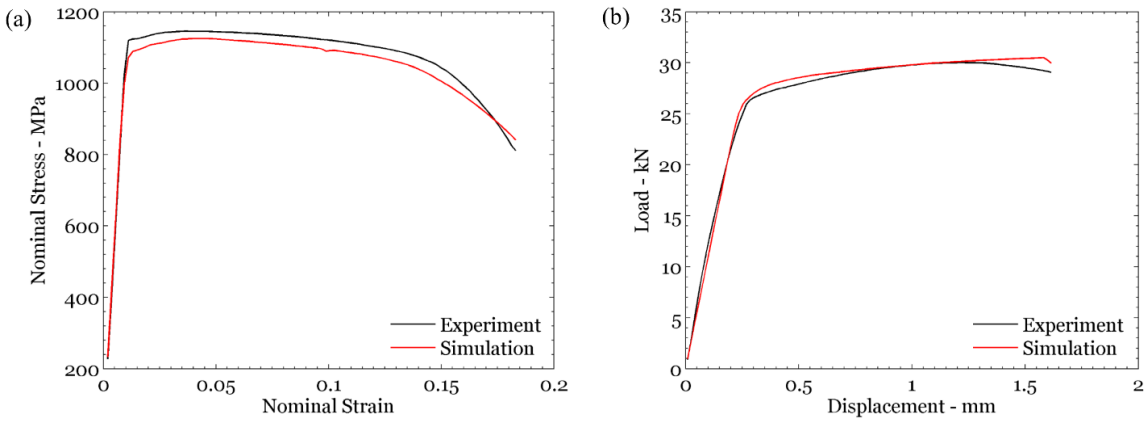

Figure 4.3: Simulated and experimental load elongation curves for the fast-rate calibration experiments. (a) RD tension and (b) VA shear.

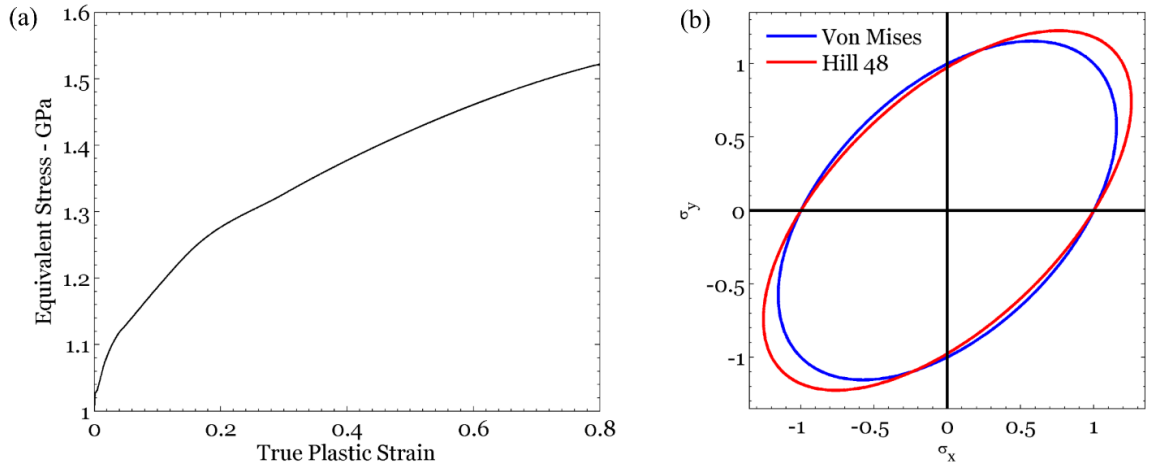

Figure 4.4: (a) The strain hardening behavior extracted by the inverse problem. (b) One projection of the yield surface extracted by the inverse problem, compared with the von Mises surface for reference.

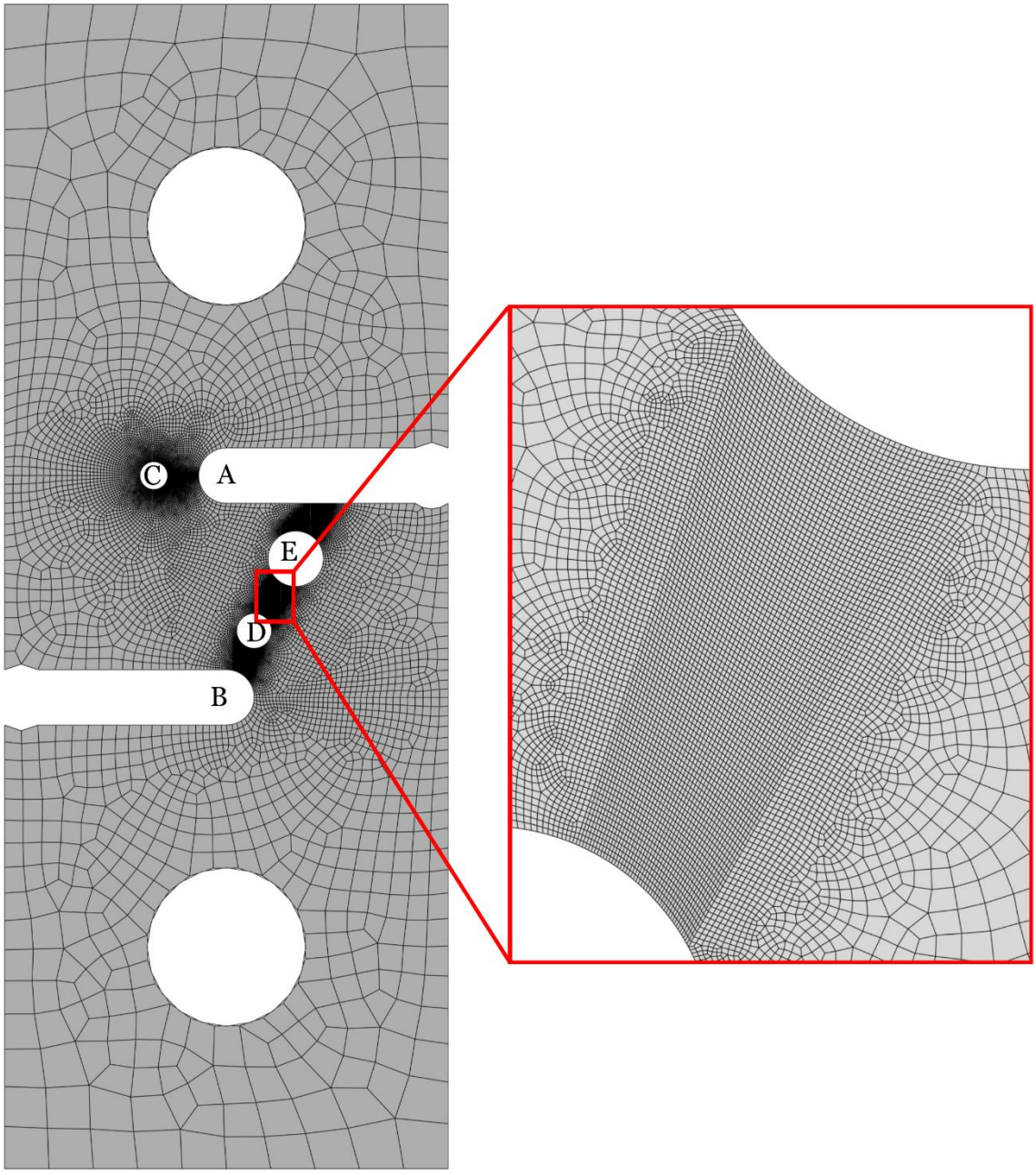

Figure 4.5: Finite element mesh used for the slow-rate challenge geometry prediction

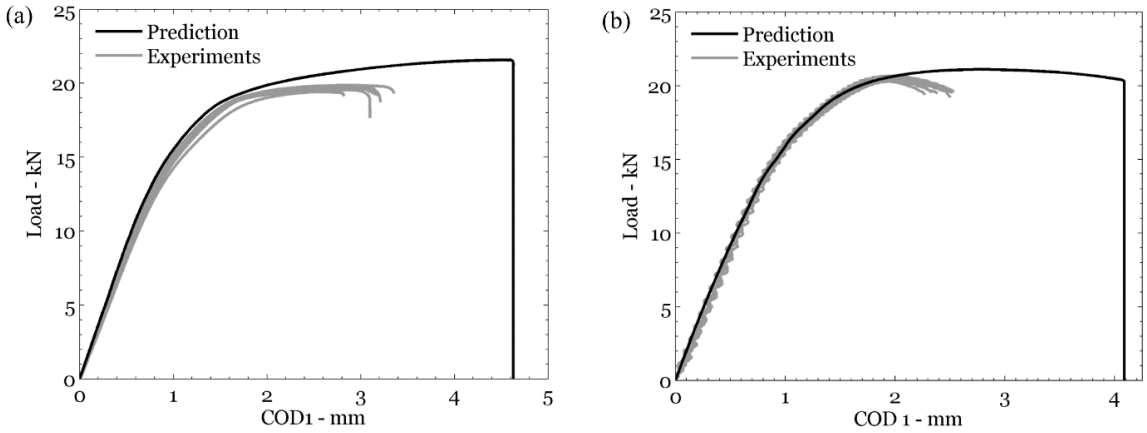

Figure 4.6: Predicted and experimentally observed load-COD1 behavior for (a) slow-rate and (b) fast-rate tests.

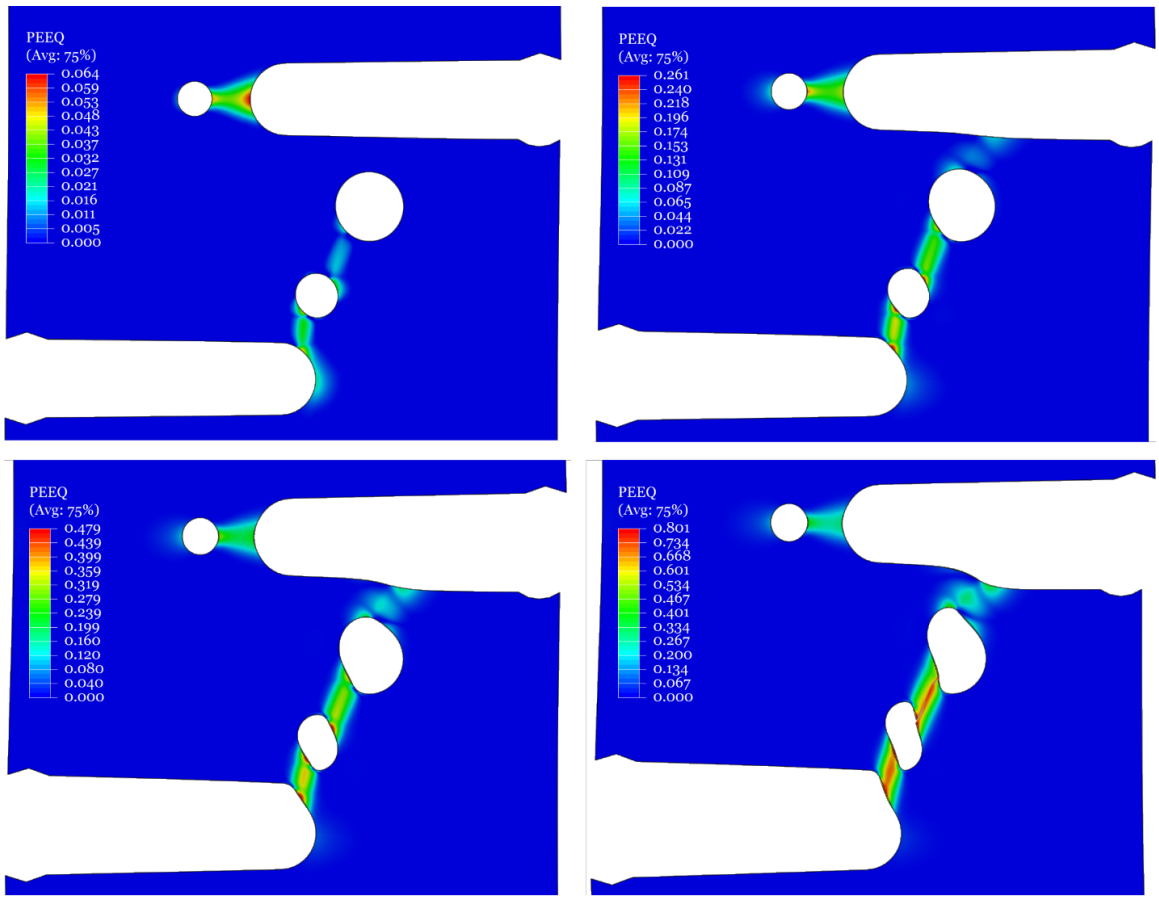

Figure 4.7: Predicted equivalent plastic strain field on the mid-plane of the challenge geometry for the slow-rate at (a) COD1 = 1 mm, (b) COD1 = 2 mm, (c) COD1 = 3 mm, (d) COD1 = 4.63 mm (ligament *BD* is intact, *DE* is severed by a crack)

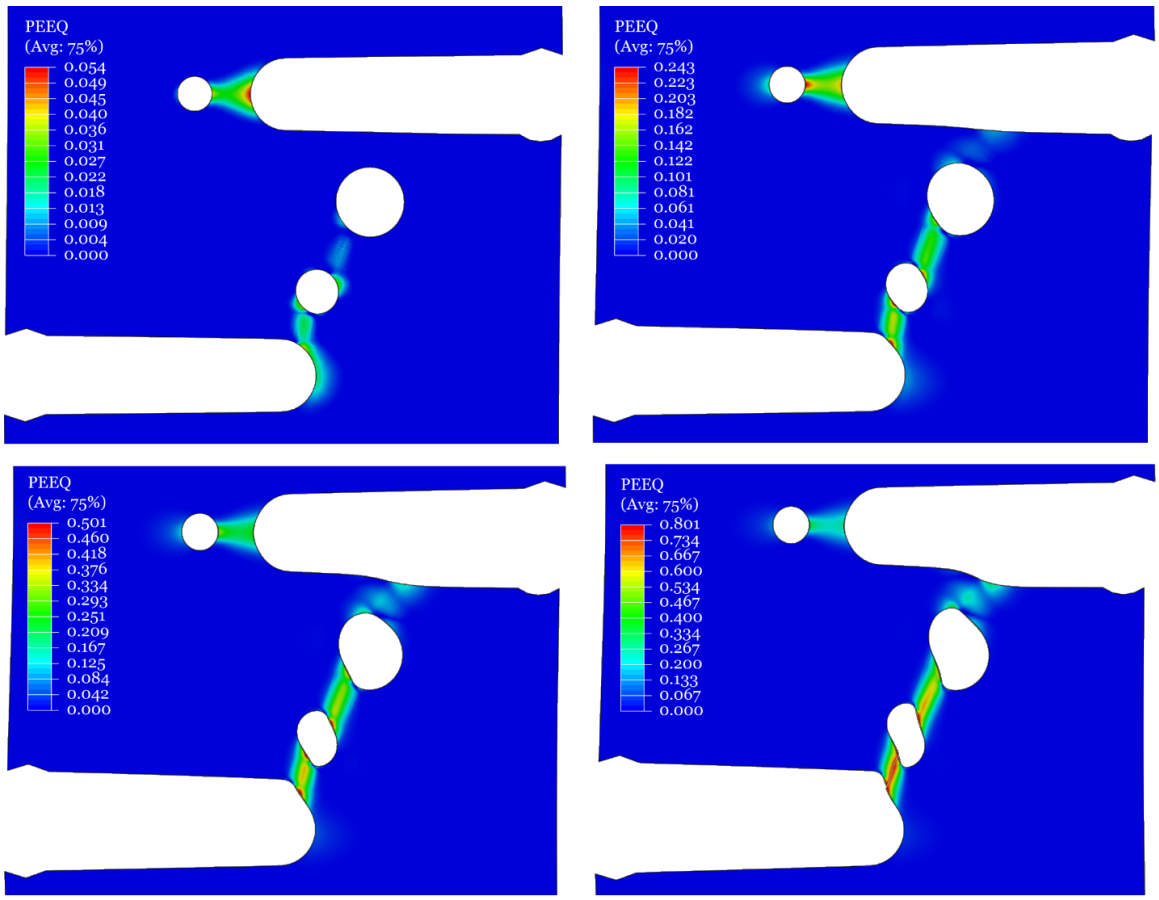

Figure 4.8: Predicted equivalent plastic strain field on the mid-plane of the challenge geometry for the fast-rate at (a) COD1 = 1 mm, (b) COD1 = 2 mm, (c) COD1 = 3 mm, (d) COD1 = 4.09 mm (ligament *DE* is intact, *BD* is severed by a crack)

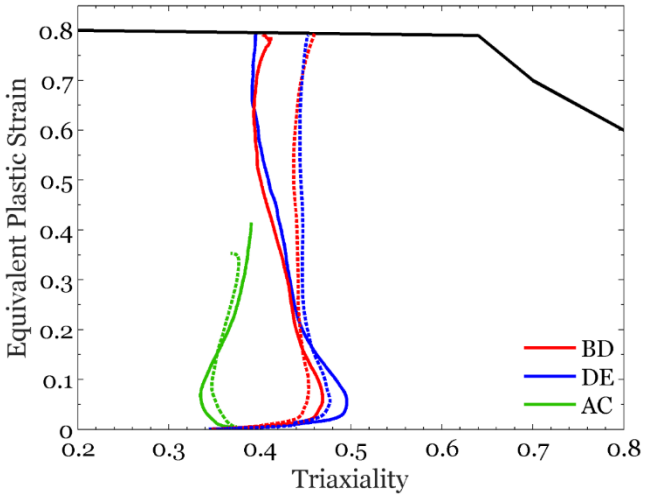

Figure 4.9: Equivalent plastic strain variation with triaxiality for the most critical elements in ligaments *BD*, *DE*, and *AC*. Solid and dashed lines are for the slow- and fast-rates, respectively

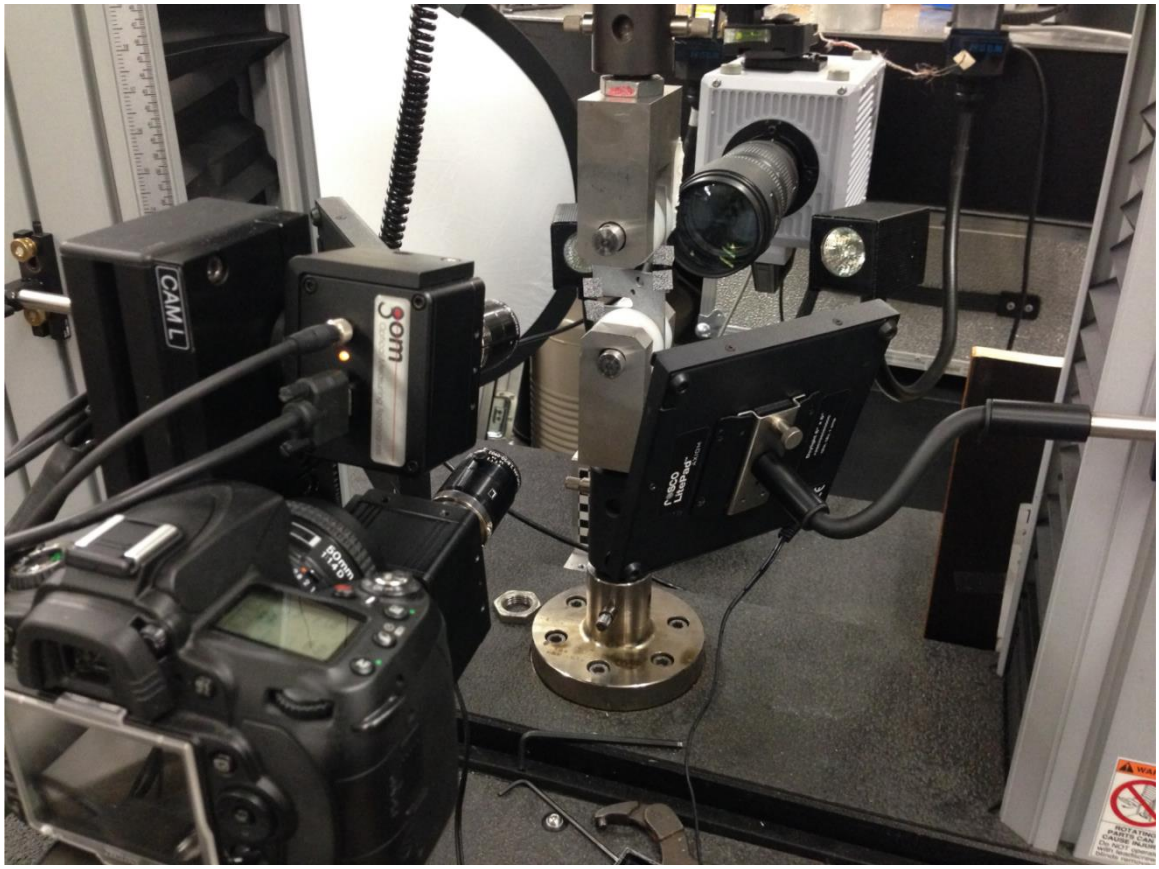

Figure 4.10: Experimental setup showing a challenge specimen mounted in an electromechanical load frame surrounded by four lights and being observed by: a DSLR camera for COD measurements, two CCD cameras for 3D-DIC, and a high speed camera to resolve the crack sequence.

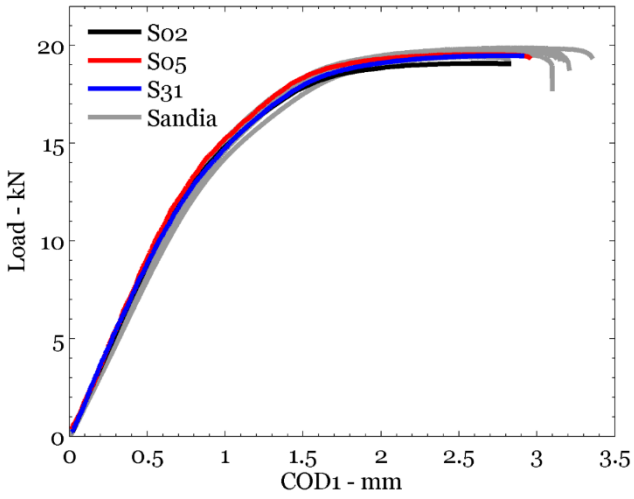

Figure 4.11: Load variation with COD1 compared to the results from SNL

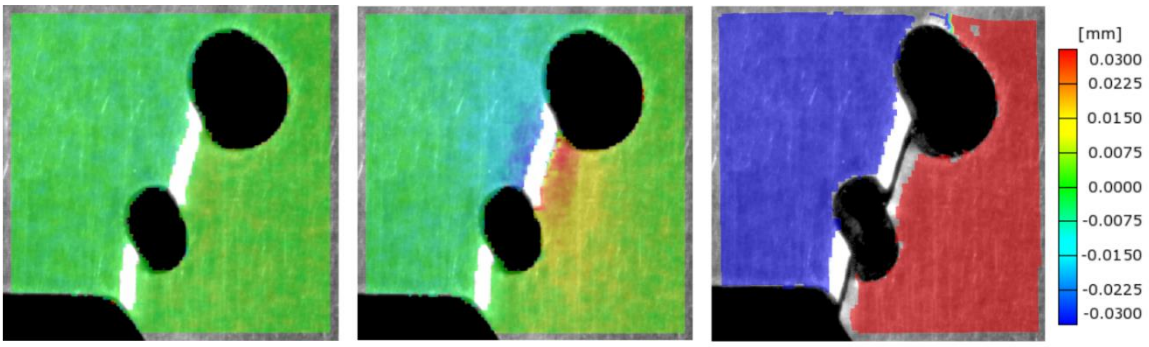

Figure 4.12: Three sequential images from the high speed camera with the DIC displacement field overlaid. Positive displacement is downward. (a) Ligaments *BD* and *DE* intact, (b) ligament *BD* intact with ligament *DE* fully cracked, and (c) both ligaments fully cracked.

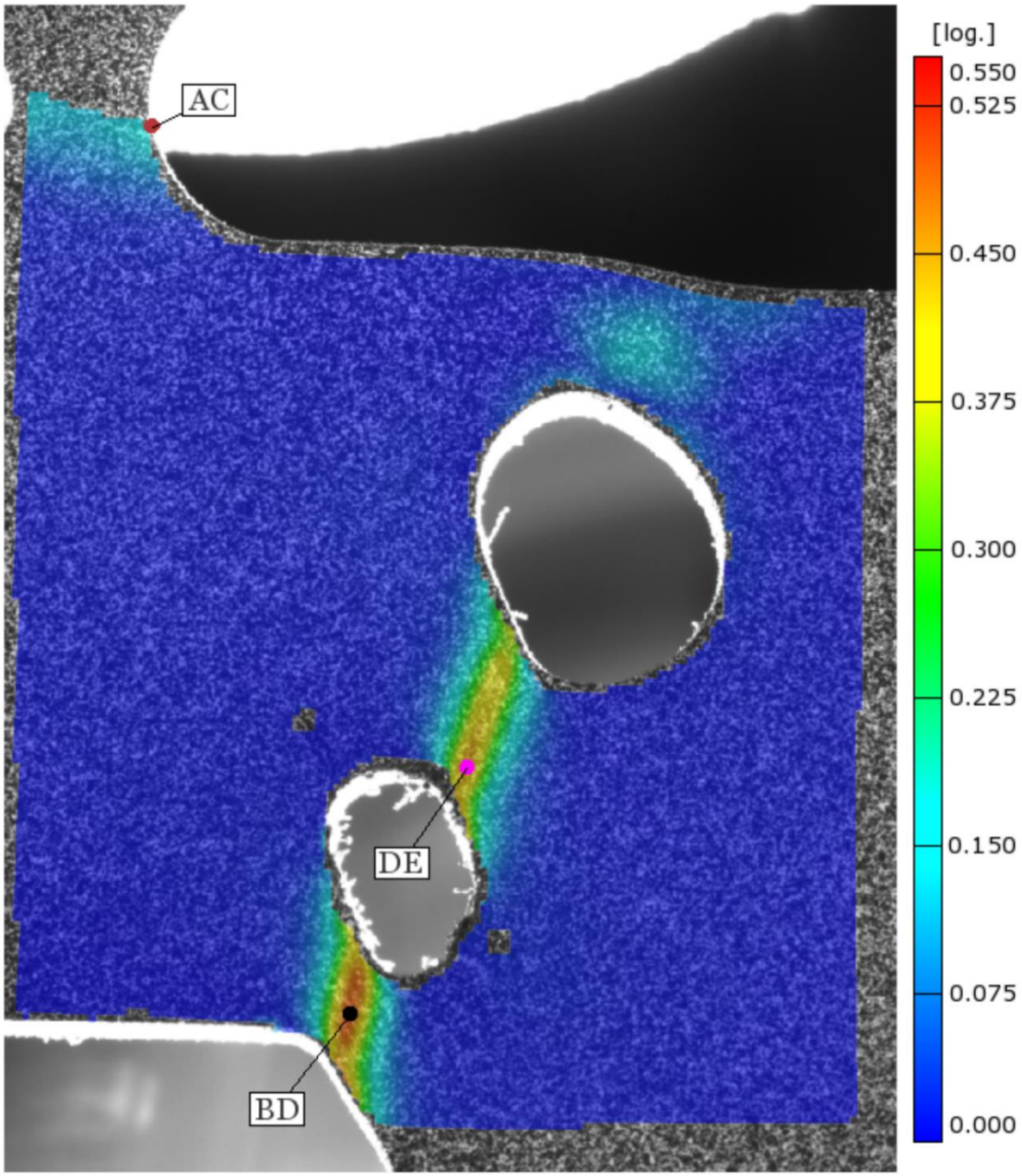

Figure 4.13: Overlay of the principal strain field for sample 13 on the image used for DIC. Data from the three points identified in the ligaments are plotted in Figure 4.14.

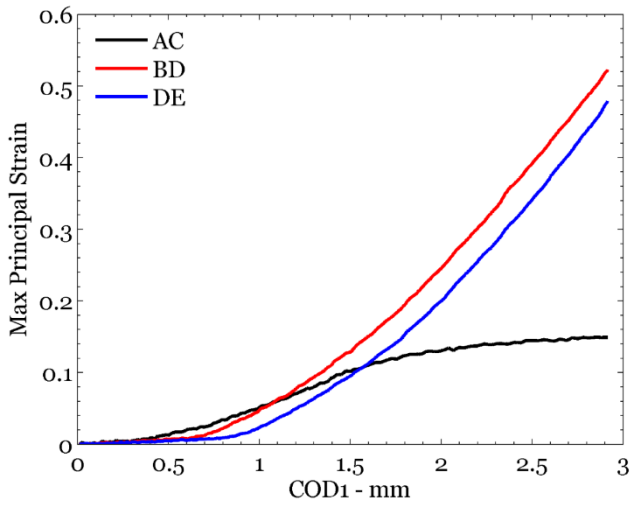

Figure 4.14: Maximum principal strain variation with COD1 for sample 5 at the locations identified in Figure 4.13.

Figure 4.15: Upper side fracture surface of ligament *BD* from sample five. The small dimples visible here are prevalent on the rest of the fracture surface. There is also a region of large dimples adjacent to an area that has been scraped by the opposing fracture surface to become nearly featureless. This pair of features appears at a modicum of other locations.

Figure 4.16: Region of the lower side fracture surface of ligament *BD* from sample five that directly opposes the region shown in Figure 4.15. The large dimples correspond to those visible in Figure 4.15.

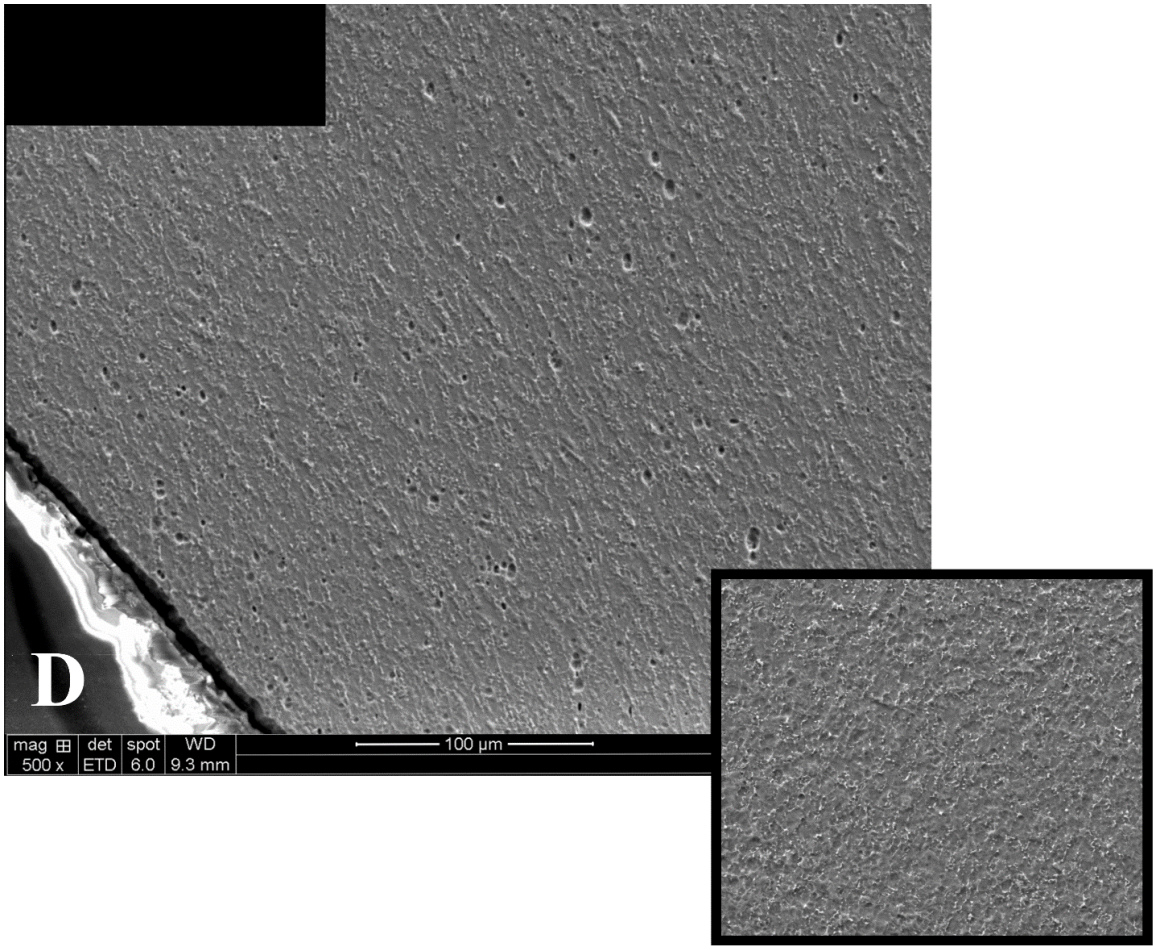

Figure 4.17a: Observation of voids on the mid-plane near the surface of hole *D* from an interrupted test. Inlay shows the unstrained appearance of the surface at the same magnification.

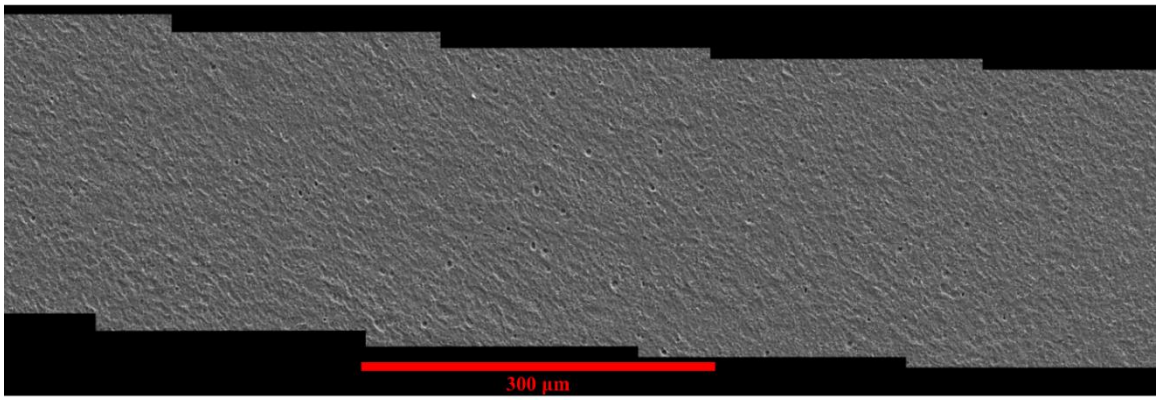

Figure 4.17b: Observation of voids on the mid-plane in the ligament *BD*.

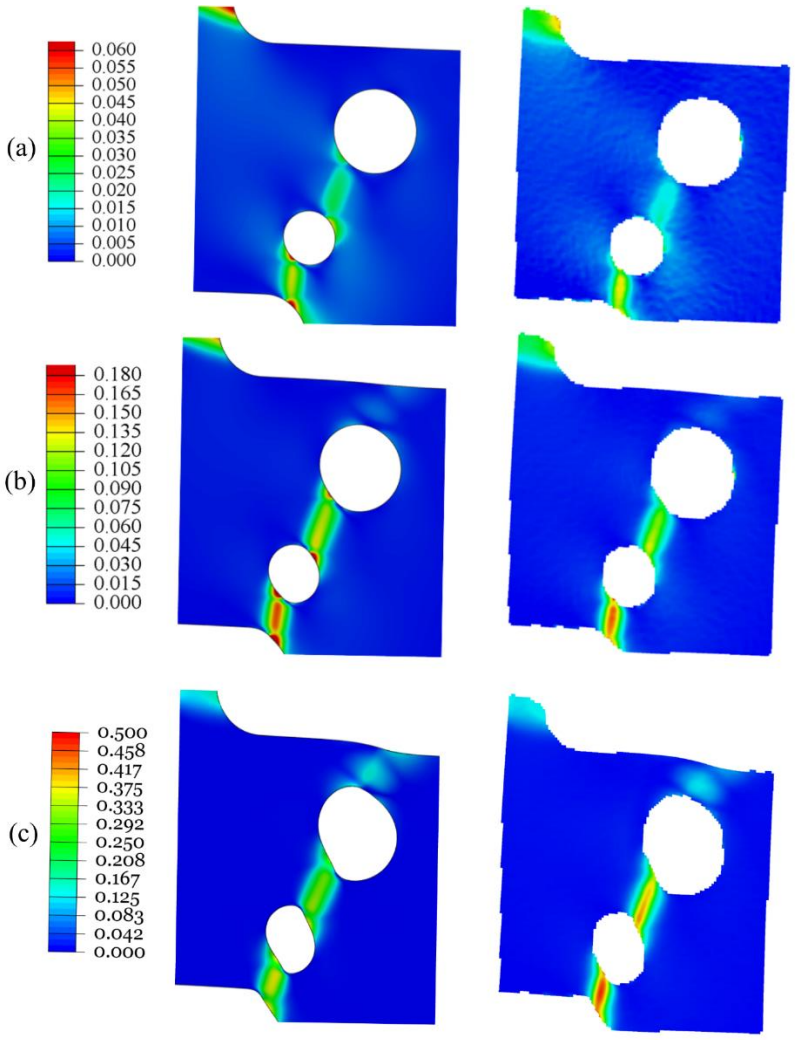

Figure 4.18: Comparison of the first principal strain fields for the prediction (first column) and those measured with 3D-DIC at (a) COD1 = 1 mm, (b) COD1 = 1.75 mm, and (c) COD1 = 2.0 mm

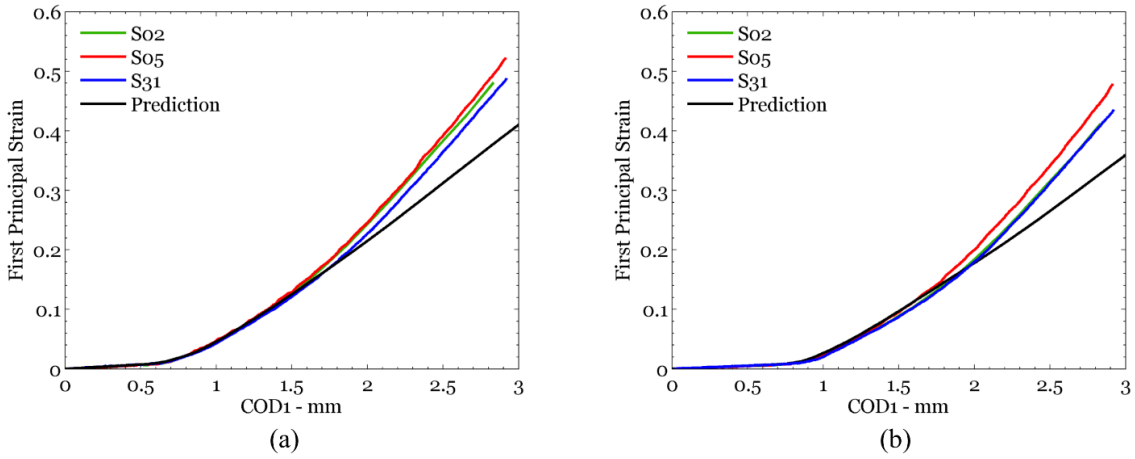

Figure 4.19: Comparison of the maximum principal strain development between the prediction and experimental DIC measurements for ligaments (a) *BD* and (b) *DE*.

Chapter 5: Extraction of Elastic-Plastic Constitutive Properties from Three-Dimensional Deformation Measurements

5.1 INTRODUCTION

The effort to characterize the mechanical behavior of materials is an ongoing scientific pursuit with deep roots. For most of its history, this effort has been geared toward the development of test methodologies that provide simple, inexpensive, and yet reliable characterization of material properties. This has resulted in a number of standardized tests, such as those developed by ASTM, ISO, and other standardization organizations around the world. For the characterization of the constitutive response of materials, these methods are typically based on establishing a known state of deformation and measuring the force required to impose such deformation. The simplest example of this is the standard tensile test in which a prismatic specimen of length L and cross sectional area A is pulled along its length in a testing machine, ensuring a uniform state of stress and strain within a middle region of the specimen. The elongation over a selected "gage length" of the specimen as well as the force applied at the end grips of the specimen are measured; in some cases, the changes in cross-sectional dimensions are also monitored. Since the material in the gage length is subjected to homogeneous deformation, the global measurements of force and elongation of the specimen are readily converted to the stress-strain behavior of the material under test. While this approach works quite well during the early stages of deformation – and forms the backbone of engineering characterization of elastic and elastic-plastic properties for most materials – it is limited in its ability to provide appropriate characterization of the material behavior at very large deformations because of the inability of most test configurations to sustain

homogeneous deformations at all strain levels and stress states; material instabilities (Lüder's bands) and structural instabilities (such as diffuse necking at the Considère point) intervene even in the case of the simple tensile test and localize the deformation over smaller regions of the specimen. The use of measurements of the changes in cross-sectional dimensions and the Bridgman correction for the stress concentrating effect of a diffuse neck are early examples of efforts to account for the nonuniformity of the deformation field. However, they only account for nonuniformity in an average sense. Since further deformation accumulates only within these localized regions, the resulting inhomogeneity of the deformation and stress fields renders the global measurements irrelevant in the *direct identification* of the material constitutive model beyond the onset of such localization. Hence, interpretation of the global response of the specimen in terms of the local material constitutive model requires an inverse analysis. Inverse methods based on optimization techniques that seek to minimize differences between the measured global response and numerically simulated response have been developed and used in recent years. In the present work, we provide an enhancement to this method.

In spite of the long history of mechanical testing, the use of inverse methods for material property identification is a rather recent development. The reasons for the recent spurt of activities in this area are two-fold. First, techniques for efficient and accurate numerical simulation of the nonlinear problem associated with the experiments (see for example, Chen, 1971, Needleman, 1972), and the computational power to exploit such methods have developed significantly in the last two decades. Second, techniques for the accurate experimental determination of the kinematic field over large domains of the specimen have recently advanced significantly with the development of digital image correlation and the associated high-resolution full-field imaging techniques. This allows for the extraction of the material properties through an optimization process that

compares full-field measurements of the deformations with numerical simulations. An early example of this effort is the work of Norris et al (1978) who performed a simulation of the axisymmetric deformation of a tensile specimen with round cross-section and through an iterative process obtained the flow stress-strain curve for an A533-B nuclear pressure vessel steel; they showed that the difference between this curve and one obtained by using a Bridgman correction (together with the measured necking cross-sectional dimensions) was about 10% at a strain level of 100%.

A proper optimization formulation, in which the deviation between the experimental measurements and numerical simulations is used to generate an objective function that is minimized to determine the material parameters, has been investigated by Mahnken and Stein, (1994, 1996), Gelin and Ghouati (1995) and Ghouati and Gelin (1998), Meuwissen et al. (1998), Kajberg and Lindkvist (2004), Coorman et al. (2008) and many others in recent years. Mahnken and Stein (1996) discuss the inverse problem (IP) in terms of an objective function that compares experimental and simulated displacements at selected points in the nonuniform deformation field of an arbitrary specimen; this was implemented within the framework of the infinitesimal strain formulation. As an example, they determine the material properties from a compact-tension fracture test geometry. The displacements near the tip of a compact-tension fracture specimen in a Baustahl St52 were determined using a grid method and then compared with numerical simulations obtained from a finite element simulation. They demonstrated that the elastic-plastic material properties could be extracted through such inverse identification schemes. Gelin and Ghouati (1995) formulated a similar optimization problem, with an objective function that was nearly identical to that of Mahnken and Stein (1996) – based on the difference between the experimentally measured and numerically calculated displacements at selected points; this scheme was

used to determine the material properties of a 3014 aluminum alloy from a plane-strain compression test. Ghouati and Gelin (1998) used the same procedure to calibrate a Voce model for aluminum alloy sheet material, including Hill anisotropy; in one example, these authors use a comparison of a punch load vs displacement measurement from a deep punching experiment to perform the material property extraction. More recently, Kajberg and Lindkvist (2004) used a similar approach; two different hot-rolled steels were examined. The in-plane displacements (and strains) were determined through a two-dimensional image correlation method. The objective function used in the optimization procedure accounted for the two in-plane components of displacements, the equivalent plastic strain as well as the global loading on the specimen. They demonstrated the fitting of a piecewise linear or a power-law model using the optimization procedure. Cooreman et al. (2008) explored identification of the elastic plastic material response with a cruciform specimen with a central hole to generate a complex stress/strain state; the surface strains were measured with a three-dimensional image correlation technique and then used in an optimization routine where the objective function was based on the individual strain components in the plane of the sheet; they were able to calibrate the Hill anisotropic plastic model, together with a Swift type power-law model of the hardening behavior.

Many of the articles discussed above also discuss the limitations of this inverse approach, driven by the errors in the experimental data, errors in the models, and the sensitivity of the optimization techniques themselves. The examples discussed above clearly indicate the power of the inverse method in the identification of material properties to strain levels at which continued homogeneous deformations are unsustainable. With the commercial developments in the area of digital image correlation techniques for displacement measurements, the availability of high-fidelity experimental

measurements has increased significantly in recent years, and a corresponding increase is seen in the application of these measurements in such inverse methods as applied to the determination of the constitutive properties of materials. A review article by Avril et al (2008) discusses applications of such inverse methods, but with a focus on the determination of elastic properties. Here we present an application of the inverse method to extract the anisotropic material properties of a ductile structural metallic alloy deformed to very large strain levels.

5.2 INVERSE PROBLEM IN MATERIAL PROPERTY CHARACTERIZATION

Consider a specimen with arbitrary geometry Ω as illustrated in Figure 5.1. The external forces $\mathbf{F}^e$ are applied on a subset $\partial\Omega_t$ during the experiment and displacement constraints, if any, are applied on $\partial\Omega_u$. In typical standardized experiments the only measured quantities are the applied external force $\mathbf{F}^e$, the displacement $\mathbf{\Delta}^e$ corresponding to this force application region, and one internal displacement δ^e measured in the specimen's gage section. $\mathbf{F}^e$ and δ^e can be normalized to provide the material behavior during states of homogenous deformation (presuming such a state is realized) and global structural response when deformation is heterogeneous. In order to gather additional relevant information about the material behavior after the deformation becomes heterogeneous, further measurements are essential. We will restrict[3] attention to measurements on parts of the surface of the specimen $\partial\Omega_v \subset \partial\Omega_t$ that is a subset of the traction boundary; specifically, for the optical measurements that we have in mind, this is

[3] This restriction arises from the desire to use measurements in the wavelengths at which the specimen is opaque; in principle, the use of x-ray tomography (Babout et al. 2001), laminography (Helfen et al. 2013), and other tools could provide information on the interior, but such methods are still, under development, limited to identifying damage, experimentally expensive and await further development.

a portion of the traction boundary that is free from obstructions for visual observation and measurements. By necessity, these measurements are kinematic, yielding the displacements $\mathbf{u}(\mathbf{x})$ for $\mathbf{x} \in \partial\Omega_v$. It is the addition of these displacement measurements that enriches the experimental data set and thus enhances the quality of constitutive model that can be extracted from it.

Corresponding to any such experiment there is an associated boundary value problem (BVP) of the following form that needs to be solved:

$$\begin{aligned} &\nabla \cdot \boldsymbol{\sigma}(\mathbf{x}) = 0 \qquad \forall \mathbf{x} \in \Omega \\ &\mathbf{u}(\mathbf{x}) = \mathbf{u}^*(\mathbf{x}) \quad \forall \mathbf{x} \in \partial\Omega_u \\ &\mathbf{t}(\mathbf{x}) = \boldsymbol{\sigma}(\mathbf{x})\mathbf{n} = \mathbf{t}^*(\mathbf{x}) \quad \forall \mathbf{x} \in \partial\Omega_t \end{aligned} \tag{5.1}$$

where $\boldsymbol{\sigma}(\mathbf{x})$ is the Cauchy stress tensor, $\mathbf{n}$ is the unit outward normal, and $\mathbf{u}^*(\mathbf{x})$ and $\mathbf{t}^*(\mathbf{x})$ are prescribed functions. In order to solve this BVP a material model must be specified relating the strains to the stresses; this material model could be of any type – elastic, inelastic, time-dependent, damaging or evolving, strain-rate dependent, etc. Although there is great flexibility in what material model can be used, identification of the appropriate form of the constitutive model is an extremely important task that must be based on the characteristics of the observed data and the underlying physics. For the present purpose, we will simply indicate that the constitutive model will be parameterized by the set $\mathbf{d} = \{d_1 = E, d_2 = \nu, d_3, d_4, \cdots d_N\}$ representing the set of N material parameters. If the parameters $\mathbf{d}$ contained in the material model are known *a priori*, then the forward solution of the BVP can be calculated to determine the state of the specimen under the applied boundary conditions. However, if material characterization is the problem of interest, the parameters $\mathbf{d}$ in the material model are then unknown and instead, certain aspects (usually, kinematic) of the specimen's state are measured during the course of the

experiment as described above. This presents the opportunity to set up an IP where the solution is no longer the state of the specimen, but rather the values of the parameters that define the constitutive model. The goal of solving the IP is to find the optimal values for each parameter of the constitutive model employed. Optimality, of course, is defined in the sense of minimizing an objective function whose aim is to represent the deviation between the experiment and simulation in some quantitative manner. The choice of constitutive parameters that minimizes the objective function is recognized as the best choice of parameters for the selected constitutive model. This does not guarantee that the constitutive model selected is the optimal choice for the material; just that the one selected is tuned to its optimal configuration for the given problem, for the given data, under the selected objective function.

The optimal configuration of the selected material model is the solution to the IP. In order to find the optimal configuration, this BVP is solved using *trial* constitutive properties, and the results are compared against the experimental measurements. Differences between the solution of the BVP and the experimental observations are penalized. This process is repeated while changing the trial constitutive properties until satisfactory agreement is found between the experiment and solution to the BVP. The details of the process allow for a diversity of approaches to solve the IP, where neither the solution nor the method to obtaining it is unique. Specifically, there are ample choices in selecting the objective function, constitutive model, method of solving the BVP, and optimization scheme used for parameter selection. Each choice will alter the final solution to the IP, but the former choice is most central to the solution to the IP, while each latter choice is less intertwined with the solution of the IP. This work does not focus on the details for selecting the best objective function, constitutive model, etc., but rather

on establishing the perspective that the IP can be used as a method to guide the collection of experimental data and then put it to use in the most efficient manner.

In order for the IP to guide the material characterization process, first it must be decided what constitutive information is being sought by solving the IP (e.g. in this work both the stress-strain behavior of the material and information about the material's anisotropy are to be probed). Then feasible experimental measurements that are relevant to the desired constitutive properties can be determined, to be used later in the objective function for the IP. It has been shown by works such as those by Tardif and Kyriakides (2012) and Gross and Ravi-Chandar (2014) that the global structural response is relevant to the constitutive information being extracted in this work. However, these past works also show that while matching the global structural response is necessary, it is not sufficient to capture the material constitutive properties fully; as discrepancies have been found between experiments and simulation when the IP uses the global response exclusively as a basis for parameter identification. In fact, it is quite intuitive that very similar global responses can be formed from different local fields; simply stated, optimization based on global structural response is under-constrained. Thus, it is proposed that matching the local deformation fields in addition to the global structural response will result in additional constraints and thereby enable better characterization of the material behavior. The local deformation field is selected to evaluate the fitness of any candidate set of parameters for the selected material model not only because error in this field has already been observed, but also because the full field surface deformation can be obtained easily and inexpensively through the use of digital image correlation (DIC).

It should be emphasized that the value of the local displacement measurements are highest during processes of inhomogeneous deformation. Such deformations provide

the most economical path toward comprehensive constitutive characterization because numerous stress-states can be sampled in a few test configurations, thus lowering the cost of an experimental program. However, the impression should not be taken that this approach is a replacement for experimental results; rather, it is a systematic method to maximize and use every relevant piece of experimental data. Then, due to the increased efficiency of each experiment, a lesser quantity of experiments is necessary to collect the same amount, if not even more information about the material behavior. The exact formulation of the IP will be discussed in Section 5.6 after describing the experimental program.

5.3 EXPERIMENT

The material used in this work is 15-5 precipitation hardened stainless steel taken from a nominally 3.175 mm thick sheet produced by AK Steel (West Chester, Ohio). Dog-bone shaped tensile test specimens were fabricated using wire EDM and were subsequently heat treated to the H-1075 condition[4]. The dimensions are shown in Figure 5.2. The cross section of the specimen was chosen to be square so as to minimize the influence of geometric asymmetries on the deformation. This feature is essential, as it allows for a near optimal observation of the anisotropic mechanical behavior of the plate without geometrically constraining the strain development. While a circular cross section is the optimal geometry for such an observation in the sense that natural anisotropy will be revealed through the tests, the fabrication of such a specimen from a thin sheet is far more labor intensive and potentially fraught with errors arising from the machining process. Regardless, the goal here is clear; the tensile test that provides the most insight

[4] The authors would like to thank Dr. B.L. Boyce of Sandia National labs for performing the heat treatment.

into the material properties is performed in preference to conventional tests that further convolute this information into the structural response. Once the best possible characterization of the material is performed, this information can be used with the greatest level of success in any structural configuration.

The tension test was performed at a quasi-static nominal strain rate of 2×10^{-4} s^{-1} in an electromechanical load frame (Instron Model 5582). The flared ends of the specimen were gripped in self-tightening mechanical wedge grips. The tensile direction is parallel to the rolling direction of the sheet. The gauge section of the specimen is cut with a small curvature so that there is a gradual reduction of cross sectional area going from the shoulders of the specimen to the center[5]. The center cross section is reduced by about 0.8% from the cross section near the shoulder. This geometry provides an imperfection that does not cause any sharp gradients, and is also simple to model in the BVP. The applied load was monitored with a load cell with a range of 100 kN and a resolution of 4.8 N. According to the manufacturer specifications, the uncertainty in load is 28 N. In addition to the measurement of the cross-head motion, the strain over a one inch gauge length was measured with an extensometer belonging to the ISO 9513 0.5 classification. While these are the typical global measurements obtained in most tensile tests, here a 3D-DIC scheme was used to provide additional displacement and strain measurements. A stereo imaging system was positioned such that two adjacent surfaces of the specimen were visible to each camera, providing surface measurements on one face that lies in the plane of the sheet, and another that spans the thickness of the sheet (hereafter referred to as the front and side surfaces, respectively), as indicated schematically in Figure 5.2 by the shaded regions. An ARAMIS 3D-DIC system was used in obtaining the images;

[5] Similar specimens have been used by other researchers: see Tardiff and Kyriakides, (2012) and Boyce et al. (2014) for recent examples of such use.

pictures with a frame size of 1624 by 1236 pixels and a resolution of 12.3 μm/pixel were obtained at specified time increments and synchronized with the corresponding global measurements of the load, cross-head displacement, and gage strain. These images were processed using the ARAMIS 3D-DIC software with a sub-image size of 20 by 20 pixels and a step of 5 pixels to obtain the deformation over the field of interest with an uncertainty of 1 μm, and strains to within 2000 με over a 125 μm gauge length. Deformation history is tracked at over 12000 points, with a spatial resolution of 63 μm between observations. In addition, the average strain over a 20 mm gage length was estimated from the DIC measurements and used instead of the mechanical extensometer measurements. While DIC has been used in recent years (for example, in 2D by Kajberg and Lindkvist, 2004, and in 3D by Coorman et al. 2008), the key innovation introduced in the measurement presented here over those in the literature is that the 3D deformation data are acquired simultaneously over two planes that were initially orthogonal to each other, aligned along directions of rolling symmetry. This additional surface data permits a partial evaluation of the plastic anisotropy in the material.

Figure 5.3 shows the global response of the tensile specimen plotted as the variation of the nominal stress vs the gage strain and exhibits features that are typically observed in tension tests. The initial elastic response is followed by a sharp knee as the specimen yields; the early portion of the plastic response developed a very small load drop after a nominal strain of about 0.9%, indicative of a possible instability, but was quickly followed by a hardening response until a nominal strain of 7.6%. This corresponds to the Considère strain for this material, and indicates the onset of necking. The nominal stress begins to drop beyond this point as the neck continues to grow and eventual failure of the specimen occurred at a nominal strain of 17%. The modulus of elasticity was calculated from the initial elastic response to be 196 GPa, and the 0.2%

offset yield stress was determined to be 1.1 GPa. The nonuniformity of the strain field was revealed clearly through the 3D-DIC images and is explored further here. Contour plots of the maximum true (logarithmic) principal strain field $\varepsilon_1(\mathbf{x})$ on the front and side surfaces are shown in Figure 5.4, corresponding to selected nominal strain levels indicated in Figure 5.3. Similar data are available for the strain field $\varepsilon_2(\mathbf{x})$ on the front surface and $\varepsilon_3(\mathbf{x})$ on the side surface, but are not shown for the sake of brevity. As can be seen from these images, the strain field develops heterogeneously in the specimen, right after the onset of yielding, but this is quite a mild heterogeneity. The local load maximum at a nominal strain level of $\varepsilon_1 \sim 0.0093$ does not seem to be related to Lüder's bands, as can be inferred from the diffuse development of the strain between both ends of the specimen; this nonuniformity is likely due to imperfections in the specimen dimensions, alignment of the specimen or other geometric features. Presumably, the initiation site of this heterogeneity lies close to the stress concentration located near the specimen's shoulder or where one of the extensometer clips is located, but these locations were outside the camera's field of view, and thus the nucleation of heterogeneity could not be identified. The heterogeneous strain field persists until necking begins, consequently the strain field never returns to a homogeneous state after the elastic regime. The neck occurs within the field of view of the cameras and occurs approximately 8 mm away from the point of minimum cross section, likely due to the presence of a machining or material defect at this location. The nucleation point of the neck does not coincide with the nucleation point of the heterogeneity that directly followed the elastic regime. Beyond the Considère strain, the development of large deformations inside the neck is clearly identified by the 3D-DIC measurements; the peak strains approaching unity are observed at the deepest point in the necked region. The data set corresponding to the displacement and strain fields on the front and side surfaces of

the specimen at numerous nominal strain increments in the plastic region constitutes the primary additional information that is to be used in the optimization scheme for the identification of material response; this is developed further in the next section. However, the kinematic data are already rich enough to provide additional insight into the material behavior as indicated below.

A direct analysis of the experimental results shows evidence of the material anisotropy. Figure 5.5a shows a contour map of the maximum true (logarithmic) principal strain field $\varepsilon_1(\mathbf{x})$ just prior to rupture in the region of the neck. Note that a logarithmic strain of nearly one has been measured at the center of the neck at this stage. The small black and red dots indicate locations along the midline of each surface; the variations of longitudinal and transverse strains along these lines are plotted in Figure 5.5b at seven different states throughout the test. It can be observed that the spatial variation of longitudinal strain $\varepsilon_{11}(x)$ is nearly identical on both surfaces of the specimen for the entire duration of the test while more transverse strain $\varepsilon_{33}(x)$ accumulates on the side surface than the transverse strain $\varepsilon_{22}(x)$ on the front surface. This is not only a clear evidence of the anisotropy of the plastic response, but also a direct quantitative measurement of this anisotropy.

The stress state on the surface of the specimen, in the deepest part of the neck (identified by the two large black dots in Figure 5.5a) is approximately in uniaxial tension throughout the entirety of the test. Therefore, results from these points can provide information about a uniaxial stress state up to high levels of strain (approaching a logarithmic strain of 1.0). Figure 5.6 shows a slightly nonlinear variation that is observed by plotting the transverse strains at the deepest part of the neck on both the front and side surfaces against the longitudinal strains at the same location. The nonlinearity is clear evidence of evolving plastic anisotropy of the material under these loading conditions.

Significant texture changes must occur at this location during the test, as grains become highly elongated in the direction of the applied load. However, it appears that this texture change does not greatly influence the ratio of transverse strains; a plot of the transverse strains ε_{22} vs ε_{33} at the deepest point of the neck is found to be nearly linear as shown in Figure 5.7. The slope of the best fit line provides one of Lankford's parameters: $d\varepsilon_{22}/d\varepsilon_{33} = 0.895$ even to levels of strain beyond which the parameter is typically investigated. But performing the same linear fit to strain data averaged over the entire surface prior to necking, or even for the same two points from Figure 5.7 prior to necking, gives Lankford's parameter to be 0.958 and 0.940 respectively. The differences between these measurements could be caused from the state of stress at the deepest part of the neck being only approximately uniaxial, the heterogeneous deformation prior to necking, or because Lankford's parameter evolves with deformation. In order to explore this behavior further, additional, higher resolution measurements are necessary. Aleksandrovic et al. (2009) performed such measurements with contact methods (limiting the investigation to pre-necking strain levels) and found that Lankford's parameter evolves, even at small levels of strain. Such a resolution has not been pursued in the current work, as the goal here is to characterize anisotropy indirectly and up to large strain levels. The information gathered from DIC provides a useful range in which to search for the Lankford parameter, which will be treated as a constant to simplify the modeling effort in the IP. If the perspective that Lankford's parameter is well described as a constant is taken, then it can be concluded that the retexturing of the material from a uniaxial stress path causes changes to the plastic anisotropy that are near to being transversely symmetric.

5.4 MATERIAL MODEL

Implementation of the inverse method for identification of the material response requires the specification of an appropriate constitutive model, with the goal of the inverse problem being the estimation of the optimal set of parameters for the selected constitutive model. Because the optimization process will provide the best-fit parameters for *any* constitutive model, the selection of an appropriate constitutive model requires knowledge of the specific material, its deformation mechanisms, and the appropriate constitutive framework in which the material is to be modeled. For the case of ductile metals, we note that some authors have used a strain-softening model, such as the Gurson-Tvergaard-Needleman model, to capture the load drop that occurs beyond the Considère strain under uniaxial loading conditions in ductile materials (see for example Fratini et al, 1996; Bernauer and Brocks, 2002). However, the necking deformation that occurs at the Considère strain is a structural instability that appears even in the absence of material softening; micrographic examination of the material in the vicinity of the neck obtained from interrupted tests as well as the failed specimens provide sufficient evidence of the absence of damage in the necked region to equivalent true plastic strain levels of around unity (see for example Tardif and Kyriakides, 2012; Ghahremaninezhad and Ravi-Chandar, 2012). Therefore, in this work, we model the elastic-plastic deformation of the 15-5 PH stainless steel as an elasto-plastic strain-hardening solid without damage; damage will eventually occur resulting in final failure of the specimen, but at strain levels beyond those considered in this work. .

The plastic response is modeled by the flow theory with isotropic hardening; the Hill (1948) yield criterion with an associated flow rule is used, as it provides a suitable representation of the yield surface and is assumed to be capable of modeling the primary anisotropic features of 15-5 PH stainless steel. This criterion is written as follows:

$$F\left(\sigma_y-\sigma_z\right)^2+G\left(\sigma_z-\sigma_x\right)^2+H\left(\sigma_x-\sigma_y\right)^2+2L\sigma_{yz}^2+2M\sigma_{xz}^2+2N\sigma_{xy}^2=\sigma_0^2 \quad (5.2)$$

Two additional assumptions are applied to the above criterion: first, we set $G+H=1$; this assumption provides scaling for all of the material constants by fixing the equivalent plastic stress at yield to be equal to the stress that causes yield from the single tensile test analyzed in this work. The second assumption sets all of the shear coefficients to be equal to their isotropic values, $L=M=N=1.5$. Since these shear stresses are nearly nonexistent in the tension test, it is not possible to estimate their influence on yielding simply from the uniaxial tension test. A test with different geometry is required in order to obtain a calibration of these parameters. This leaves two degrees of freedom in the yield criterion, and thus two parameters that must be obtained through the IP.

In order to model the stress-strain curve, a rather non-traditional model is used. Conventionally, the stress-strain curve is modeled through some functional form; for example, the Ramberg-Osgood model, Swift model, Voce model, etc. are used to capture power law, exponential dependence, etc. However, it is clear from the nominal stress-strain curve for the 15-5 PH stainless steel, that the true stress-strain relation prior to the necking strain (recall that the deformation prior to the Considère point is heterogeneous for this material so direct observation of the behavior is not possible and representation by the form for the stress-strain relation is required) is more complicated than can be produced by these typical models. Additionally, it is quite possible that the stress-strain behavior cannot be adequately characterized as a single power law over the large strain range investigated here. Even further, while functional forms of the above type are useful in obtaining analytical solutions, they pose no particular advantage when computational simulations are to be performed; any representation meeting suitable continuity requirements can be used. In addition to being sufficiently smooth, whichever form is

used should obey a couple of well-known physically-based rules regarding the strain hardening of metals that have been obtained from extensive studies of plastic flow: 1) the stress strain curve should be monotonically increasing and 2) the tangent modulus of the curve should decrease monotonically with increasing strain in the high strain regime (for materials where slip is the only mechanism for plastic flow). For the 15-5 PH stainless steel, it is postulated that the instability directly following the elastic regime is structural, not material; therefore the stress-strain representation is restricted to be of strictly monotonically increasing type for the entire strain range, however the tangent modulus will be allowed to increase in the small plastic strain range.

Prior to selecting a form for the stress-strain relation, it is useful to examine what qualities are desirable in its representation. First and foremost, the representation must obey the two rules set out above, but any additional constraints beyond these two rules degrade the attractiveness of a candidate representation. For example, linear hardening satisfies both of the requirements, but is not a strong candidate because it imposes the extra and unphysical constraint that the tangent modulus is constant. Similarly, the conventional stress-strain representations impose unphysical constraints that influence the solution of the IP. During the optimization process, it is not the role of the stress-strain representation to limit the variety amongst the trial stress-strain curves. The representation should allow freedom for the optimization scheme to drive the stress-strain curve to a shape that minimizes the objective function, constrained only by the two criteria above. An example of a representation that does not impose additional constraints is a tabular definition with numerous entries. However, this is undesirable as well because the IP will have equally numerous parameters that must be optimized, making it too expensive to be solved.

To balance freedom of the representation with the number of parameters required, splines are a strong candidate. An arbitrary amount of flexibility can be included through the inclusion of additional knot points, yet a stress-strain curve can be well represented with generous spacing between knot points. Specifically, monotonically increasing splines are attractive since they satisfy the first rule mentioned above if the knot points are monotonically increasing, and typically satisfy the second rule if the slopes of lines connecting subsequent knot points are monotonically decreasing. A few options exist in this family, and the monotone preserving spline developed by du Preez and Maré (2013) is selected over the more classical example by Fristch and Carlson (1980) due to its ability to produce a more varied set of curves with a fixed number of knot points. This capability is important in the current work because the number of knot points and their abscissa (strain) values are chosen *a priori*, and different curves are created by selecting different ordinate (stress) values at the knot points. Using a more flexible spline makes the optimized stress strain curve less dependent on the number of knot points and the particular values chosen for their abscissa. However, since the final curve is still dependent on these two factors, care was taken to select points that were predicted to be near segments of the stress strain curve where changes in curvature occur most rapidly. There is a single parameter to be found by the IP for each knot point, so striving for the minimal number of knot points that can provide a good representation of the real stress-strain curve is of practical importance. Based on a prediction of what the optimized stress-strain relation may be, the monotone preserving spline (with the number of knot points, $N_p = 7$) of du Preez and Maré (2013) was chosen to represent the stress-strain curve for 15-5 PH. The fixed strain levels of the spline points, as well as the optimized stress level (found from solving the IP) at each point are shown in Table 5.1. The representation takes the form:

$$\sigma = \frac{1}{\varepsilon}\left(a_i + b_i\left(\varepsilon - \varepsilon_i\right) + c_i\left(\varepsilon - \varepsilon_i\right)^2 + d_i\left(\varepsilon - \varepsilon_i\right)^3\right) \quad \varepsilon_i \le \varepsilon \le \varepsilon_{i+1} \tag{5.3}$$

where ε_i, $i = 1, 2, \ldots N_p$ are the prescribed strain levels at the knot points, and the four constants a_i, b_i, c_i, and d_i, need to be determined for each segment of the spline ($4n-4$ unknowns). Of these, $3n-4$ equations for these constants are produced by enforcing that the spline passes through the knot points and that the spline is C^1 continuous. The final n equations needed to uniquely define the spline are produced by estimating the slope at the knot points to be equal to that of a quadratic that passes through each knot point and its neighbor on either side; the end point slopes are estimated by setting the second derivative to be zero. Further details, including explicit formulas for this representation are given by du Preez and Maré (2013). It should be mentioned that the monotone preserving spline does not directly guarantee a monotonically increasing stress strain curve, only that the product of stress and strain is monotonically increasing. This feature stems from the original purpose for which the curve was intended, i.e. prediction of bond yield curves, where stress and strain are replaced by spot rate of interest and time, respectively, and the monotonically increasing product of the two guarantees that no arbitrage opportunities exist. In order to guarantee that a curve in which the product of stress and strain is monotonically increasing with strain would translate to a stress-strain curve that has the same property, the strain values were given a large shift (here 109 was used) when calculating the stress. Then the shift was removed from the strains so that the curve fell on the proper domain, starting from zero strain. In total, nine material parameters are to be found; two to describe anisotropy and another seven for the stress-strain relation.

5.5 NUMERICAL SIMULATION OF THE BVP

As indicated earlier, it is unimportant what method is used to solve the BVP for use in the IP, as long as the method is sufficiently accurate. From a practical standpoint the faster the BVP can be solved the better, particularly because it will need to be solved repeatedly. It is for this reason that several different solution methods for the BVP have been pursued by other investigators when solving the IP, many of these methods putting an emphasis on low computational cost. Nevertheless, for the problem at hand—as well as many others of interest—heterogeneous 3D fields with finite deformations prevail, and nonlinear, incremental constitutive models are required. To handle these factors, sufficiently accurate solutions of the BVP could only be obtained through numerical methods. Here, the commercial finite element code ABAQUS has been used to obtain the solutions. The model used in this work takes advantage of the three-fold symmetry of the tensile test, so only one eighth of the tensile specimen is modeled. The mesh discretization is shown in Figure 5.8; 5,800 elements (21,417 DOF) with linear shape functions and full integration (element C3D8) are used, with a refined mesh in the region where necking occurs. The smallest mesh dimension in the undeformed configuration is 76 μm, the volume of such elements corresponding to the volume of approximately 25,000 grains of the material being modeled. The problem is solved using Abaqus/Standard and each solution takes approximately 255 seconds to solve on a workstation with four cores.

5.5 OPTIMIZATION

5.5.1 Comparison between experiment and simulation

The combination of observing the deformation field in the experiment and using FEM to solve the BVP allows many options for comparison between the two. The first step in making an informed comparison is recognizing which of the experimental results will be best for comparison, and then committing to leave them unaltered through the comparison process. It is obvious that the net load carried by the specimen should be used for comparison and is a straightforward quantity to compare between experiment and simulation. In contrast, there are many choices for the deformation measurements, the first of which is selecting the region of the specimen over which the error will be quantified. In the tensile test, only the region of necking continues to accumulate strain past the Considère point. Consequently, this is the only region of the specimen that will provide new information about the material's behavior after the onset of necking. Thus, only the necking region has been chosen as the area of interrogation for the deformation field. Additionally, there are several methods of how the simulated deformation field can be compared to the experimental, which in its most pure form is captured by the raw images. However, these images are not convenient for analyzing the deformation so they are processed with DIC to measure the experimental displacement field. This field, which is the direct output produced from correlating the images, is usually manipulated to estimate the strain field (there are many different approaches to calculate the strain field from the displacement).

It is between these three choices – the raw images, the displacement field, and the strain field –that we must compare the experimental results to the FEM results. Of course, some combination of all three may be chosen, and it is likely that each comparison is superior over the others for certain stages along the optimization process. For example,

image comparison will likely result in nearly random error values if the FEM results deviate from the observations by more than the period size of the speckle pattern. However, once the FEM displacement field's error reduces to subpixel values, image comparison will allow for the use of the experimental field with minimal error (since there will be no error from DIC or strain field approximation, only the measurement and simulation error will remain). For simplicity, this work is restricted to use only one of these methods for comparison. The displacement field is selected because the errors are quite low (a fraction of the pixel size), yet there is no difficulty in making systematic comparisons even when the FEM results greatly deviate from the experimental observations.

5.5.2 Avoidance of spatial bias in the displacement error

The use of the displacement field in the objective function presents some challenges for creating an objective function that are not present if the strain field is used instead. Rigid motion originating from frame and specimen compliance contributes to the displacement field and must be accounted for. It is also appropriate to account for misalignments normal to the direction of the load line (which also modifies the stress state by causing a small amount of bending); however, inclusion of this motion destroys the symmetry of the problem at hand. To preserve the symmetry, the misalignments and associated bending were neglected, justified by the fact that the measured transverse motions were about two orders of magnitude smaller than the longitudinal motion. Accounting for rigid motion along the load line is handled by specifying that the center of the neck remains at the same longitudinal coordinate value across all stages of deformation. As a result, the coordinate system is not fixed in space, but rather translates

with the longitudinal position of the neck, both in the experiment and simulation. Rigid body motion causing lateral displacements are accounted for at each deformation state by fitting a plane to a patch outside the necking region on each of the two surfaces observed. Based on the axial strain variation on these patches, a normal vector (side normal is the *y*-direction, front normal is the *z*-direction) for each surface in the unstrained state is found with the current rigid body rotations. The cross product of the two normal vectors gives the *x*-direction vector for the specimen in the current state. Transverse translations are made by shifting the location of each fit plane to a location calculated from the expected Poisson contraction and the reference position of the plane. The coordinate system is constructed the same way for both the experiment and FE results to provide spatial synchronization.

An additional hurdle to jump when using the displacement field is the prescription of how the displacement discrepancies between simulation and experiment should contribute to the objective function. The choice of features for synchronization (in this case, the center of the neck and the centerline of the specimen) influences the magnitude of deviation in displacement at each point being interrogated. For example, by definition, the *x*-component of displacement error is zero at the center of the neck for both the experiment and simulations, and error stack-up will cause larger deviations at points further from the neck. A good objective function should minimize the bias caused by error stack-up. An advantage of making strain comparisons between the experiment and model is that error stack-up does not occur, thus the strain based objective function eliminates this contribution to spatial bias. A careful selection of the error measure is needed when comparing displacement fields in order to minimize this bias.

5.5.3 The objective function

The simplest and most common objective function that has been used in the literature considers matching the global response; here, the objective function is written as follows[6]:

$$\phi = \sum_{i=1}^{N_t} \frac{\left| F_i^{\exp} - F_i^{\sim} \right|}{\left| F_i^{\exp} \right|} \tag{5.4}$$

where N_t is the number of deformation states (nominal strain levels) at which the experimentally measured force, $F_i^{\exp}$ is to be compared with the force $F_i^{\sim}$ calculated from the numerical simulation. From here on, we will refer to the results obtained from optimizing the above objective function as the *load-optimized* result and the function itself as the *displacement-blind* objective function. In the present work, the objective function is augmented and given in terms of a combination of the global force as well as the displacement field obtained from the 3D-DIC measurements:

$$\phi = \sum_{i=1}^{N_t} \left[\frac{1}{3} \sum_{j=1}^{N_n} \sum_{k=1}^{3} w_{j,k} \frac{\left| u_{k,i,j}^{\exp} - u_{k,i,j}^{\sim} \right|}{\left| u_{k,i,j}^{\exp} \right|} + w_{Fi} \frac{\left| F_i^{\exp} - F_i^{\sim} \right|}{\left| F_i^{\exp} \right|} \right] \tag{5.5}$$

where N_t is the number of deformation states (nominal strain levels) observed and N_n is the number of points at which both the experimental and numerical results were compared, hereafter called interrogation points. Typically, we set $N_t \sim 600$ and $N_n \sim 170$, although many more potential interrogation points were available both in the experiment and simulation. Only points within the most active region of the neck were

[6] It is common to use the square root of the sum of squared error (L_2 norm), with the underlying assumption that the errors are from random fluctuations in the experimental quantities and therefore could be idealized as Gaussian distributed. Here, systematic errors in the numerical solution dominate the random experimental fluctuations so we have taken the absolute value (L_1 norm) for the error. While the L_2 norm is dominated by large errors, the L_1 norm accumulates all errors uniformly.

included. The weights for the load error, w_{Fi}, were all set to unity. The weights for the displacement error, $w_{j.k}$, were produced by examining the level of equivalent plastic strain observed in the experiment at each interrogation point and at all levels of deformation. The observations were then sorted into approximately 100 bins covering the range of strains observed. Each weight is then produced by taking the inverse of the population of the bin to which its strain observation belongs. This method of weighting is used to make sure that the objective function has equal weight from each level of strain. This is advantageous over weighting each observation equally, because then the strain levels that are most common will dominate the objective function, and the relatively few observations at high strain levels will be suppressed. For every loading state, each component of the displacement error is normalized by its own component of the experimentally measured displacement. Then the error of these three components of displacement are summed over all the interrogation points. Counting the displacement error of each component individually rather than using the Euclidian distance error at each point provides the objective function greater sensitivity to the parameters that model anisotropy. Otherwise, the much larger longitudinal displacements easily overwhelm the smaller transverse ones, causing them to have little influence on the objective function. The choice of normalization in Eq.(5.5) combats spatial error (Velay et al. 2007), most easily demonstrated by considering the value of the objective function when a homogeneous strain field is observed in the experiment and the simulation predicts a homogenous strain field of different magnitude. Every interrogation point in Eq.(5.5) will have an identical contribution to the objective function, regardless of where spatial synchronization occurs. If the displacements were not normalized by some measure of the *local* deformation field, then a strong spatial bias would be present in the objective function. Choosing a different point for synchronization would produce a different value

for the function. In fact, for this example the displacement error measure from Eq.(5.5) is identical to that of a strain error; if strain were considered as the primary field for comparison, the objective function would be written as:

$$\phi = \sum_{i=1}^{N_t}\left[\frac{1}{3}\sum_{j=1}^{N_n}\sum_{k=1}^{3}\frac{\left|\varepsilon_{i,j,k}^{\exp}-\varepsilon_{i,j,k}^{\sin}\right|}{\left|\varepsilon_{i,j,k}^{\exp}\right|}+\frac{\left|F_i^{\exp}-F_i^{\sin}\right|}{\left|F_i^{\exp}\right|}\right] \tag{5.6}$$

This strain based objective function is not used because the experimentally calculated strain field has larger errors than the displacement field. This is a result of differentiating the displacements to compute the strain field and the large strain gradients present in necking deformation. Strain based comparisons are not attractive if the gradients are not likely to be resolved well by the gauge length used for strain computation. From here on, we will refer to the results obtained from optimizing the objective function in Eq.(5.5) as the *displacement-optimized* result and the function itself as the *displacement-aware* objective function. The results presented in Section 5.7 compare the use of the objective function in Eq.(5.5) with the objective function that does not consider the deformation field given in Eq.(5.4). A more in depth investigation of objective function selection is recognized as being vital to understanding the best way to solve the IP, but is not pursued here. It is also important to consider the sensitivity of these error measures, and to explore the choice of experimental input on model calibration, but the latter topic is not considered here.

5.5.4 Selection of parameters

Due to the computational expense of performing each simulation, it is not feasible to construct a well sampled hypersurface of the objective function. Therefore, solution of the IP requires a robust method to alter the constitutive properties of the model from one

iteration to the next. Fortunately, from the perspective of parameter selection, the IP is a simple constrained minimization problem. A number of linear constraints are set between the parameters that define the stress strain relation in order to enforce its monotonicity as well as decreasing tangent modulus, and also bounds on the anisotropy parameters are set to prevent them from deviating far from the range that is expected from direct analysis of the experimental observation. There have been numerous optimization methods developed for this class of problems. Here the genetic algorithm (implemented in MATLAB as *gamultiobj* for multi-objective optimization or *ga* for single) is selected due to its efficiency in highly non-linear, global optimization problems with large parameter spaces.

The optimization procedure is started by creating a random pool of trial material models with at least 500 members that satisfy the bounds and constraints. From this pool, effort is made to select the 50 members that best span the parameter space to use as the initial population for the genetic algorithm. Subsequently 600 function evaluations (spanning 12 generations) were performed seeking optimization of the Pareto front (the set of solutions for the parameters) in order to produce a refined initial population for the global minimization problem. The objective functions were decomposed by breaking apart the function in Eq.(5.5) into three different contributions for each knot point of the spline used to represent the stress-strain curve, as shown below:

$$\phi_s^{(1)} = \frac{1}{3}\sum_{i=N_{t,(s-1)}}^{N_{t,s}}\sum_{j=1}^{N_f}\sum_{k=1}^{3}\frac{\left|u_{k,i,j}^{\exp}-u_{k,i,j}^{\sin}\right|}{\left|u_{k,i,j}^{\exp}\right|}$$

$$\phi_s^{(2)} = \frac{1}{3}\sum_{i=N_{t,(s-1)}}^{N_{t,s}}\sum_{j=1}^{N_s}\sum_{k=1}^{3}\frac{\left|u_{k,i,j}^{\exp}-u_{k,i,j}^{\sin}\right|}{\left|u_{k,i,j}^{\exp}\right|} \quad 1\le s\le N_p \tag{5.7}$$

$$\phi_s^{(3)} = \sum_{i=N_{t,(s-1)}}^{N_{t,s}}\frac{\left|F_i^{\exp}-F_i^{\sin}\right|}{\left|F_i^{\exp}\right|}$$

where, N_f and N_s are the number of interrogation points on the front and side surfaces, respectively. The intervals $N_{t,s}$ for subdividing the number of deformation states are chosen by estimating the deformation state where the minimum cross section inside the neck is dominated by strains that exceed ε_s, the value of the strain corresponding to s^{th} knot point with zero indicating the reference state. Separating the single objective function of Eq.(5.5) in this way allows the effect of changing each individual model parameter to be analyzed more independently. Complete decoupling of the parameters cannot be achieved due to the history dependence of plastic deformations and relationship between the deformation field (which determines the area of the minimum cross section) and the net load carried by the specimen. The deformation error on the two surfaces are kept separate from each other in case the errors in the transverse components of the deformation field on a single surface are more sensitive to one of the two anisotropy parameters.

Once the multi-objective optimization is complete, the 50 members of the Pareto front with the lowest values for Eq.(5.7) are then used as the initial population for finding the global minimum using the genetic algorithm. The global optimization was allowed to run for 850 function evaluations (spanning 17 generations). Figure 5.9 show the progression of the objective function value for the best member of each subsequent population. To probe whether the global minimum has been found, the same process used to create the initial population for the multi-objective optimization was performed with more restrictive bounds on the parameters, centered on the optimal parameter set just found. This time the random initial population was fed straight into the global optimization and allowed to run for another 850 function evaluations. The displacement-optimized solution achieved a lower objective function value than found when seeded with the Pareto front. However, the load-optimized results did not achieve a lower

objective function value. To see if the objective function could be lowered further, MATLAB's pattern search algorithm was used with the best result found from the previous optimization runs. This final optimization run was successful in lowering the load-optimized objective function value by an additional 11%, however the lowest displacement-optimized objective function value was barely improved upon, dropping by less than one percent.

For optimization with each objective function, about a week of continuous running on a computer with four cores was spent on the four optimization runs described above. It is important to restate that the goal of this work is not to pursue the most efficient optimization method. Due to the high cost of function evaluations, this optimization problem appears to be one that could be greatly sped up by the use of Bayesian optimization techniques, but no such investigation has been done for this problem here.

5.6 RESULTS AND DISCUSSION

The simulation that minimizes each of the objective functions considered will now be compared to the experimental observations. Figure 5.10 shows a comparison of the nominal stress strain curve measured in the experiment to that produced by the load- and displacement-optimized simulations. Quantitatively, the agreement is excellent with a mean relative error of 0.23% and a standard deviation of 0.19% for the load-optimized case. The displacement-optimized case also matches well with a mean relative error of 0.55% and standard deviation of 0.42%. Despite this excellent quantitative agreement, some features are not captured as well by these solutions. The small load drop after the elastic regime is not present in the load-optimized case; however, it is present in the

displacement-optimized case. Also, the simulated Considère point occurs at a strain of 8.9% and 9.2% in the load- and displacement-optimized cases respectively, instead of the experimentally measured 7.6%.

Looking at the errors in the displacement field, Figure 5.11 shows the magnitude of the displacement error vector for the load-optimized case color mapped onto the experimentally measured surfaces just before rupture. The error is relatively uniform across both the front and side faces of the neck with a mean of about 42 μm and a standard deviation of about 4.3 μm. Figure 5.12 shows the same information for the displacement-optimized case; note that the color scale is now magnified to indicate the error values since they are significantly smaller. The error shows substantial variation at a couple of locations with a mean of about 16 μm and a standard deviation of about 3.3 μm. In order to track the accumulation of error with loading, the spatio-temporal variation of the displacement error is shown in Figures 5.13 and 5.14 for the load-optimized and displacement-optimized cases. The variation of displacement error on a line that runs near the midline of the front surface ($x_2 \sim 0, x_3 = h/2$) is computed for every level of deformation and assembled to create a contour plot where the abscissa corresponds to the spatial location, the ordinate to time step (equivalently to the nominal strain) and the color indicates the displacement error on a scale indicated by the color bar. The displacement error tends to increase with deformation, while showing strong spatial uniformity. The maximum displacement error occurs shortly before rupture and has a value of just over 54 μm for the load-optimized case while it has a value of just over 29 μm for the displacement-optimized case.

In order to compare these results to previous investigations (Tardif and Kyriakides, 2012; and Gross and Ravi-Chandar, 2014), a comparison of the necked shape is considered in Figures 5.15 and 5.16. Although the profiles used in the previous

investigations were obtained through edge-tracing methods, the 3D measurements in the present work enable a comparison along the specimen mid-plane; therefore, the plots correspond to a plot of $u_3(x_1, 0, h/2)$ (front surface) and $u_3(x_1, h/2, 0)$ (side surface). It is found that the load-optimized solution produces a necked profile that does not deviate far (no more than 39 μm) from the experimental surface on either surface. The displacement-optimized case deviates even less, with 26 μm and 14 μm of deviation on the front and side surfaces respectively at the location of peak strain. A side-by-side video of the strain distribution in the displacement-optimized simulation and experiment can be found as Supplementary Material SM9 for this dissertation. Additionally, videos showing the spatial distribution of error over time on both surfaces for the displacement- and load-optimized cases are also included as SM10 and SM11, respectively.

The results of the optimization process provide a calibration of the material stress-strain curve; these results are now examined quantitatively. It should be noted that the results of the optimization process require interpretation/judgment to determine their applicability. In other words, the optimization process provides the best fit model that is sensitive to the objective function and the task of determining which objective function is appropriate to the model examined is not addressed in this process. We approach this through a comparison of the results obtained from displacement-blind and displacement-aware objective functions. In exchange for a slightly higher error in the nominal stress strain curve than the load-optimized model carries (0.55% instead of 0.23%), the displacements are tracked to a much better accuracy in the displacement-optimized model. The mean Euclidean displacement error just before rupture for the load-optimized model over the region shown in Figure 5.11 is ~ 6.1%. The displacement-optimized model lowers this error to ~ 2.3%, while the nominal stress-strain error remains small. Despite equal weighting in the displacement-aware objective function (Eq.(5.5)), the

displacement-optimized model carries a larger error in the displacement field than it does in the nominal stress-strain curve. It is possible that unequal weighting in the objective function could be advantageous, but this has not been investigated in this study. To get another perspective on how the two models stack up against each other, the load-optimized case produces a displacement-aware objective function value that is ~15% higher than the displacement-optimized model, indicating a measure of the combined load and displacement error. The displacement-optimized model also fares better in comparison to experimental necked geometry (Figures 5.15 and 5.16), however there is still some room for improvement. Nonetheless, the evidence suggests that use of the displacement-aware objective function does in fact provide better matching of the experimental observations by the optimized simulation.

The effect of considering displacements in the objective function can be seen in the resulting behavior for the material derived from the optimization process. The true-stress vs true (logarithmic) plastic strain corresponding to load and displacement optimized cases are shown in Figure 5.17. The parameters of the spline fit that corresponds to the best fit in either case are shown in Table 5.1. The first thing to note is that, although these correspond to the same experimental result, the extracted stress-strain curves are quite different. The largest difference between the stress-strain curves for both objective functions comes out at logarithmic plastic strains in excess of 0.25. At and above this level of strain the tangent modulus for the displacement-optimized model is less than that for the load-optimized model. At a logarithmic plastic strain of 0.5 the load-optimized model exhibits a tangent modulus that is about 25% greater than the displacement-optimized model. Although this difference may not appear to provide a drastically different looking strain hardening curve, it does have an important effect on localization behavior. Localization will occur at lesser levels of deformation in the

displacement-optimized model than the load-optimized. In practice, this result is particularly important because the displacement-optimized strain hardening behavior is more conservative than the load-optimized. Since the same material model has been used in the same set of simulations, this difference in the stress-strain curve is completely due to the formulation of the objective function. We contrast this with the stress-strain curve for a nominally similar material that was extracted by Gross and Ravi-Chandar (2014) who used a power-law hardening model (see Figure 5.2 of Gross and Ravi-Chandar, 2014), and therefore fewer degrees of freedom; the true stress vs true strain variation obtained in that work was quantitatively and qualitatively different from the result in the present work because of the differences in the material model. In addition to material model dependence, one could make a conjecture that using a strain-based objective function as in Eq.(5.7) might result in yet another stress-strain curve. Discrimination between these different results can be achieved only through additional considerations of the suitability of these objective functions (and material models) themselves. For the present purposes, we can satisfy ourselves by considering that the displacement-optimized result has captured more elements of the measured response correctly with the chosen material model.

In addition to more compliant strain hardening behavior, the displacement-optimized model provides significantly different results for the parameters defining anisotropy. The Lankford parameter identified by the load-optimized and displacement-optimized cases are 0.945 and 0.917, respectively. Figure 5.18a shows the sensitivity of the load-optimized objective function to changes in the Lankford parameter and the ratio of long transverse to longitudinal yield stresses. This objective function proves to be insensitive to the Lankford parameter – as it should be since we are only matching the overall load and the axial displacement without influence from the specific partition of

the transverse strains – making it clear that the value for the Lankford parameter selected to minimize this objective function cannot be trusted. Although the load-optimized objective function is sensitive to the ratio of yield stresses, sensitivity to a parameter is necessary but not sufficient to having found a meaningful value for it. As seen in Figure 5.18b, the displacement-optimized objective function is sensitive to both the Lankford parameter and the ratio of yield stresses; this is a result of driving the displacements on two mutually orthogonal surfaces to match the experimental measurements. Importantly, this projection of the objective function has a single, well defined minimum point that appears to be reasonable for the material investigated.

The displacement-optimized case can be further investigated by examining how the strain accumulation compares to that observed in the experiment. Figure 5.19 shows the variation of transverse strain with longitudinal strain measured at the deepest part of the neck for both the experiment and the displacement-optimized simulation. The simulated curves match the experimental data quite well. Such correlation suggests that the anisotropy evolves very weakly for this material when subjected to a nearly uniaxial stress-path, and that most of the nonlinearity in this plot is due to evolution in the stress-path. The load-optimized result has not been included in this comparison, as it has already been shown that this case is not capable to determine the anisotropy.

It should be noted that we have considered the problem of constitutive model extraction from *a single* experiment. There are three major considerations associated with this process. First, the choice of specimen geometry and loading has restricted the range of stress states that could be examined in this test. As a single test, the tensile test studied here is actually ill-suited for the purpose of determining the complete constitutive behavior, as it only explores a small region of stress space, albeit to high levels of strain. The tensile test may be much more useful if the IP is solved while considering several

experimental results simultaneously, spanning tensile, compressive, shear, and combined stress states. For both experimental and computational efficiency, it is likely that a carefully chosen geometry that deforms to span a large swath of the stress space up to high levels of strain is the best choice for the IP. Then, a multiobjective optimization process can be performed for extraction of the constitutive response, where the objective function aims to match all experimental results simultaneously. This will permit spanning a greater portion of the stress space; such generalization is a straightforward extension of the procedure utilized in the present work and poses no new challenges in principle, other than the size of the computational effort required.

Second, validation experiments that are distinct from the set of experiments used to calibrate the model are needed in order to corroborate both the strain hardening and anisotropic behavior found from the IP. The nature of the optimization process produces a material model that best fits the BVP of the IP, not necessarily a BVP of engineering interest. For this reason there is great importance to carefully select the BVP for the IP to be one that causes the material model to be well-suited for a broad set of problems. However, validation experiments that consider different stress paths should be examined with similar requirements on matching between experiments and simulations, with the displacement-aware objective function. The effort undertaken after the Sandia Fracture Challenge in 2012 (Gross and Ravi-Chandar, 2014) provides an example of such validation. In that work, the stress-strain curve was extracted from a load-optimized simulation and then used to predict the response of a structural configuration; fortunately, the structural configuration experienced a similar load path as the test configuration and the calibration worked reasonably well. However, a broader range of validation simulations and experiments are needed in order to affirm the suitability of the IP pursued in the present work.

Finally, although we have performed a deterministic extraction of the material parameters by forcing a fit of the model to the experiment, it is important to consider stochastic effects that may arise from multiple sources. First, there is material variability that is inevitable due to variations in manufacturing conditions; therefore, fitting to just one experiment will not capture the variability in response. Second, there are geometric variations that arise from specimen fabrication and mounting procedures; the Sandia Fracture Challenge (Boyce et al. 2014) provided a good example of the response being significantly different in nominally identical specimens, but simply due to geometric variability. Lastly, the desired boundary conditions are imposed through specific experimental arrangements and may suffer variability in implementation. Assuming that all systematic experimental defects have been eliminated, these stochastic effects generally provide for variations in the measured response that must be taken into account in formulating and solving the inverse problem. For example, the use of experimentally measured boundary conditions in the numerical simulations may provide an even better fit to the objective function and greater model efficacy for displacement-optimized material models. One pathway towards incorporating such stochastic effects is to consider a number of repeat experiments under each loading condition, and to use Bayesian inference to identify not only the mean value of the material parameters, but also the covariance of each material parameter in the calibration process; the effort associated with this is significantly greater, but has the potential to provide appropriate material parameter identification.

5.7 CONCLUSION

The problem of material property identification in elastic-plastic materials has been investigated. Specifically, an inverse method for constitutive property calibration from an experimental data set is described. The input to the inverse problem is the behavior of a tensile specimen, characterized either in terms of its load vs elongation behavior alone or in combination with the deformation measurements measured by 3D DIC on two orthogonal surfaces. The optimization was accomplished based on two different formulations: load-optimized, in which just the global load on the specimen at different macroscopic extensions of the specimen was matched and displacement-optimized, in which in addition to the global load, details of the local displacement field in the vicinity of the neck was used to generate a displacement-aware objective function. The material was modeled using a flow theory of plasticity with isotropic hardening and with the Hill (1948) anisotropic yield criterion. The resulting boundary value problem was solved using the numerical finite element code ABAQUS/Standard. The optimization process was achieved using the genetic algorithm in MATLAB. The following are the main conclusions of the work:

- Both the load-optimized and displacement-optimized cases provide very good match between the experimental and simulated nominal stress vs nominal strain variation.
- The error in displacements over the entire field in the vicinity of the neck is smaller in the displacement-optimized formulation.
- The stress-strain curves identified from the two different optimization cases are significantly different for equivalent plastic strain levels greater than about 0.25
- The anisotropy parameter (Lankford parameter) obtained from the two different optimization cases was quite different; in the case of the displacement-optimized

formulation, this parameter was well constrained directly from the experimental measurements of the strains in two orthogonal planes.

The availability of full-field displacement measurement methods, such as digital image correlation method, has now made it possible to pose the problem of material property identification in structural materials; the combination of this method with numerical solutions methodologies, such as the finite element method, makes for a powerful tool for material property identification as illustrated in the present work. Additional effort is required to identify an appropriate objective function for the optimization and to handle uncertainties arising from fluctuations.

Table 5.1: The optimized parameters defining the stress strain curve and plastic anisotropy for the load and displacement-optimized cases. Note that there were only two degrees of freedom in the anisotropy, however all the resulting parameters for the yield criterion and the Lankford parameter are listed for completeness.

Load-Optimized						**Displacement-Optimized**				
Strain	Stress *GPa*		Anisotropy			Strain	Stress *GPa*		Anisotropy	
0.003	1.069		*r*	0.9450		0.003	1.071		*r*	0.9170
0.008	1.082		*F*	0.8662		0.008	1.088		*F*	0.6750
0.02	1.098		*G*	0.5141		0.02	1.101		*G*	0.5216
0.1	1.205		*H*	0.4859		0.1	1.210		*H*	0.4784
0.2	1.260					0.2	1.259			
0.45	1.352					0.45	1.330			
1.3	1.608					1.3	1.563			

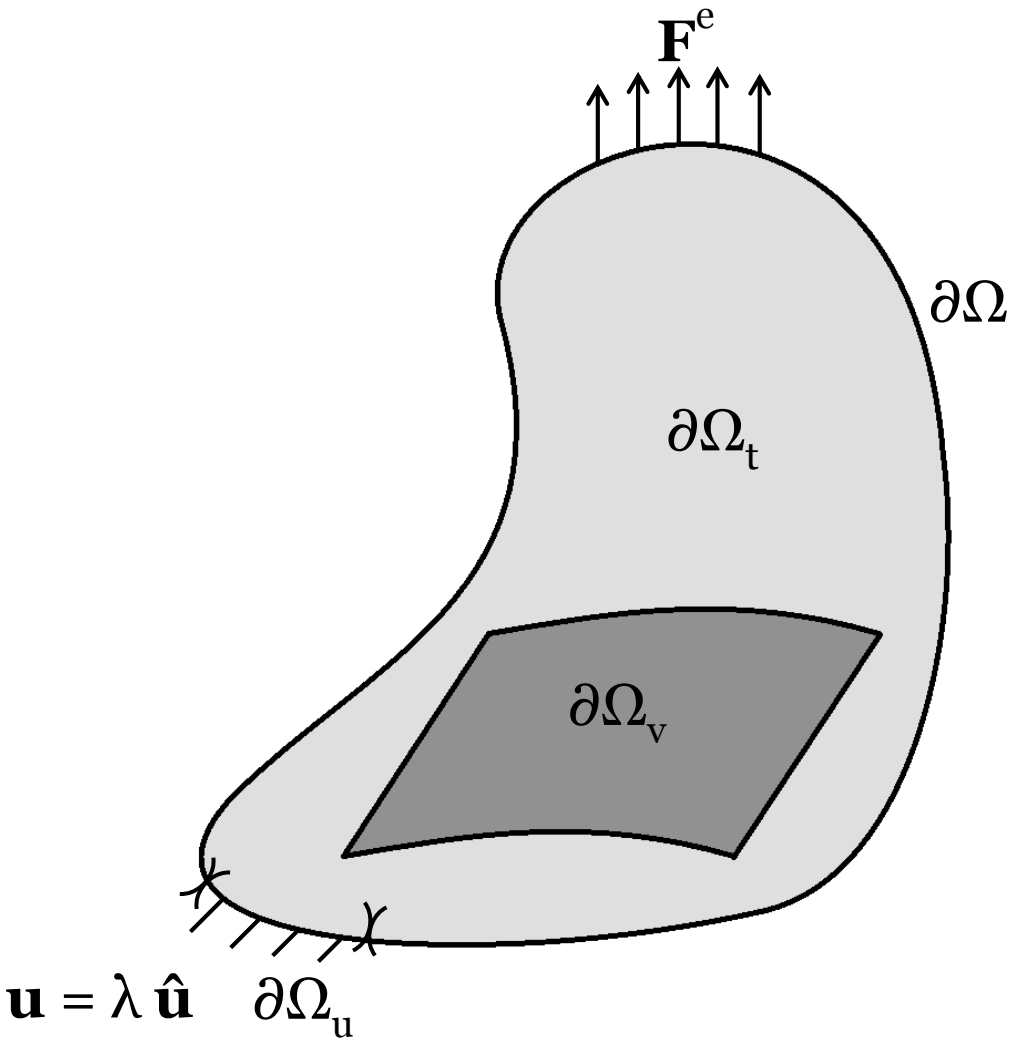

Figure 5.1: A generic boundary value problem indicating the region of observation for acquiring additional kinematic measurements for use in the inverse problem.

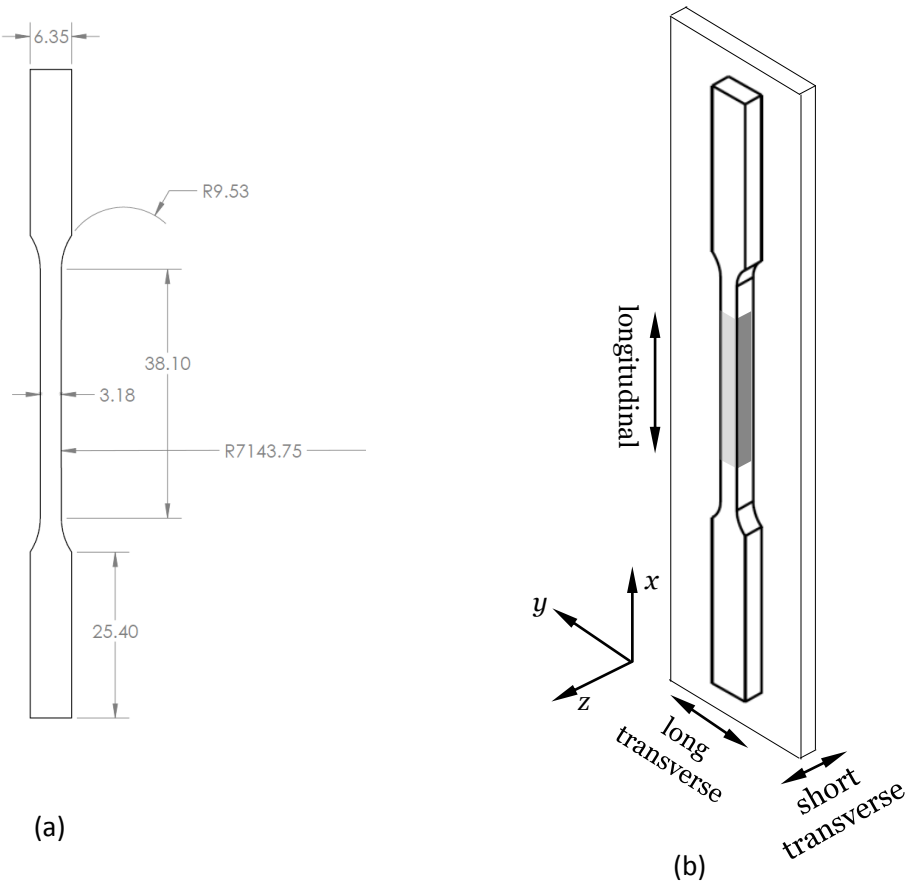

Figure 5.2: (a) Drawing of the tensile specimen with dimensions in mm. Note the small curvature over the gauge section and square cross section. (b) Orientation of the tensile specimen relative to the natural directions of texture in the sheet. This is also the perspective that the specimen is viewed from by the stereo imaging system to capture deformation information on two orthogonal surfaces. The shaded area is the region observed by the imaging system.

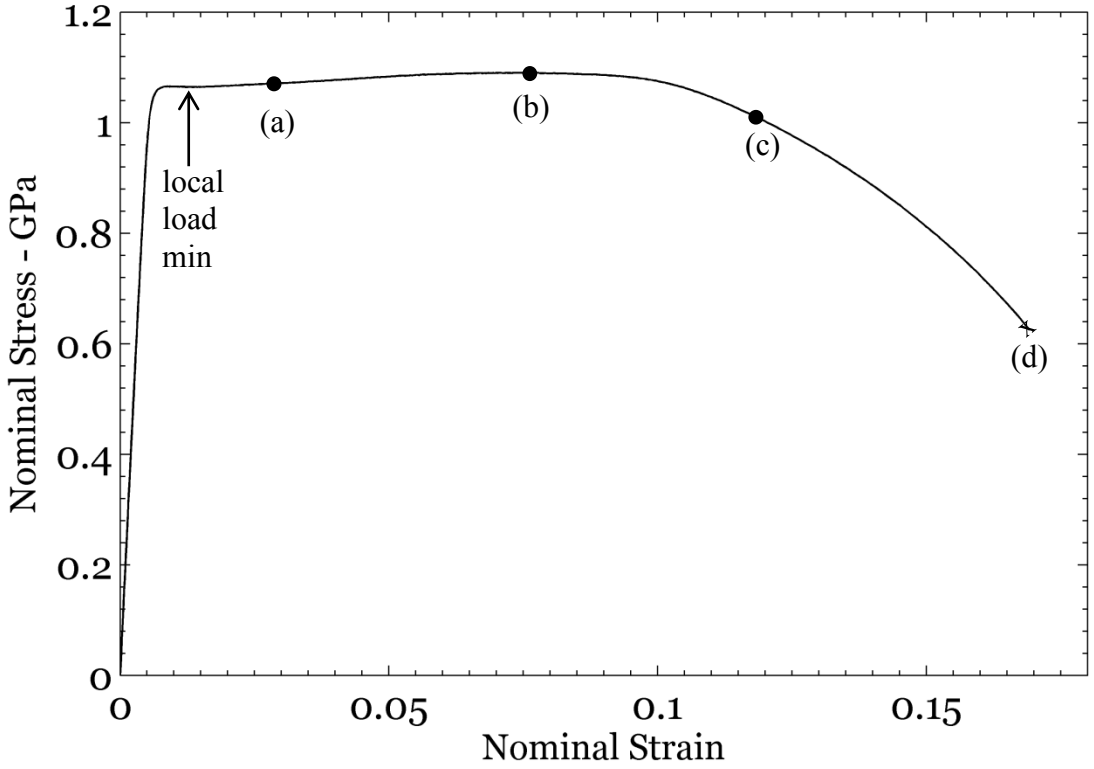

Figure 5.3: Nominal stress strain curve for 15-5 PH in the H-1075 condition. Strain was measured with a DIC-based extensometer, completely spanning the necked region. The first load peak occurs at a strain of about 0.9%, the minimum is reached at a strain of about 1.4%, and the onset of necking occurs at a strain of about 7.6%. Full field strain contours are shown in Figure 4 at the points marked (a)-(d).

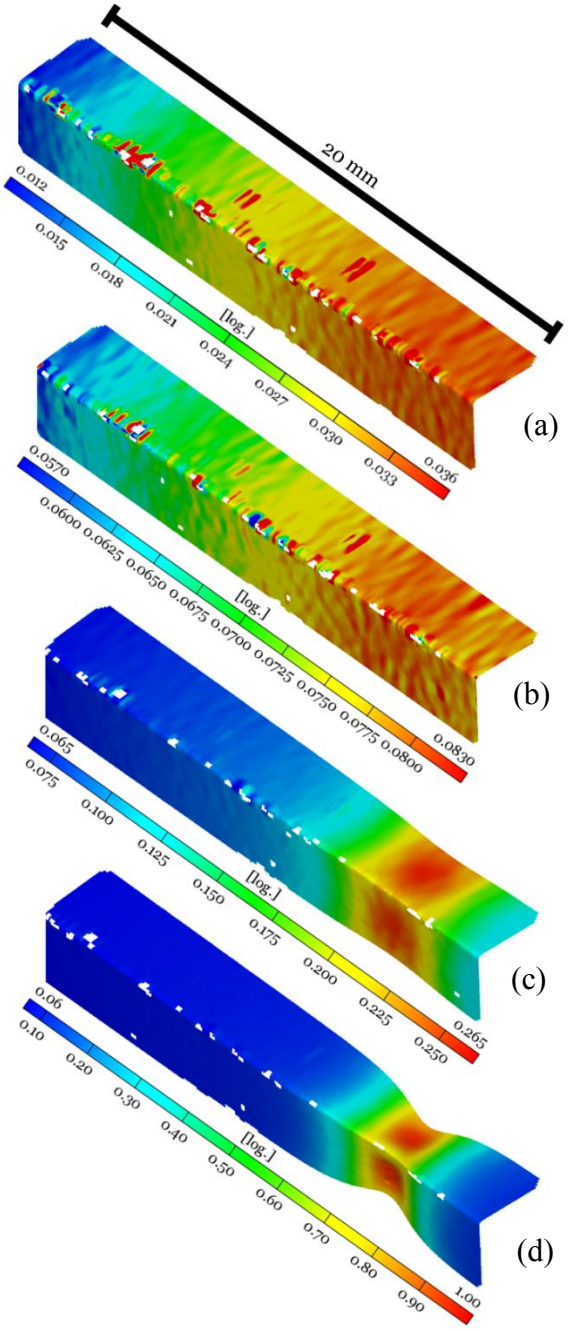

Figure 5.4: Spatial variation of the maximum true (logarithmic) principal strain field $\varepsilon_1(\mathbf{x})$ as measured from 3D-DIC at stages (a) - (d) marked in Figure 3. The front surface is the one below the corner and the side surface above. The white spaces are where DIC failed to correlate due to proximity to the specimen's corner or local defects in the speckle pattern. No filtering, smoothing, or interpolation have been used in calculating the strain field.

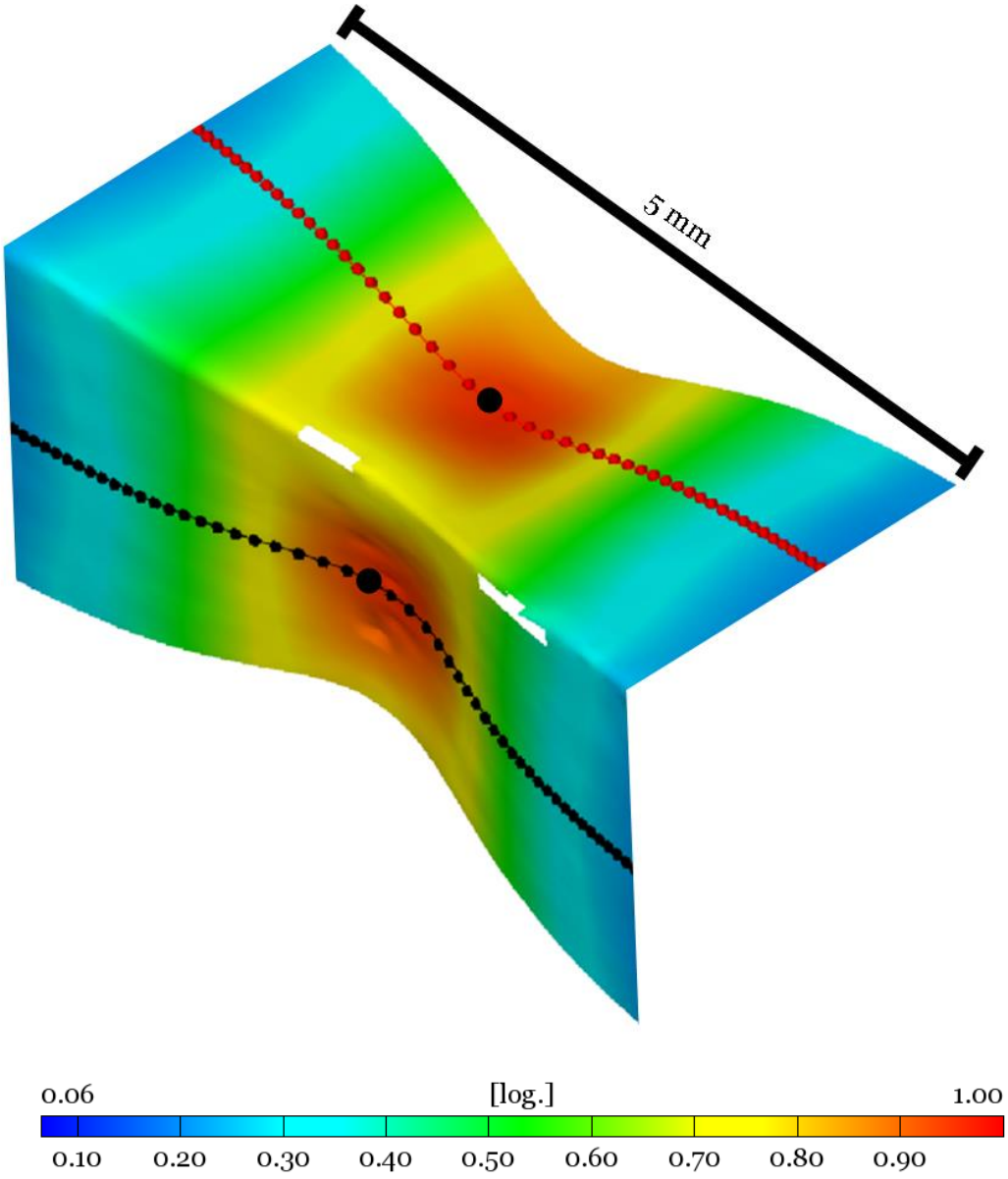

Figure 5.5: (a) Spatial variation of the true (logarithmic) strain field $\varepsilon_1(\mathbf{x})$ as measured from 3D DIC just prior to rupture. The maximum true strain measured is around one. The small black and red dots indicate locations along the midline of each surface where the spatial variation of strain is plotted in Figure 5b. The two large black dots are located at the center of necking. At these locations the stress state remains approximately uniaxial throughout the test. Strain data from these two points are used in Figures 5.6 and 5.7.

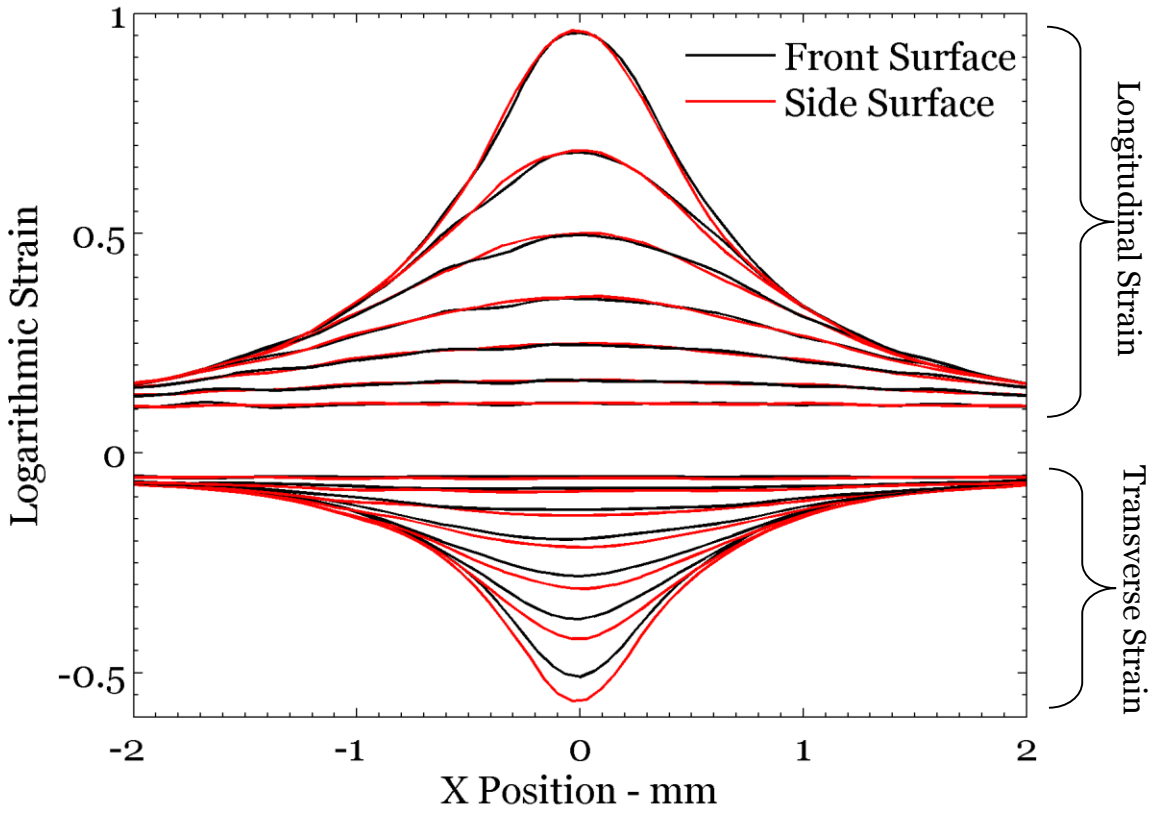

Figure 5.5: (b) Spatial variation of the longitudinal and transverse strains on both surfaces plotted at 30 second intervals for the last three minutes of the test (nominal strain values of 0.106, 0.117, 0.129, 0.142, 0.155, and 0.169). The longitudinal strains on both surfaces remain nearly identical to one another though the duration of the test. Transverse strains accumulate more rapidly on the side surface than the front, indicating a lower stiffness in the short transverse direction than long transverse.

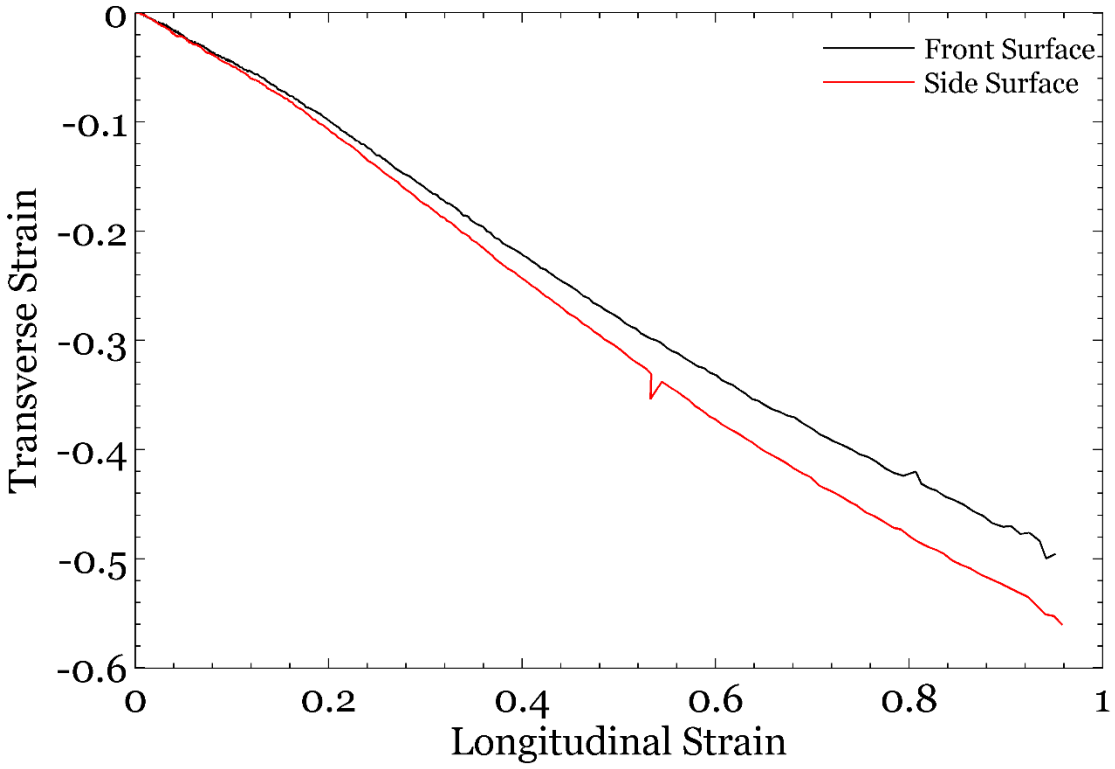

Figure 5.6: Variation of the transverse strain with respect to longitudinal strain at the deepest point in the neck on the front and side surfaces. The transverse strains develop nonlinearly with continued longitudinal straining, thus indicating that the anisotropy maybe evolving throughout the test. Evolution appears to be the most rapid around a longitudinal strain of 0.14, where the curvature of the lines reaches their maximum magnitude.

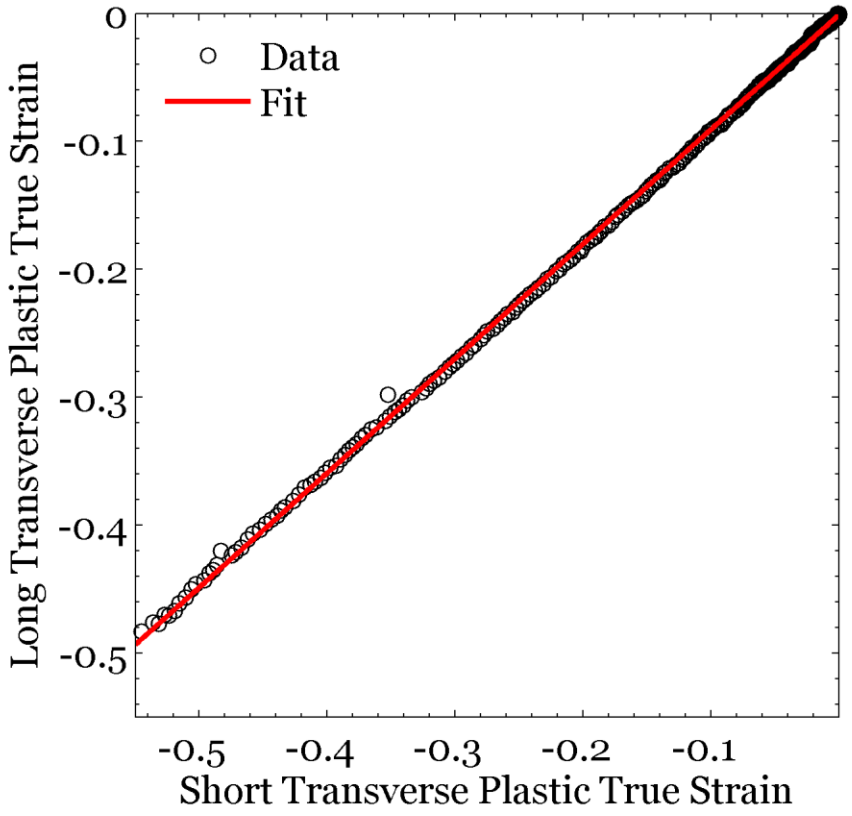

Figure 5.7: The transverse strains on both surfaces plotted against each other. The variation is nearly linear, with the slope of the line providing one of Lankford's parameters as 0.895. When investigated closely, the Lankford parameter is not constant; it varies most rapidly at the low strain range and then settles to a nearly constant value with increasing strain. This behavior is discernable from the measurements taken in this experiment, but the level of uncertainty is high to investigate this behavior closely.

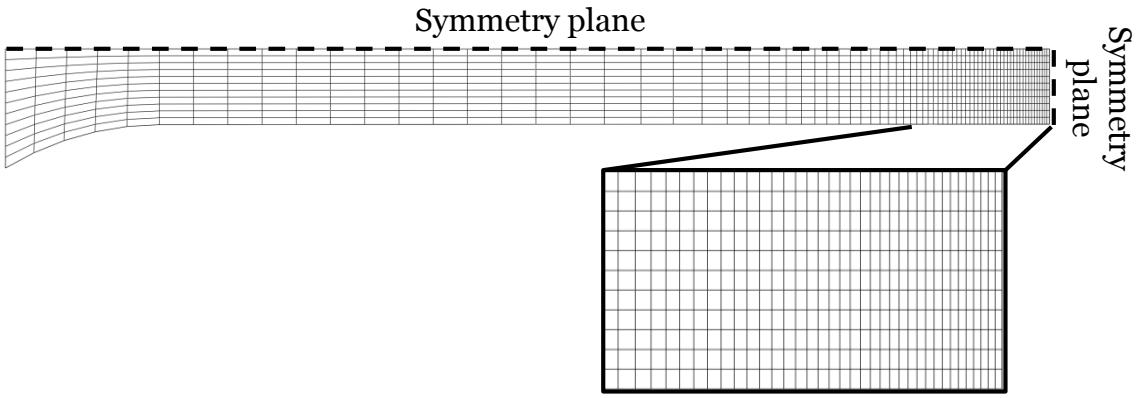

Figure 5.8: Spatial discretization used for the FE model. Two of the three symmetries used are visible. Necking occurs at the symmetry plane on the right, where the refined mesh is located. The smallest mesh dimension is 76 μm.

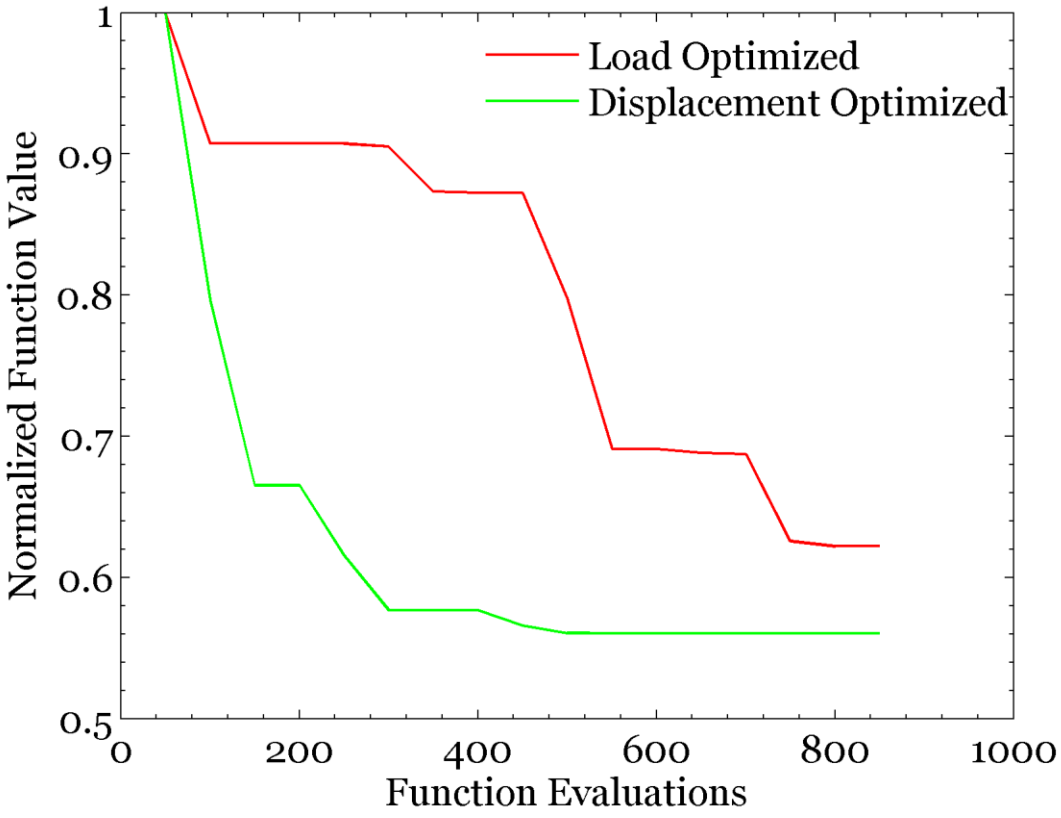

Figure 5.9: Objective function value for the best member of each generation throughout the global optimization procedure. The curve is flat when a lower value for the objective function has not been found from the previous generation.

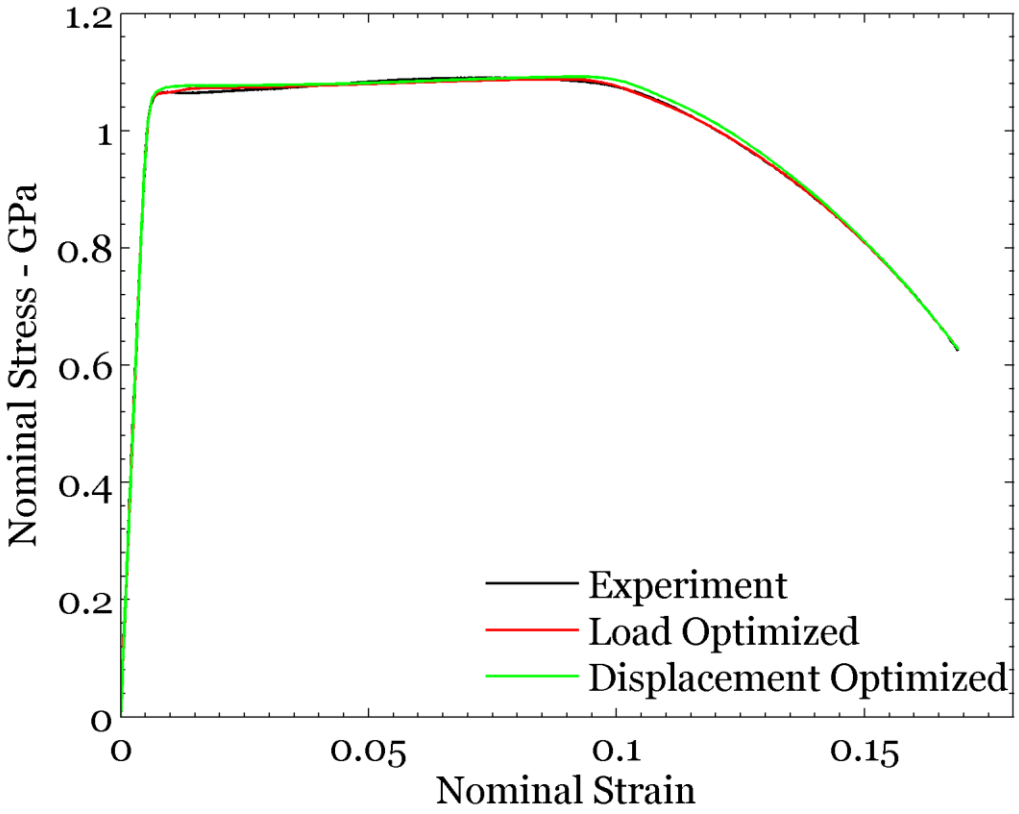

Figure 5.10: Comparison of the nominal stress strain curves produced by both objective functions to the experimental observation. Both of the simulated curves closely follow the experimental result.

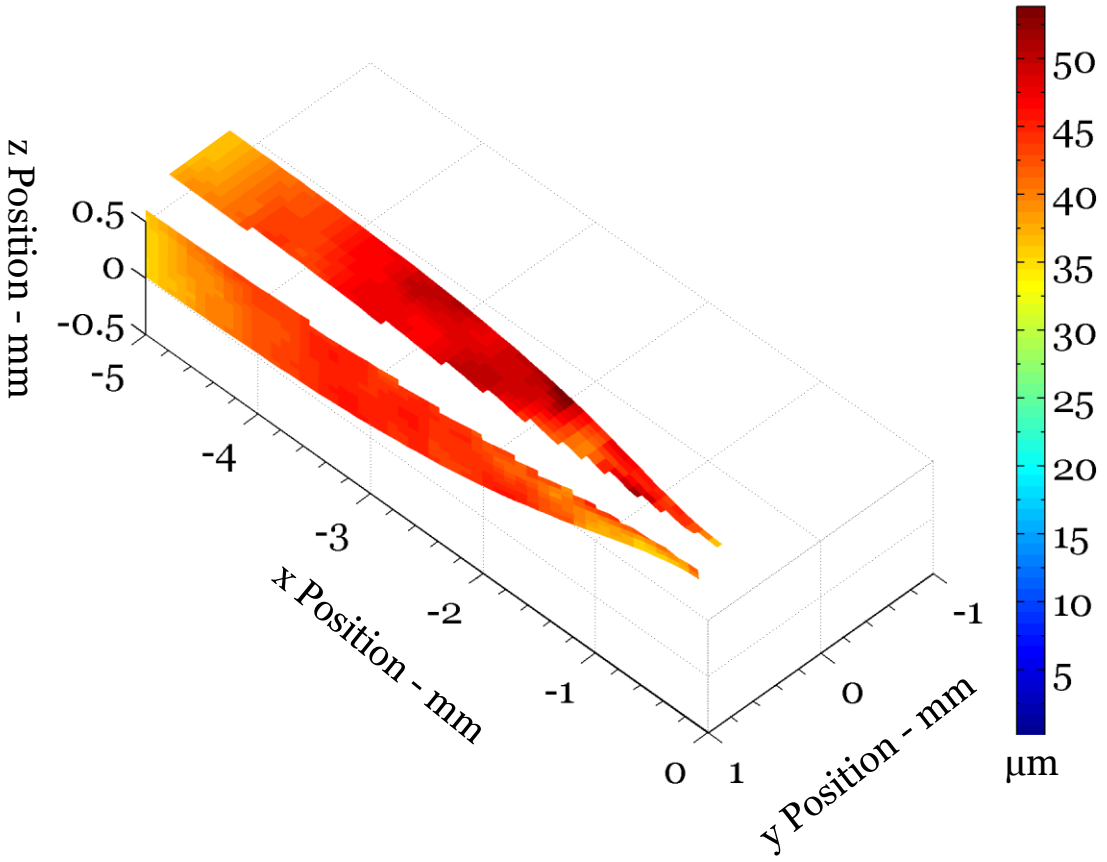

Figure 5.11: Spatial distribution of the displacement error for the load optimized material just before rupture. The front surface is the lower area and the side surface is the upper area. The center of the neck is located at x=0. The region shown is not the entire surface, but corresponds to $x < 0$, $y > 0$, and $z > 0$. Error is relatively uniform across both surfaces within and beside the necked region.

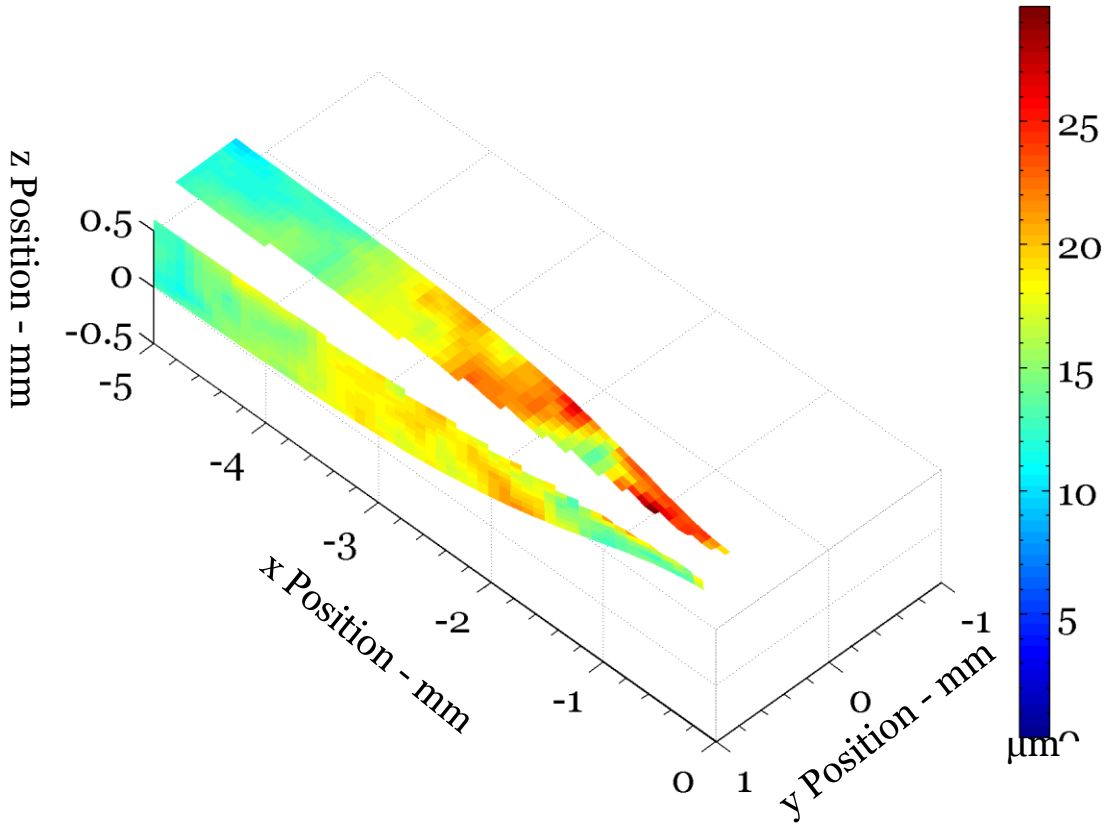

Figure 5.12: Spatial distribution of the displacement error for the displacement optimized material just before rupture. The front surface is the lower area and the side surface is the upper area. The center of the neck is located at x=0. The region shown is not the entire surface, but corresponds to $x < 0$, $y > 0$, and $z > 0$. Error tends to be lower on the front surface and varies along the axis of the specimen.

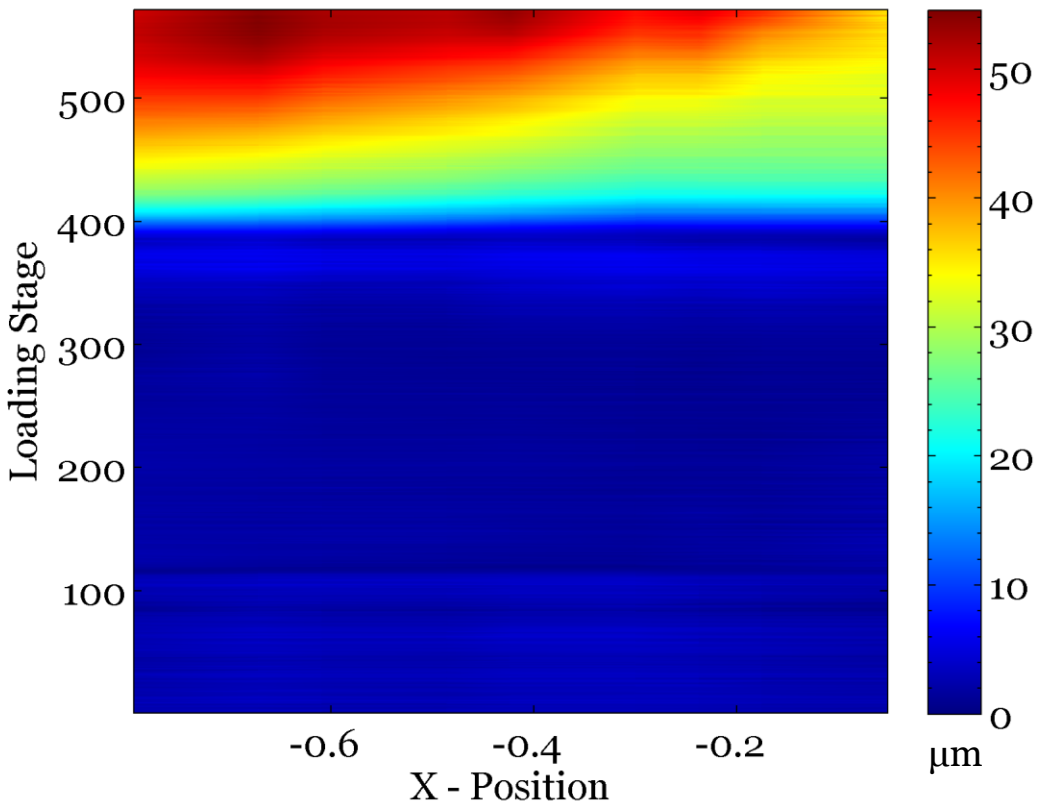

Figure 5.13: Spatial (x-axis) and temporal (y-axis) variation of the displacement error along a line near the midline of the front surface for the load optimized material. Errors that are relatively spatially uniform increase most rapidly during necking.

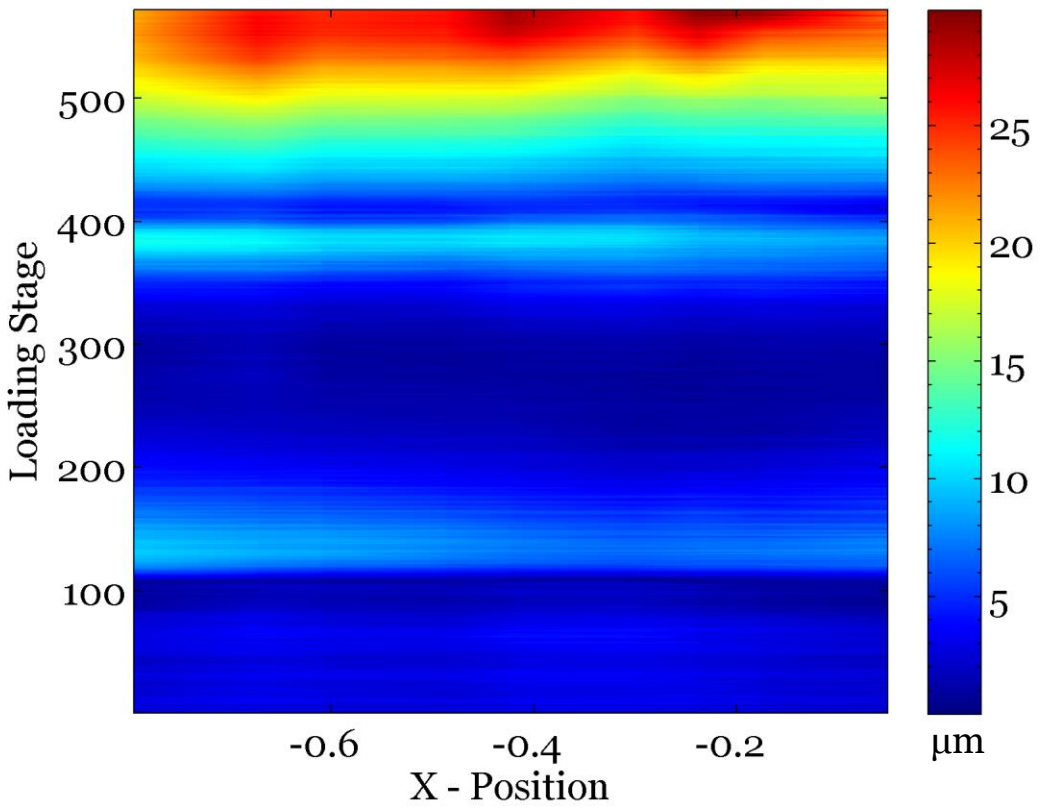

Figure 5.14: Spatial (x-axis) and temporal (y-axis) variation of the displacement error along a line near the midline of the front surface for the displacement optimized material. Errors that are relatively spatially uniform increase most rapidly during necking.

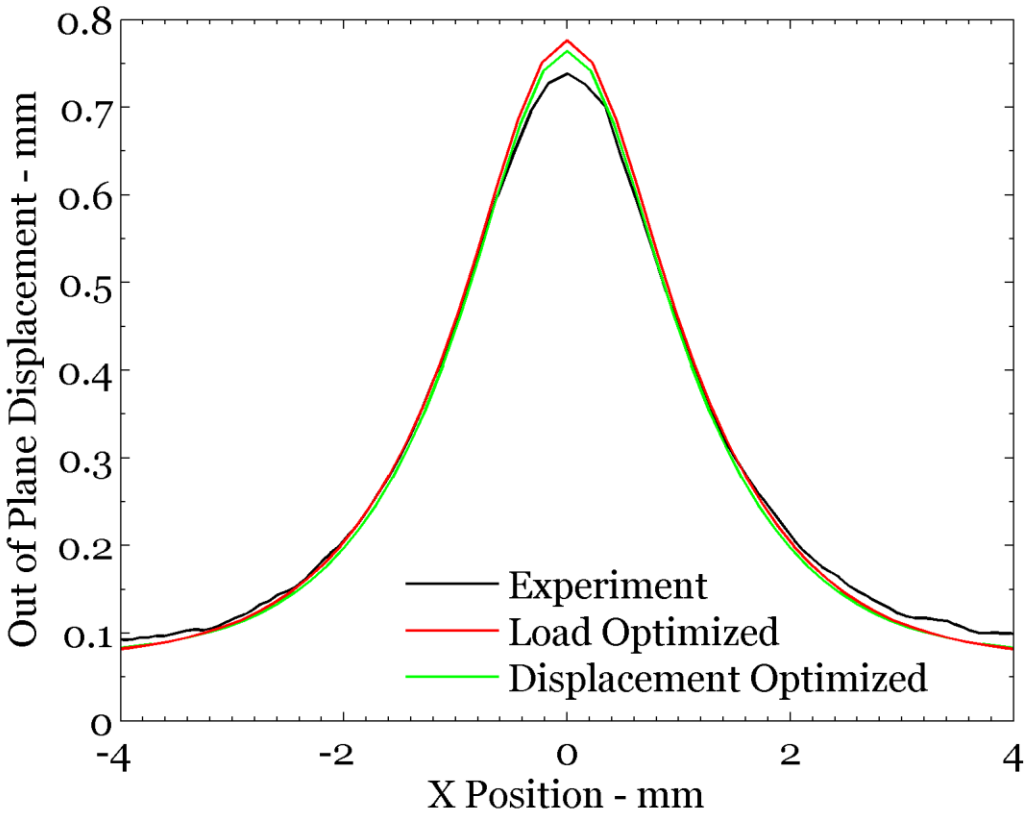

Figure 5.15: Out of plane displacement on the midline of the front surface in the necked region. Both load and displacement optimized materials show satisfactory agreement.

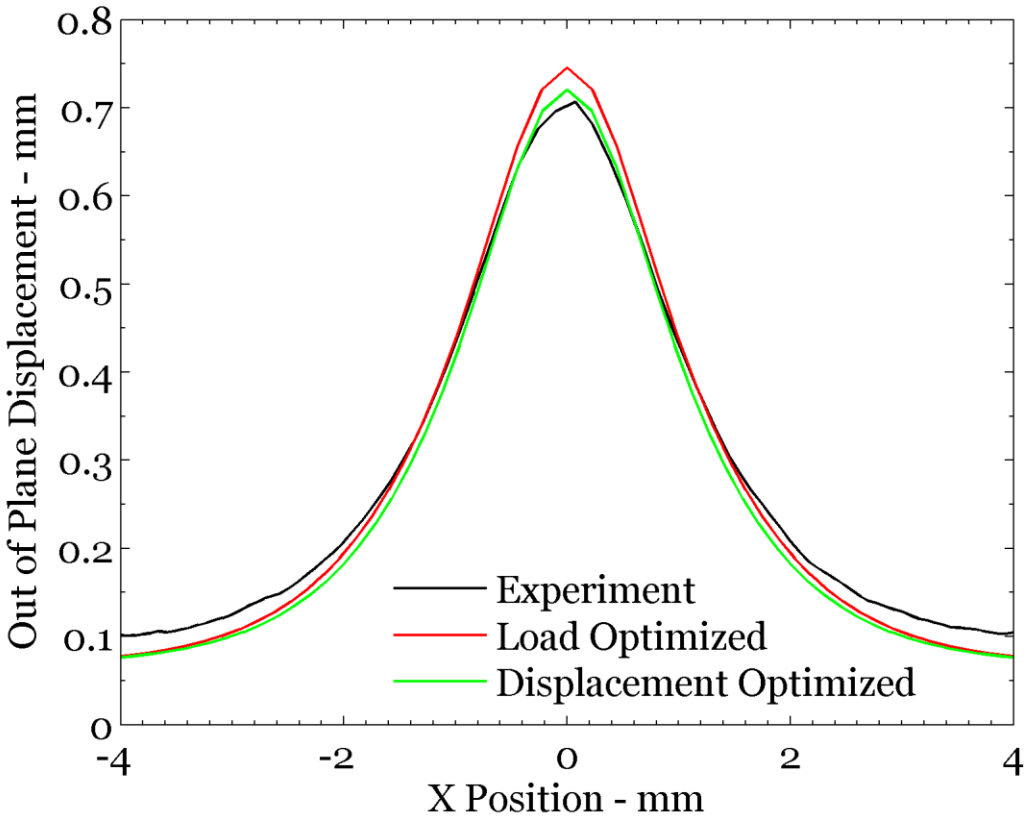

Figure 5.16: Out of plane displacement on the midline of the side surface in the necked region. The displacement optimized material matches the experimental result much closer than the load optimized material does.

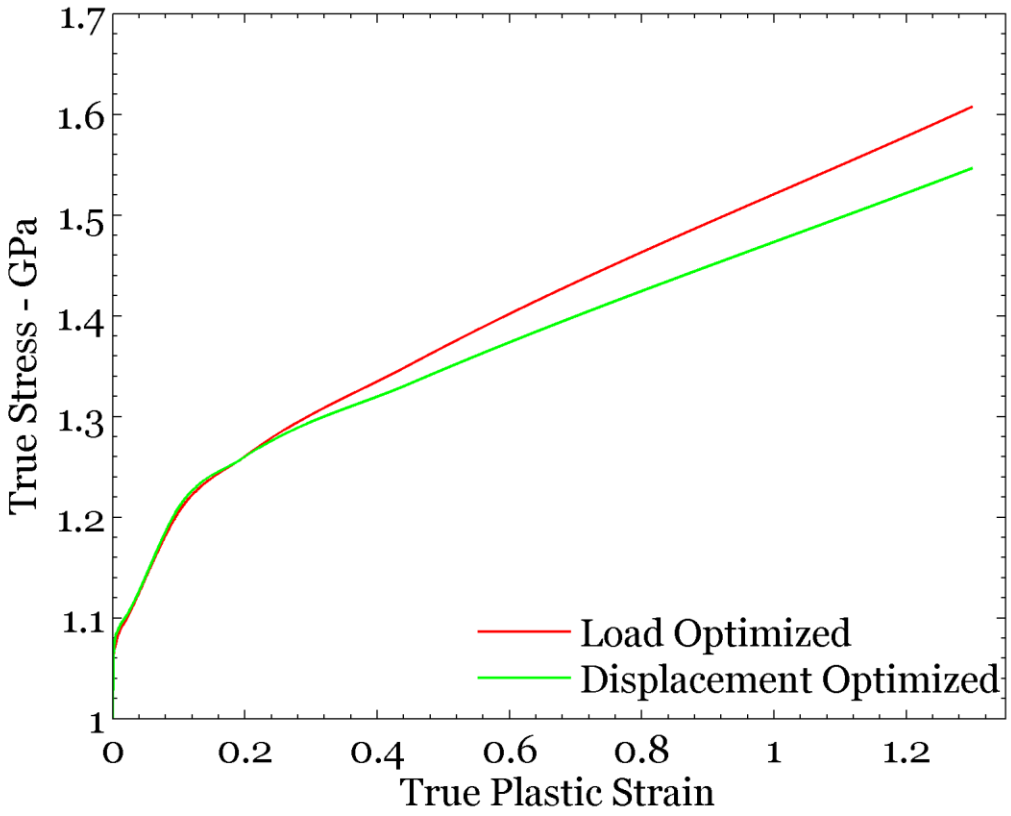

Figure 5.17: Strain hardening behavior for load and displacement optimized materials. The displacement optimized material is more compliant at high strains. The tangent modulus of the load optimized material is almost 25% stiffer at a (logarithmic) plastic strain of 0.5.

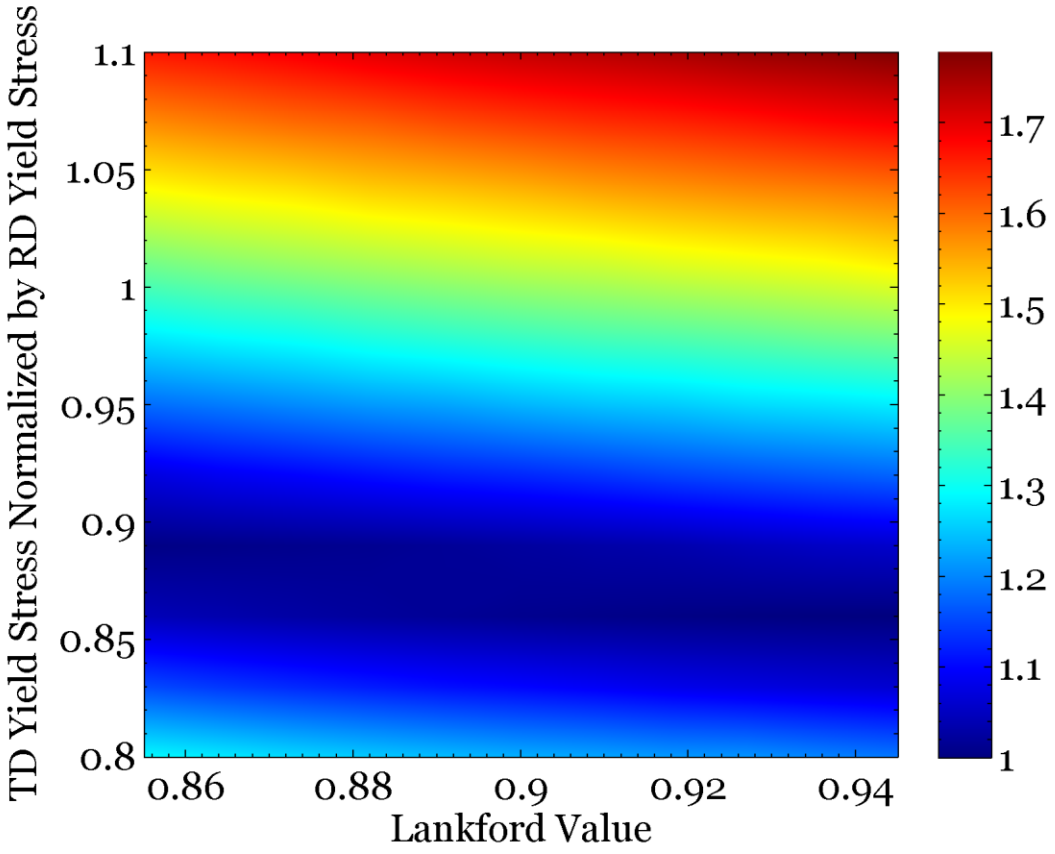

Figure 5.18: (a) Sensitivity of the displacement blind objective function to changes in the model parameters that define anisotropy. Data was produced using the load optimized strain hardening behavior and the values are normalized by the minimum. This objective function is not sensitive to changes in Lankford's value.

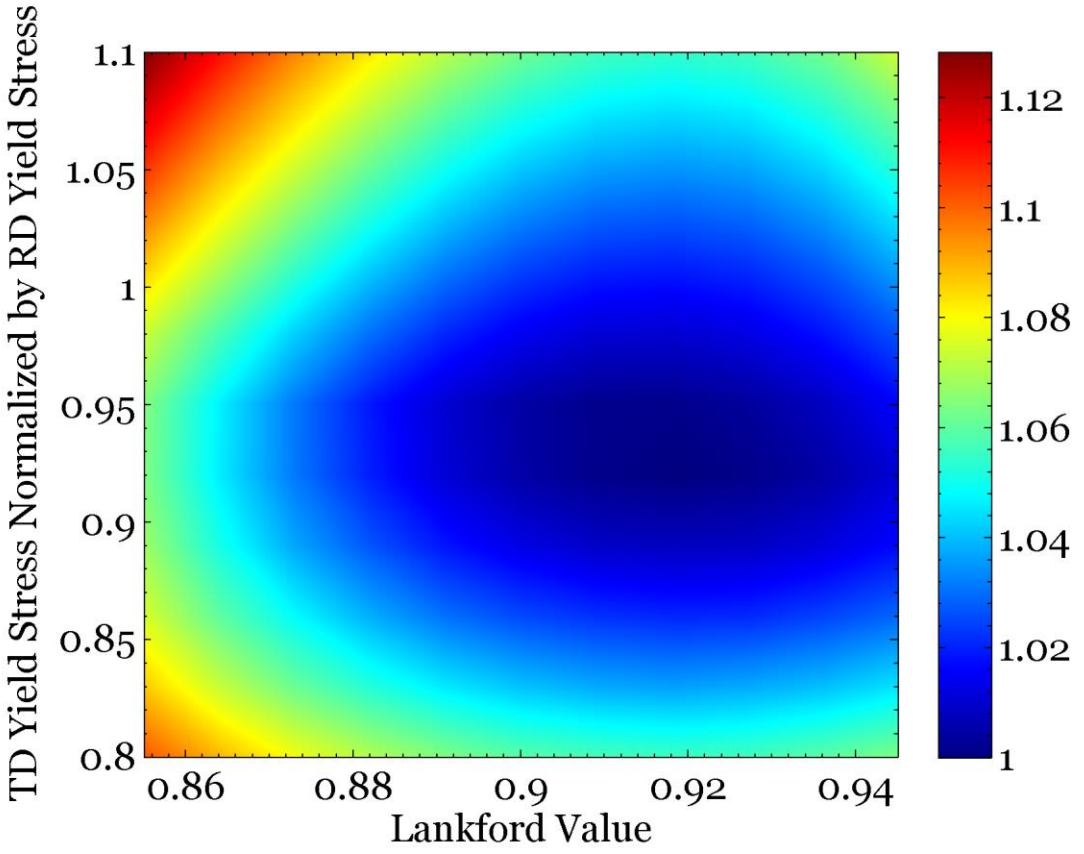

Figure 5.18: (b) Sensitivity of the displacement aware objective function to changes in the model parameters that define anisotropy. Data was produced using the displacement optimized strain hardening behavior and the values are normalized by the minimum. This objective function is sensitive to both parameters that define anisotropy.

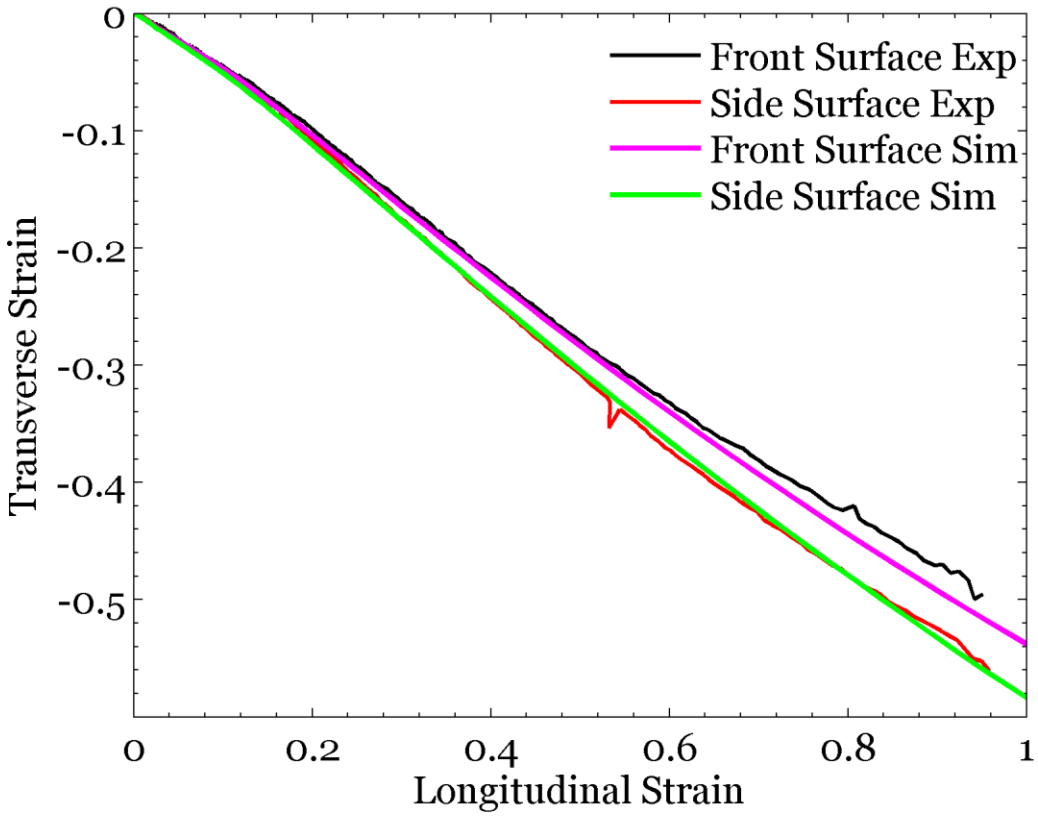

Figure 5.19: Variation of the transverse strain with respect to longitudinal strain at the deepest point in the neck on the front and side surfaces. The results from the simulation with the displacement-optimized material parameters are overlaid on the experimental measurement.

Chapter 6: Conclusion

6.1 SUMMARY

Several aspects related to the prediction of ductile failure have been investigated. Specifically, the failure mechanisms in Al 6061-T6 sheet have been investigated in detail through loading with *in situ* SEM imaging, complete predictions of ductile failure have been performed to assess where improvements are necessary, and a general method for using local deformation data to extract constitutive models from large experimental data sets has been developed. The findings from these separate, yet related studies, illuminate a consistent picture of the ductile failure process and make clear what is essential and what is unnecessary to model ductile failure.

The *in situ* testing of Al 6061-T6 unambiguously shows the large strain, in excess of 2.5, that can be endured by this material in shear dominated loading. It has been demonstrated that the material response is matrix dominated and that strain hardening continues unabated, even up to this very high level of strain. The voids initially present in the microstructure show little evolution with deformation, and are not found to be important for either deformation or failure. The second phase particles are observed to crack and debond as a deformation mechanism, as the resulting cavities halt growth once compatibility with the matrix deformation is achieved. As a whole, it has been shown that no damage mechanisms exist for this material under shear dominated loading.

The modeling implication gleaned from *in situ* testing is that continuum damage models are unnecessary and are based on mechanisms that do not even exist in some materials. Thus, implementation of a simpler class of models, strain-to-failure models, is better suited for the prediction of ductile failure. The successful blind prediction of the

failure behavior for a novel sample in the first Sandia Fracture Challenge has verified the efficacy of strain-to-failure models for this purpose. The effectiveness of these models is also supported by the quality of the prediction in the second Sandia Fracture Challenge, however, this exercise has also emphasized the need for highly accurate plasticity modeling in order to make robust failure predictions.

In order to reduce the experimental effort required to calibrate a highly accurate plasticity model, local field measurements in addition to conventional global measurements have been used for inverse plasticity model calibration. The inclusion of local deformation data is shown to have a significant effect on model calibration. For tensile test data enriched with displacement measurements on two surfaces of the specimen, this data is able to constrain an anisotropy model that is insensitive to the global measurements alone.

6.2 Future Work

The *in situ* testing of a variety of materials is essential to verify the applicability of the conclusions made here for a particular form of aluminum to other alloys of the same base metal and different metals altogether. It would be particularly interesting to include a material that may exhibit voiding in this study, such as Ti-6Al-4V, to determine the conditions that cause void growth and the effect that a dilute void population has on the material, although such a phenomenon may only occur in a minority of materials. Also, testing with larger specimens, where the deformation gradient is on a far larger scale than the microstructure would provide a wealth of quantitative data about the mechanisms identified in the current work. Also, the use of X-ray tomography is needed to verify whether the mechanisms observed on the surface also occur in the interior.

Further opportunities also exist to refine the use of local field data for inverse calibration of material models. A study of objective functions is essential to determine the characteristics of a function that is optimal for mapping experimental observation to constitutive model parameterization. Then, the design and use of a test specimen that can span a large swath of the stress space in a single test up to high levels of strain should be performed. Such a specimen, or suite of specimens, will decrease the number of experiments required to calibrate sophisticated plasticity models. A constitutive model calibrated with this reduced experimental program should be validated against a separate calibration using the full set of experiments required for direct calibration.

References

Aleksandrovic S, Stefanovic M, Adamovic D, and Lazic V (2009), Variation of Normal Anisotropy Ratio r during Plastic Forming. *Strojniški vestnik*, *55*(6), 392-399.

Avril S, Bonnet M, Bretelle AS, Grediac M, Hild F, Ienny P, Latourte F, Lemosse D, Pagano S, Pagnacco E, and Pierron, F (2008), Overview of identification methods of mechanical parameters based on full-field measurements. *Experimental Mechanics*, *48*(4), 381-402.

Babout L, Maire E, Buffière J, Fougères R, (2001), Characterization by x-ray computed tomography of decohesion, porosity growth and coalescence in model metal matrix composites. *Acta Materialia*, **49**(11), 2055–2063

Bao Y and Wierzbicki T (2004), On fracture locus in the equivalent strain and stress triaxiality space, *International Journal of Mechanical Sciences*, **46**, 81-98.

Barbe F, Decker L, Jeulin D, and Cailletaud G (2001), Intergranular and intragranular behavior of polycrystalline aggregates. Part 1: FE model. *International journal of plasticity*, *17*(4), 513-536.

Barbe F, Forest S, and Cailletaud G (2001), Intergranular and intragranular behavior of polycrystalline aggregates. Part 2: Results. *International journal of plasticity*, *17*(4), 537-563.

Beese AM, Luo M, Li Y, Bai Y and Wierzbicki T (2010), Partially coupled anisotropic fracture model for aluminum sheets, *Engineering Fracture Mechanics*, **77**, 1128-1152.

Bernauer G and Brocks W (2002), Micro-mechanical modelling of ductile damage and tearing – results of a European numerical round robin, *Fatigue and Fracture in Engineering Materials and Structures*, **25**, 363-384.

Boyce BL… Gross AJ, Gharimaninezhad AJ, Ravi-Chandar K,…et al. (2014), The Sandia Fracture Challenge: blind predictions of ductile tearing, *International Journal of Fracture*, **186**, 5-68.

Boyce BL, et al. (2015), The Second Sandia Fracture Challenge: predictions of ductile failure under quasi-static and moderate-rate dynamic loading, *International Journal of Fracture*, submitted.

Bridgman, PW (1952), *Studies in large plastic flow and fracture*. New York: McGraw-Hill.

Carroll JD, Abuzaid WZ, Lambros J and Sehitoglu H (2013), On the interactions between strain accumulation, microstructure and fatigue crack behavior, *International Journal of Fracture*, **180**, 223-241.

Chen WH (1971), Necking of a bar, *International Journal of Solids and Structures*, **7**, 685-717.

Cooreman S, Lecompte D, Sol H, Vantomme J, and Debruyne D (2008), Identification of mechanical material behavior through inverse modeling and DIC. *Experimental Mechanics*, *48*(4), 421-433.

du Preez PF and Maré E (2013), Interpolating yield curve data in a manner that ensures positive and continuous forward curves, *South African Journal of Economics and Management Sciences,* **16**, 395-406.

Fratini L, Lombardo A, and Micari F (1996), Material characterization for the prediction of ductile fracture occurrence: an inverse approach, *Journal of Materials Processing Technology*, **60**, 311-316.

Fritsch FN and Carlson RE (1980), Monotone piecewise cubic interpolation, *SIAM Journal of Numerical Analysis*, **17.2**, 238-246.

Fukuhara M and Sanpei A (1993), Elastic moduli and internal frictions of Inconel 718 and Ti-6Al-4V as a function of temperature, *Journal of Materials Science Letters*, **12**, 1122-1124.

Hill R, (1948), A theory of the yielding and plastic flow of anisotropic metals, *Proceedings of the Royal Society of London Series A – Mathematical and Physical Sciences*, **193**, 281-297.

Gelin JC and Ghouati O (1995), An inverse method for material parameters estimation in the inelastic range, *Computational Mechanics*, **16**, 143-150.

Ghouati O and Gelin JC (1998), Identification of material parameters directly from metal forming processes, *Journal of Materials Processing Technology*, **80-81**, 560-564.

Ghahremaninezhad A and Ravi-Chandar K (2011) Ductile failure in polycrystalline OFHC copper, *International Journal of Solids and Structures*, **48**, 3299-3311, 2011

Ghahremaninezhad A and Ravi-Chandar K (2012), Ductile failure behavior of polycrystalline Al 6061-T6, *International Journal of Fracture*, **174**, 177-202.

Ghahremaninezhad A and Ravi-Chandar K (2013), Ductile failure behavior of polycrystalline Al 6061-T6 under shear dominant loading, *International Journal of Fracture*, **180**, 23-39.

Ghahremaninezhad A and Ravi-Chandar K (2013), Crack nucleation under shear dominant loading, *International Journal of Fracture*, **184**, 253-266.

Gross AJ and Ravi-Chandar K (2014), Prediction of ductile failure using a local strain-to-failure criterion, *International Journal of Fracture*, **186**, 69-91.

Gross AJ and Ravi-Chandar K (2015), On the extraction of elastic-plastic constitutive properties from three-dimensional deformation measurements, *Journal of Applied Mechanics*, **82, 071013**.

Haltom SS, Kyriakides S, and Ravi-Chandar K (2013), Ductile failure under combined shear and tension, *International Journal of Solids and Structures*, **50**, 1507-1522.

Helfen L, Morgeneyer T, Xu F, Mavrogordato M, Sinclair I, Schillinger B, Baumbach T (2012) Synchrotron and neutron laminography for three-dimensional imaging of devices and flat material specimens, *International Journal of Materials Research*, **2012**(2), 170–173

Hill R, (1948), A theory of the yielding and plastic flow of anisotropic metals, *Proceedings of the Royal Society of London Series A – Mathematical and Physical Sciences*, **193**, 281-297.

Johnson GR and Cook WH (1985), Fracture characteristics of three metals subject to various strains, strain rates, temperatures and pressures, *Engineering Fracture Mechanics*, **21**, 31-48.

Kanit T, Forest S, Galliet I, Mounoury V, Jeulin D (2003), Determination of the size of the representative volume element for random composites: statistical and numerical approach, *International Journal of Solids and Structures*, **40**, 3647-3679.

Kajberg J and Lindkvist G (2004), Characterization of materials subjected to large strains by inverse modeling based on in-plane displacement fields, *International Journal of Solids and Structures*, **41**, 3439-3459.

Kammers AD and Daly S (2013), Digital image correlation under scanning electron microscopy: methodology and validation. *Experimental Mechanics*, ***53***(9), 1743-1761.

Lesuer DR, Kay GJ, LeBlanc MM (2001), Modeling large strain, high-rate deformation in metals. UCRL-JC-134118, Lawrence Livermore National Laboratory.

Nahshon K and Hutchinson, JW (2008), Modification of the Gurson model for shear, *European Journal of Mechanics - A/Solids*, **27A**, 1-17.

Mahnken R and Stein E (1994), The parameter identification for visco-plastic models via finite-element-methods and gradient-methods, *Modeling and Simulations in Materials Science and Engineering*, **2**, 597-616.

Mahnken R and Stein E (1996), A unified approach for parameter identification of inelastic material models in the frame of the finite element method, *Computational Methods in Applied Mechanics and Engineering*, **136**, 225-258.

McClintock FA (1968), A criterion for ductile fracture by the growth of holes, *Journal of Applied Mechanics*, **35**, 363-371.

Meuwissen MHH, CWJ Oomens, FPT Baaijens, R Petterson and JD Janssen, (1998) Determination of the elasto-plastic properties of aluminum using a mixed numerical-experimental method, *J Materials Processing Technology*, **75**, 204-211

Needleman A (1972), A numerical study of necking in circular cylindrical bars, *Journal of the Mechanics and Physics of Solids*, **20**, 111-127.

Norris DM, Moran B, Scudder JK, and Quinones DF (1978), A computer simulation of the tension test, *Journal of the Mechanics and Physics of Solids*, **26**, 1-19.

Orowan E (1948), Fracture and strength of solids, *Report on Progress in Physics*, **12**, 185-232.

Peirs J, Verleysen P, and Degrieck J (2012), Novel technique for static and dynamic shear testing of Ti6Al4V sheet, *Experimental Mechanics*, **52**:7, 729-741.

Puttick KE, (1960), Shear component of ductile failure, *Philosophical Magazine*, **5**, 759-762.

Rice JR and Tracey DM (1969), On ductile enlargement of voids in triaxial stress fields, *Journal of the Mechanics and Physic of Solids*, **17**, 201-217.

Rice JR (1976), The localization of plastic deformation, in Proceedings of the 14th International Congress on Theoretical and Applied Mechanics, Delft, Vol.1, 207-220.

Sutton MA, Li N, Garcia D, Cornille N, Orteu JJ, McNeill SR, Schreier HW, and Li X (2006), Metrology in a scanning electron microscope: theoretical developments and experimental validation, *Measurement Science and Technology*, **17**:10, 2613.

Tardif N and Kyriakides S (2012), Determination of anisotropy and material hardening for aluminum sheet metal, *International Journal of Solids and Structures,* **49**, 3496-3508.

Tipper CF (1949), The fracture of metals, *Metallurgia*, **39**, 133-137.

Velay V, Robert L, et al., (2007), Behaviour model identification based on inverse modeling and using optimal full field measurements: application on rubber and steel, *AIP Conference Proceedings*, **907**, 33-38.

Yin Q, Soyarslan C, Isik K, and Tekkaya AE (2015), A grooved in-plane torsion test for the investigation of shear fracture in sheet materials, *International Journal of Solids and Structures*, **66**, 121-132.

Zhang WJ, Reddy BV, and Deevi SC (2001), Physical properties of TiAl-base alloys, *Scripta Materialia*, **45**, 645-651.